

UNCLASSIFIED

---

AD **256 559**

---

*Reproduced  
by the*

ARMED SERVICES TECHNICAL INFORMATION AGENCY  
ARLINGTON HALL STATION  
ARLINGTON 12, VIRGINIA



**BEST  
AVAILABLE COPY**

---

UNCLASSIFIED

NOTICE: When government or other drawings, specifications or other data are used for any purpose other than in connection with a definitely related government procurement operation, the U. S. Government thereby incurs no responsibility, nor any obligation whatsoever; and the fact that the Government may have formulated, furnished, or in any way supplied the said drawings, specifications, or other data is not to be regarded by implication or otherwise as in any manner licensing the holder or any other person or corporation, or conveying any rights or permission to manufacture, use or sell any patented invention that may in any way be related thereto.

AD-256559

WADD Technical Report 01-78

STELLAR ABERRASCOPE STUDY

FINAL REPORT

R. Lillestrand	C. Grosch
J. Hamilton	J. Carroll
R. Carlson	J. McGillicuddy
C. Eumurian	G. Beck

Mechanical Division of  
GENERAL MILLS, INC.  
Minneapolis 13, Minnesota

Contract No. AF 33(616)-7400

DECEMBER 1960

NAVIGATION AND GUIDANCE LABORATORY  
WRIGHT AIR DEVELOPMENT DIVISION  
WRIGHT-PATTERSON AIR FORCE BASE  
UNITED STATES AIR FORCE  
OHIO

XEROX

\$ 15.00

355 900

STELLAR ABERRASCOPE STUDY

FINAL REPORT

R. Lillestrand	C. Grosch
J. Hamilton	J. Carroll
R. Carlson	J. McGillicuddy
C. Eumurian	G. Beck

Mechanical Division of  
GENERAL MILLS, INC.  
Minneapolis 13, Minnesota

101-3-2  
XEROX

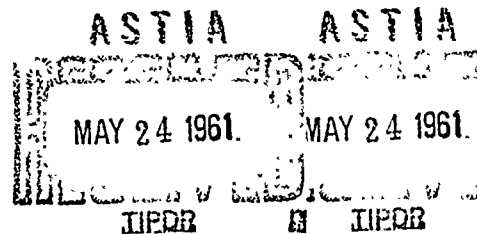
DECEMBER 1960

GMI Report No. 2141

Navigation and Guidance Laboratory

Contract Nr AF 33(616)-7400  
Project Nr 5216  
Task Nr 50855

WRIGHT AIR DEVELOPMENT DIVISION  
AIR RESEARCH AND DEVELOPMENT COMMAND  
UNITED STATES AIR FORCE  
WRIGHT-PATTERSON AIR FORCE BASE, OHIO

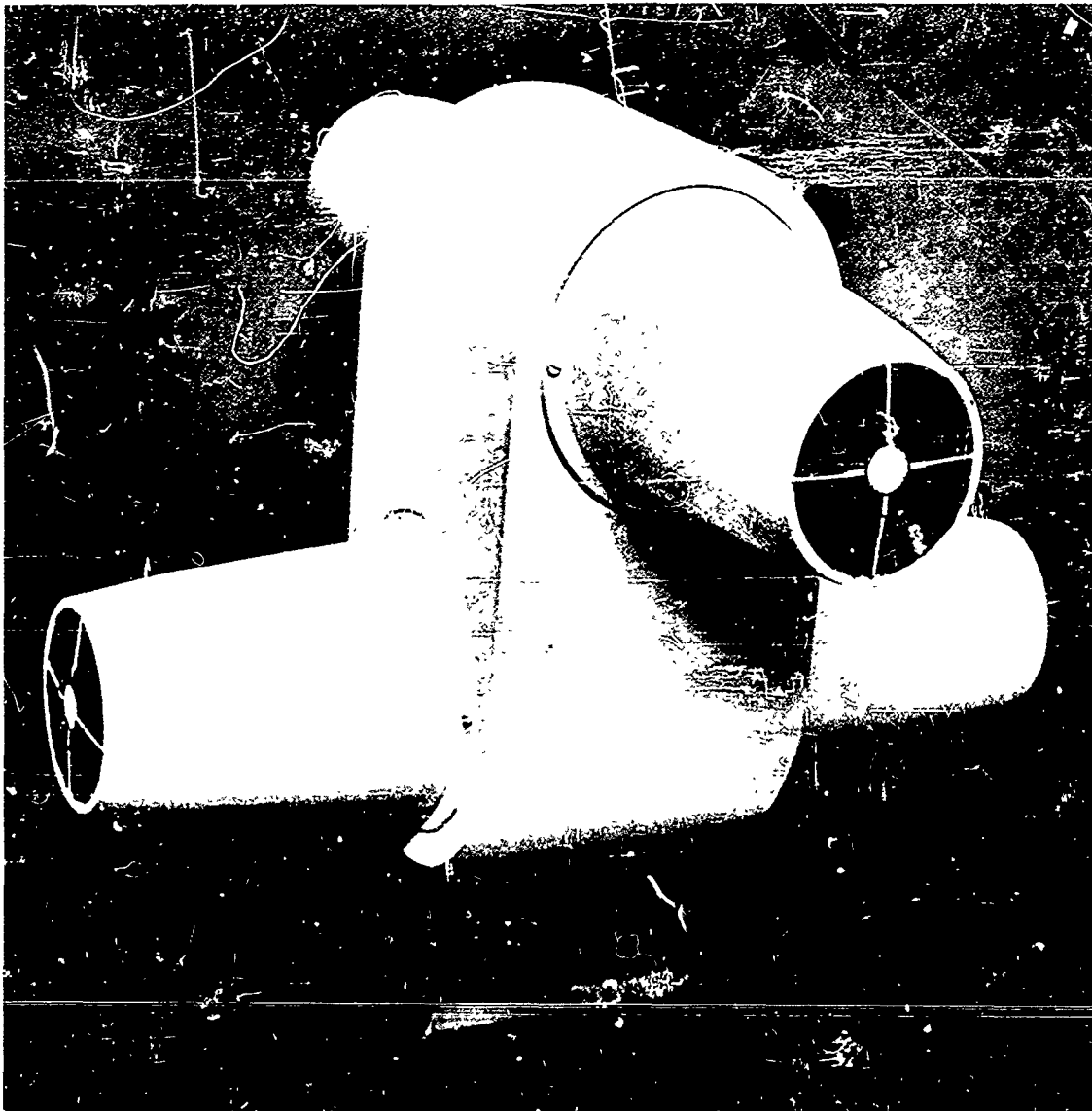


NOTICES

When Government drawings, specifications, or other data are used for any purpose other than in connection with a definitely related Government procurement operation, the United States Government thereby incurs no responsibility nor any obligation whatsoever; and the fact that the Government may have formulated, furnished, or in any way supplied the said drawings, specifications, or other data, is not to be regarded by implication or otherwise as in any manner licensing the holder or any other person or corporation, or conveying any rights or permission to manufacture, use, or sell any patented invention that may in any way be related thereto.

Qualified requesters may obtain copies of this report from the Armed Services Technical Information Agency, (ASTIA), Arlington Hall Station, Arlington 12, Virginia.

Copies of WADD Technical Reports and Technical Notes should not be returned to the Wright Air Development Division unless return is required by security considerations, contractual obligations, or notice on a specific document.



Model of Aberrascope

FOREWORD

This report was prepared by General Mills, Inc., Minneapolis, Minnesota, on Air Force contract AF33(616)-7400, under Task Nr 50855 of Project Nr 5216, "Stellar Aberrascopes Study Final Report". The work was administered under the direction of the Navigation and Guidance Laboratory, Wright Air Development Division. Captain David May and Mr. John Zing provided technical cognizance for the laboratory.

The studies presented began in June 1960, were concluded in December 1960, and represent an effort of the Tracking and Control Laboratory, Engineering Department, General Mills, Inc. Charles Eumurian was the engineer responsible for directing the study.

Although the study was a group effort, the chief contributors and their fields of interest were: R. Lillestrand, concept design; C. Eumurian, J. McGillicuddy, and G. Beck, mechanization; J. Hamilton, detectors; R. Ginsberg, optics; R. Carlson, instrumentation; J. Carroll, error analysis; and C. Grosch, system analysis.

This report concludes the work on contract AF33(616)-7400.

ABSTRACT

A satellite orbiting about a celestial body, equipped with a device for star tracking, will observe that the stars sometimes pass behind or emerge from the limb of the body. It is shown that a measurement of the times of six independent horizon star transits will permit the determination of the six parameters of the satellite orbit with respect to inertial space. From the orbital elements, the altitude and sub-satellite point can be determined as a function of time in a self-contained manner.

Since the topographic irregularities of the planetary surface and the variability of the atmospheric transmission due to clouds and other sources of attenuation in the atmosphere might introduce large errors into the transit time measurement, it is proposed that star transit measurements be made while the light ray is still high in the atmosphere. The time of star transit can then be defined as that instant at which the refraction or the attenuation of a star image has built up to some predetermined value. Each celestial body requires special study based on the characteristics of its atmosphere - if it has any. In the case of the earth an investigation has been made of the use of atmospheric refraction or spectral absorption at altitudes ranging from 100,000 to 200,000 feet. As a result it appears that rms errors in the altitude of the constant density surface will not exceed a distance of one mile.

In contrast with spectral absorption which is a scalar quantity, the atmospheric refraction is a two dimensional vector. Thus, by measuring the direction of the refraction in inertial space as well as using its magnitude to derive the transit time measurement, it is possible to derive all of the orbital elements with only three independent horizon star transits. If we can assume that the



orbit is circular to an acceptable degree of approximation, it is possible to derive all of the information necessary for a self-contained navigation system from only one star transit. This can be done by measuring the two components of the refraction vector plus the time rate of change of refraction.

An error analysis has shown that typically this technique will enable us to define our position to within about two miles for an earth satellite if each rms transit time error is one-tenth of a second. Error sensitivity coefficients are shown for various orbital planes. Of particular note is the fact that the orbital period can be determined with extreme accuracy, and therefore the semi-major axis of the satellite orbit can be calculated to an accuracy considerably better than one mile.

By means of additional star transits or by measuring the time of passage into and out of the shadow caused by the sun, it is possible to define more than the six basic parameters. The two or three parameters of an aspherically shaped isorefraction surface can be derived, thereby giving an estimate of the shape of the central body. If the planet is a spheroid, the spatial orientation of the axis of symmetry can be computed. In addition, an independent determination can be made of the mass of the planet.

The refraction measuring instrument (aberrascopes) consists essentially of a pair of opposed optical systems which are attached to a central housing containing the error detection system. The identical optical systems are the Dahl-Kirkham type with a 100 inch focal length, 4 inch aperture and 8 inch separation between the secondary and the primary mirrors. Vycor brand glass will be used for the mirrors and 36% Nickel (Invar) will be used for the optical system housing. The wall thickness of the conical optical housing will be 0.05 inches,

this thickness will be sufficient to meet the rigidity and vibration requirements. The housing for the central portion of the aberrascope will be fabricated of lighter materials than Invar in order to reduce the over-all weight. The over-all length of one aberrascope is envisioned as being 24 inches. A system of two aberrascopes is pictured in the frontispiece and the over-all dimensions are 24 inches x 24 inches x 16 inches. It will probably weigh 50 pounds and consume 80 watts of power. The measurement accuracy of the instrument will be 0.1 seconds of time; it will essentially be a time measuring instrument. The over-all system accuracy which can be achieved is 2 miles or smaller (one sigma error).

In place of rotating the entire aberrascope, the knife edge error detector alone will be rotated. This gives the single-axis instrument a two-axis capability. The rotating knife edge can be made small and completely encapsulated in its own environment, thus avoiding the problems of rotating elements in a vacuum. The motor which will drive the rotor will be built right around the knife edge bar. The incoming stellar radiation will pass thru a window on the rotating error detector package and will impinge upon the rotating knife edge. From this knife edge, the stellar radiation will be reflected onto an ellipsoidal mirror which has alternate transparent and reflecting surfaces. Thus the energy will either be reflected or will pass thru the mirror. A second ellipsoidal mirror will reflect the energy which passes thru the first mirror into a second path. Thus the energy will ultimately arrive at one of two photomultiplier tubes, depending on the type of surface encountered at the first mirror.


It is difficult to abstract the rotating error detector: the body of this report must be studied in order to appreciate the salient features of this

device. This rotating error detector is the very heart of the aberrascope and its unique capability (in combination with the photomultiplier tubes) can be summed as follows:

1. The incoming radiation is used 100% of the time.
2. One photomultiplier tube can perform the entire tracking function exclusive of the operation of the other tube.
3. Chopping of the incoming radiation is performed by rotating the image, thus simplifying the system.
4. The rotating knife-edge operates in a sealed environment.

The entire rotating error detector package is translated with four servo drives into a null position where the stellar image impinges exactly on the center of the knife edge. The outputs of the aberrascope will then be the output of two interferometers which measure the translation of the center of the rotating error detector. When one star line-of-sight dips into the atmosphere, refraction will build up and one end of the rotating error detector will shift accordingly. When this motion (refraction) has built up to a prescribed level (8 to 10 seconds of arc), time will be recorded and an occultation will be said to have occurred.

The equations for determining the orbital parameters from the occultation times are given in the body of this report. The solution of these equations as well as the equations for determining the position over the earth from the orbital parameters will thus locate the sub-satellite point on the surface of the earth as well as indicate the altitude above the surface of the earth.

  
\_\_\_\_\_  
Manager  
Tracking and Control Laboratory

### RECOMMENDATIONS

As a result of the information contained in this report the following recommendations can be made at the present time:

- 1) Since the potential accuracy of the aberrascopes occultation technique is about ten times greater than the aberrascopes aberration technique, it is recommended that the occultation technique be used for low altitude self-contained earth satellite navigation systems.
- 2) Since long term thermal stability is not necessary when using the occultation technique, it is recommended that a non-rotating aberrascopes design be used. This will result in a considerable simplification in the instrument design.
- 3) Since the refraction measurement provides twice as much information at each star transit as does the spectral attenuation measurement and since the potential accuracy of the refraction technique is greater than the spectral attenuation measurement, it is recommended that the definition of star transit time be based on a purely refraction measuring instrument. It is also recommended that this instrument be designed to measure both the magnitude and direction of the refraction.
- 4) Since the effect of instrument errors is smaller if we track stars to low altitudes and since at these low altitudes there is a concomitant increase in scattered background radiation from the sun, it is recommended that we relax our diametricity requirement in the star selection in order to obtain brighter stars. If we consider stars deviating from diametricity by as much as  $2^\circ$ , we can hope to find pairs of  $M \leq 4$ . This reduction of about 3 magnitudes from the requirement for the aberration system will yield an increase of about 15 times in intensity. It will also tend to relax the initial acquisition problems.
- 5) Since the Rayleigh scattering drops off in a manner proportional to  $\lambda^{-4}$ , and since the sun's radiation peaks at  $\lambda = 5,000 \text{ \AA}$ , it is recommended that we investigate the use of photo multipliers or photo conductive cells for operation in the spectral region from 5,000 - 10,000 angstroms. This will call for a search for bright low-temperature stars in contrast with the high-temperature stars required for the precise tracking when making the aberration measurement.

- 6) Since the added instrumentation for measuring the time of passage into the earth's shadow will be minimal, it is recommended that we add to the basic star tracking system the capability of measuring the times of ingress or egress of the sun, and that this measurement be made in the region of the  $\text{CO}_2$  absorption line at 4.3 microns.
- 7) Since the principal value of our system lies in the fact that it can be made completely self-contained and since most viewing geometries will permit many more than six independent measurements, it is recommended that we immediately initiate an investigation of the requirements for a satellite-borne computer. The investigation of calculational procedures should take cognizance of the fact that the most accurate measurement will be the stellar transit time, the next most accurate the solar transit time, the next most accurate the direction of the refraction vector in inertial space and the least most accurate will be the measurement of refraction rate.
- 8) The measurement of the magnitude of the refraction to an accuracy of 0.25 to 0.5 seconds of arc will be sufficient to keep the instrument error equal to or less than the meteorological errors. However, the measurement of the direction of refraction should ideally be good to about  $1/2000$  radian in order to yield an error of 2 miles on the earth's surface. This implies an rms accuracy of 0.02 seconds of arc in a 40 second of arc refraction measurement. Because of the desirability of using the direction as well as the magnitude refraction information, it is therefore recommended that we attempt to achieve an accuracy of 0.05 to 0.1 seconds of arc when measuring the atmospheric refraction with the non-rotating aberrascope.

# TABLE OF CONTENTS

I. Introduction . . . . .	1
II. Guidance System Based on Measurement of Stellar Occultation Time .	3
A. Transit Time Measurement Only . . . . .	3
B. Maximum Information Derivation . . . . .	7
1. Time Measurement . . . . .	9
2. Direction of Refraction . . . . .	9
3. Time Function of Magnitude of Refraction . . . . .	10
C. Combination of Measurement Techniques . . . . .	11
III. Phenomenological Considerations . . . . .	14
A. Methods of Defining Transit Time . . . . .	14
1. Atmospheric Refraction . . . . .	15
2. Atmospheric Attenuation . . . . .	22
a. Absorption . . . . .	23
b. Scattering . . . . .	27
c. Differential Refraction . . . . .	29
d. Scattered Radiation from the Sun . . . . .	30
e. Emission from the Earth's Atmosphere . . . . .	35
f. Large-Scale Variation of Absorbing Components . . . . .	35
g. Small-Scale Variations of Absorbing Components . . . . .	36
B. Meteorological Data . . . . .	36
1. Atmospheric Density and Temperature . . . . .	36
a. Height Variation of 30 km Surface . . . . .	41
b. Height Variation of 48 km Density Surface . . . . .	42

# WADD Technical Report 61-78

c.	Data Calculations . . . . .	44
d.	Short Term Fluctuations . . . . .	46
2.	Atmospheric Spectral Absorption . . . . .	47
C.	Star Selection . . . . .	64
IV.	System Error Analysis . . . . .	78
A.	Physical Errors . . . . .	78
B.	System Equations for the Occultation Technique . . . . .	87
C.	Results of Error Analysis . . . . .	92
V.	Instrument Design . . . . .	102
A.	General Description . . . . .	102
B.	Optical System . . . . .	108
1.	Structural Analysis . . . . .	108
a.	Structural Deflections Under Static Forces . . . . .	111
b.	Evaluation of Deflections and Shapes . . . . .	126
c.	Weight Calculations . . . . .	127
d.	Conclusions from Static Load Analysis and Weight Calculations . . . . .	127
e.	Structural Response to Dynamic Loads . . . . .	134
(1)	Cantilever Beam Vibrations . . . . .	135
(2)	Thin Shell Vibrations . . . . .	139
(3)	Torsional Vibrations . . . . .	162
f.	Thermal Effects . . . . .	163
g.	Gyroscopic Torque . . . . .	163
h.	Summary and Conclusions . . . . .	166
2.	Detail Design . . . . .	168

C.	Rotating Error Detector . . . . .	172
1.	Principle of Operation . . . . .	172
2.	Optical System . . . . .	172
3.	Mechanical Configuration . . . . .	175
4.	Error Detector Logic . . . . .	179
a.	Polar Coordinate Logic . . . . .	180
b.	Cartesian Coordinate Logic . . . . .	184
c.	Synchrous Demodulation . . . . .	184
D.	Articulation of Rotating Error Detector . . . . .	191
1.	Detector Mounting . . . . .	191
2.	Detector Drive . . . . .	193
E.	Photomultiplier Configuration . . . . .	196
VI.	Configuration of Star Trackers . . . . .	202
	References . . . . .	210
	Distribution List . . . . .	212



## LIST OF ILLUSTRATIONS

FIGURE NO.	TITLE	PAGE NO.
1	Sources of Occultation . . . . .	4
2	Percentage of Celestial Sphere Occulted in One Rotation by Earth at Various Satellite Altitudes . . . . .	8
3	Combination of Measurements for Determination of Orbital Parameters . . . . .	12
4	Transit Velocity at Various Satellite Altitudes . . . . .	16
5	Estimated Total Atmospheric Refraction for Grazing Ray at Various Altitudes . . . . .	18
6	Sensitivity of Occultation Altitude to Error in Measurement of Atmospheric Refraction . . . . .	20
7	Refraction and Refraction Rate as a Function of Time for an Orbit of 300 Nautical Mile Altitude . . . . .	21
8	Ozone Absorption . . . . .	24
9	Molecular Oxygen Absorption . . . . .	25
10	Percentage Transmission of Light Horizontally Through Atmosphere . . . . .	28
11	Fractional Loss in Star Intensity . . . . .	31
12	Percentage Transmission Due to Differential Refraction in the Atmosphere . . . . .	32
13	Photoelectrons per Second at Various Occultation Altitudes .	34
14	Comparison of Instrument and Meteorological Errors . . . . .	40
15	Latitudinal Variation of Ozone Center of Gravity . . . . .	48
16	Seasonal Variation of Ozone Center of Gravity . . . . .	49
17	Spectral Absorption of Grazing Ray at Various Altitudes . .	52
18	CO <sub>2</sub> Absorption Path as a Function of Grazing Altitude for A Ray Passing Through the Atmosphere . . . . .	53

FIGURE NO.	TITLE	PAGE NO.
19	Altitudes at which 50% Attenuation of Solar Intensity is Obtained for Various Satellite Altitudes . . . . .	59
20	Altitudes at which 54% Attenuation of Solar Intensity is Obtained for Various Satellite Altitudes . . . . .	60
21	Correction Factors for Stars . . . . .	64a
22	Star Declination Selection for any $\Omega$ . . . . .	73
23	Star Declination Selection for $\Omega : \alpha + 135^\circ \leq \Omega \leq \alpha + 360^\circ$ . . . . .	74
24	Star Declination Selection for $\Omega : \alpha + 180^\circ \leq \Omega \leq \alpha + 360^\circ$ . . . . .	75
25	Time for Regression vs. Radius of Orbit . . . . .	77
26	In-Plane Star Pairs . . . . .	80
27	Error Sensitivity Coefficient $\frac{\partial \rho_s}{\partial \rho_o}$ at Various Satellite Altitudes . . . . .	83
28	Error Sensitivity Coefficient $\frac{\partial \rho_s}{\partial \rho_t}$ at Various Satellite Altitudes . . . . .	85
29	Error in Eccentricity $\sigma(e)$ vs. $\Omega$ . . . . .	95
30	Error in Argument of Perigee $\sigma(\omega)$ vs. $\Omega$ . . . . .	95
31	Error in Time of Perigee $\sigma(T_o)$ vs. $\Omega$ . . . . .	95
32	Error in Inclination $\sigma(i)$ vs. $\Omega$ . . . . .	96
33	Error in Angle to Line of Nodes $\sigma(\Omega)$ vs. $\Omega$ . . . . .	97
34	Aberrascopes Structural Arrangement . . . . .	110
35	Cantilever Beam Equivalent . . . . .	113
36	Conical Shell . . . . .	115
37	Moment of Inertia Consideration . . . . .	116
38	Beam Problem Parameters . . . . .	125
39	Deflection at End Position of Aberrascopes under $10^{-2} g$ Loading . . . . .	129
40	Slope at End Position of Aberrascopes under $10^{-2} g$ Loading . . . . .	130

FIGURE NO.	TITLE	PAGE NO.
41	Slope at Secondary Mirror Relative to Primary Mirror . . . .	131
42	Total Weight of Aberrascopes Configuration . . . . .	132
43	Circumferential Waves . . . . .	139
45	Axial Waves . . . . .	140
46	Location of Nodes . . . . .	140
47	Middle Surface Displacements . . . . .	142
48	Frequency of Vibration with No Axial Waves . . . . .	160
49	Frequency of Vibration with One Axial Wave . . . . .	161
50	Mass Moment of Inertia . . . . .	164
51	Aberrascopes Gyroscopic Reaction Torques . . . . .	165
52	Optical System for Aberrascopes . . . . .	171
53	Simplified Diagram of Error Detector . . . . .	173
54	Silvered Mirror Patterns . . . . .	174
55	Optical Conditions in Error Detector . . . . .	176
56	Circuit for Obtaining Polar Error Signals . . . . .	182
57	Filtered Output of Error Signals . . . . .	183
58	Diode Matrix, Sensor Count 1 . . . . .	185
59	Diode Matrix, Sensor Count 10 . . . . .	186
60	Diode Matrix, Sensor Count 28 . . . . .	187
61	Diode Matrix, Sensor Count 19 . . . . .	188
62	Circuit for Synchronous Demodulation . . . . .	189
63	Error Detector Support and Articulation System . . . . .	192
64	Drive Mechanism for Rotating Error Detector . . . . .	195
65	Reliability Comparison of Photomultiplier Arrangements . . .	198

FIGURE NO.	TITLE	PAGE NO.
66	Ratio of Probabilities of Failure . . . . .	199
67	Star Trackers for Satellite Attitude Control and Transit Time Measurements . . . . .	203
68	Occultation Boundaries for Various Numbers of Diametrically Opposed Star Pairs . . . . .	205
69	Star Tracker Geometry . . . . .	206
70	Occultation Boundaries for Two Star Tracker Arrangement for 300 Nautical Mile Orbit . . . . .	209

## I. INTRODUCTION

This report is the second and final report being submitted to the Wright Air Development Division in accordance with the requirements of Air Force contract number AF 33(616)-7400 which is entitled: "Theoretical Investigation of New or Unexplored Techniques for Recoverable Orbital Vehicles". The previous quarterly report presented an analysis of the guidance problem in the light of an aberration sensing instrument. The analysis of the various aspects of an aberration measuring instrument were given. At the same time, a preliminary analysis was given to the consideration of an instrument which measured occultation time for a given star. From the occultation time measurements, the orbital parameters and finally the position over the earth can be established.

While it was stated in the last quarterly report that the instrument design under consideration could be used for either the aberration or the occultation techniques, further study has shown the feasibility of changing some of the original instrument design characteristics in order to take full advantage of the occultation technique. This technique does have distinct advantages and its use will simplify the instrument design but will limit its use to the occultation method. The body of this report describes in detail the phenomenological basis on which the occultation measurements can be made. In addition, the salient features of the occultation instrument will be pointed out. The instrument is now called the "non-rotating aberrascope". In general two of these units, mounted 90° to each other, will be used for determination of the orbital parameters.

Again, as predicted in the last quarterly report, this report emphasizes the actual design of an instrument. Drawings of various portions of the instrument as well as detail specifications are "Manuscript released by the authors, December 1960, for publications as a WADD Technical Report."

included in this report. Some quotations on the cost of castings and other out-of-house purchased parts have been received. Thus, we are well prepared to move ahead into the prototype development as the next logical step in this satellite guidance program.

## II. GUIDANCE SYSTEM BASED ON MEASUREMENT OF STELLAR OCCULTATION TIME

A non-rotating aberrascope can be used to measure the times of transit of a star behind the earth, and it can provide information regarding the direction of the refraction in inertial space. With these measurements it is possible to determine all of the orbital elements by observing three star transits. If we add a number of simple infrared sensitive photoconductive cells to measure the time at which the satellite passes into and out of the earth's shadow, only two star transits are needed to determine the orbital elements.

By measuring the refraction rate or the intensity loss due to differential refraction, additional information can be obtained regarding the altitude of the satellite. These two measurements lead to greater errors than the stellar or solar transit time measurements, so they are expected to be used only in making first approximations of the orbital parameters.

### A. Transit Time Measurement Only

An observer stationed on a satellite can determine his orbital parameters by observing the times at which at least six known stars are occulted by the planet about which he is rotating. Having determined the parameters of his orbit he can predict his position relative to the planet as a function of time, and he therefore has a completely self-contained navigational system. The calculations and discussion given below reveal some of the factors involved in designing such a system.

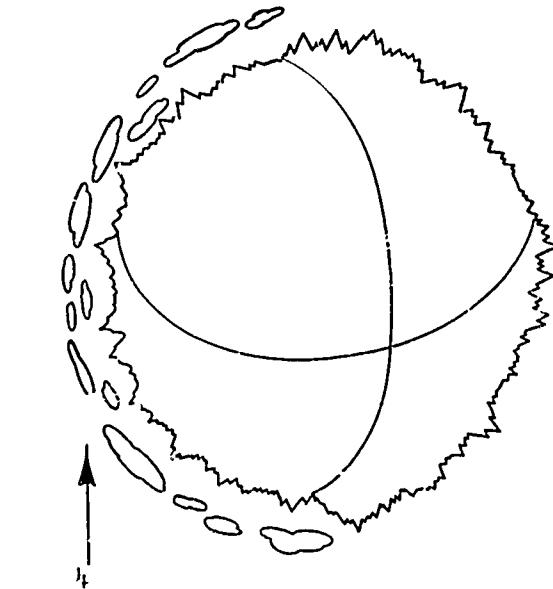
The first problem encountered with a navigation system based on the measurements of stellar occultation times is that of the irregular shape of the earth and the presence of clouds at various altitudes. These effects are illustrated in Figure 1. Since the highest mountains

Figure 1

SOURCES OF OCCULTATION

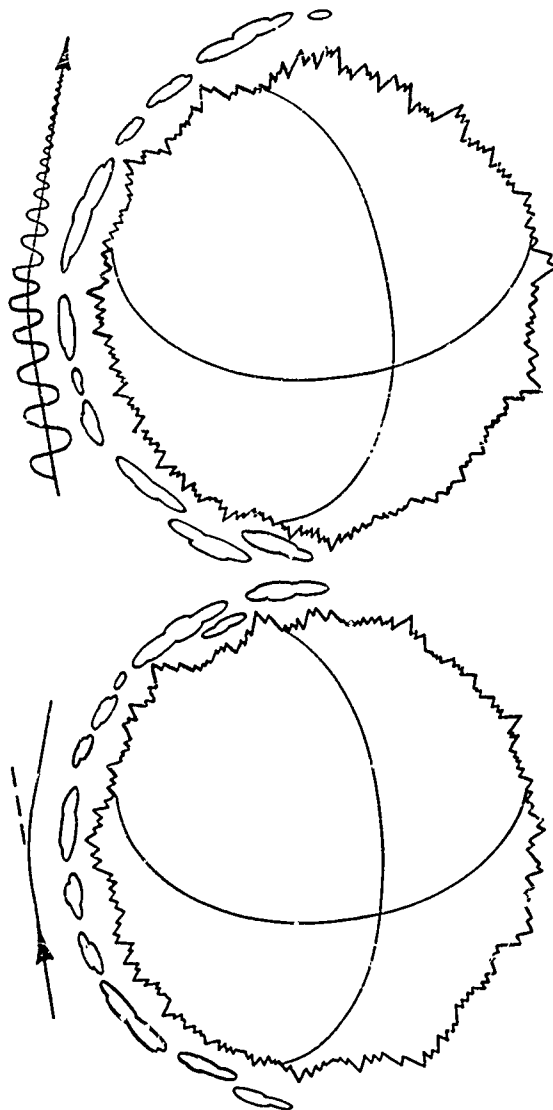
LESS THAN 10 MILES  
ABOVE SEA LEVEL

- a) mountains
- b) clouds



MORE THAN 10 MILES  
ABOVE SEA LEVEL

- a) atmospheric refraction
- b) atmospheric absorption and scattering





rise to more than five miles, a limitation to accuracy is immediately imposed. Clouds present an even greater source of error in that they are sometimes observed at altitudes in excess of ten miles. These two sources of error could be circumvented by using for occultations some phenomenon which lies at altitudes in excess of those where clouds are observed.

Two possibilities are shown in Figure 1. One of these is based on the measurement of atmospheric refraction and the other on the measurement of the atmospheric absorption of starlight in various spectral regions. These techniques will define an "occultation surface" surrounding the earth. This surface will be defined as the point at which the atmospheric refraction or the spectral absorption builds up to some predetermined value.

To obtain the ultimate accuracy achievable with the navigation system, an occultation surface must be selected possessing an altitude characteristic which can be accurately predicted. For example, if an occultation surface is used based on the absorption caused by ozone in the .20 to .29 micron region of the spectrum, an attenuation of the signal from the star of 50% might, on the average, be observed at an altitude of 115,000 feet (35 km.). But it is well known that the ozone composition of atmosphere undergoes extreme latitudinal and seasonal variation, and in order to achieve the best possible navigational accuracy it would be necessary to correct for these variations. If the altitude characteristic of the "occultation surface" were defined on the basis of atmospheric refraction, corrections due to seasonal and latitudinal variations in the temperature and density of the atmosphere would also have to be made; however, the isorefraction surfaces are not

expected to fluctuate as widely as the ozone isoabsorption surfaces.

If the satellite were rotating around a planet with an unknown mass, and if the altitude of the occultation surface is not known, an additional occultation measurement would be required for each of the additional parameters to be determined. For example, if one assumed that the occultation surface had the shape of an ellipsoid of revolution, two additional occultations would be needed to define the parameters of this surface. If the planet itself had an aspheric shape, this could also be determined with additional stars, however, a more accurate determination could probably be obtained by noting the secular variations in the longitude of the node and in the argument of the perigee over a large number of orbital rotations

Since the semi-major axes of the orbit is a function of the orbital period only, we have

$$a = \left[ \frac{T \rho_e g^{1/2}}{2\pi} \right]^{2/3} \quad \begin{array}{l} a = \text{Semi Major Axis} \\ T = \text{Period of Orbit} \\ \rho_e = \text{Radius of Earth} \\ g = \text{Gravity at Earth's Surface} \end{array} \quad (1)$$

and therefore by measuring the time from one occultation of a given star to the next occultation of this star, we can computer the semi-major axes in a particularly simple manner. In addition, the systematic errors in the measurement of occultation time cancel out in determining the orbital period, and thus this parameter can be determined with great accuracy.

From Equation (1), we can determine the accuracy with which the occultation time must be measured. If  $\sigma(a)$  is the rms error in the calculation of the semi-major axis and  $\sigma(T)$  the rms error in the measured orbital period, we can write

$$\frac{\sigma(T)}{T} = \frac{3}{2} \frac{\sigma(a)}{a} .$$

6

For low altitude earth satellite orbits,  $a \approx 4,000$  miles and  $T \approx 100$  minutes. Since the errors caused by the uncertainty in the altitude of the occultation surface are of the order of  $1/2$  m.m.e, the accuracy with which  $\sigma(T)$  should be measured in order to contribute a comparable error is  $\sigma(T) \approx 1$  second.

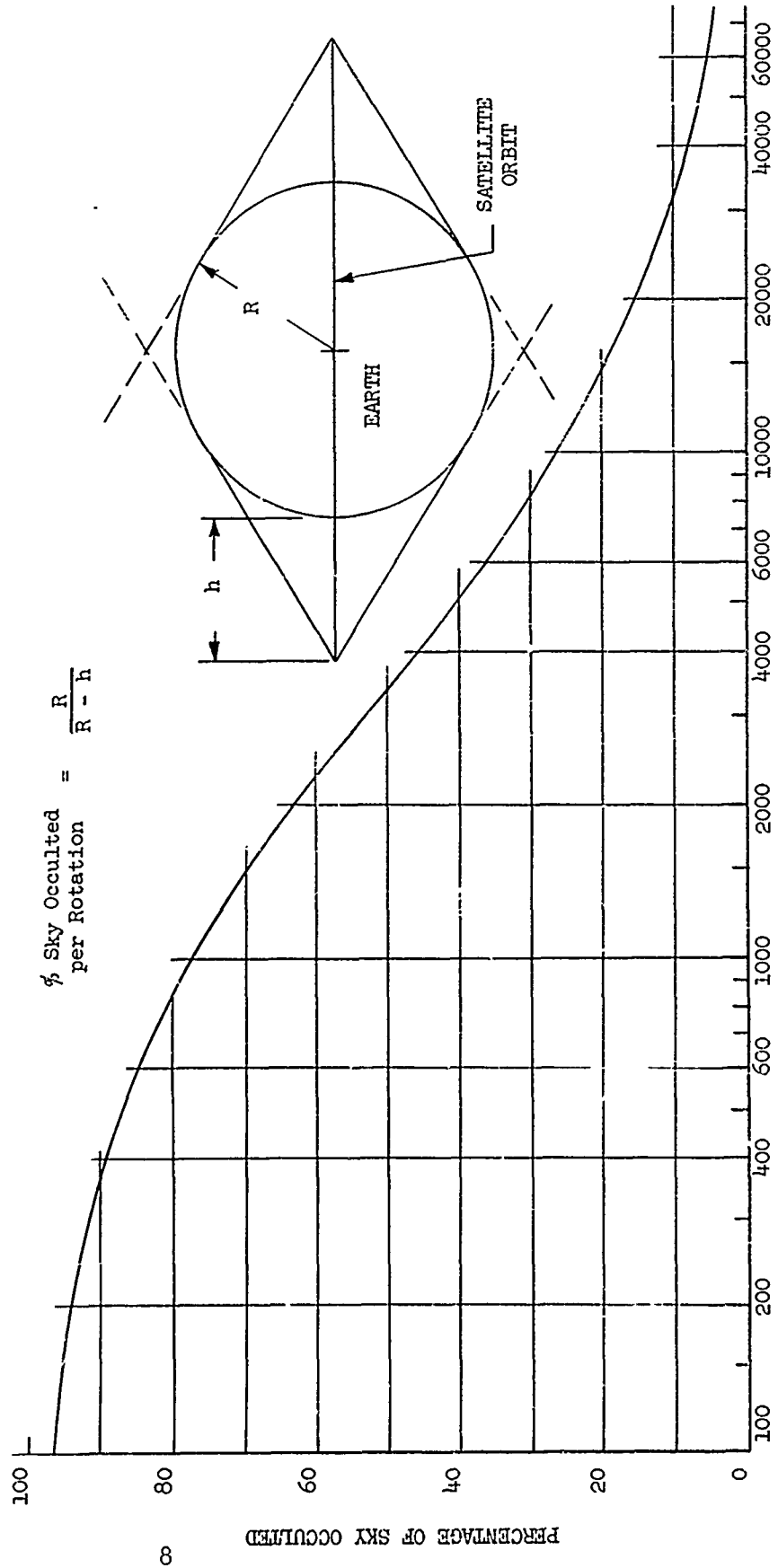
The occultation technique finds its greatest value for low altitude satellite orbits. This becomes evident from Figure (2) where we have shown the relation between the orbital altitude and the percentage of the sky occulted by the figure of the earth during one rotation of the satellite. For a circular orbit of 400 n. miles altitude, stars lying in 90 per cent of the sky will be occulted during each rotation, while for orbits of 40,000 miles altitude, only about 8 per cent of the sky is swept out during each rotation. This altitude problem is further compounded by the fact that orbits which are inclined relative to the earth's equator will undergo a nodal regression due to the oblateness of the earth. This results in certain periods in which those stars whose position are close to the axis of the orbital plane will undergo no occultation.

#### B. Maximum Information Derivation

Thus far we have considered the use of the occultation technique to form a self-contained navigation system in which only occultation time measurements are used to define the orbital parameters. The refraction measurement provides no more information than the spectral absorption as a means of defining the occultation event.

Refraction may, however, be regarded as a two dimensional vector having direction as well as magnitude - in contrast with spectral absorption which is purely a scalar quantity. Thus, the following

Figure 2  
 PERCENTAGE OF CELESTIAL SPHERE "OCCULTED" IN ONE  
 ROTATION BY EARTH AT VARIOUS SATELLITE ALTITUDES



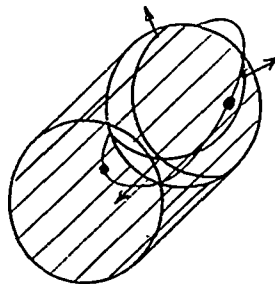
information can be derived from each occultation measurement if the atmospheric refraction is measured.

- 1) Occultation time, seconds,  $T$
- 2) Direction of refraction, radians,  $\beta$
- 3) Time function of magnitude of refraction,  $R(t)$

These are listed in order of accuracy from the standpoint of the self-contained determination of the orbital elements. If we are dealing with a circular orbit, it is possible to determine all of the elements of the orbit from a single star transit measurement in the following manner.

#### 1. Time Measurement

As a result of the measurement of the star transit time, we know that we are somewhere on the surface of an elliptical cylinder at the time of the star transit. This is shown below.



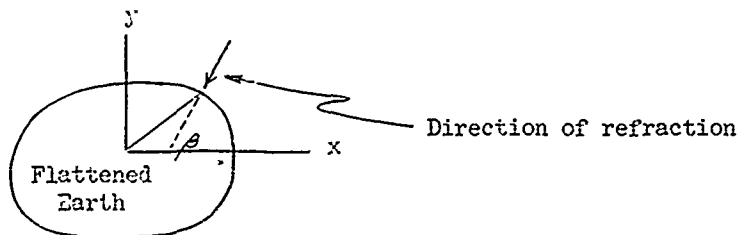
The direction of the axis of this cylinder is given by the position of the star we are tracking, its shape, by the shape of the isorefractive layer and, ultimately, by the shape of the earth.

The errors in the time measurement will not introduce an error of more than one or two miles.

#### 2. Direction of Refraction

Having established that we are somewhere on a certain cylinder, the measurement of the direction of the refraction enables us to determine that we are somewhere along a line on this cylinder - this line being

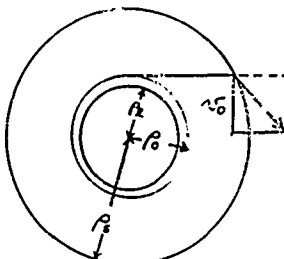
a straight one lying parallel to the axis of the elliptic cylinder.



If we can measure the refraction to 0".1 when the magnitude is 50"0, then the error in direction will be of the order of 1/1000 mins. At the radius of the earth this will correspond to about  $3600/500 = 7$  n. miles error in position.

### 3. Time Function of Magnitude of Refraction

By measuring the rate of change of refraction it is possible to estimate the semi major axis of the orbit (assumed in this case to be circular).



$$v_0 = \frac{\rho_e g^{1/2} (\rho_s^2 - \rho_0^2)^{1/2}}{\rho_s^{3/2}}$$

Where we know  $\rho_0$ ,  $g$  and  $\rho_e$  directly, we can solve for  $v_0$  as follows.

The atmospheric refraction may be written

$$R = K_0 \exp[-K_1(\rho_t - \rho_0)]$$

$$R = -K_0 R \dot{\rho}_t = -K_0 R v_0$$

$$\therefore v_0 = -R/K_0 R$$

Since we can measure  $R$  and  $\dot{R}$ , we can compute  $v_0$ . Knowing  $v_0$  we can compute  $\rho_s$ .

At  $R = 50 \text{ sec.}$ , the value of  $\dot{R}$  is probably of the order of  $50 \text{ sec/sec.}$  Probably  $\delta R$  could be held to  $0.1 \text{ sec.}$ , but  $\delta \dot{R}$  will probably be of the order of  $1 \text{ sec/sec.}$

This means that  $\frac{\delta v_0}{v_0} \approx 2 \times 10^{-2}$ . From Figure (4) it can be shown that for a 300 mile orbit  $\frac{\Delta v}{\Delta h} = \frac{2,000 \text{ ft/sec}}{150 \text{ miles}} = 17 \text{ ft/sec/mile}$

Since  $v_0 \doteq 9,000 \text{ ft/sec}$

$$\delta v_0 = 180 \text{ ft/sec}$$

and therefore  $\delta h = \frac{1 \text{ mile}}{17 \text{ ft/sec}} (180 \text{ ft/sec})$

$$\delta h \doteq 10 \text{ miles}$$

### C. Combinations of Measurement Techniques

The basic navigation technique under consideration is that of the measurement of star transit times, but the foregoing discussion leads to the consideration of several other measurements which, when combined with the basic technique, yield either

- 1) additional parameters, such as the mass of the planet or the shape of the transit surface,
- 2) a complete determination of the s.s.x orbital parameters in less than one complete rotation of the satellite, or
- 3) a more accurate determination of the orbital elements by selecting the calculation technique yielding the smallest values of the error sensitivity coefficients.

Figure (3) contains a summary of the various combinations of measurements. In this figure one series contains the cases in which only the times of ingress are measured; another series contains the cases in which the ingress times plus the times of egress occur in the earth's shadow (reacquisition is a problem if the egress occurs in an atmosphere illuminated by the sun); the last case contains the general solution in which all ingresses and egresses are included. In each of

Figure 3

COMBINATIONS OF MEASUREMENTS WHICH FORM THE BASIS  
FOR THE DETERMINATION OF THE ORBITAL PARAMETERS

Transit Time Measurements	No. of Stars Occulted per Rotation	NO. OF MEASUREMENTS PER SATELLITE ROTATION																							
		2	3	4	5	6	7	8	9	10	11	12	13	14	15	16	17	18	19	20	21	22	23	24	
Ingress Only	2	X			O																				
					+		⊕																		
	4				X		O		+		⊕														
Ingress Plus Shadow Egress	2			X		O	+		⊕																
	4						X		O				+		⊕										
All Ingress & Egress Events	2				X		O	+		⊕															
	4																		⊕						

Legend:

x = Stellar Transit Time Measurements only

O = Stellar Transit Time Measurements plus Solar Transit Time Measurement

⊕ = Stellar Transit Time Measurements plus Refraction Direction

⊕ = Stellar Transit Time Measurements plus Solar Transit Time Measurements & Refraction Direction



these cases there may be either two or four stars occulted per rotation. This occurs because the stars are picked in diametrically opposite pairs.

In order of accuracy for instrumentation now under consideration, the following additional measurements can be made:

- 1) time of passage into earth's shadow,
- 2) direction of refraction in inertial space, and
- 3) refraction rate as a function of time.

Various combinations of these techniques are shown in Figure (3). For example, if we measure the time of ingress only, if four stars are occulted per rotation and if we measure the direction of the refraction vector at each ingress, then Figure (3) shows that nine measurements are available per satellite rotation.

The use of the refraction rate information is not shown in Figure (3), since this information is not very accurate and will be used primarily for the first estimate of the orbital parameters rather than for the final calculation. In deriving Figure (3) it was assumed that at the completion of 360° rotation one additional measurement would be used to determine the semi-major axis. It is not known whether all of the combinations shown in Figure (3) are independent and therefore additional analysis is needed regarding this question.

The measurement of star transit times alone leads to certain conditions in which the orbital parameters either cannot be determined or are subject to large errors. Thus, perhaps the most important point to be made as a result of Figure (3) is that the addition of refraction direction and solar transit time measurements results in an extremely flexible system with many alternative methods of calculating the orbital parameters. The price of this flexibility is very small, in that the additional measurements require little additional instrumentation.

### III. PHENOMENOLOGICAL CONSIDERATIONS

#### A. Methods of Defining Transit Time

As starlight moves into the earth's atmosphere or emerges from behind the earth, the dynamic response of the detection instrument must not limit the measurement of time. The faster the rate of ingress or egress, the more difficult the instrument design problem.

Consider the geometry shown below, where the following symbols are used:

$R_e$  = radius of planet

$R_o$  = radius to occulting layer

$R_s$  = radius to satellite

$\Theta$  = angle from point of tangency of ray on occulting surface to satellite

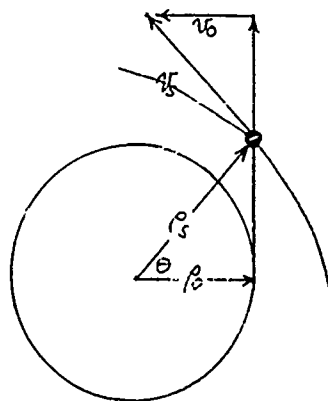
$g$  = gravitational acceleration at  $R_e$

$h$  = satellite altitude =  $R_s - R_e$

$v_s$  = velocity of satellite

$v_o$  = component of satellite velocity perpendicular to occulting surface at point of tangency of ray

For the present example, assume that we are dealing with a spherically shaped planet and a circular satellite orbit.



$$V_o = V_s \sin \theta$$

$$\text{but } \sin \theta = \frac{(\rho_s^2 - \rho_o^2)^{1/2}}{\rho_s}$$

$$V_s = \rho_s \left( \frac{g}{\rho_s} \right)^{1/2}$$

Therefore

$$V_o = \frac{\rho_s^{1/2} g^{1/2} (\rho_s^2 - \rho_o^2)^{1/2}}{\rho_s^{3/2}}$$

To find the maximum value of  $V_o$  we let  $\frac{dV_o}{d\rho_s} = 0$ ,

And therefore  $\rho_s = \sqrt{3} \rho_o$ . For the earth  $\rho_o \doteq 3450 \pm 30$

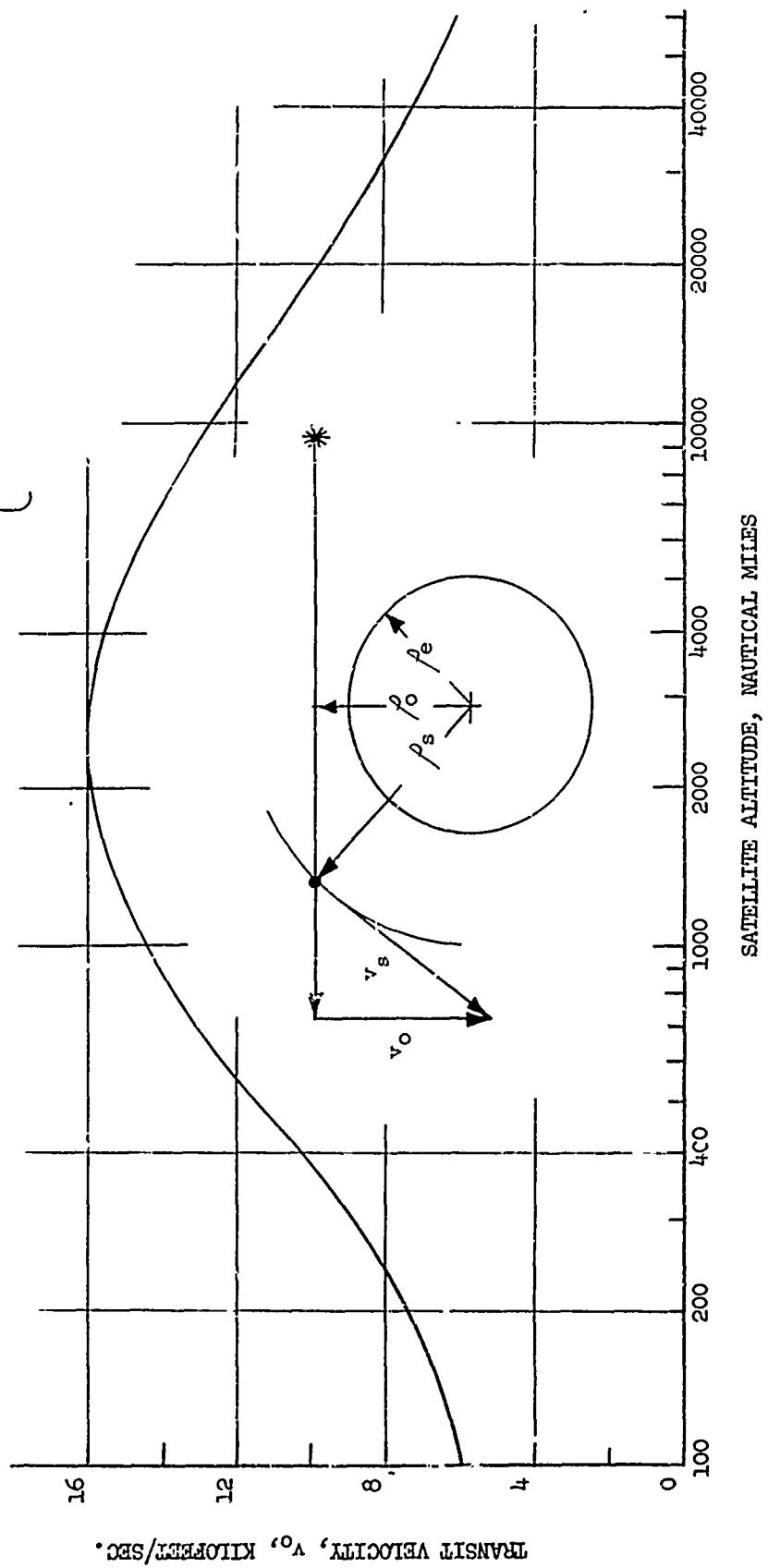
n. miles, and therefore the velocity  $V_o$  will be a maximum for satellite orbits of  $\rho_s = 6030$  n. miles, or satellite altitude = 2580 n. miles, above and below this altitude  $V_o$  will be smaller, and therefore the instrument dynamic response problem will be easier. At  $h = 2580$  n. miles, the value of  $(V_o)_{\text{max.}} = 16,000$  feet/sec. The value of  $V_o$  at various satellite altitudes is shown in Figure (4). The nature of the function is such that  $V_o$  varies surprisingly little over the usual range of altitudes considered for earth satellites.

#### 1. Atmospheric Refraction

One of the modes of operation of the system previously described is that of defining the star transit time on the basis of some predetermined magnitude of atmospheric refraction. As will be evident from the charts shown later, the change in the refraction caused by the atmosphere is so fast compared with the change in the

Figure 4  
TRANSIT VELOCITY AT VARIOUS SATELLITE ALTITUDES

$\left\{ \begin{array}{l} (v_o)_{\text{max.}} = 16000 \text{ ft/sec} \\ h = 2600 \text{ n. miles} \end{array} \right\}$



velocity aberration that the latter may be neglected.

Figure (5) shows the approximate refraction for rays grazing through the atmosphere at various altitudes. At an altitude of 200,000 feet the refraction was assumed to be 1 second of arc, while at 100,000 it was assumed to be 60 seconds of arc. If we assume an exponential atmosphere, the relation between refraction and altitude can therefore be written

$$R = 3.64 \times 10^3 \exp(-4.10 \times 10^{-5} h)$$

where  $R$  is in seconds of arc and  $h$  in feet.

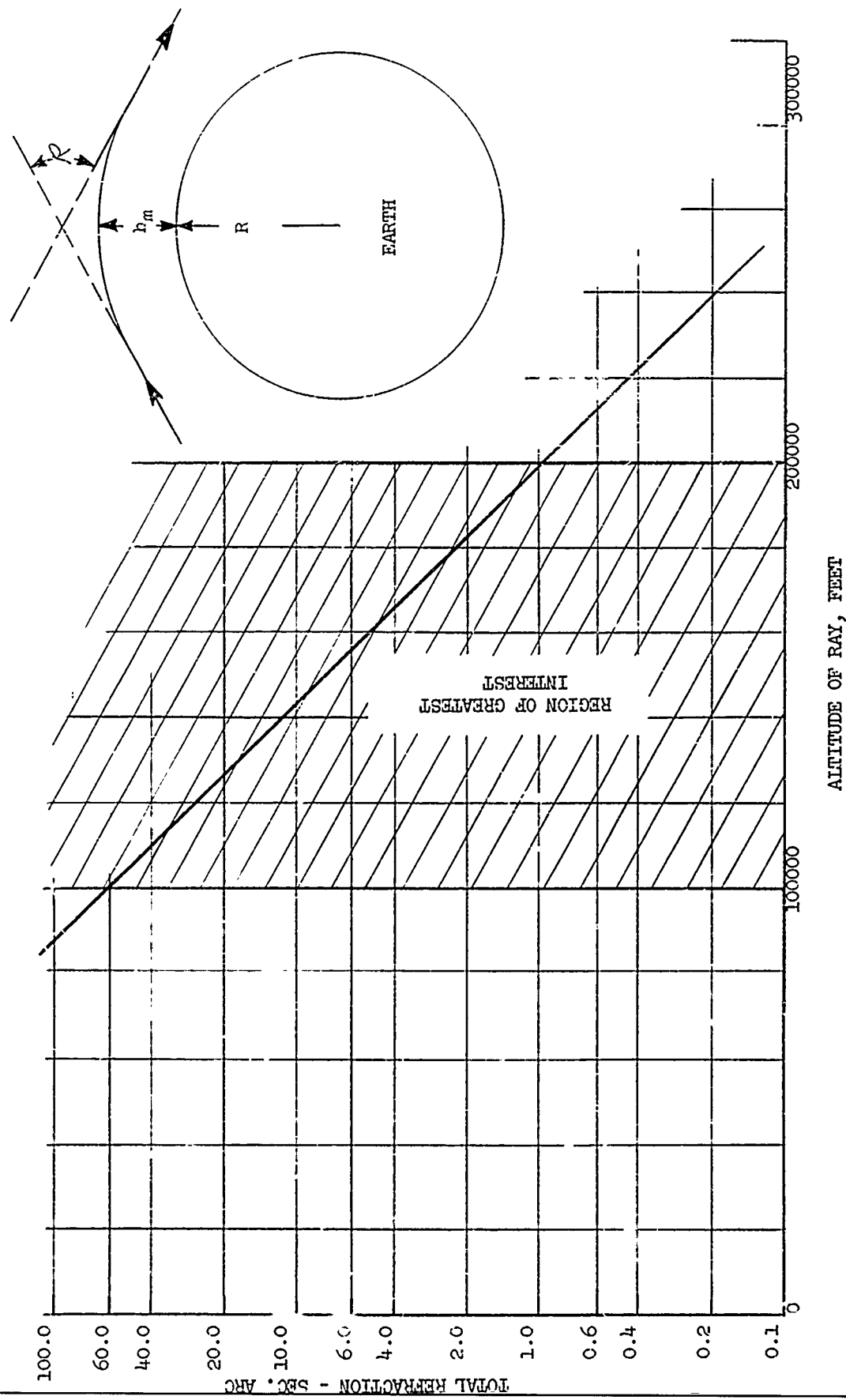
In selecting the magnitude of the refraction,  $R_0$  for the transit time measurement one must take account of the following factors.

- 1) How predictable is the iscrefraction surface in question?
- 2) Are extensive seasonal and altitudinal corrections necessary?
- 3) Are these corrections known?
- 4) How accurately can the star tracking instrument measure the refraction?
- 5) What tracking problems arise because of the scattered radiation from the sun?
- 6) Is the atmospheric attenuation of the starlight sufficiently small at the level in question to permit  $R_0$  to be measured?

Requirements (5) and (6) can be best satisfied by selecting an occultation altitude which is extremely high. Requirements (1), (2), and (3) tend to disqualify both the very high and the very low altitudes. Requirement (4) disqualifies the very high altitudes. Thus, if we are to make the optimum selection of the altitude of the occultation surface we must pick one lying at an intermediate altitude. On the basis of the factors mentioned above, it would appear that this surface should lie between 100,000 and 200,000 feet above sea level.

Figure 4

ESTIMATED TOTAL ATMOSPHERIC REFRACTION FOR GRAZING RAY AT VARIOUS ALTITUDES



To illustrate how the accuracy of the star tracking instrument affects the altitude measurement, we can derive the refraction-altitude sensitivity coefficient from the above equation. We then obtain

$$\frac{dh}{dK} = -6.70 \exp(4.1 \times 10^{-5} h) \frac{\text{feet}}{\text{sec. of arc}}$$

This sensitivity coefficient gives the number of feet of error in the occultation surface resulting from a given error in the measurement of the atmospheric refraction.

Figure (6) is a graph of this equation. It shows that an error of 1 second of arc causes an altitude error of only 400 feet at an altitude of 100,000 feet. As the altitude increases, the effect of an angular error in the measurement of the refraction increases very fast - particularly above 150,000 feet. Thus unless an extremely accurate instrument for angular measurement is used, it would be desirable to use an occultation surface lying below 150,000 feet.

On the other hand, if an occultation surface lying below 150,000 feet is selected, the response of the instrument must be very fast. This can be seen from Figure (7) where the magnitude of the atmospheric refraction as a function of time is plotted on the left hand ordinate. On the right hand ordinate the refraction rate is plotted as a function of time. This is derived from the equation

$$\frac{dK}{dt} = -.149 \left( \frac{dh}{dt} \right) \exp(-4.10 \times 10^{-5} h) \frac{\text{seconds arc}}{\text{second time}}$$

In the case of Figure (7) an orbit of 300 n. miles altitude and an occultation surface of 150,000 feet were assumed.

Had an occultation surface lying at 130,000 feet been selected, it would be necessary to make the refraction measurement while it was

Figure 6

SENSITIVITY OF CALCULATED ALTITUDE TO ERROR  
IN MEASUREMENT OF ATMOSPHERIC REFRACTION

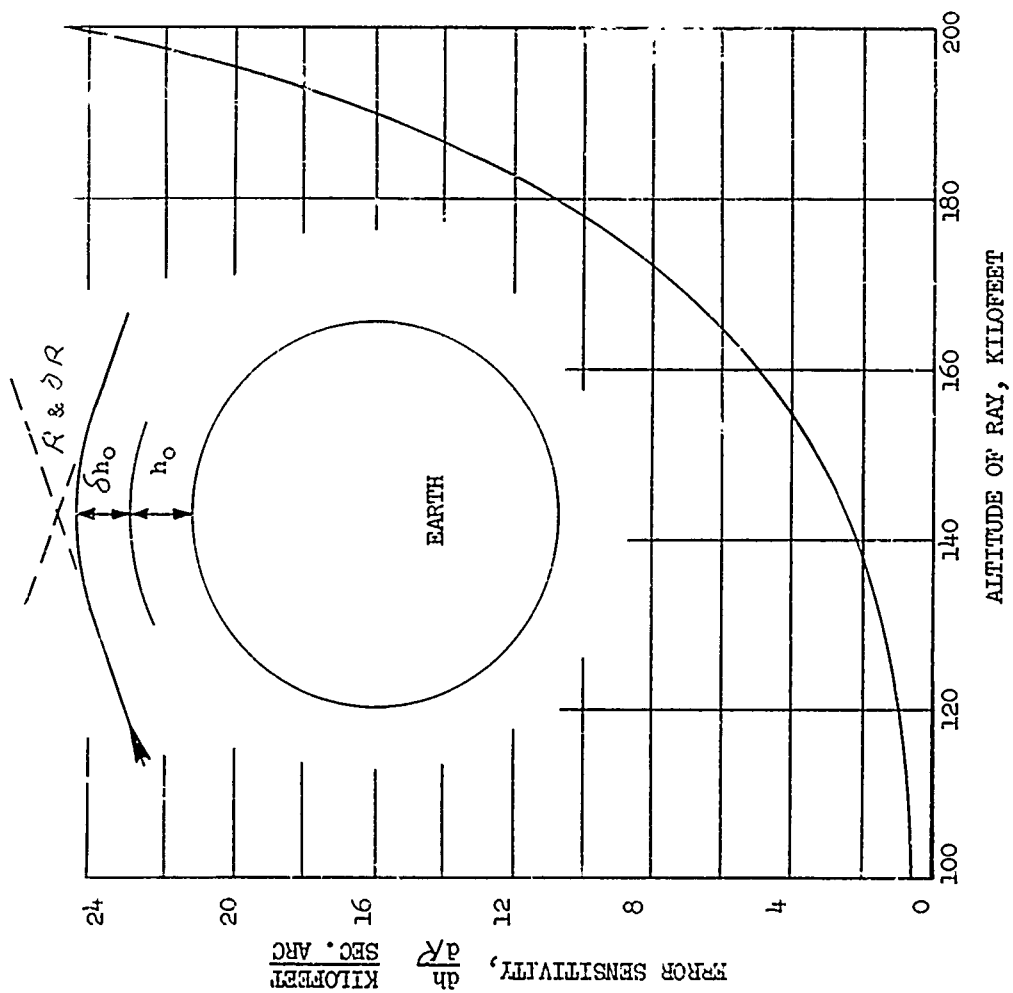
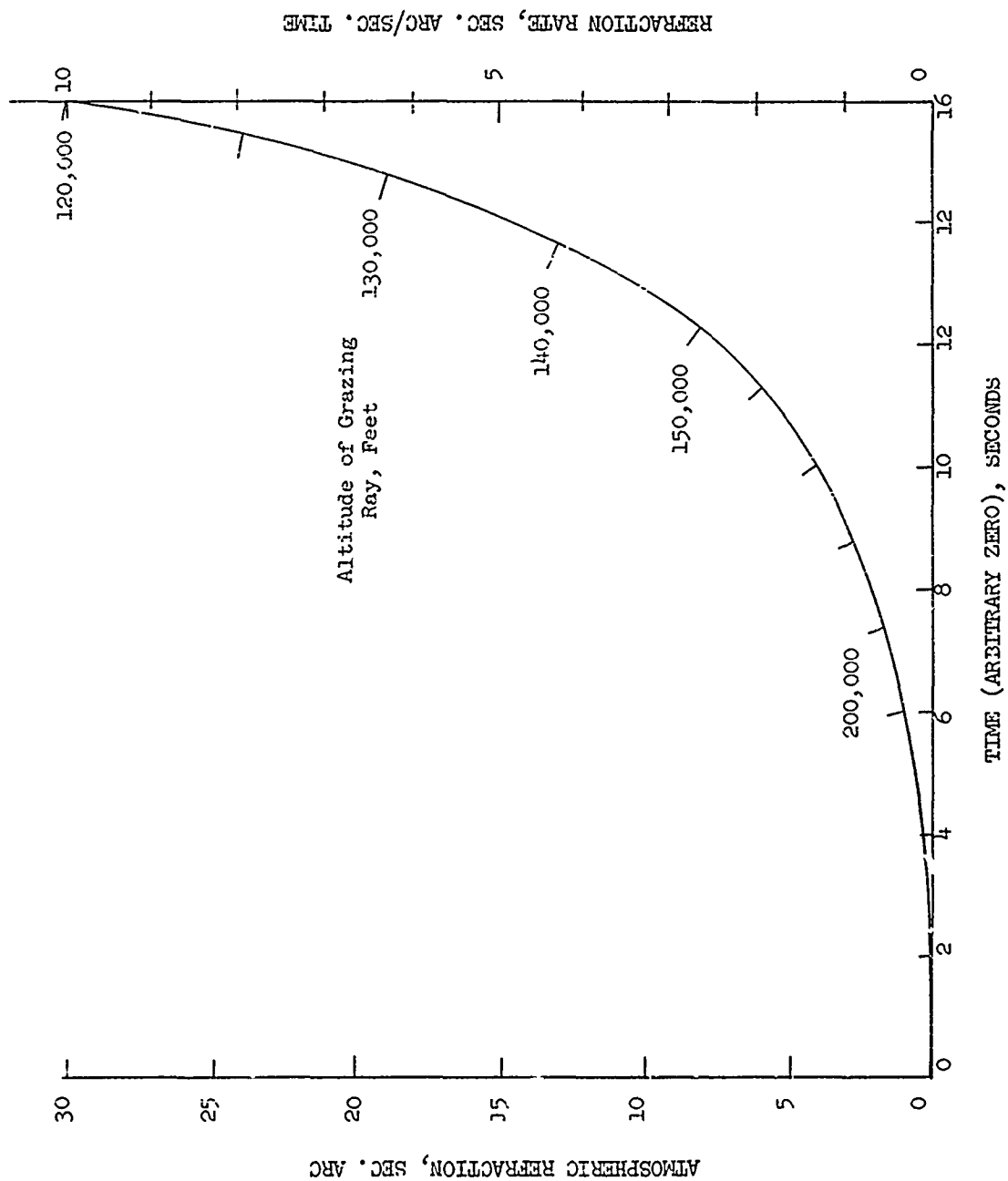




Figure 7  
REFRACTION AND REFRACTION RATE AS A FUNCTION OF  
TIME FOR AN ORBIT OF 300 N. MILES ALTITUDE



changing at a rate of about 6.3 seconds of arc per second of time. This raises a question of the possibility of building an instrument which measures the rate of change of atmospheric refraction rather than the absolute value of atmospheric refraction.

The remainder of the problems associated with the evaluation of the six factors affecting the selection of the altitude of the occultation are meteorological in nature and are discussed in a subsequent paragraph.

## 2. Atmospheric Attenuation

It is possible to define star transit on the basis of the spectral intensity rather than the atmospheric refraction. Some of the problems associated with this measurement are considered in this paragraph.

First, it should be pointed out that the spectral intensity is a scalar quantity while atmospheric refraction is a vector quantity. Thus, if we measure spectral intensity at each transit we obtain only half as much information as we do by measuring atmospheric refraction.

The received signal at the telescope will vary in intensity at a given altitude of transmission through the atmosphere for a variety of reasons. Some of these are listed below:

- 1) absorption of stellar radiation by atmosphere,
- 2) scattering of stellar radiation by atmosphere,
- 3) differential refraction of stellar radiation by atmosphere,
- 4) scattering of solar radiation by atmosphere to create background noise,
- 5) radiation from the atmosphere itself,

- 6) large scale variation of absorbing and scattering components such as  $O_3$ ,  $H_2O$ , and small particles,
- 7) small scale variation of meteorological conditions which, to some extent, can be avoided by seasonal and latitudinal corrections.

In general, all of these phenomena can contribute errors to the transit time measurement. The following paragraph discusses the selection of a spectral region and occultation altitude which will minimize these errors.

a. Absorption

We would like to pick a spectral region in which something like 50 per cent absorption\* occurs at an altitude in excess of 60,000 feet in order to make the definition of star transit time independent of local cloud cover and meteorological variations. This requirement immediately restricts us to the ultraviolet region of the spectrum. In the visual portion of the spectrum the absorption is too small; in the near infrared, where  $H_2O$  or  $CO_2$  absorption bands might be used, the intensity of starlight is not adequate.

In the ultraviolet region of the spectrum the absorption resulting from  $O_2$  and  $O_3$  is shown graphically in Figures (8) and (9).

(1) Ozone - A gaussian distribution of ozone was assumed having its peak at 25 km and a  $\ell^{-1}$  width of 10 km. Then, using the absorption coefficients for  $\lambda = 2,000-3,000 \text{ \AA}$ ,<sup>1</sup> the per cent transmission was plotted against  $h$  with  $\lambda$  a parameter. For this wave length range, we find that .25  $\mu$  has the cutoff highest in

---

\* We could consider the altitude at which 50 per cent scattering takes place (or a combination of scattering and absorption), but if the spectral region in question gives a large scattering of starlight, it also yields a large background intensity due to scattered sunlight. This is not desirable.

Figure 8  
 OZONE ABSORPTION PERCENTAGE TRANSMISSION THROUGH  
 GAUSSIAN LAYER OF OZONE CENTERED AT 25 KM WITH WIDTH OF 10 KM AT MAX.  $\times e^{-1}$

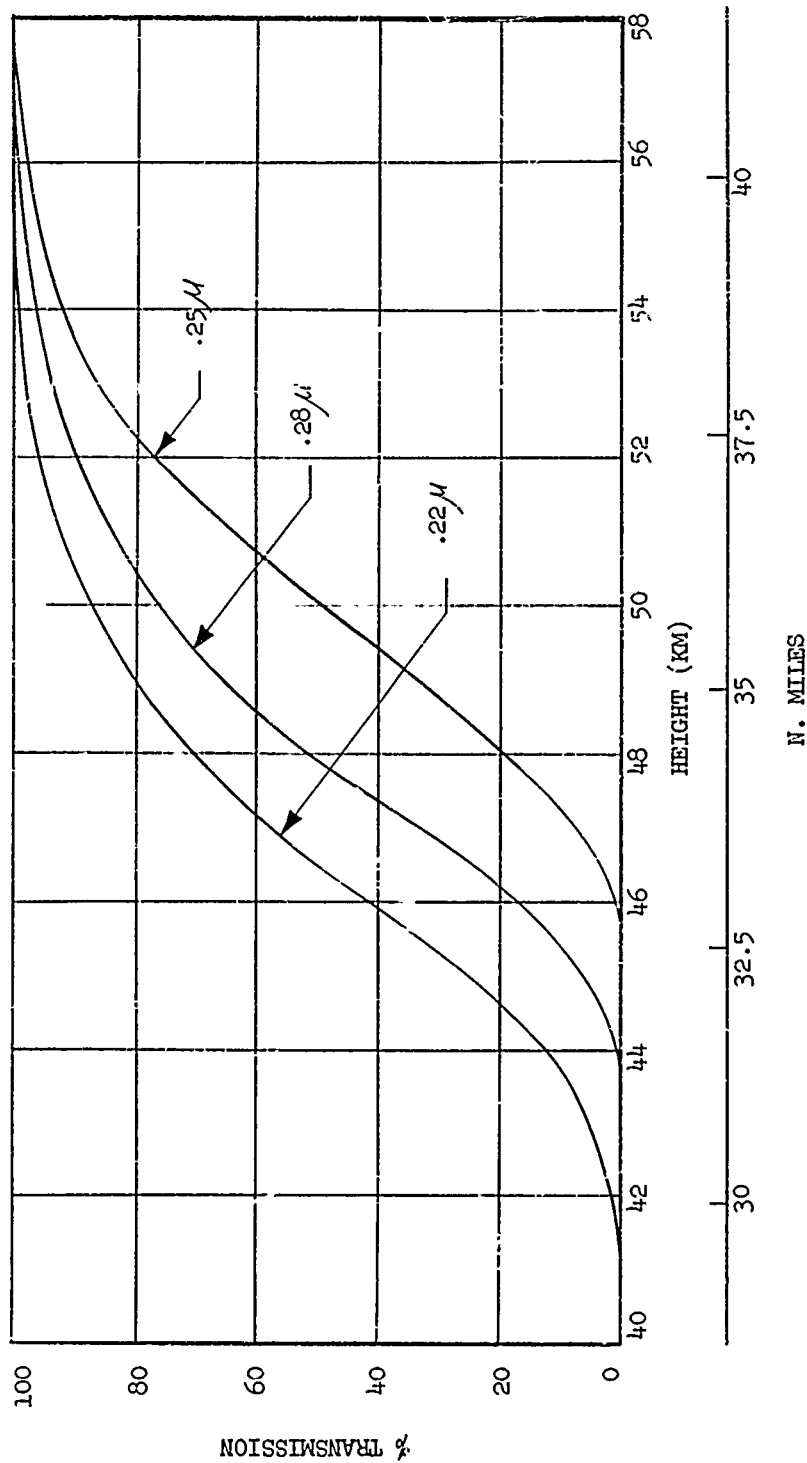
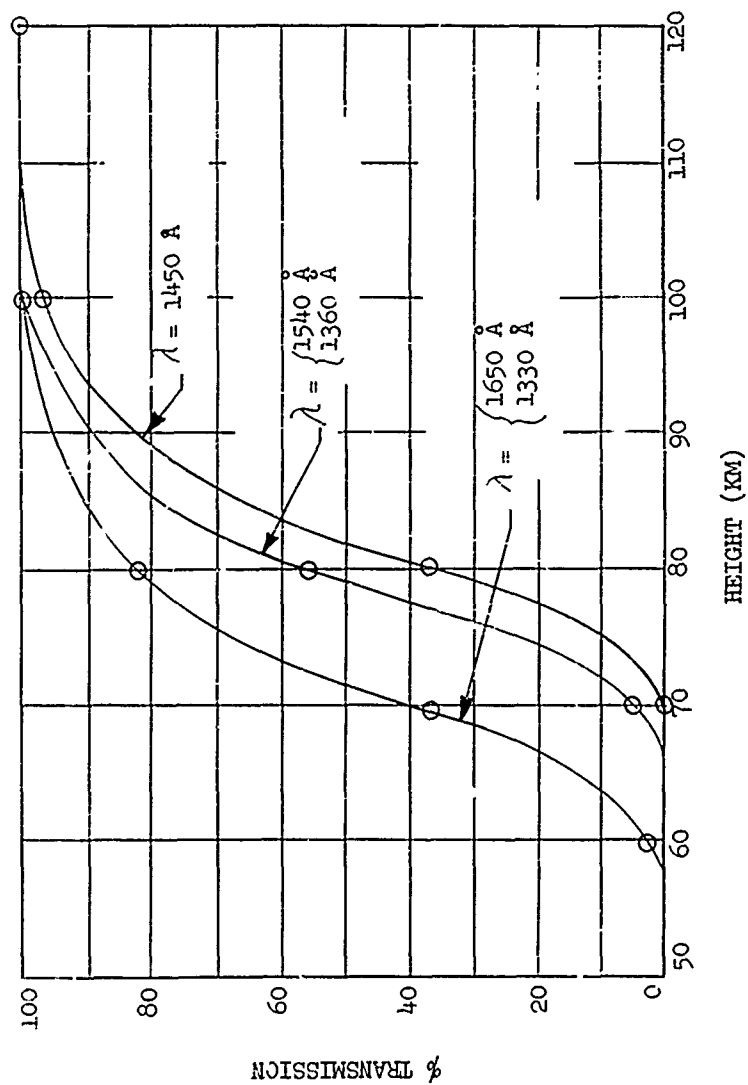


Figure 9  
MOLECULAR OXYGEN ABSORPTION, PERCENTAGE TRANSMISSION  
IN THE STRONG ABSORPTION REGION FOR  $C_2$



the atmosphere. This is shown in figure (8).

(2)  $O_2$  - Again using the air masses calculated in the section on scattering, and assuming that  $O_2$  constituted 22 per cent of this, and using absorption coefficients for  $O_2$ , the percentage transmission is plotted against  $h$ , against using  $\lambda$  as a parameter. Here  $\lambda = 1450 \text{ \AA}$  is the wave length yielding the maximum cutoff altitude. This is shown in Figure (9).

From Figures (8) and (9) the following summary is made of the altitudes at which a 50 per cent atmospheric absorption for radiation in the various regions of the spectrum occur.

<u>SPECTRAL REGION, <math>\text{\AA}</math></u>	<u>ALTITUDE, KM</u>	<u>PRIMARY ABSORBING CONSTITUENT</u>
1330 - 1650	72	$O_2$
1360 - 1540	79	$O_2$
1450	82	$O_2$
2200	46.5	$O_3$
2500	50	$O_3$
2800	48	$O_3$

In general, the altitude for 50 per cent absorption increased as the near ultraviolet at  $3,000 \text{ \AA}$  is approached. Were it not for the extreme fluctuation in the atmospheric ozone content, the region from 2,200-2,800 angstroms could be very attractive. While the  $O_2$  content does not fluctuate to an objectionable extent, its primary absorption lies in a region of the spectrum which is largely unexplored. A star would require a temperature of  $20,000^\circ \text{ K}$  to peak at  $1,500 \text{ \AA}$ , and it would be desirable to use O or B spectral classes if this region of the spectrum were used. For the stars down to 8.5 visual magnitude, approximately 10 per cent are O or B

stars, and thus the selection of stars is considerably restricted by operation in the  $O_2$  regions of the spectrum.<sup>3</sup>

b. Scattering

Atmospheric scattering has two effects. It creates background radiation and it attenuates the signal being detected. The following paragraph discusses the latter effect.

Rayleigh's scattering law indicates that the intensity of scattered radiation is proportional to  $\lambda^{-4}$ . Thus the region in which the highest absorption levels are obtained at the short wave lengths is also the region in which the greatest scattering attenuation is obtained. However, as is evident from Figure (10), the signal loss due to atmospheric scattering is not appreciable above 30 km. Since absorption is 99 per cent for  $O_2$  by 60 km and  $O_3$  by 40 km, it is evident that the scattering attenuation may be neglected.

In deriving Figure (10) observations were made which deserve the following comments. The number of air masses encountered in a horizontal line through the atmosphere at a height h was calculated.<sup>4</sup> Then using P. Moon's<sup>5</sup> results

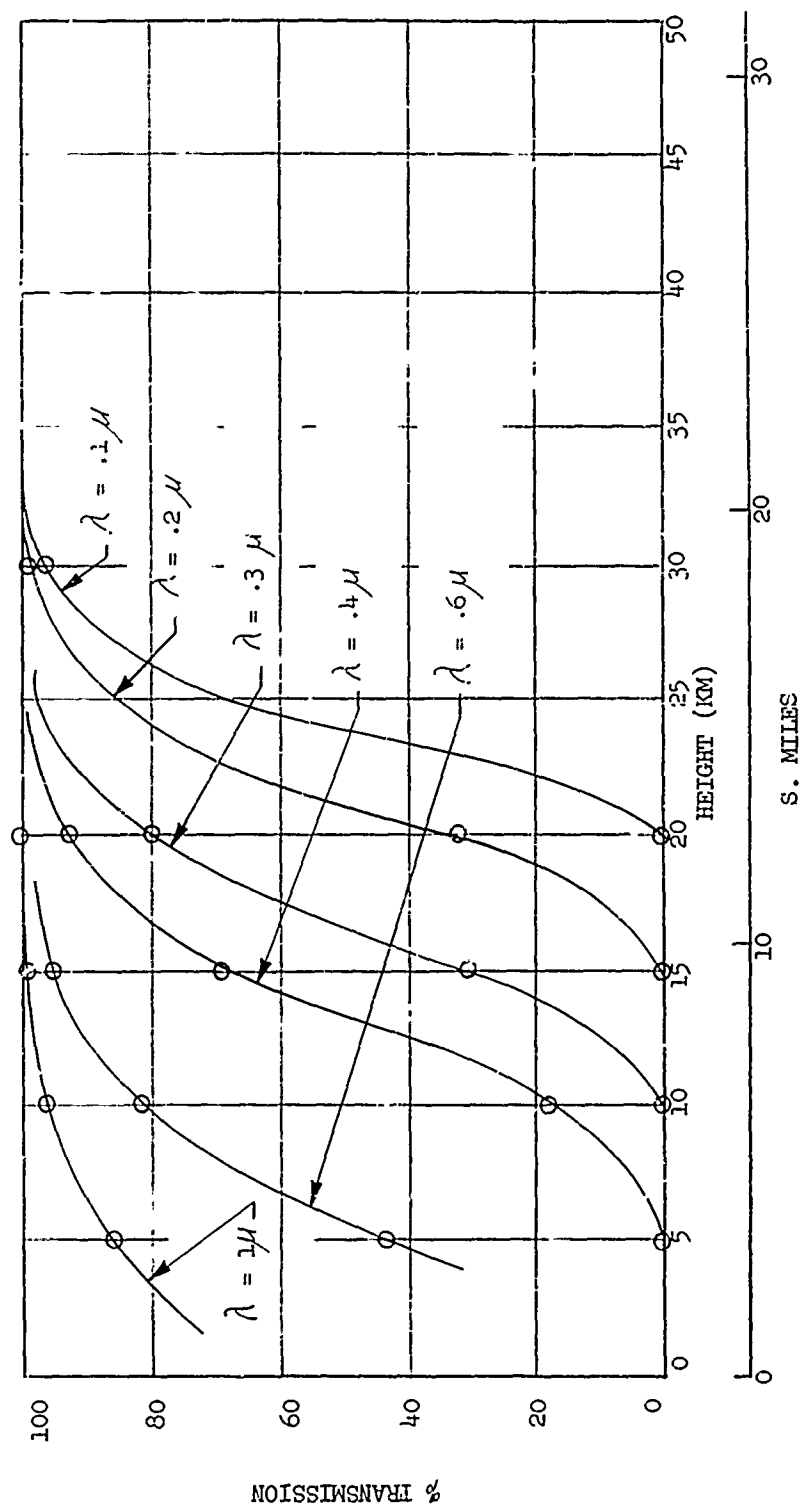
$$\tau = (\tau_{a\lambda}) \frac{pm}{760} = 10 \frac{kpm}{760}$$

This gives the transmission coefficient,  $\tau_\lambda$ , for scattering as a function of the scattering coefficient,  $\tau_{a\lambda}$ , at normal pressure and temperature for one air mass. m is the number of air masses calculated above, p is pressure in mm at height h, and  $\tau$  is taken as a function of wave length.<sup>5</sup>

Since p and m are functions of h, and k is a function of  $\lambda$ , we plotted  $\tau_\lambda$  in per cent against h using  $\lambda$  as a parameter.

Now p is really too high since it is calculated at the point of

Figure 1C  
 PERCENTAGE TRANSMISSION OF LIGHT HORIZONTALLY THROUGH  
 ATMOSPHERE AS FUNCTION OF MINIMUM APPROACH OF RAY DUE TO ATMOSPHERIC SCATTERING



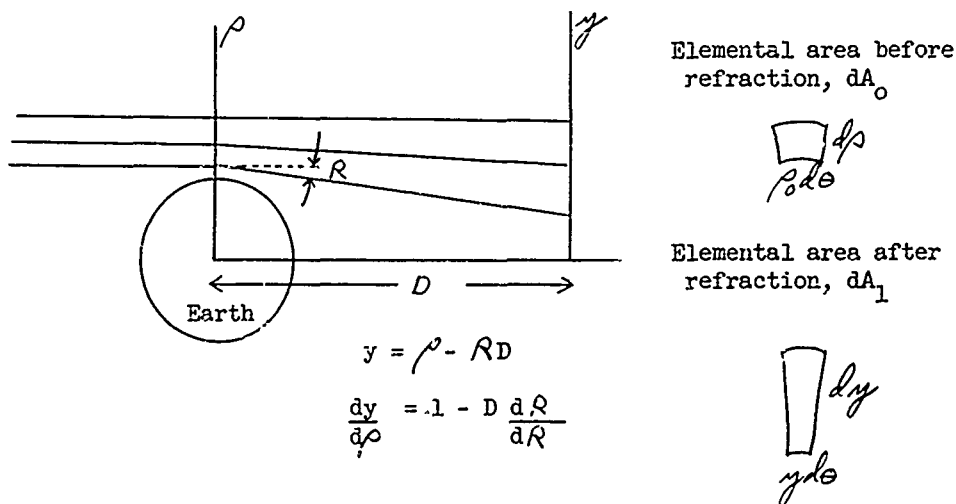


greatest density along the path. But for smaller  $p$ , the graphs merely get moved to lower heights.

### c. Differential Refraction

Because of the fact that refraction increases as a ray dips into the atmosphere, the intensity of the ray is reduced. The atmosphere acts like a negative lens and disperses the radiation. Under certain conditions the loss in signal strength due to differential refraction is greater than that resulting from absorption and scattering. In general, the effect of differential refraction becomes greater as the altitude of the satellite increases.

In order to show how this occurs, consider the sketch shown below.



The change in intensity is equal to the ratio of the elemental areas

$$\frac{dA_0}{dA_1}. \text{ Thus } I = \frac{dA_0}{dA_1} = \frac{\rho \frac{d\rho}{dy} \frac{d\theta}{d\rho}}{y \frac{d\rho}{dy} \frac{d\theta}{d\rho}} = \left(\frac{\rho}{y}\right) \left(\frac{d\rho}{dy}\right)$$

$$I = \frac{1}{\left(1 - \frac{D}{\rho} \frac{dR}{d\rho}\right) \left(1 - D \frac{dR}{d\rho}\right)}$$

But  $R = K_0 \exp(-K_1 [\rho_0 - \rho_e])$  and  $\rho = \rho_0$ , therefore

$$\frac{dR}{d\rho_0} = -K_1 R \text{ and } I = \frac{1}{\left(1 - \frac{D}{\rho_0} R\right) (1 + DK_1 R)}$$

Since we are not interested in satellite altitudes greater than  $10^5$  miles or in atmospheric refractions greater than 100 seconds of arc, the maximum value of  $\frac{D}{\rho_s}$  is approximately

$$\frac{104,000 \times 100 \times 4.85 \times 10^{-6}}{3450} = 1.46 \times 10^{-2}$$

We may therefore use the following approximation

$$I = \frac{1}{1 - D \left( \frac{dR}{d\rho_0} \right)}$$

The values of  $R$  and  $\frac{dR}{d\rho_0}$  can be obtained from equations given earlier.

When expressed in units of radians and nautical miles we may write

$$R = 1.765 \times 10^{-2} \exp [-.249 (\rho_0 - \rho_e)] \text{ radians}$$

$$\frac{dR}{d\rho_0} = -.249 R \frac{\text{radians}}{\text{n. mile}}$$

When these values are graphed, Figure (11) is obtained. This figure shows that if the ray penetrates to 100,000 feet (corresponding to about 60 seconds of arc refraction), the effect of differential refraction can be significant - even for low altitude orbits. Using the ozone absorption with 50 per cent attenuation at about 160,000 feet, a satellite altitude of 1000 n. miles will produce an effect of differential refraction not exceeding 2 per cent.

A slightly different form of the inensity function is shown plotted in Figure (12). A satellite altitude of 300 miles was assumed and the relation between height and per cent transmission was derived.

#### d. Scattered Radiation from the Sun

When the viewing geometry is such that ingress or egress takes place in an atmosphere illuminated by the sun, the background radiation must be considered. Scattered radiation from the sun presents the greatest problem in the visual region of the spectrum where the maximum of the solar radiation lies. For wave lengths below the solar maxima at  $\lambda = 5,000 \text{ \AA}$ , the intensity per unit wave length may be approximated by the Wien radiation formula

Figure 11

FRACTIONAL LOSS IN STAR INTENSITY CAUSED BY  
ATMOSPHERIC DIFFERENTIAL REFRACTION FOR VARIOUS  
LEVELS OF REFRACTION AND SATELLITE ALTITUDE

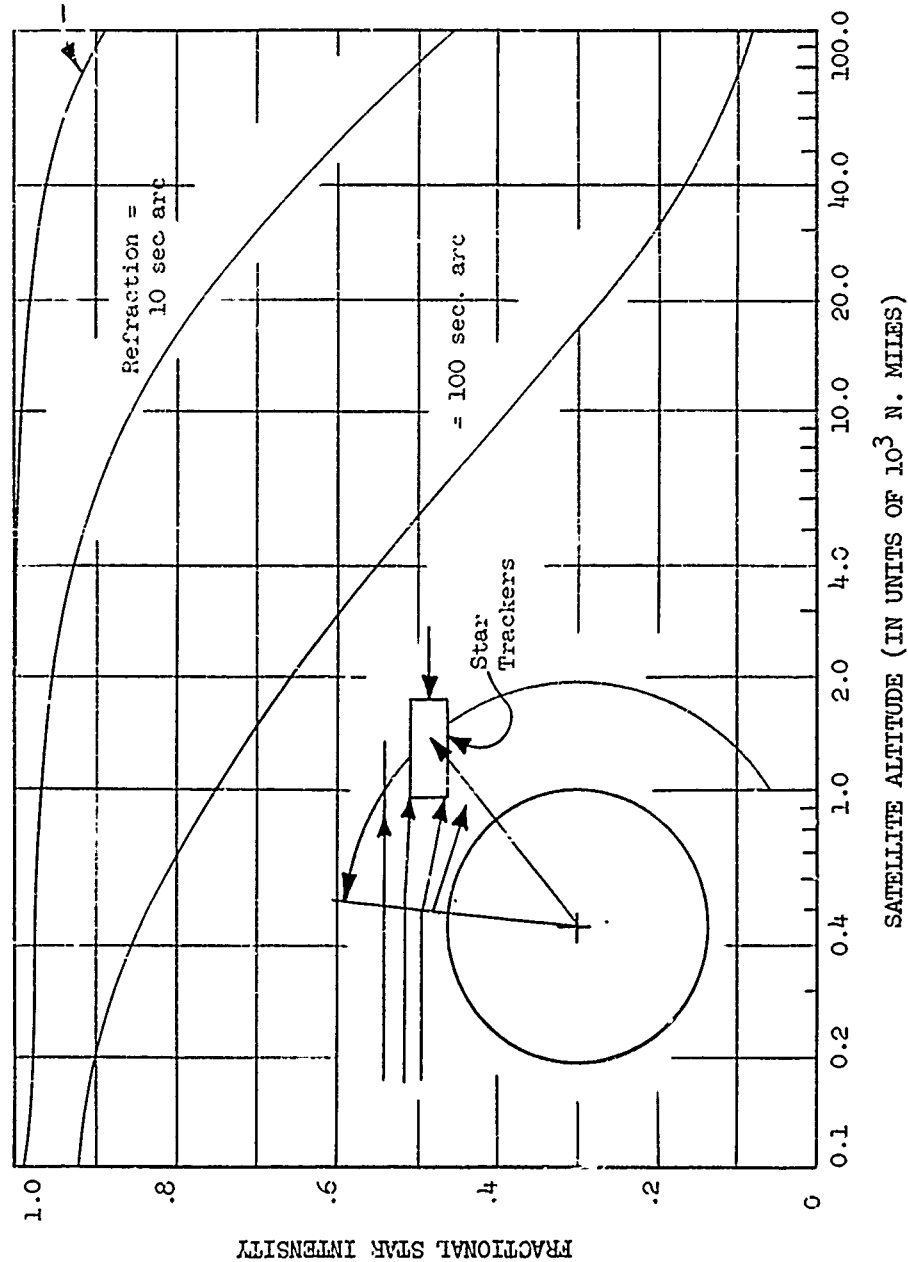
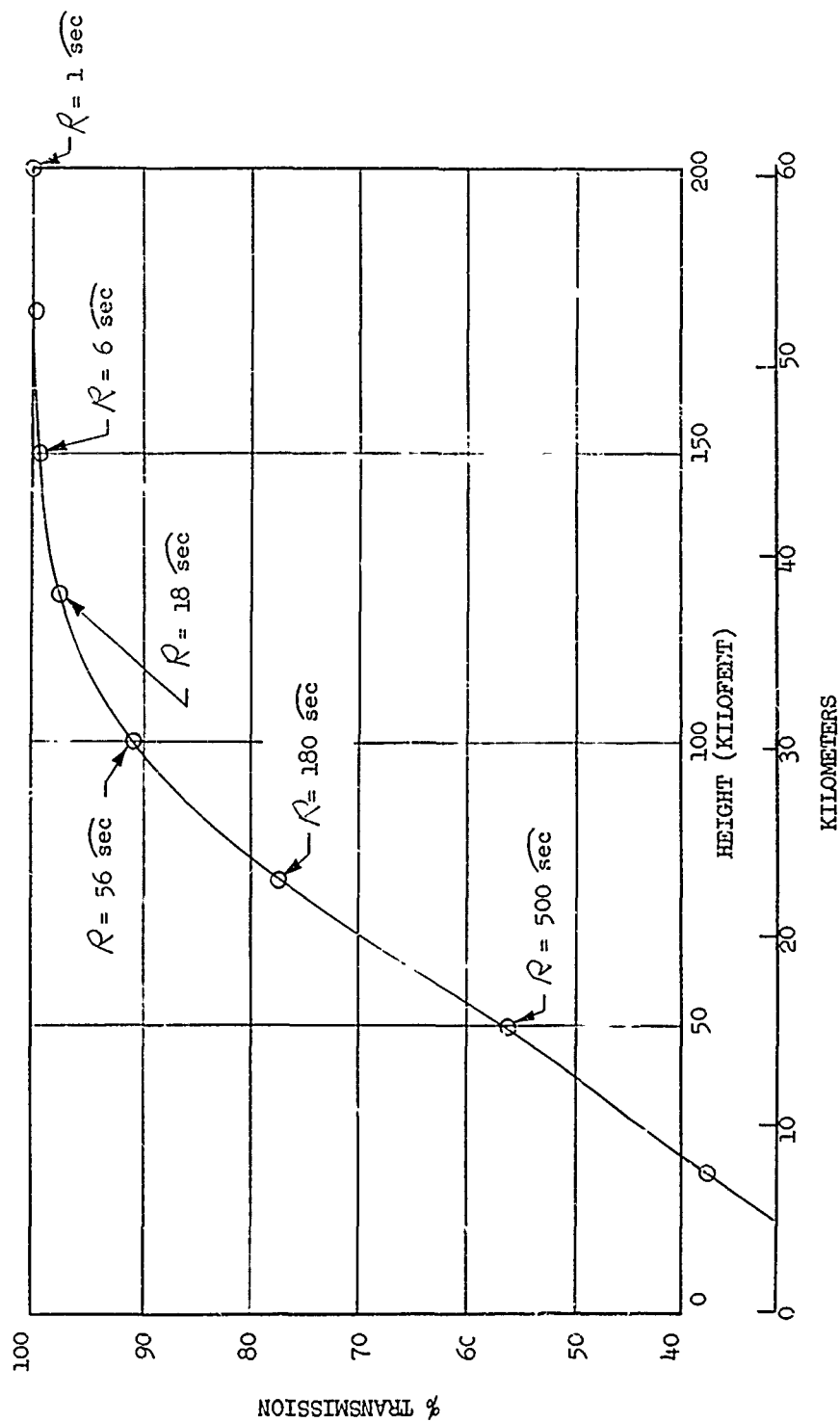


Figure 12

PERCENTAGE TRANSMISSION DUE TO DIFFERENTIAL REFRACTION IN THE  
ATMOSPHERE AS A FUNCTION OF DISTANCE OF CLOSEST APPROACH OF  
RAY TO THE EARTH - - 300 S. MI. ORBIT



which states  $I_{\lambda} \lambda = \frac{K_1}{\lambda^5 \exp\left(\frac{ch}{\lambda kT}\right)}$

The Rayleigh scattering law states that

$$I_{\lambda} \lambda = \frac{K_2}{\lambda^4}$$

Therefore, since net scattering is proportional to the amount of solar radiation to be scattered times the scattering coefficient, we obtain as a measure of the scatter intensity

$$I = I_{\lambda} \lambda \cdot \lambda = \frac{K_3}{\lambda^9 \exp\left(\frac{ch}{\lambda kT}\right)}$$

To find the wave length at which the maximum of  $I$  is reached we let

$$\frac{\partial I}{\partial \lambda} = 0, \text{ and obtain the equation } \frac{ch}{\lambda kT} = 9$$

Since  $\frac{ch}{k} = 1.439 \times 10^4$  when  $\lambda$  is in microns and  $T$  in  $^{\circ}K$ , we have for the sun, letting  $T = 6,000^{\circ}K$ ,

$$\lambda_0 = .2665 \text{ microns}$$

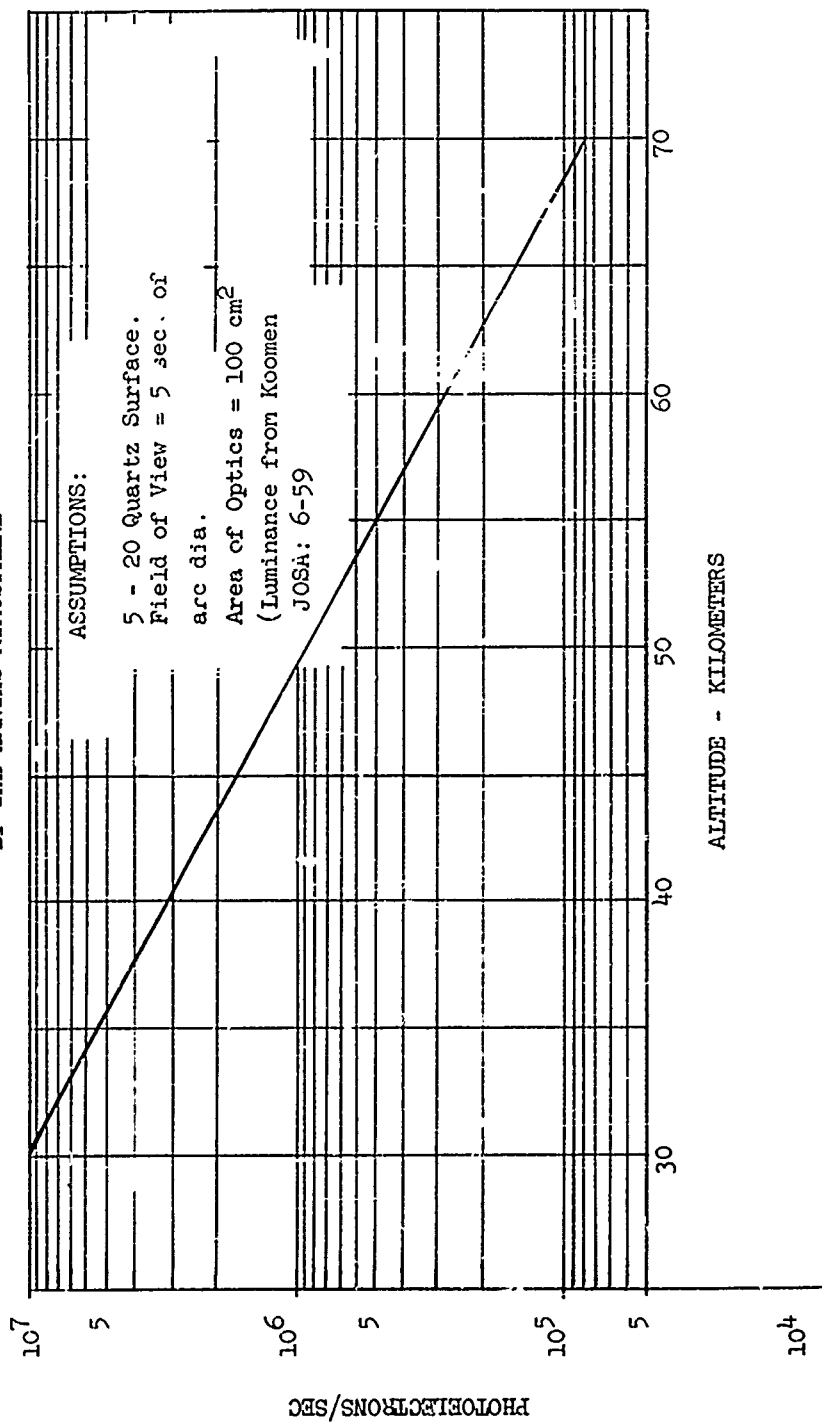
Thus, a wave length of 2,600 Å presents the least favorable situation regarding scattered radiation from the sun. Of course, this conclusion applies per unit wave length only, and it may be expected that the effect of scattered solar radiation will be greatest, i.e. least favorable, in the ozone region of the spectrum. At  $\lambda = 1,500 \text{ Å}$  in the  $O_2$  region the solar effect per unit wave length interval will be reduced to

$$\frac{I(\lambda = 1,500)}{I(\lambda = 2,660)} = \left(\frac{.266}{.150}\right)^9 \left(\frac{e^{9.00}}{e^{16.00}}\right) = \frac{176}{11,000} \quad 1.6 \times 10^{-2}$$

Thus, the  $O_2$  region has a considerable advantage over the  $O_3$  region. Figure (13) shows the effect of scattered solar radiation for a spectral region from roughly 2,500 to 4,000 Å. The FOV of the

Figure 13

PHOTOELECTRONS PER SECOND AT VARIOUS OCCULTATION  
ALTITUDES WHICH HAVE TILR SOURCE IN SOLAR RADIATION SCATTERED  
BY THE EARTH'S ATMOSPHERE



telescope was assumed to have a diameter of only 5 seconds of arc - a value which is probably the best that can be achieved. Since a star of B spectral class and 3rd magnitude will yield approximately  $10^6$  photoelectrons per second, it is apparent that scattered radiation will become troublesome at altitudes below 163,000 feet (as many photoelectrons as in the signal). Since the 50 per cent absorption point for ozone occurs at about 160,000 feet, it is apparent that solar scattering will be a serious problem for operation in the ozone region of the spectrum.

e. Emission from the Earth's Atmosphere

Emission from the earth's atmosphere in the wavelength regions of interest is so small that it can be neglected.

At very high altitudes in the thermosphere, high kinetic temperatures are observed; however, the atmospheric density is so small that the radiation is insignificant. At the lowest altitude, the ray will pass (for ozone) at the level of the mesopause where the temperature reaches a maximum of about 300° K. At this temperature and for  $\lambda \leq 2$  microns, only  $10^{-5}$  of the total self-emission is included.

f. Large-Scale Variation of Absorbing Components

Of the gases of the atmosphere which undergo large-scale variations,  $O_3$  and  $H_2O$  are the most important. Generally, the variation of  $O_3$  is sufficiently great to result in rms errors in the altitude of the isoabsorption level of at least 3 or 4 miles. The major  $H_2O$  absorption bands lie in the infrared and have not been considered as a source of stellar attenuation.

Additional data describing the atmospheric ozone fluctuation is contained in a later paragraph.

g. Small-Scale Variations of Absorbing Components

The other gases of the atmosphere (other than  $O_3$  and  $H_2O$ ) are not subject to such extreme variations and thus their use as absorption media is considerably more attractive. The major factor affecting the absorptivity of these gases are the diurnal, seasonal, and latitudinal variations of density at any given level.

B. Meteorological Data

1. Atmospheric Density and Temperature

The classical theory of refraction for a ray passing through a planetary atmosphere provides the expression

$$R = (n_o - 1) \left[ \frac{2\pi \rho_o}{H} \right]^{1/2}$$

where  $H = \frac{RT}{\bar{M}g}$

where  $R$  = refraction in radians

$n_o - 1$  = modulus of refractivity at the altitude

$\rho_o$  = distance of closest approach of ray to center of earth

$R$  = gas constant

$T$  = absolute temperature

$\bar{M}$  = mean molecular weight of atmospheric gases

$g$  = gravitational acceleration at  $\rho_o$

Since  $(n_o - 1)$  is proportional to the air density,  $D$ , and since the mean molecular weight  $\bar{M}$  may be assumed to be constant at the altitudes in question, the atmospheric refraction is

$$R = \frac{K_o D}{T^{1/2}}$$

Meteorological data indicates that at any given altitude the statistical fluctuation in temperature is smaller than the statistical fluctuation in density. If we assume that the



statistical fluctuations in D and T are not correlated we may write

$$\sigma(R) = R \left[ \left\{ \frac{\sigma(D)}{D} \right\}^2 + \frac{1}{4} \left\{ \frac{\sigma(T)}{T} \right\}^2 \right]^{1/2}$$

Because  $\sigma(T)/T$  is smaller than  $\sigma(D)/D$ , and because T appears under the square root thus generating the factor 1/4, we may estimate the rms fluctuation of the refraction from the rms fluctuation of the density as follows:

$$\sigma(R) \doteq R \left[ \frac{\sigma(D)}{D} \right]$$

The problem of determining the rms error in the occultation altitude now can be expressed as a problem in determining the statistical fluctuation in the altitude of the isopycnic surfaces ( $D = \text{const.}$ ).

In making estimates of the atmospheric refraction for a grazing ray, the first approximation can be obtained by multiplying the sea level refraction at 90° zenith angle by twice the density ratio.

$$R(h) = 2 R(0) \left( \frac{D_0}{D_{sl}} \right)$$

This has been done in deriving the curves shown earlier.

The next refinement in the refraction calculation is to correct for the scale height, H, at the various altitudes. Since  $H = RT/\bar{M}g$ , we must consider the variation of T, g and  $\bar{M}$  with altitude. Below 100 km we may assume that  $\bar{M} = 28.97$ , so that the principal sources of variation lie in g and T.

Newall<sup>6</sup> gives the values shown on the table on the next page.

<u>HEIGHT (km)</u>	<u>TEMPERATURE (°K)</u>	<u>g(cm/sec<sup>2</sup>)</u>	<u>SCALE HEIGHT (km)</u>
1.216	291.0		8.53
5	276.8		7.83
10	230.8		6.78
15	209.1		6.16
20	212.8		6.28
25	223.0		6.59
30	231.7	276.4	6.85
35	244.5		7.24
40	262.5	967.3	7.79
45	271.3		8.06
50	270.8	964.3	8.06
55	265.8		7.93
60	252.8	961.3	7.55
65	235.0		7.03
70	218.0	958.4	6.53
75	209.1		6.27
80	205.0	955.4	6.16

Since the refraction R, is proportional to the inverse square root of H, an inspection of the above data shows that the maximum error in using the assumption of constant H is less than 20 per cent. This would correspond to an altitude error of about 5,000 feet at the altitudes where we will be working.

Since the refraction of a grazing ray is related to the vertical density gradient, the fact that the atmosphere is not isothermal creates an additional complication because the existence of a  $(-\frac{\partial T}{\partial \rho_0})$  term creates a source of density gradient other than the exponential

atmosphere. In the final case it will be necessary to integrate numerically over various atmospheric paths.

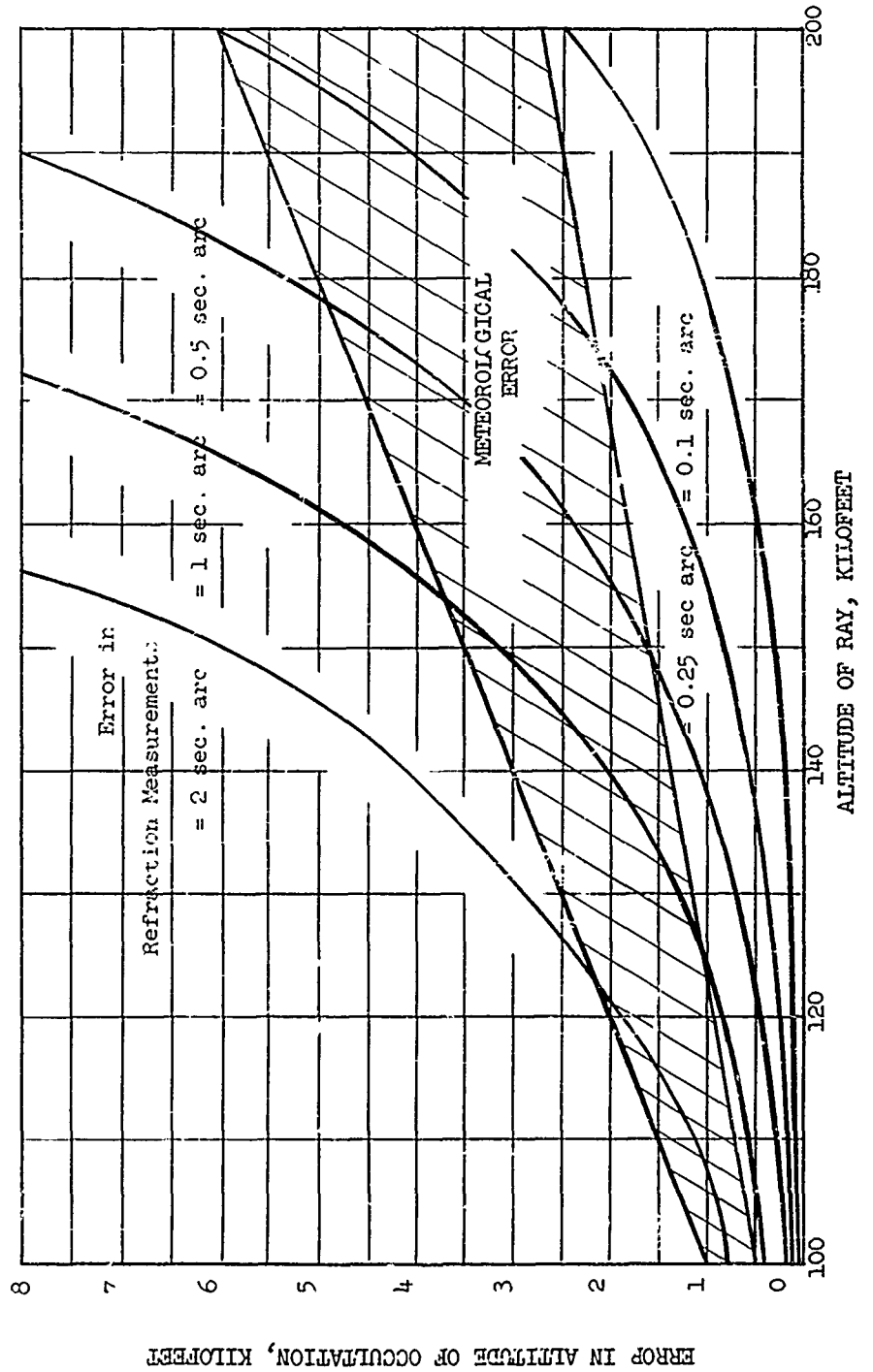
Figure (14) shows the data contained in Figure (6) expressed in terms of the error in feet resulting from various errors in the measurement of atmospheric refraction. Also shown in Figure (14) are the approximate errors in the altitude of the isorefractive level due to meteorological fluctuations. The two extremes represent the case in which the best available latitudinal and seasonal corrections are used and the case in which no seasonal or latitudinal corrections are used. These limits have been estimated and are described later in this section.

It is evident from Figure (14) that an instrument error in the measurement of atmospheric refraction of 1 to 2 seconds of arc at an altitude of 100 to 120,000 feet will lead to an error which is comparable with the meteorological errors. However, there are several reasons why operation at these altitudes is not desirable. They are

- 1) As shown in Figure (13), background radiation from the sun is very great. Probably only measurements in the sun's shadow can be made at these altitudes.
- 2) At 100,000 feet the rate of change of refraction is about 22 sec of arc/sec time, and the dynamic response of the instrument must be very rapid. This requires a wide band width; however, a wide band width is antithetic to precise tracking in the presence of large amounts of background noise
- 3) Since we wish to measure both the time of egress as well as ingress, we must be able to acquire and stably track an emerging star at 100,000 feet. This will be extremely difficult if we have a small FOV (necessary for tracking in the presence of large amounts of background radiation).

The net result of these factors is that the transit time should be defined for altitudes in the neighborhood of 150,000 feet. If we wish to keep the instrument errors small compared with the meteorological

Figure 14  
COMPARISON OF INSTRUMENT AND METEOROLOGICAL ERRORS



errors, and if we make nominal seasonal and latitudinal corrections, it is apparent from Figure (14) that an instrument with an accuracy of 0.25 to 0.5 seconds of arc can be justified.

a. Height Variation of 30 km Surface

This paragraph discusses the problems of finding the seasonal and latitudinal height variation of a density surface which varies about the 30 km level. The data selected for use in this study is published in the ABMA Climatological Ringbook. This report gives monthly tables of mean and standard deviations of density for various altitudes over ten selected stations.

The monthly values listed at the 28 through 31 km levels were combined into seasonal values. This was done for only nine stations, since one of the ten did not have sufficient values at these levels. The mean and  $\pm 3 \sigma$  density values were plotted at their respective levels for each season of each station. A preliminary study of these graphs showed that the  $1.86 \times 10^{-2} \text{ kg m}^{-3}$  density surface could be expected to occur around the 30 km level. Therefore, the maximum and minimum height values of this density surface were tabulated for each season and these values were plotted according to the latitude of the station. Thus we get a height versus latitude graph showing the 99 per cent variability limits of this particular density surface.

The results indicate that a small variation occurs at all seasons over the tropics centered at about 30 km. The polar regions show a general increase in height of the surface from winter to summer with a very small variation during summer. The mid-latitudes show the same general trend as do the polar regions, but have more variation

during summer.

For any given season and latitude we may generalize by saying that the density surface will be within  $\pm 0.5$  km of the mean level 99 per cent of the time. In fact, considering all seasons and all latitudes, we may generalize by saying that the  $1.86 \times 10^{-2} \text{ kg m}^{-3}$  density surface will be within  $\pm 1$  km of the 30 km surface.

b. Height Variations of 48 km Density Surface

In order to investigate the index of optical refraction at high altitude, a study was carried out on a strong parameter of this index, the density of the atmosphere. This study, in essence an extension of a previous study covered in a Memo dated 29 April 1960, involves the height variation of a density surface occurring in the neighborhood of 150,000 feet. Due to the dearth of the data at this altitude, the conclusions drawn must of necessity be considered as preliminary and "rough".

Various speculations have been made as to density variations at a given height at high altitudes but none, to the writer's knowledge, of the variation of the height of a given density surface. Goody<sup>8</sup> quotes an early study by Whipple, Jacchia and Kopal to the effect that the upper stratosphere shows a marked seasonal variation in density and that the upper atmosphere does not seem to react to day-to-day changes in surface temperatures. From rocket data, Whipple<sup>9</sup> concludes that there is little evidence of a diurnal variation but that atmospheric densities are greater in summer than in winter. As to latitudinal variations he states that there is no indication of density variation between the equator and latitude  $33^\circ \text{ N}$  but meteoric and acoustic data do indicate increasing densities with increasing latitude.

Kellogg<sup>10</sup> states that Soviet rocket observations up to 80 km show that the Arctic summer densities are about the same as mid-latitude densities; however, Arctic winter densities are 10-20 per cent lower than mid-latitude densities. Kellogg also states that, in the 30-80 km range, the day-to-day variations of density are greater at Churchill, Canada, than at White Sands, New Mexico, especially during winter.

LaGow, et al<sup>11</sup> studied the Arctic atmosphere using rocket data from Churchill (59° N). They find, in the 30-70 km range, that the summer values are 5-10 per cent higher than those derived by the Rocket Panel from data taken at White Sands (32° N). Also, in the 25-40 km range at Churchill, winter densities are lower than summer densities.

Jones, et al<sup>12</sup> studied atmospheric densities using a falling sphere technique. Flights were made at White Sands, Wallops Island (38° N), Churchill and on shipboard (49-65° N). The White Sands and Wallops flights showed little density variations. Winter densities over Churchill were generally lower than at White Sands. In one particular instance, over a 2-day period at Churchill, the 50 km density increased about 80 per cent. This was associated with abrupt stratospheric warming.

In summarizing the reports mentioned above, the following conditions seem to prevail in the upper atmosphere. The summer densities are greater than the winter densities. This implies the movement of an isopycnic level to higher altitudes in summer. Diurnal variations are slight in general, but there may be large changes in late winter or early spring due to abrupt stratospheric warming. Latitudinally there seems to be little variation in isopycnic heights from the equator up to about

35° N. Then the levels increase in height with increasing latitude up to the polar regions where they remain constant during summer but show a decrease during winter.

c. Data Calculations

To establish more firmly the above hypothesis and obtain some order of magnitude of the height variations, a search was made for actual data from which height variations on an isopycnic level could be readily calculated. A group of high altitude radiosonde flights were made over Berlin (53° N) which allowed estimates to be made. Values of density versus height of the 10 mb and 5 mb pressure surfaces were plotted on semi-log paper. For spring months there were 42 values at the 10 mb surface and 13 values at the 5 mb surface. For summer months there were 40 and 19 values, and for winter there were 27 and 9 values. Lowenthal<sup>13</sup> published a group of summertime high-altitude radiosonde data from 7 stations. From this data 15 density-height values for 10 mb and higher were found for Portland, Oregon; 31 for Narsarsuaq, Greenland; 11 for Denver, Colorado; 30 for Belmare, New Jersey; 10 for Long Beach, California; 14 for Chanute, Illinois; and 11 for Goose Bay, Canada. All these values were again plotted on semi-log paper. Finally Elterman<sup>14</sup> presents a few values from White Sands, New Mexico (6 for summer, 12 for fall) obtained using a search-light technique.

By assuming a linear relation between height and log density, straight line envelopes were determined for the seasons at the various stations. Due to the sparse data, these envelopes were assumed to contain plus or minus one standard deviation of density-height values. From these graphs the mean height and standard deviation of the



$4.5 \times 10^{-6} \text{ gm/cm}^3$  isopycnic level was determined and plotted on a height versus latitude graph. This isopycnic level occurs around 39.5 km (about 130,000 feet) and it does show an increase in height with increasing latitude over the mid-latitudes. Insufficient data for other seasons did not permit a latitudinal variation graph to be made. The actual values, however, are presented below.

Height of  $4.5 \times 10^{-6} \text{ gm/cm}^3$  Level

<u>Location</u>	<u>Season</u>	<u>Mean Ht (km)</u>	<u>Std Dev (km)</u>
White Sands	Fall	39.2	0.6
Berlin	Spring	38.5	0.4
Berlin	Winter	36.6	0.6

The summer standard deviations of almost all the stations were 0.2 km.

The results of this study may be summarized as follows

(keeping in mind the scarcity of data):

- 1) At altitudes of the order of 130-150,000 feet, the isopycnic surfaces are at lower levels during the winter than during the summer.
- 2) Latitudinally the isopycnic surfaces vary little in the tropics, increase altitude with latitude in the sub-tropical and mid-latitudinal ranges and remain level over Polar regions during winter. The increase in height between tropical and Polar regions appears to be the order of 1-1.5 km.
- 3) The height variations of the isopycnic surfaces are smaller during summer than during the other seasons. During summer 99 per cent of the height values will fall within 2,000 feet of the mean seasonal height. During winter this variation increases to 6,000 feet.
- 4) One reason why the spring and winter variations are larger than the summer variation may be because of the abrupt stratospheric warming which occurs during late winter or early spring.

#### d. Short Term Fluctuations

It is known that the equal density surfaces fluctuate in more or less predictable manner according to latitude and season. By correcting for the effect of these fluctuations the accuracy of our transit time measurement can be considerably improved. The question arises, however, of effect of short-term fluctuations in the altitude of the isopycnic surface.

From meteor data it has been observed<sup>15</sup> that at a mean height of 78 km (256,000 feet) the total seasonal range corresponded to a height variation of 8.6 km (28,000 feet). If this is a more or less sinusoidally varying function, the rms seasonal fluctuation is about 9,000 feet. By correcting for this seasonal fluctuation, the rms error can be reduced to 2,000 or 3,000 feet.

It was observed that the correlation is not improved by a comparison with the actual ground temperature at that date rather than with the general average. Thus, the correlation is truly a seasonal one which does not measure local variations. No effects associated with synoptic weather fronts, deviant temperatures in the lower stratosphere, sunspot numbers, lunar-hour angle or solar-hour angle are conspicuous. From further meteor observations Jacchia<sup>16</sup> finds evidence that the seasonal effect decreases with increasing height, becoming small and uncertain around the 100 km level.

The data from Jacchia supports the contention that seasonal and latitudinal corrections are of the greatest importance in the refinement of the star transit time measurements.

In comparison with these two sources of fluctuation, the random component or the component correlated with other physical phenomena

are small. In addition, our light ray traverses a considerable length through the atmosphere and therefore allows considerable averaging. For example, a ray at minimum altitude of 150,000 feet traverses a length of 1,000 miles from the time it passes through the 200,000 foot level to the time it emerges from this level.

## 2. Atmospheric Spectral Absorption

In the use of spectral absorption for the definition of star transit times, the ozone absorption is the most attractive. At wave lengths longer than 3,000 angstroms the absorption drops off rapidly and the ray penetrates too low in the atmosphere before sufficient absorption takes place. At wave lengths shorter than 2,000 angstroms the 50 per cent absorption point is achieved at very high altitudes, which is desirable, but it involves a region of the spectrum which is largely unexplored and which imposes a severe restriction on the number of stars usable for the measurement.

Unfortunately, the ozone content of the atmosphere undergoes a wide variation from hour-to-hour, day-to-day, season-to-season and from one latitude to another. Figures (15) and (16) are illustrative of this point. Thus, in the case of ozone it is probably not possible to predict the altitude of a given isoabsorption level more accurately than 8,000 to 10,000 feet (rms). Because the accuracy potential of determining altitude by refraction measurements is at least twice as good as this, and because simpler seasonal and latitudinal corrections must be made, ozone spectral absorption is not recommended.

In the case of the sun, however, the use of spectral absorption is recommended. The sun is such an extended target that a single refraction measurement cannot be made because light emanates simultaneously

Figure 15  
LATITUDINAL VARIATION OF OZONE CENTER OF GRAVITY

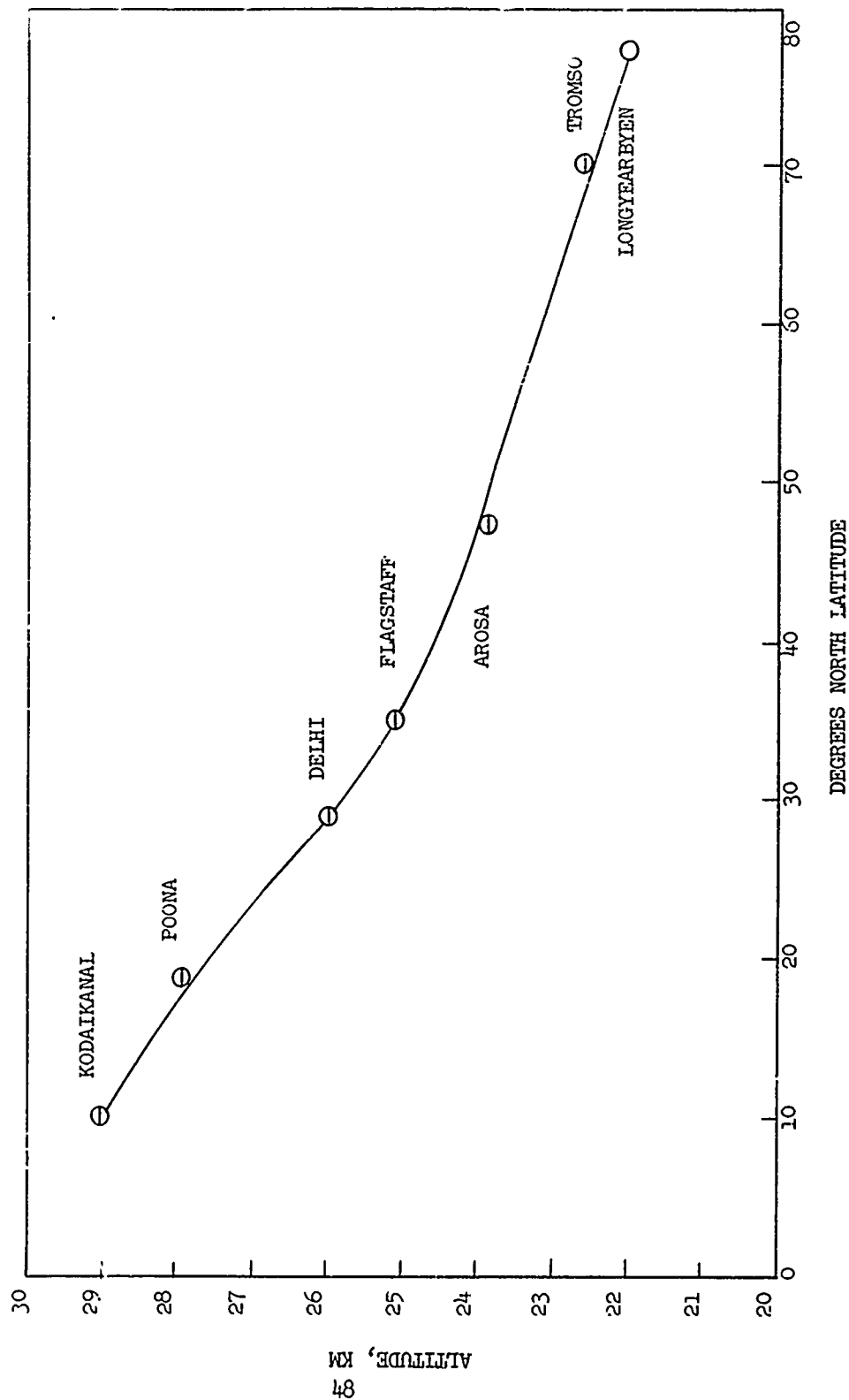
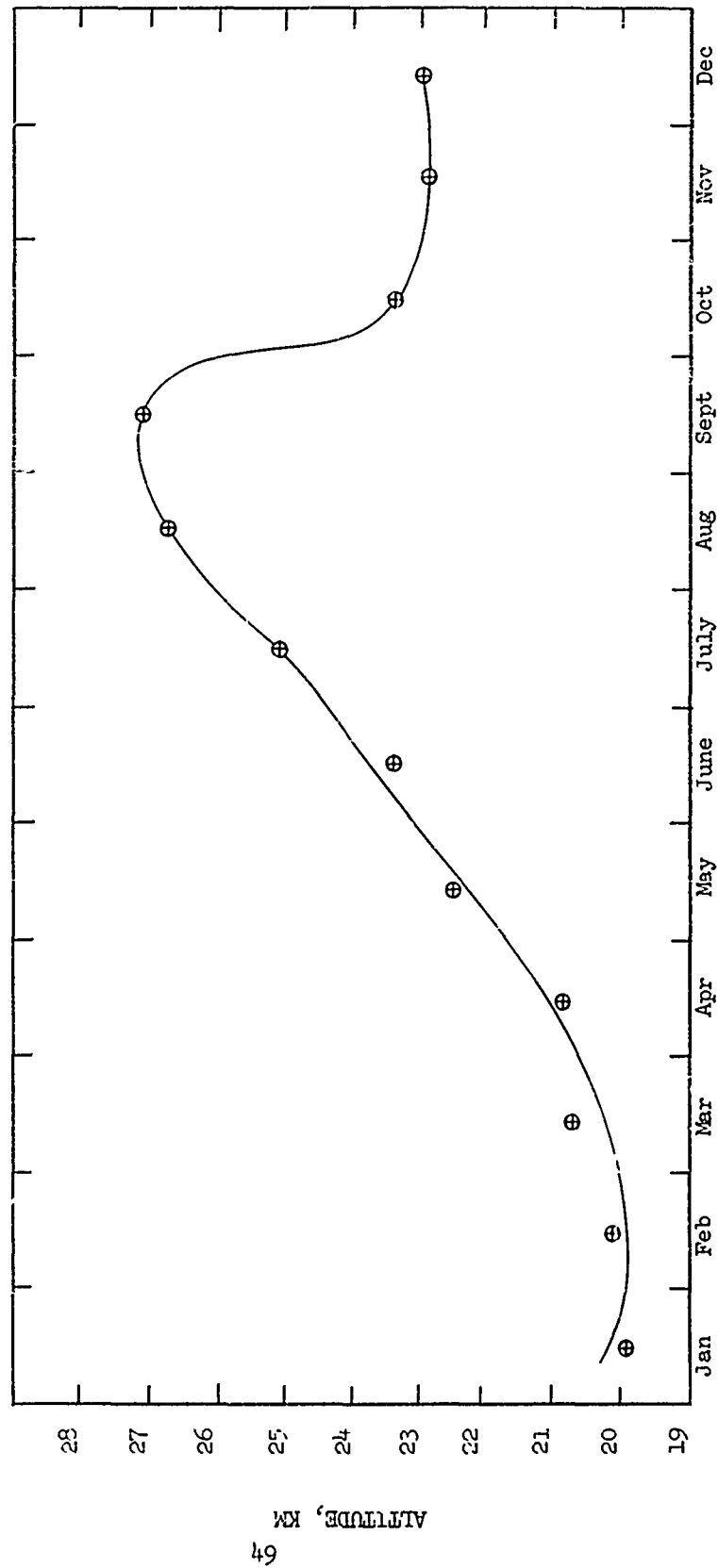


Figure 16  
SEASONAL VARIATION OF OZONE CENTER OF GRAVITY AT FLAGSTAFF



from opposite edges of the sun's disk. Considerable accuracy is achievable by measuring absorption because the absorption lines of a predictable distributed component of the atmosphere such as  $\text{CO}_2$  can be used. In this case we will be working in the mid-infrared region of the spectrum. (In the case of the stars, there is insufficient energy in this region of the spectrum and we are restricted to operation at wave lengths generally less than 1 micron.)

A number of infrared absorption lines for  $\text{CO}_2$  are shown in Table I. These lines range from 1.4 to 15 microns, and vary in usable width from 0.06 microns to 0.2 microns. Shown in this table is the equivalent sea level path for 50 per cent absorption for various wave lengths. This data has been obtained from Altshuler.<sup>17</sup>

Because of their strength, the two most attractive absorption lines are those at 2.7 and 4.3 microns. The 2.7 micron line is also a point of high absorption of  $\text{H}_2\text{O}$  - one of the most variable components of the atmosphere. Because of this and because the 4.3 micron line has greater absorptivity, it is this latter line which is recommended.

Figure (17) shows the magnitude of the spectral absorption at various altitudes for the 4.3 micron  $\text{CO}_2$  line. Fifty per cent absorption is obtained at an altitude of 160,000 feet or 49 km. At the 50 per cent point for radiation from a point source, an error of 1 per cent of the original intensity creates an equivalent error of 600 feet in altitude. Unfortunately, the sun is not a point source and one must resort to a numerical integration over an extended region of altitudes to determine the altitude at which its intensity is reduced to some value such as 50 per cent. This will be discussed later.

The data shown in Figure (17) have been derived with the aid of Figure (18) assuming that the atmospheric attenuation is proportional

TABLE I  
INFRARED ABSORPTION LINES OF CO<sub>2</sub>

WAVE LENGTH (MICRONS)	SEA LEVEL PATH FOR 50% ABS.(km)	BANDWIDTH (MICRONS)	ALTITUDE OF GRAZING RAY FOR 50% ABSORPTION (km)
1.4	3000	$\pm .04$	0
1.6	3000	.04	0
2.0	100	.03	7
2.72	.9	.06	28
4.3	.025	.08	45
4.85	.45	.06	10
5.2	200	.06	4
9.32	60	.07	9
9.55	80	.06	8
10.30	200	.10	4
10.6	250	.05	3
15.0	.0035	.10	54

Figure 17  
SPECTRAL ABSORPTION OF GRAZING RAY AT VARIOUS ALTITUDES  
FOR WAVE LENGTH REGION, 4.22 - 4.38 MICRONS

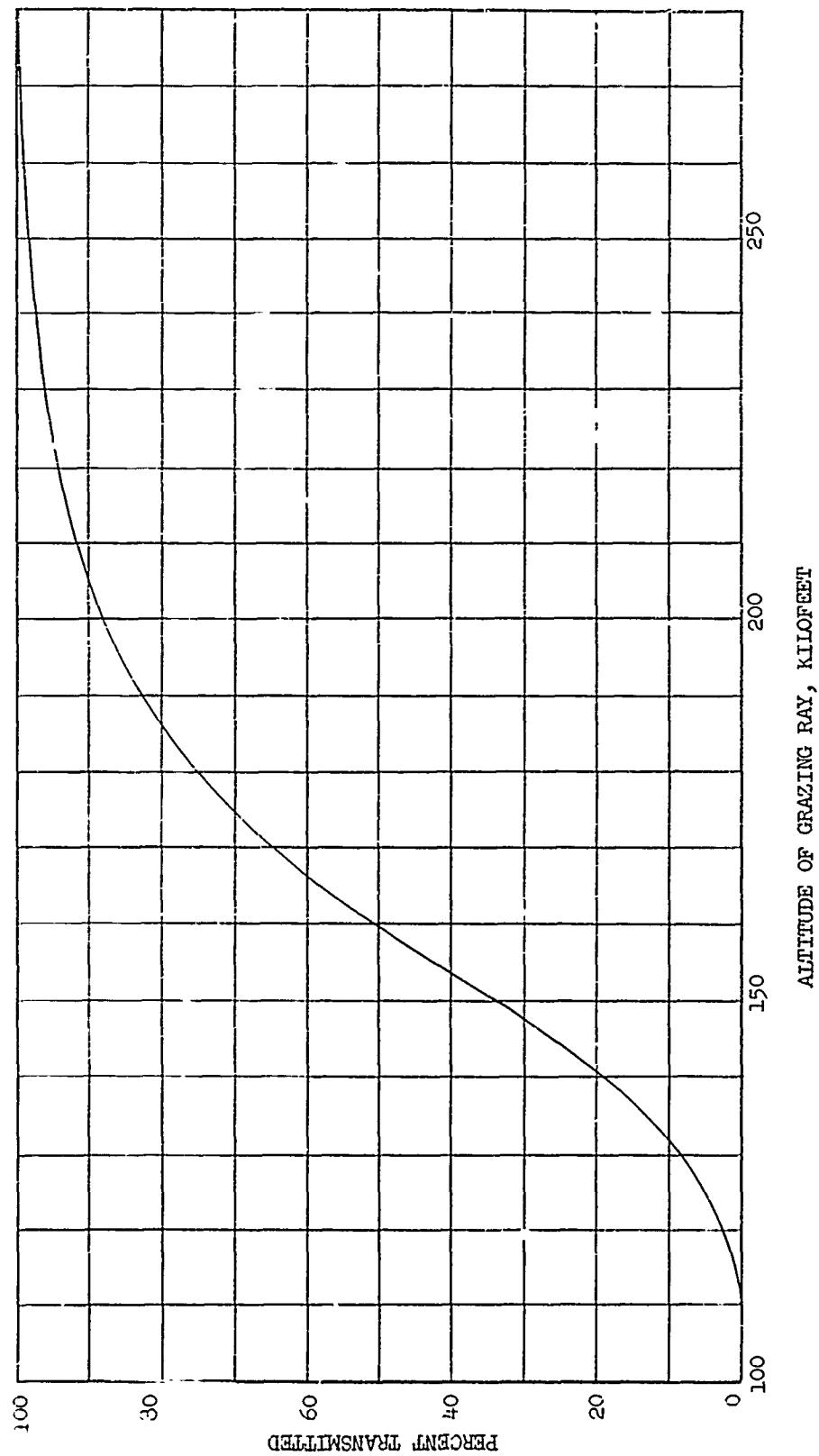
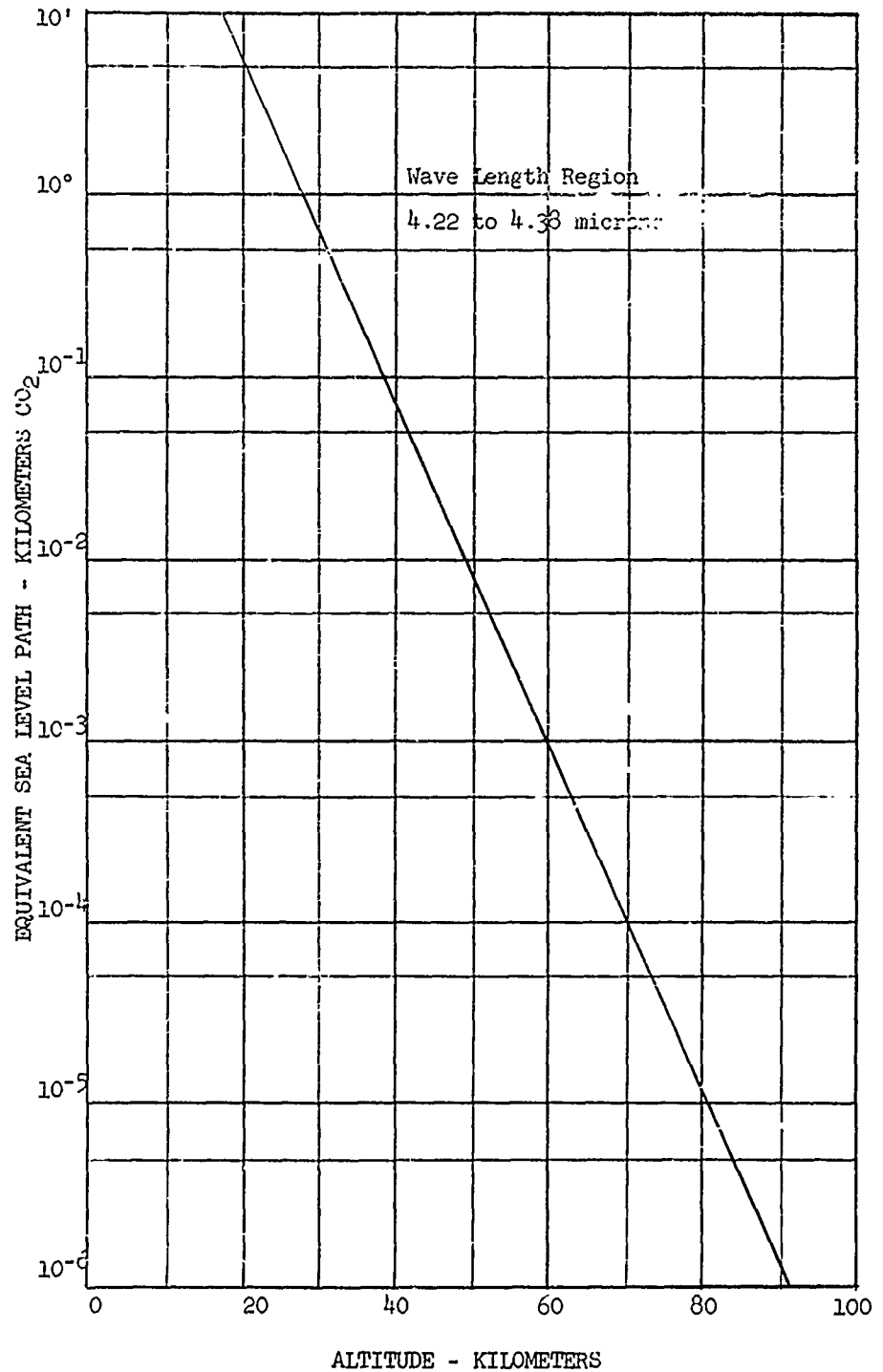




Figure 18

CO<sub>2</sub> ABSORPTION PATH AS A FUNCTION  
OF GRAZING ALTITUDE FOR A RAY  
PASSING THROUGH THE ATMOSPHERE



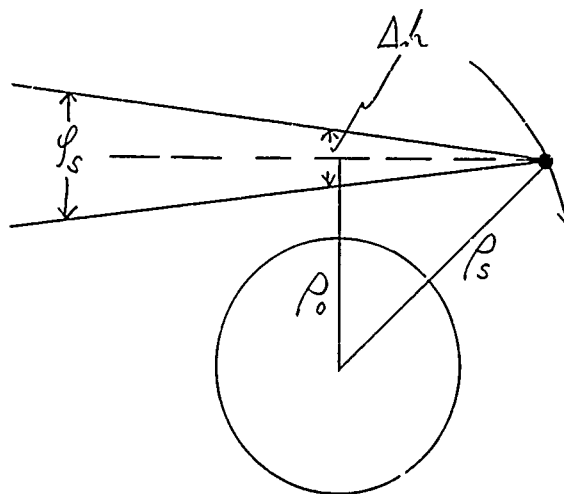
to an exponential function of the pressure to the  $3/2$  power rather than to the air mass alone. After establishing the equivalent sea level path, the per cent transmission was calculated for the various sea level paths.<sup>18</sup>

Because the sun represents an extended source, the altitude at which, say, 50 per cent attenuation of its signal occurs is a function of the satellite altitude. This occurs because of the shape of the spectral absorption curve shown in Figure (17), and because of the effects of differential refraction. Were it not for these effects, the 50 per cent occultation surface would be very nearly cylindrical as it is for a star. The correction problem would be even more difficult with some other attenuation level because the corrections would have to be superimposed on a conical shape.

If atmospheric refraction is disregarded, the diameter of the sun at the point of tangency of the grazing ray can be written in the form

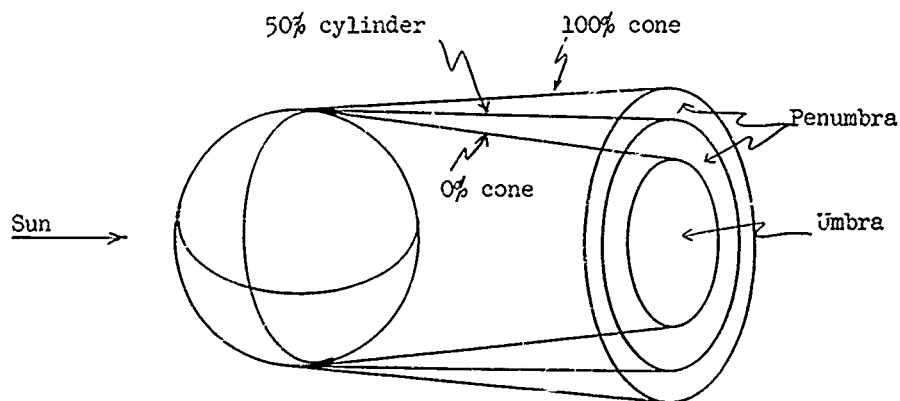
$$\Delta h = D \varphi_s = 9.305 \times 10^{-3} \sqrt{\rho_s^2 - \rho_0^2}$$

where the apparent diameter of the sun at the mean earth distance is taken as  $9.3048 \times 10^{-3}$  radians



For comparative purposes with Figure (17), the values of  $\Delta h$  at various satellite altitudes are shown in Table II. Time did not permit a calculation of the apparent occultation altitude as a function of satellite altitude; however, it is apparent that the correction function will be very complex for satellite altitudes greater than 1,000 miles.

The sketch shown below shows the shapes of the occultation surfaces for various percentage transmissions for the simplified case where the earth is considered to have no atmosphere.



It was mentioned previously that the altitude at which 50 per cent of the solar energy (at  $\lambda = 4.22$  to  $4.38$  microns) is absorbed by the earth's atmosphere varies as the altitude of the satellite varies. Table III shows the various correction factors which must be applied.

If the sun were a point source, and if the satellite were at very low altitudes, the altitude at which 50 per cent attenuation is observed would be 160,000 feet.

TABLE II  
 DIAMETER OF SUN AT POINT OF TANGENCY  
 FOR GRAZING RAY AT VARIOUS SATELLITE ALTITUDES

SATELLITE ALTITUDE S. MILES	SOLAR DIAMETER FEET
100	44,000
300	77,600
1,000	147,300
3,000	257,000
10,000	658,000
30,000	----
100,000	5,100,000

TABLE III  
 ALTITUDE OF GRAZING RAY WITH 50% SOLAR ENERGY  
 TRANSMISSION FOR VARIOUS SATELLITE ALTITUDES

SATELLITE ALTITUDE (miles)	CORRECTION TERMS, FEET				ALTITUDE FOR 50% INTENSITY
	Spectral Absorption	Differential Refraction	Refractive Bending	Earth Curvature	
100	+700	+5	-100	-0	160,600
300	+2000	+350	-200	-0	162,200
1,000	+4500	+900	-350	-50	165,000
3,000	+6800	+3600	-550	-150	169,700
10,000	+15800	+6800	-1200	-850	180,400

The spectral absorption correction term can be derived from Figure (17) and from Table II. The light extinction due to differential refraction can be derived from curves of the type shown in Figure (11). These values were obtained by taking the extinction at the center of the solar image and are therefore only approximate. The refractive bending has been derived from Figure (5). The earth curvature correction results from the fact that, for satellites at large distances from the earth, the image of the earth coming across the sun is curved. The last column of Table III shows the altitude at 50 per cent absorption including the correction terms which must be applied. Figure (19) shows the corrected 50 per cent absorption altitude as a function of satellite altitude.

Since the uncertainty in the altitude of the isopycnic surfaces is about one-half mile at these altitudes, this kind of altitude correction need be made only for solar occultations taking place when the satellite altitude is greater than 500 miles.

If possible, we would like to avoid complicating the system by making this altitude correction. Probably the easiest way of doing this is by selecting an attenuation level which is less than 50 per cent and whose occultation surface is (without the correction terms) a cone which gets smaller as the satellite altitude increases. Generally, this will be a linear function of the distance of the satellite from the point of closest approach of the ray to the earth; however, it will not be a linear function of satellite altitude. As a result, the dotted curve shown in Figure (20) is obtained after assuming that the detector discrimination level is set for 46 per cent atmospheric attenuation.

Figure 19  
 ALTITUDE AT WHICH 50% ATTENUATION OF SOLAR INTENSITY  
 IS OBTAINED FOR VARIOUS SATELLITE ALTITUDES

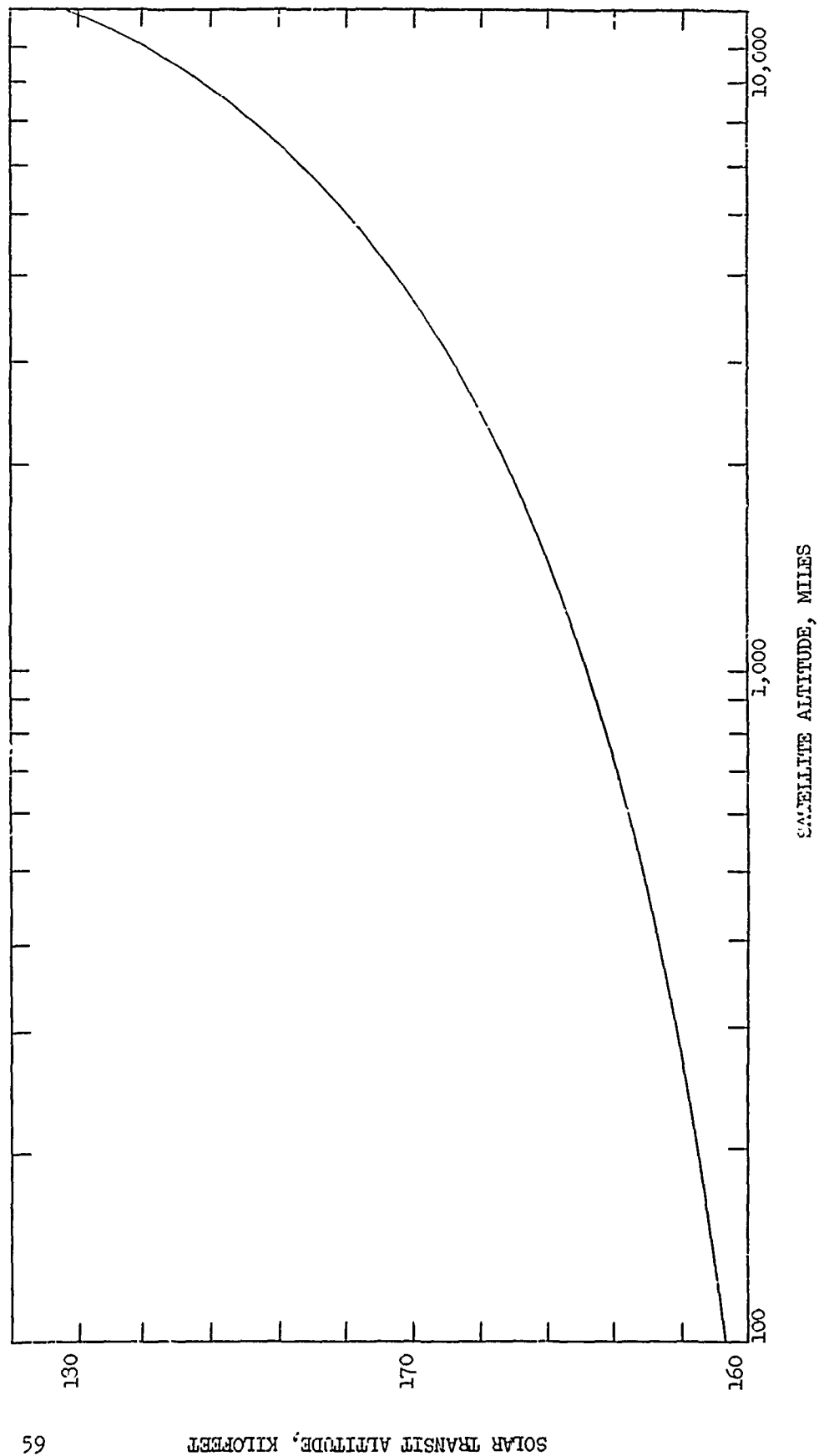
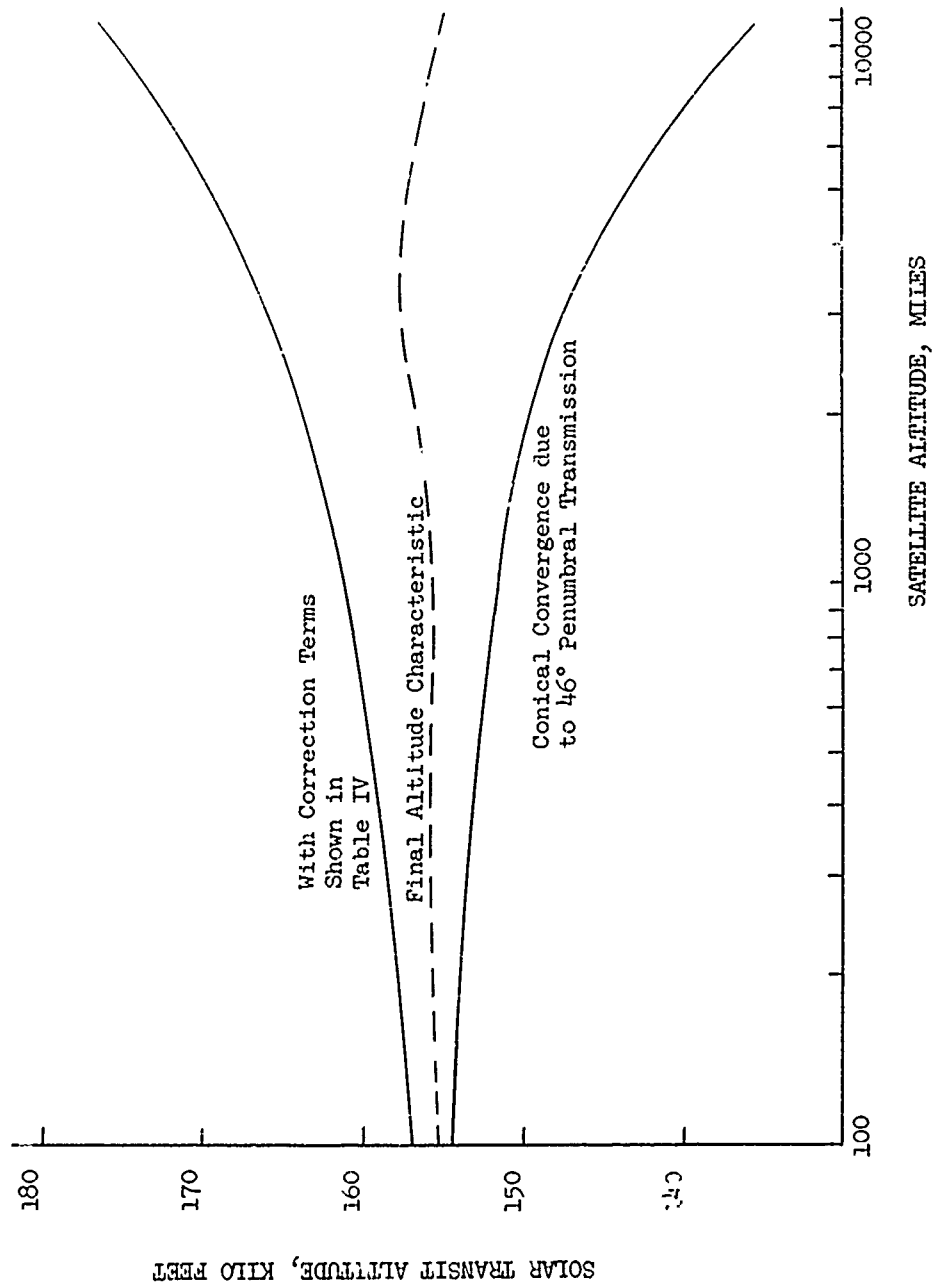
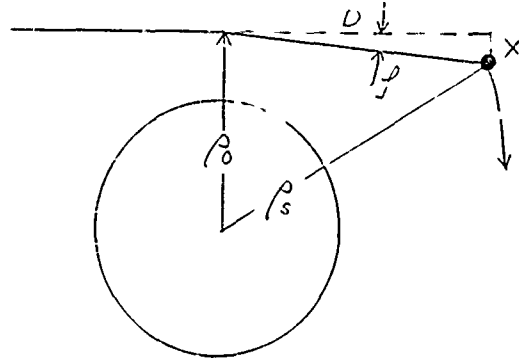


Figure 2C  
ALTITUDE AT WHICH 54% ATTENUATION OF SOLAR INTENSITY  
IS OBTAINED FOR VARIOUS SATELLITE ALTITUDES





In deriving Figure (20) it was assumed that the shape of the cone must be such that a convergence of 21,400 feet results when the satellite is at an altitude of 10,000 s. miles as shown in the sketch below.



Where:

$$r_s = 14,000 \text{ miles}$$

$$r_0 = \dots + 160,000 \text{ feet}$$

$$D = 13,400 \text{ miles}$$

$$X = 21,400 \text{ feet}$$

Since  $X = 4.05$  miles, the angle  $f = 3.03 \times 10^{-4}$  radians. The diameter of the sun is  $9.305 \times 10^{-3}$  radians, therefore, the discrimination level must be set such that

$$\frac{\Delta I}{I} = \left( \frac{3.03 \times 10^{-4}}{9.305 \times 10^{-3}} \right) \frac{4}{\pi} = .0414$$

Thus we will obtain a cone with the proper apex angle if the transmission level is set at about 46 per cent (4 per cent less than 50 per cent).

Under these conditions Table III must be modified. In the first place, an attenuation level of 54 per cent is achieved at an altitude of approximately 156,000 feet. To the other correction factors (which will be approximately the same), we must add the conical convergence factor. When this is done we obtain Table IV.

The rms deviation from a cylindrical occultation surface for a range of satellite altitudes out to 10,000 miles does not exceed 1,000 feet. By proper selection of the discriminating intensity for the solar transit

TABLE IV  
 ALTITUDE OF GRAZING RAY WITH  
 46% SOLAR ENERGY TRANSMISSION  
 FOR VARIOUS SATELLITE ALTITUDES

SATELLITE ALTITUDE (miles)	CORRECTION TERMS, FEET		Altitude for 46% Intensity
	Factors from Table IV	Conical Convergence	
100	+600	-1,400	155,200
300	+2,200	-2,600	155,800
1,000	+5,000	-4,800	155,800
3,000	+9,700	-8,400	157,300
10,000	+20,400	-21,400	155,000

time measurement, the occultation surface can for all practical purposes be made cylindrical.

### C. Star Selection

In the last quarterly report<sup>19</sup>, star pairs were considered which deviated from diametricity by less than 3 minutes of arc. This was a necessity for the rotating aberrascopes since collinearizing wedges of larger angles would introduce significant errors into the system. Now, for a non-rotating aberrascopes, the collinearizing wedge is not required and the axes of the two optical systems can deviate mechanically by the same angle as the star pair. The deviation from diametricity can now be as large as 2.5 degrees and stars of visual magnitude 3.5 or brighter can be considered. The star distance from the solar ecliptic was to be a minimum of 20 degrees.

The use of the 3.5 visual magnitude restriction reduces the number of stars available from the general catalog to 259 from which eight pairs were found that satisfied the basic criteria. These star pairs are listed as pairs No. 1 through 8 in Table V. A further stipulation that the two star pairs be orthogonal within 20 degrees reduced the list of eight pairs to one pattern of four stars.

In order to obtain other star pairs the visual magnitude restriction was eased to a value of 4.7 or brighter. Using this new value a manual search of the Atlas Coeli 1950.0, by Antonin Becvar, was made to find stars that appeared to satisfy the prior stated conditions of diametricity and ecliptic distance. The total search produced a list of 35 pairs which are listed in Table V. This listing includes a few pairs which deviate from diametricity by as large an angle as 3.3 degrees and were included because of their desirable brightness. Of the pairs listed, those numbered down to pair No. 25 meet the requirement of distance from the ecliptic.

In order to compare the brightness of the stars under consideration, a correction based on temperature of the star is necessary. The correction as a function of temperature is shown in Figure 21. A star of spectral

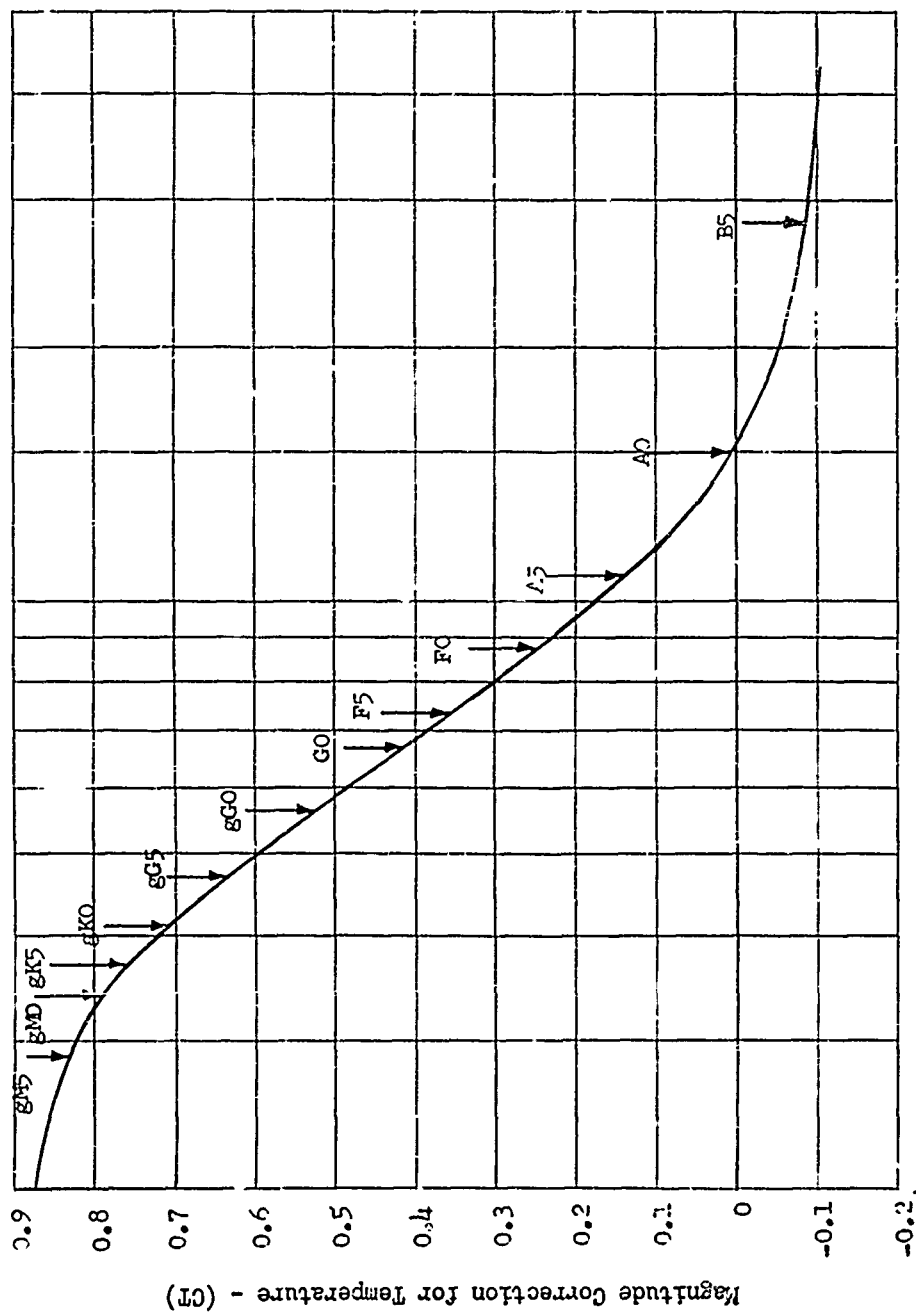


Figure 21. Correction Factors for Stars

class A0 is used as the basis for the correction; stars of other spectral classes must have an appropriate correction added to the apparent magnitude in order to obtain the corrected magnitude. Thus the magnitude corrected for type ( $M_T$ ) is the sum of the visual magnitude ( $M_V$ ) and the correction factor (CT). The corrected star magnitudes are shown in Table V along with the other pertinent facts about the stars in question.

In general, this study thoroughly covers the 3.5 magnitude and brighter stars, whereas those star pairs between 3.5 and 4.7 magnitude are studied only to a questionable extent. To determine more adequately star pairs that exist in magnitudes brighter than 4.7 it is concluded that a computer study would be needed. The study would have to be based on stars that had the magnitude corrected for spectrum classification and as such would require investigation of stars up to a visual magnitude of approximately 5.0 or brighter. With the magnitude determined and the criteria for diametricity, ecliptic distance and orthogonality established, an accurate list of all stars meeting the desired conditions can be obtained.

As a result of the present study it appears that at least six pairs of stars can be found which have magnitudes equal or less than 4.3, and diametricity equal or less than 3.25 degrees. These pairs are listed in Table VI. From this table it appears that if magnitude is the prime consideration, the stars in group one should be used. This group also has pairs with deviations from diametricity of 1.5 degrees.

Thus far, the star selection criteria have been such factors as magnitude, spectral class, deviation from diametricity for the pair of stars, distance from the ecliptic and finally, the angle between two pairs of stars in the grouping of four required for the aberrascopes system. In addition to these considerations, stars must be selected whose positions satisfy the geometrical requirements of the problem. The basic requirement with respect to the geometry is that the stars be selected so as to be occulted by the earth at some points in the satellite orbit. It is obvious that if no occultations occur, no occultation times can be measured.

The necessary and sufficient condition that an occultation of a star occur is the following:

$$c \geq \cos i \sin \delta - \sin i \cos \delta \sin (\alpha - \Omega) \equiv f(\delta)$$

where  $c = R/a$

$R$  = Radius of occulting sphere

$a$  = Radius of orbit

$i$  = Inclination of orbit

$\delta$  = Declination of star

$\alpha$  = Right ascension of star

$\Omega$  = Angle to line of nodes of orbit

The assumptions made are that the occulting body is a sphere and that the satellite orbit is circular. If we assume that the orbital inclination is between zero and ninety degrees and also, that the declination of the star in question is also between zero and ninety degrees, a necessary and sufficient condition that an occultation occur for any value of the angle to the line of nodes ( $\Omega$ ) is the following:

$$c \geq \sin(i + \delta) \qquad 0 \leq \Omega \leq 360^\circ$$

## STAR PAIRS .

TABLE V

No.	General Catalog No.	R.A. 1950	Decl. 1950	Type	Mag. Apparent	Mag. Correct for Type	Variation from Diametricity (degrees)	Distance from Ecliptic (degrees)
1	147	00 06 29.8	58 52 27	dK2	2.42	2.72	.278	58
	16724	12 12 28.6	-58 28 15	B3	3.08	3.03		
2	792	00 37 39.3	56 15 49	gK0	2.47	3.17	1.380	51
	17052	12 28 22.7	-56 50 01	M4	1.61	2.44		
3	1400	01 06 55.5	35 21 22	gM0	2.37	3.22	2.445	28
	18039	13 17 46.7	-36 26 57	A2	2.91	2.97		
4	2572	02 06 33.6	34 45 06	dA5	3.08	3.09	1.493	23
	19033	14 03 43.9	-36 07 30	gGA	2.26	2.66		
5	3664	03 01 09.6	53 18 44	F7&A3	3.08	3.13	1.822	36
	20418	15 08 40.8	-51 54 38	G5	3.50	4.20		
6	5164	04 13 46.5	-62 35 55	G5	3.36	4.06	1.490	84
	22101	16 23 18.5	61 27 37	gG6	2.89	3.59		
7	6226	05 03 00.2	41 10 08	B3	3.28	3.23	2.265	18
	23180	17 08 34.0	-43 10 31	A7n	3.44	3.64		
8	12831	09 15 45.1	-59 03 54	F0	2.25	2.50	3.316	75
	29848	21 17 23.2	62 22 24	A7n	2.60	2.80		
9	645	00 30 08.4	62 39 22	F0	4.24	4.20	3.25	59
	17374	12 44 47.1	-59 24 57	B1	1.50	1.46		
10	1715	01 22 31.5	59 58 34	A4	2.80	2.90	.847	51
	18087	13 19 23	-60 43 37	B5	4.62	4.52		
11	2477	02 00 49.2	42 05 27	K0	2.28	2.98	1.069	30
	18874	13 55 13.3	-41 51 27	B3	4.05	4.00		



## STAR PAIRS

TABLE V  
(cont.)

No.	General Catalog No.	R.A. 1950	Decl. 1950	Type	Mag. Apparent	Mag. Correct for Type	Variation from Diametricity (degrees)	Distance from Polaris (degrees)
12	3300	02 41 44.5	-14 04 10	B5	4.39	4.29	.735	30
	19777	14 38 45.6	13 56 30	A2	3.87	3.91		
13	3484	02 56 21.9	-40 30 15	A2	3.42	3.92	.704	57
	20226	15 00 3.7	40 35 12	G5	3.63	4.23		
14	9747	07 16 51.6	-67 51 57	F5	4.02	4.37	.501	90
	26520	19 12 32.9	67 34 25	K0	3.24	3.94		
15	2289	01 50 46.4	63 25 30	B3	3.44	3.39	.362	52
	18845	13 54 00.4	-63 26 34	K0	4.68	5.38		
16	2756	02 14 43.4	-51 44 35	B8	3.78	3.68	.155	65
	19269	14 14 23.7	51 35 50	A5	4.78	4.83		
17	3463	02 50 46.2	-75 16 17	K2	4.70	5.42	.912	89
	20029	14 50 49.7	74 21 35	K5	2.24	2.99		
18	4730	03 52 59.5	62 55 41	R9	4.87	4.77	.435	43
	21332	15 50 43	-63 16 43	F0	3.04	3.29		
19	7287	05 46 03.9	-51 05 02	A3	3.94	4.04	.400	75
	24221	17 47 52.5	50 47 31	A2	5.09	5.29		
20	7587	05 57 33.2	-03 04 29	K0	4.68	5.38	.152	27
	24509	17 58 08.4	02 55 56	B5p	3.92	3.82		
21	11959	08 39 24.1	-15 45 45	K0	4.98	5.68	.506	34
	28780	20 37 18.9	15 44 04	A5	3.86	4.01		
22	12923	09 19 45.0	-62 11 28	K0	4.86	5.56	.330	78
	29848	21 17 23.2	62 22 24	A5	2.60	2.75		

# STAR PAIRS

TABLE V  
(Cont.)

No.	General Catalog No.	R.A. 1950	Decl. 1950	Type	Mag. Apparent	Mag. Correct for Type	Variation from Diametricity (degrees)	Distance from Ecliptic (degrees)
23	15340	11 06 51.6	44 46 12	K0	3.15	3.85	.758	39
	32270	23 -7 32.1	-45 31 05	G5	4.10	4.73		
24	15547	11 15 47.0	33 22 02	K0	3.71	4.41	.566	29
	32450	23 16 07.7	-32 48 17	K0	4.51	5.21		
25	7587	05 57 33.2	-03 04 29	K0	4.68	5.38	.210	26
	24509	17 58 08.4	02 55 56	B5	3.92	3.82		
26	238	00 10 39.4	14 54 20	B2s	2.87	2.83	2.135	14
	16740	12 13 13.9	-17 15 52	B8	2.78	2.68		
27	2538	02 04 20.9	23 13 37	gK2	2.23	2.98	3.220	11
	19029	14 03 31.1	-26 26 33	gK3	3.48	4.26		
28	6029	04 53 44.0	33 05 20	gK3	2.90	3.65	1.811	10
	22640	16 46 55.2	-34 12 16	gG9	2.36	3.06		
29	8208	06 19 56.1	22 32 23	gM3	3.19	4.01	3.125	3
	25180	18 24 53.0	-25 27 04	gK1	2.94	3.64		
30	3391	02 47 02.1	27 03 20	B8	3.68	3.58	.700	11
	19954	14 47 20.7	-27 45 12	K2	4.63	5.38		
31	5599	04 32 54.3	10 03 35	A3	4.38	4.48	.549	12
	22332	16 34 24.1	-10 28 03	B0	2.70	2.65		
32	6306	05 06 50.1	15 32 06	F0	4.86	5.10	.210	7
	23158	17 07 30.5	-15 39 53	A2	2.63	2.68		

# STAR PAIRS

TABLE V  
(cont.)

No.	General Catalog No.	R.A. 1950	Decl. 1950	Type	Mag. Apparent	Mag. Correc. for Type	Variation from Diametricity (degrees)	Distance from Eccliptic (degrees)
33	15511	11 14 07.1	-03 22 41	A5	4.58	4.73	.386	8
	32415	23 14 34.3	03 00 32	K0	3.85	4.55		
34	16425	11 58 18.6	06 53 35	A3	4.57	4.67	.658	7
	33330	23 59 23.7	06 17 31	M6	4.66	5.46		
35	16189	11 46 30.6	14 51 06	A2	2.23	2.27	1.540	12
	32931	23 40 07.8	-14 49 18	A0	4.62	4.62		

TABLE VI  
ABERRASCOPE STAR GROUPS

Group No.	General Catalog No.	Constellation	Type	Magnitude (corrected)	Deviation from Diametricity (degrees)	Angle between Pairs (degrees)	Distance from Ecliptic (degrees)
1	2572	$\beta$ Tri	A5	3.09	1.5	102	23
	19033	$\theta$ Cen	K0	2.66			
	5164	$\alpha$ Ret	G5	4.06	1.5		84
	22101	$\eta$ Dra	G5	3.59			
2	645	$\kappa$ Cas	cBOe	4.20	3.2	99	59
	17374	$\beta$ Cru	B1	1.46			
	3300	$\pi$ Cet	B5	4.29	0.7		30
	19777	$\zeta$ Boo	A2	3.91			
3	1400	$\beta$ And	M0	3.22	2.4	99	28
	18039	$i$ Cen	A2	2.97			
	3584	$\theta$ Eri	A2	3.92	0.7		57
	20226	$\beta$ Boo	G5	4.23			

For values of the angle to the line of nodes between the right ascension of the star and the right ascension plus  $45^\circ$ , or in the range right ascension plus  $135^\circ$  to right ascension plus  $360^\circ$ , the following is a necessary and sufficient condition that occultation occur:

$$c \geq \cos i \sin \delta + (1/\sqrt{2}) \sin i \cos \delta$$

$$\alpha \leq \Omega \leq \alpha + 45^\circ$$

$$\alpha + 135^\circ - \Omega \leq \alpha + 360^\circ$$

Thus for 75% of all values of  $\Omega$ , an occultation will occur.

For values of the angle to the line of nodes between the right ascension plus  $180^\circ$  and right ascension plus  $360^\circ$ , the following is a necessary and sufficient condition that occultation occur:

$$c \geq \cos i \sin \delta$$

In this case, for 50% of all values of  $\Omega$ , an occultation will occur.

These three conditions are illustrated graphically in Figures 22, 23, and 24. As an example, (for a 300 mile orbit where  $c = .93$ ) assume that an orbital inclination of  $45^\circ$  is desired. Then, if occultation is necessary for all values of  $\Omega$ , it can be seen that stars must be selected which have a declination between  $0$  and  $23^\circ$  or between  $67^\circ$  and  $90^\circ$  where  $.93 > f(\delta)$ .

The reason for considering varying values of the angle to the line of nodes ( $\Omega$ ) is the regression of the line of nodes with time. The rate of regression ( $\Delta\Omega$ ) is given by the following:<sup>20</sup>

$$\Delta\Omega = \frac{2\pi RJ \cos i}{a(1-e^2)^{3/2}} \text{ radians/rev.}$$

where  $J$  is a constant ( $1.638 \times 10^{-3}$ ) and "e" is the eccentricity of the orbit. This equation can be used to determine the time in years required

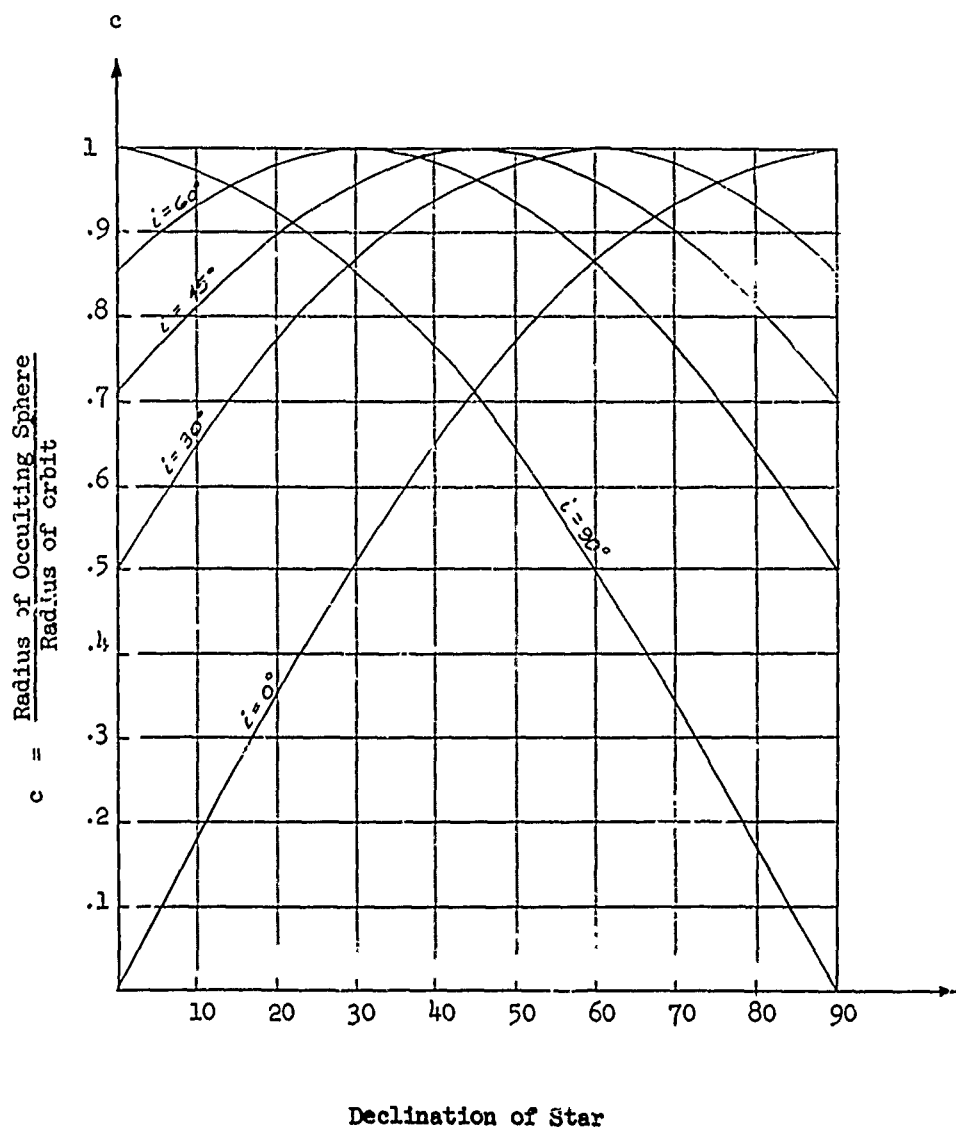


Figure 22

STAR DECLINATION SELECTION FOR OCCULTATION FOR ANY ANGLE  
TO THE LINE OF NODES OF THE ORBIT ( $\Omega$ )

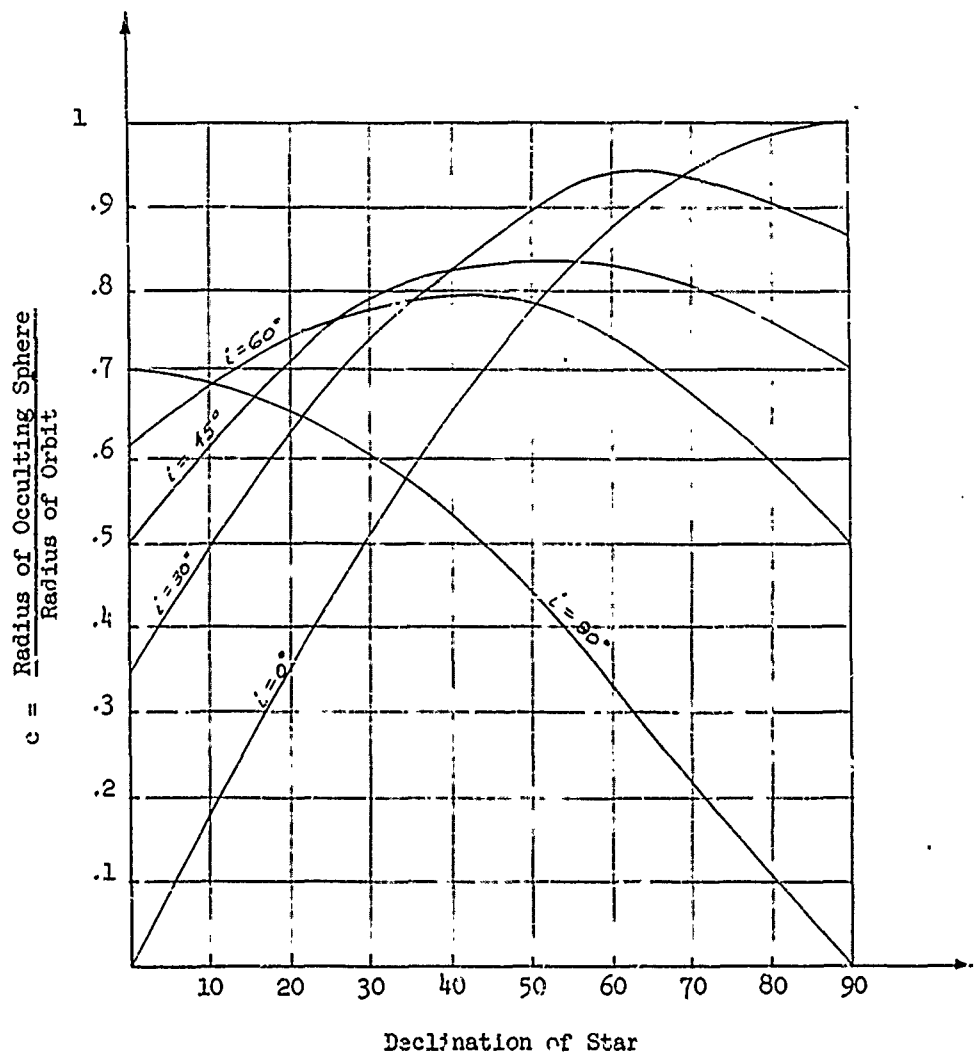


Figure 23

STAR DECLINATION SELECTION FOR OCCULTATION FOR ANGLE  
TO THE LINE OF NODES ( $\Omega$ ) AS FOLLOWS:

$$\alpha + 135^\circ \leq \Omega \leq \alpha + 360^\circ$$

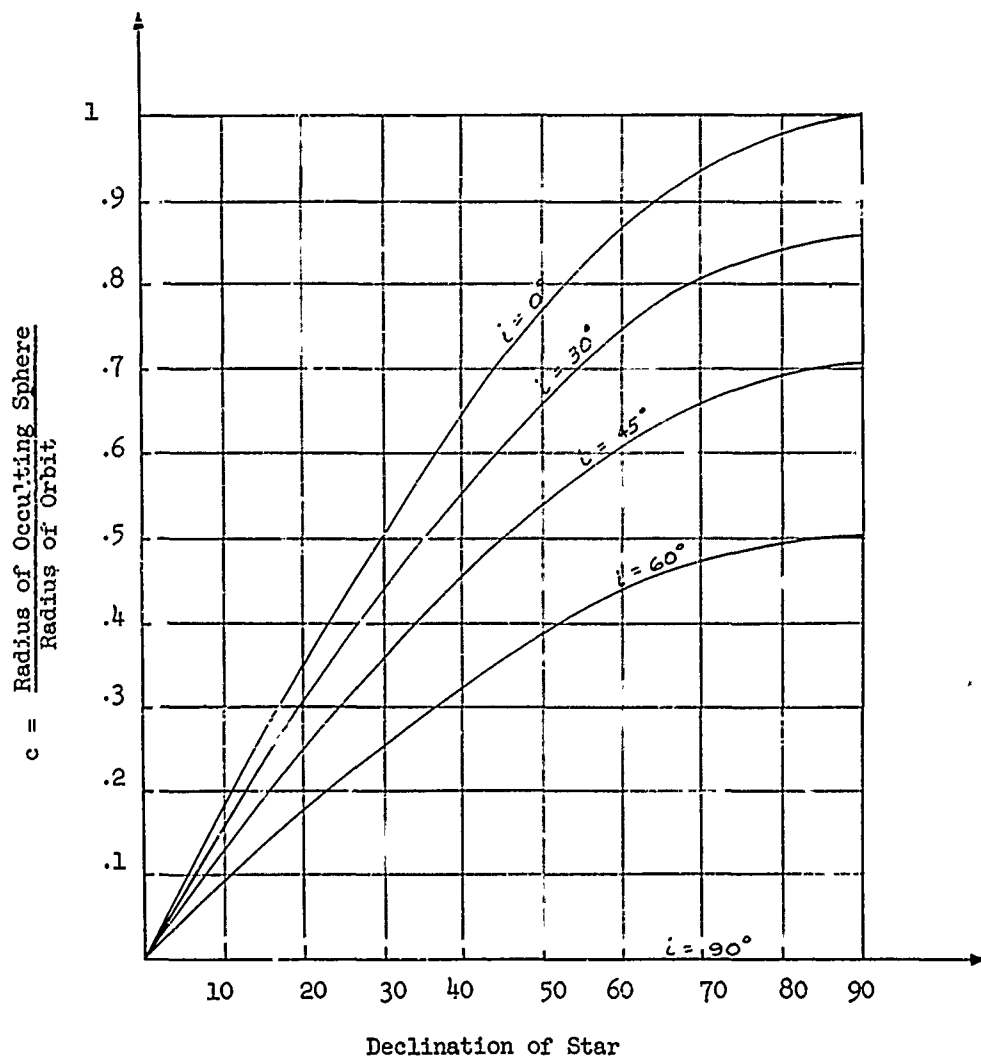


Figure 24

STAR DECLINATION SELECTION FOR OCCULTATION  
FOR ANGLE TO THE LINE OF NODES ( $\Omega$ ) AS FOLLOWS:

$$\alpha + 180^\circ \leq \Omega \leq \alpha + 360^\circ$$



for the line of nodes to regress thru an angle of  $360^\circ$ . For a circular orbit where "e" equals zero, this time in years (T) is expressed as follows:

$$T = a^{5/2} \secant i \times 10^{-9}$$

This equation is plotted in Figure 25. Thus for a 300 mile orbit at zero inclination, 1.3 years will be required for the line of nodes to regress  $360^\circ$ .

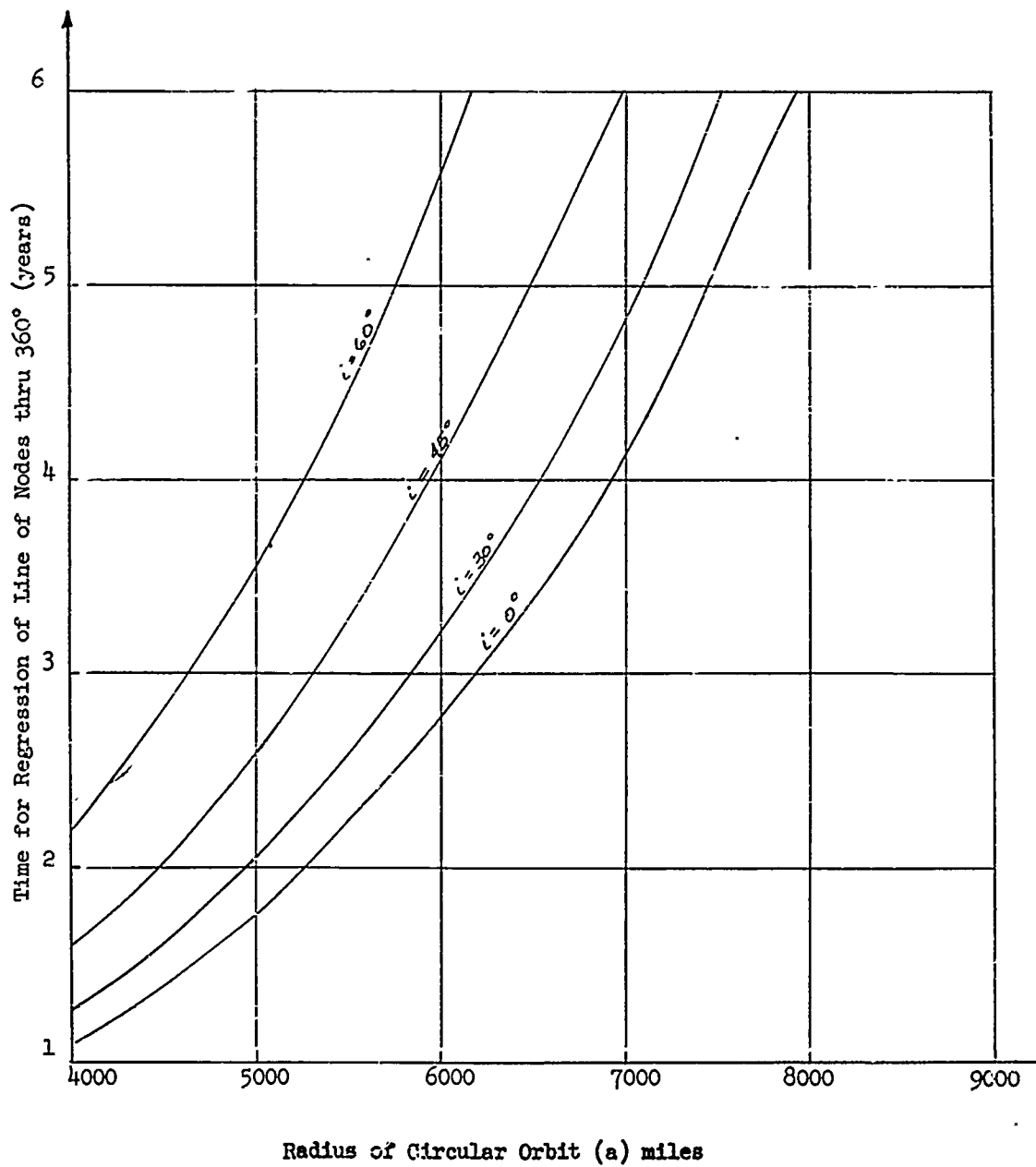


Figure 25

TIME FOR REGRESSION VS. RADIUS OF ORBIT

#### IV SYSTEM ERROR ANALYSIS

In this section two related and complimentary topics are discussed. The first concerns those errors introduced into the final calculation by the effects of meteorological irregularities and instrument errors; and the second concerns computational errors. Errors of the first topic result in errors in the measured time of occultation. Although these errors can be known and compensated, errors will still remain in the final calculation because of the facts that the system equation does not perfectly fit the problem, and the computer imposes limitation on the accuracy with which the problem can be solved.

##### A. Physical Errors

The sources of errors can be enumerated as follows:

##### 1) Meteorological Errors

- a) Systematic errors in mean latitudinal and seasonal corrections to nominal isorefraction altitude.
- b) Statistical fluctuations in atmosphere causing deviations from assumed altitude.
- c) Scintillation due to small scale inhomogeneities in the atmosphere resulting from wind shear.
- d) Background noise due to scattered radiation from the sun.

##### 2) Instrument Errors

- a) Systematic errors in measurement of the time at which refraction builds up to a preassigned value. (This error is equivalent to an angle error in the instrument refraction measurement).
- b) Random instrument errors in transit time measurement.
- c) Error due to changing aberration during refraction build-up.

- d) Error due to altitude drift of platform because stars are not perfectly diametrically opposite.
  - e) Error due to reference clock.
- 3) Computational Errors

Given a sufficiently large computer, the computational errors should be much smaller than those listed under (1) and (2); however, since our goal is a self-contained positional accuracy of about 1 mile achievable with a computer of minimum power, certain sources of computational errors will require investigation. We may not be able to ignore the ellipsoidal shape of the earth, the nodal regression, the precession of the perigee, and the problem of the rate of convergence of the successive iterations.

To indicate the influence of some of these errors, it is instructive to consider the sensitivity of the satellite altitude calculation to the errors in the altitude of the occultation surface. To do this we will examine a simplified case in which the plane of the orbit is known and in which the orbit is circular. If we select two diametrically opposed stars which lie in the orbital plane, a geometry of the type shown in Figure 26 results. (While this is valid here, see conclusions of paragraph IV B concerning in-plane stars.) The parameters shown in Figure 26 are listed below:

$\rho_s$  = Orbital radius

$\rho_o$  = Radius of occulting surface

$\rho_e$  = Radius of earth

$\gamma$  = Earth's central angle which subtends one half of the arc between ingress and egress

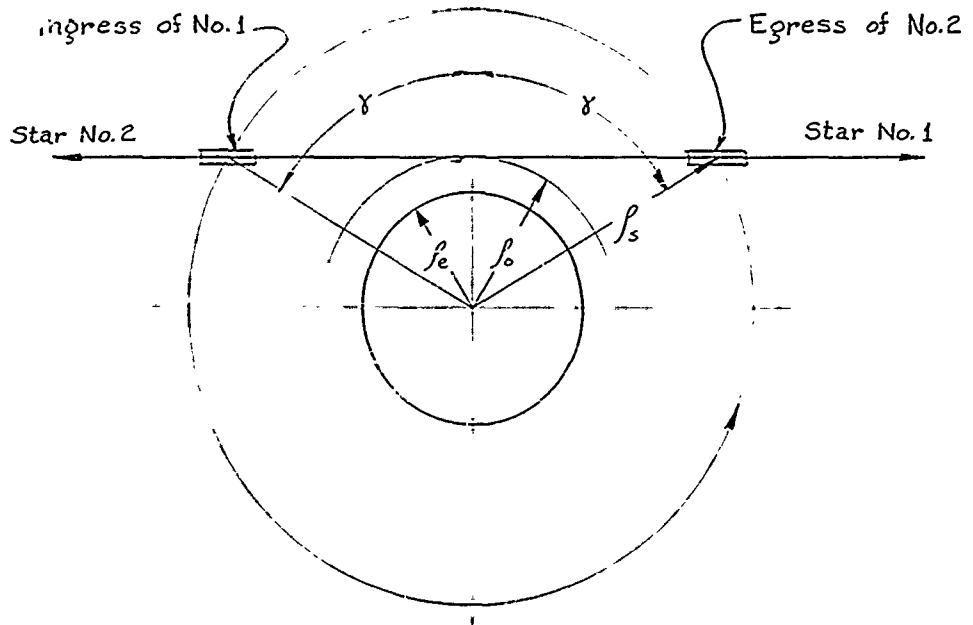


Figure 26  
In-Plane Star Pairs

Rather than calculate the value of  $\rho_s$  from the orbital period as was done previously, we will now calculate  $\rho_s$  by measuring the times of ingress of star 1 and egress of star 2.

For an inverse square law central force field and a circular orbit we may write

$$v = \rho_e \sqrt{\frac{g}{\rho_s}}$$

$$T = \frac{2\pi}{\omega} = \frac{2\pi \rho_s^{3/2}}{\rho_e g^{1/2}}$$

From the geometry shown above

$$2\gamma = 2 \cos^{-1} \left( \frac{\rho_e}{\rho_s} \right)$$

If  $t_e$  = time of egress of star 2, and

$t_i$  = time of ingress of star 1, then

$$\frac{t_e - t_i}{T} = \frac{\theta}{\pi} ;$$

therefore, 
$$\cos \gamma = \cos \frac{\pi(t_e - t_i)}{T} = \frac{\rho_o}{\rho_s}$$

$T$  is a function of  $\rho_s$  but  $\rho_s$  is an implicit function of  $\rho_o$ ,  $t_e$ , and  $t_i$ . Thus, we cannot obtain a direct solution for  $\rho_s$ . However, we can obtain the error sensitivity coefficients in explicit form.

If we assume that the errors in  $\rho_o$ ,  $t_e$ , and  $t_i$  are small and uncorrelated, then we need retain only the first order term in the Taylor's expansion and may write

$$\sigma(\rho_s)^2 = \left(\frac{\rho_s}{\rho_o}\right)^2 \sigma(\rho_o)^2 + \left(\frac{\partial \rho_s}{\partial t_e}\right)^2 \sigma(t_e)^2 + \left(\frac{\partial \rho_s}{\partial t_i}\right)^2 \sigma(t_i)^2 .$$

This amounts to separating the meteorological and instrument errors, i.e., the  $\sigma(t)$  are rms errors due only to the instrument time measurement and are not functions of the isorefractive surface errors,  $\sigma(\rho_o)$ . To determine the value of  $\frac{\partial \rho_s}{\partial \rho_o}$  we take the partial derivative of the  $\cos \gamma$  equation with respect to  $\rho_o$ . Thus

$$\frac{\pi(t_e - t_i)}{T^2} \left(\frac{\partial T}{\partial \rho_o}\right) \sin \gamma = \frac{1}{\rho_s} - \frac{\rho_o}{\rho_s} \left(\frac{\partial \rho_s}{\partial \rho_o}\right)$$

From the expression for the orbital period we can write

$$\frac{\partial T}{\partial \rho_o} = \frac{3T}{\rho_s} \left(\frac{\partial \rho_s}{\partial \rho_o}\right)$$

Therefore

$$\frac{\partial \rho_s}{\partial \rho_o} = \frac{1}{\frac{\rho_o}{\rho_s} + \frac{3}{2} \gamma \sin \gamma}$$

In the limiting cases we have  $\lim_{\rho_s \rightarrow \rho_o} \left( \frac{\partial \rho_s}{\partial \rho_o} \right) = 1$

$$\lim_{\rho_s \rightarrow \infty} \left( \frac{\partial \rho_s}{\partial \rho_o} \right) = \frac{4}{3\pi} = .425$$

Because of the maximum value  $\frac{\partial \rho_s}{\partial \rho_o} = 1$ , we can conclude that the effect of errors in the assumed altitude of the occultation surface is to create errors in the calculated satellite altitude which are no greater than the  $\rho_o$  errors. Actually, if we had completed one orbital rotation and measured T directly  $\rho_s$  would not be a function of  $\rho_o$  and therefore  $\frac{\partial \rho_s}{\partial \rho_o} = 0$ . Figure 27 shows the manner in which  $\frac{\partial \rho_s}{\partial \rho_o}$  varies with  $\rho_s$ .

If we now take the partial derivative with respect to  $t_e$  (or  $t_1$ ) in the same manner as before we obtain the expressions

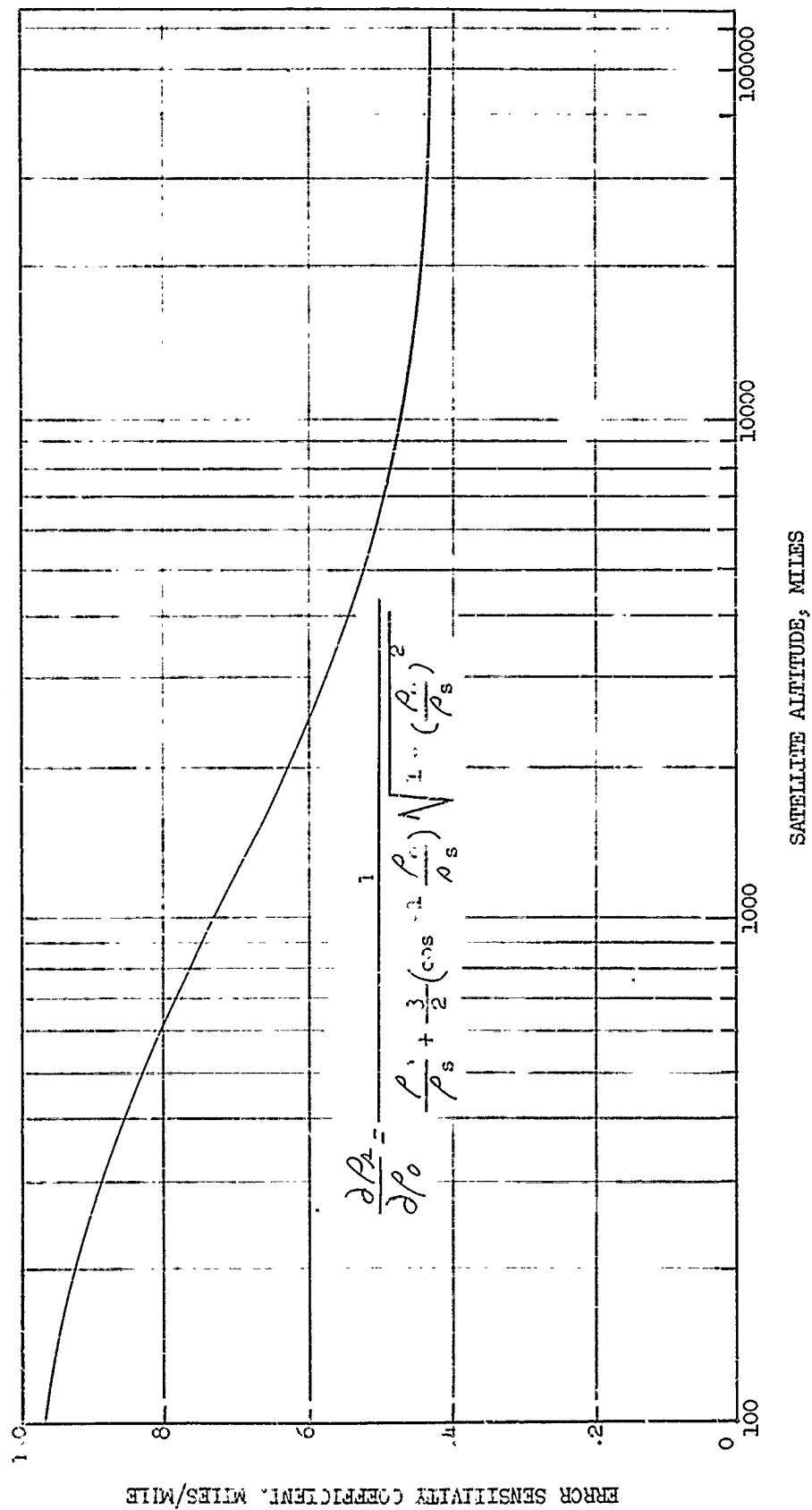
$$\left[ T - (t_e - t_1) \left( \frac{\partial T}{\partial t_e} \right) \right] \sin \gamma = \frac{\pi^2 \rho_o}{\pi \rho_s} \left( \frac{\partial \rho_s}{\partial t_e} \right) ;$$

$$\frac{\partial T}{\partial t_e} = -\frac{3 T}{\partial \rho_o} \left( \frac{\partial \rho_s}{\partial t_e} \right)$$

Therefore

$$\frac{\partial \rho_s}{\partial t_e} = -\frac{\pi \rho_s}{T} \left[ \frac{\sin \gamma}{\frac{\rho_o}{\rho_s} + \frac{3}{2} \gamma \sin \gamma} \right]$$

Figure 27  
 ERROR SENSITIVITY COEFFICIENT,  $\frac{\partial \rho_s}{\partial \rho_0}$  AT VARIOUS SATELLITE ALTITUDES





where

$$\gamma = \cos^{-1} \frac{\rho_o}{\rho_s}; \sin \gamma = \sqrt{1 - (\rho_o/\rho_s)^2}; T = \frac{2\pi}{\rho_e} \sqrt{\frac{\rho_s^3}{g}}$$

The value of this error sensitivity coefficient under the limiting cases becomes

$$\lim_{\rho_s \rightarrow \rho_o} \left( -\frac{\partial \rho_s}{\partial t_e} \right) = \lim_{\rho_s \rightarrow \infty} \left( \frac{\partial \rho_e}{\partial t_e} \right) = 0$$

An examination of the original equation will show that

$$\left( -\frac{\partial \rho_s}{\partial t_e} \right) = - \left( \frac{\partial \rho_s}{\partial t_i} \right)$$

Figure 28 shows the values of  $\left( -\frac{\partial \rho_s}{\partial t_e} \right)$  for various satellite altitudes.

Note that this sensitivity coefficient has a maximum. The location of this maximum has not been evaluated analytically, however, an inspection of Figure 28 will reveal that the maximum value of  $\frac{\partial \rho_e}{\partial t_e} = .96$ , and that this maximum lies at a satellite altitude of about 1200 miles.

One or two comments are in order regarding the implications of Figures 27 and 28 on the ultimate accuracy achieved with a system of this type. Since the rms errors in  $\rho_o$  from meteorological uncertainties are about 0.5 mile, Figure 27 indicates that the errors in the satellite altitude due to this effect alone will be equal to or less than 0.5 mile. If we allow the refraction to build up to 10 seconds of arc, then the refraction rate will range from 2 to 6 seconds of arc per second. It is not unreasonable to expect that the refraction can be read to an

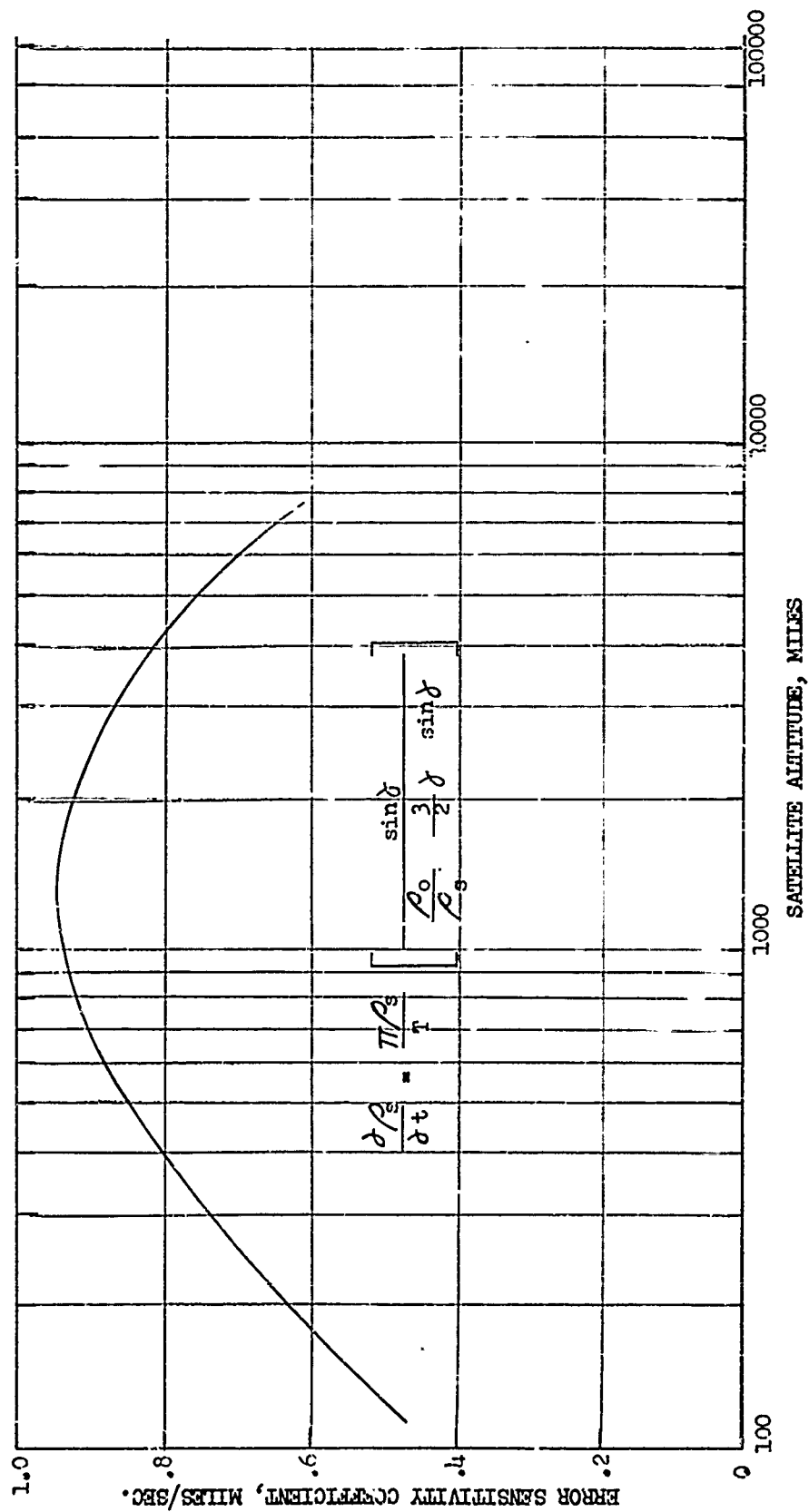


Figure 28

ERROR SENSITIVITY COEFFICIENT,  $\frac{\partial \rho_s}{\partial t}$  AT VARIOUS SATELLITE ALTITUDES

accuracy of at least 0.5 seconds of arc and therefore the instrument time error will not exceed .08 - .25 seconds. Under these conditions the maximum error in  $\rho_s$  due to instrument errors alone will be about .2 miles.

It therefore appears that the errors due to the meteorological fluctuations will be larger than the errors due to the instrument refraction errors. By determining the semi-major axis from one complete orbital rotation the effect of some of these meteorological uncertainties can be reduced. If the isorefraction surface follows some kind of reasonable function (of perhaps 2 or 3 parameters) and if the statistical fluctuations from this mathematical mode is small, then additional star transits can be used to effect a large improvement in the accuracy of the system compared with the case where one must estimate the shape of the isorefraction surface from prior data.

In some applications it is necessary to be able to calculate the satellite velocity with great accuracy. Since

$$v = \rho_e \sqrt{\frac{g}{\rho_s}}; \left(\frac{\partial v}{\partial \rho_s}\right) = -\frac{\rho_e g}{2 \rho_s^{3/2}}$$

If  $\rho_e = 3960$  miles,  $\rho_s = 3960 + 300$  miles,  $g = 32$  ft/sec, then the error sensitivity coefficient is

$$\frac{\partial v}{\partial \rho_s} = 5.54 \times 10^{-4} \text{ feet/sec/foot}$$

As was shown above, the errors in  $\rho_s$  will be of the order of one mile; therefore, the error in the calculated satellite velocity will be of the order of 3 feet/sec.

## B. SYSTEM EQUATIONS FOR THE OCCULTATION TECHNIQUE

The derivation of the equations upon which the occultation technique is based will be sketched in this paragraph. Two assumptions are first made which, while considerably simplifying the analysis, do not seriously limit the applicability of the technique. These are:

- 1) The occulting body or planet is considered a sphere. Thus, the shadow boundary formed by the stars and the planet will be a right circular cylinder extending from the edges of the planet to infinity in a direction away from the star.
- 2) The second assumption is dynamic and states that the orbit shall be a Kepler ellipse in inertial space, i.e., the satellite moves in a central force field.

The assumption (2) can be relaxed somewhat to allowing effects such as nodal regression, apsidal precession, etc., which are sufficiently small. This is valid since the proposed technique gathers sufficient data for a complete orbital determination in one satellite revolution. Although the mathematics become somewhat more complicated, assumption (1) can also be amended to include planets in the form of oblate spheroids; however, this refinement is not discussed here.

We now proceed with the analysis. Consider a cartesian coordinate (X, Y, Z) system with origin at the center of the earth, Z extending along the north pole, and X pointing toward the first point of Aries. This is called the "astronomical frame," or the inertial frame, and it is the one with respect to which the parameters of satellites are usually given.

If we employ another reference (x, y, z) frame having the same origin, but with the x-y plane containing the plane of the satellite orbit, we can write the position of the satellite with respect to the astronomical frame as:

$$\begin{pmatrix} x \\ y \\ z \end{pmatrix} = \rho_B \begin{pmatrix} \cos (\theta + \omega) \\ \sin (\theta + \omega) \\ 0 \end{pmatrix}$$

where

$$\rho = \frac{a (1 - e^2)}{1 + e \cos \theta}$$

= instantaneous radius of the satellite

a = semi-major axis of the orbit ellipse

e = eccentricity

$\omega$  = argument of perigee

$\theta$  = real anomaly (function of time)

and

$$B = \begin{pmatrix} \cos \Omega - \cos i \sin \Omega & \sin i \sin \Omega \\ \sin \Omega & \cos i \cos \Omega & \sin i \cos \Omega \\ 0 & \sin i & \cos i \end{pmatrix}$$

with

$\Omega$  = argument of the line of nodes, and

i = inclination of the orbit plane

Furthermore, under assumption (1), we can construct a third cartesian reference system ( $x'_k$ ,  $y'_k$ ,  $z'_k$ ) again having the same origin but with  $z'_k$  extending toward the star under discussion (the  $k^{\text{th}}$  star), and  $y'_k$  lying in the X-Y plane. In this frame the equation of the occulting right circular cylinder becomes

$$\begin{pmatrix} x'_k \\ y'_k \\ z'_k \end{pmatrix} = \begin{pmatrix} \rho_o \cos \mu_k \\ \rho_o \sin \mu_k \\ z'_k \end{pmatrix}$$

where  $\rho_o$  = radius of the occulting body, and

$\mu_k$  = angle in the  $x'_k - y'_k$  plane measured from the  $x'_k$  axis

Now at the moment of occultation, some point on the orbit ellipse is coincident with some point on the occulting cylinder. To mathematically obtain the implications of this physical fact, we must transform (1) into the  $k^{\text{th}}$  stellar frame ( $x'_k, y'_k, z'_k$ ) and set it equal to (2). The transformation is accomplished by means of the orthogonal matrix:

$$A_k = \begin{pmatrix} \cos \alpha_k & \sin \alpha_k & \cos \alpha_k \sin \delta_k & -\cos \delta_k \\ -\sin \alpha_k & \cos \alpha_k & 0 & 0 \\ \cos \alpha_k \cos \delta_k & \sin \alpha_k \cos \delta_k & \sin \delta_k \end{pmatrix}$$

where

$\alpha_k$  = right ascension of the  $k^{\text{th}}$  star, and

$\delta_k$  = declination of same

Thus, the final geometrical relation is embodied in the matrix equation:

$$\begin{pmatrix} \rho_o \cos \mu_{kj} \\ \rho_o \sin \mu_{kj} \\ z'_k \end{pmatrix} = \rho_j A_k B \begin{pmatrix} \cos (\theta_j + a) \\ \sin (\theta_j + \omega) \\ 0 \end{pmatrix} \quad (3)$$

Here the subscript  $j$  can take on values 1 and 2 corresponding to ingress and egress respectively.

Before obtaining the final explicit form of the equations for the occultation technique, let us examine equation (3) in the light of what can be experimentally measured. It is currently proposed to measure two quantities during an occultation. One of these is the time at which the magnitude of the refraction becomes 10 sec while the other is the direction of travel of the ray in inertial space as determined by the ratio of the two components of refraction. The latter is measured in a plane perpendicular to the sight line to the  $k^{\text{th}}$  star and therefore constitutes a determination of  $\mu_{kj}$ . The former can be used as an input to  $\theta_j$ . Thus, we can only use two of them and we shall now write these in a form more amenable to the inputs. Upon squaring and adding all three equations of (3) we find that

$$\rho_j^2 = \rho_o^2 + z_k^2 \quad (4)$$

This yields a relation independent of  $kj$ :

$$1 - \frac{\rho_o^2}{\rho_j^2} = \left[ \cos \delta_k \cos (\theta_j + \omega) \cos (\alpha_k - \lambda) \right. \\ \left. + \cos \delta_k \sin (\theta_j + \omega) \cos i \sin (\alpha_k - \lambda) \right. \\ \left. + \sin \delta_k \sin i \sin (\theta_j + \omega) \right]^2 \quad (5)$$

An equation independent of both  $\rho_o$  and  $\rho_j$  can be obtained by dividing the second equation of (3) by the first:

$$\begin{aligned}
\tan \mu_{kj} = & \left[ \cos i \sin (\theta_j + \omega) \cos (\alpha_k - \Omega) \right. \\
& \left. - \cos (\theta_j + \omega) \sin (\alpha_k - \Omega) \right] \\
& \times \left[ \sin \delta_k \cos (\theta_j + \omega) \cos (\alpha_k - \Omega) \right. \\
& + \sin \delta_k \sin (\theta_j + \omega) \cos i \sin (\alpha_k - \Omega) \\
& \left. - \cos \delta_k \sin i \sin (\theta_j + \omega) \right]^{-1}
\end{aligned} \tag{6}$$

These latter two equations form the basis for the occultation technique. The known quantities are usually  $\rho_0$ ,  $\mu_{kj}$ ,  $\alpha_k$ ,  $\delta_k$ , and  $t_{kj}$ : the time of occultation. The unknowns are  $a$ ,  $e$ ,  $i$ ,  $\omega$ , and  $T_0$ : the time at perigee (contained on  $\theta_j$ ). Since we obtain one pair of equations (5) and (6) at each occultation, it is easily seen that 3 occultations are needed to completely determine the 6 orbital parameters.

In the case of solar occultations, it does not seem feasible to determine  $\mu_{kj}$  and therefore in this case, equation (5) would be the only one usable. In this instance, one then only needs 2 stellar occultations and 2 solar occultations to determine the parameters of the satellite orbit.



### C. Results of Error Analysis

An error analysis was performed during the last few months on the equations basic to the occultation technique. In order to do this, specific orbits and stars had to be chosen, but the results seem to lend themselves to general conclusions regarding the applicability of the technique.

The stars chosen, together with some associated characteristics are listed in paragraph IIC of the first quarterly report. These form a tetrad consisting of 2 pairs of diametrically opposed stars approximately orthogonal to each other. The inclination which their plane makes with the equator is about  $60^\circ$ .

There were several sets of orbits chosen, but those which were examined closest are discussed here and exemplify the general results. The class of orbits examined herein all have the following parameter in common:

$$a = 4260 \text{ miles}$$

$$e = .01$$

$$i = /2$$

$$\omega = 0$$

$$T_0 = 0$$

The omitted parameter  $\Omega$  was allowed to take on 6 values distributed at  $60^\circ$  intervals about a circle.

While the full technique proposes to measure the time as well as the direction of the stellar ray during occultation, this analysis assumes that only time is measured. Furthermore, with the class of orbits considered, there was no  $\Omega$  for which one of the stars did not occult. Thus, during

each rotation, 8 times were measured. This represents an overdetermination of the results. Since only 6 inputs are needed to calculate all of the orbit parameters there are  $8! / (8 - 6)! 6! = 28$  possible combinations from which to do this. To further complicate matters, it was decided to calculate the semi-major axis a from the period measurement:

$$T^2 = \frac{4\pi^2}{k} a^3$$

Then the error in a amounts only to 0.47 miles for an error in the period of one second of time. Since this is considerably better than is expected from the full occultation technique, we will assume that a is given in this manner. Then only 5 parameters remain giving  $8! / (8 - 5)! 5! = 56$  possible combinations to use. Therefore a rather arbitrary selection of inputs was made according to Table VII. It might be noted here that it will be essential to select the best numerical data in the presence of redundant but independent information (if the data is dependent, the selection is not so difficult as discussed later). While a weighted average is often helpful, this will probably not be as useful in the present problem as the development of criteria for the selection of those measurements which can yield the least rms error in the final calculation of the satellite position. As a result of our instrument error analysis the most accurate measurements will be as follows in order of accuracy.

- a) star transit times, 1-2 miles
- b) solar transit times, 2-4 miles,
- c) star refraction rate, 10-20 miles
- d) star refraction direction, 20-40 miles,
- e) star intensity 30-60 miles

TABLE VII  
INPUT SELECTION

STAR	INGRESS	EGRESS
1	X	X
2	X	X
3	X	
4		

The calculation proceeded as follows: the program on the AD/ECS\* computed all the  $\frac{\partial F_k}{\partial x_j}$

where  $x_j$  are the orbit parameters. Then the inverse of the resulting  $5 \times 5$  matrix multiplied by a diagonal matrix consisting of  $\frac{\partial F_k}{\partial t_1}$  produced all 36 of the sensitivity coefficients  $\frac{\partial x_j}{\partial t_1}$

where  $t_1$  are the occultation time measurements. What is wanted in the final analysis is the sigma error:

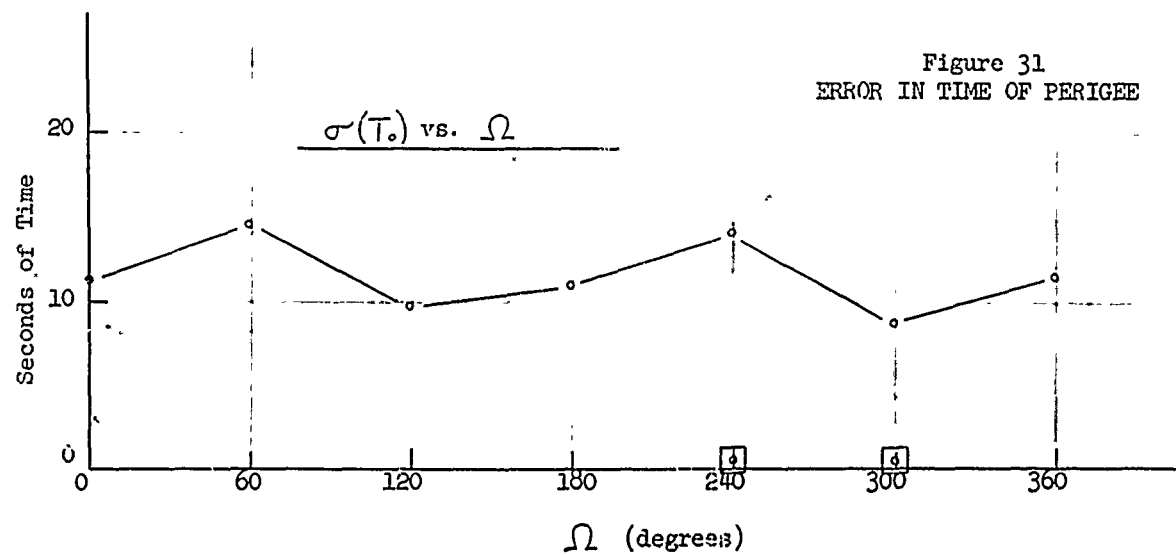
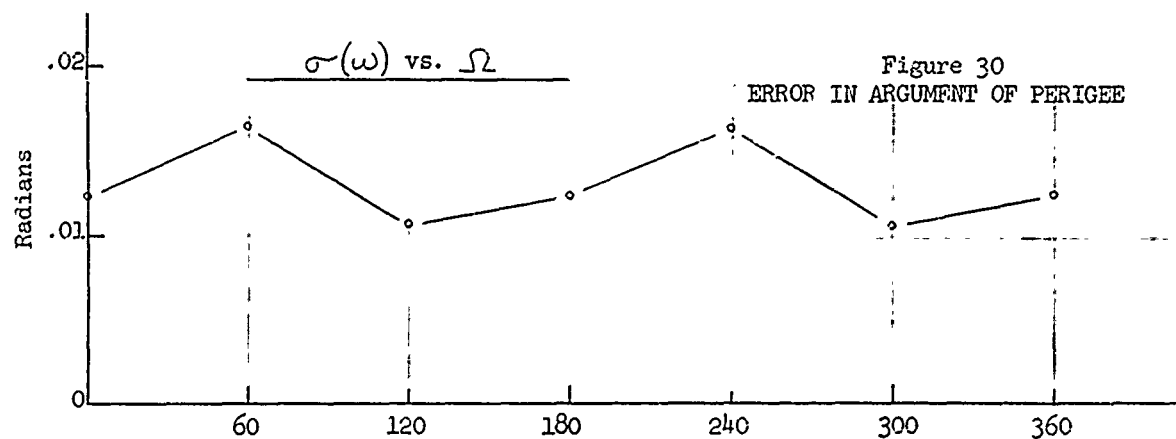
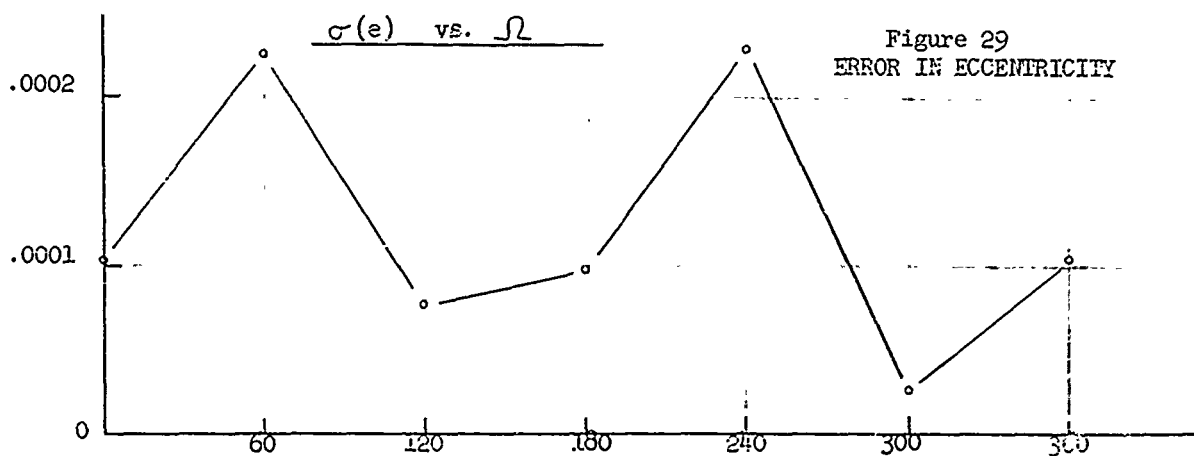
$$\sigma^2(x_j) = \sum_{i=1}^5 \left( \frac{\partial x_j}{\partial t_i} \right)^2 \sigma^2(t_i)$$

$(x_j)$  are plotted in Figures 29 through 33 against  $\Omega$  assuming that  $\sigma(t_1) = \sigma(t_2) = \dots = \sigma(t_5) = .1$  sec.

Of course, the plot of  $\sigma(a)$  vs.  $\Omega$  does not appear since this is a constant due to its method of derivation from the orbital period.

These graphs have at least one thing in common: two peaks situated at  $60^\circ$  and  $240^\circ$ . Upon examining the geometry it is found that in both of these instances, the line between the star pair 1 and 2 lies nearly in the plane of the satellite orbit. Since, as seen from Table VII nearly

\*General Mills Computer, Adaptable Digital Electronic Computer System



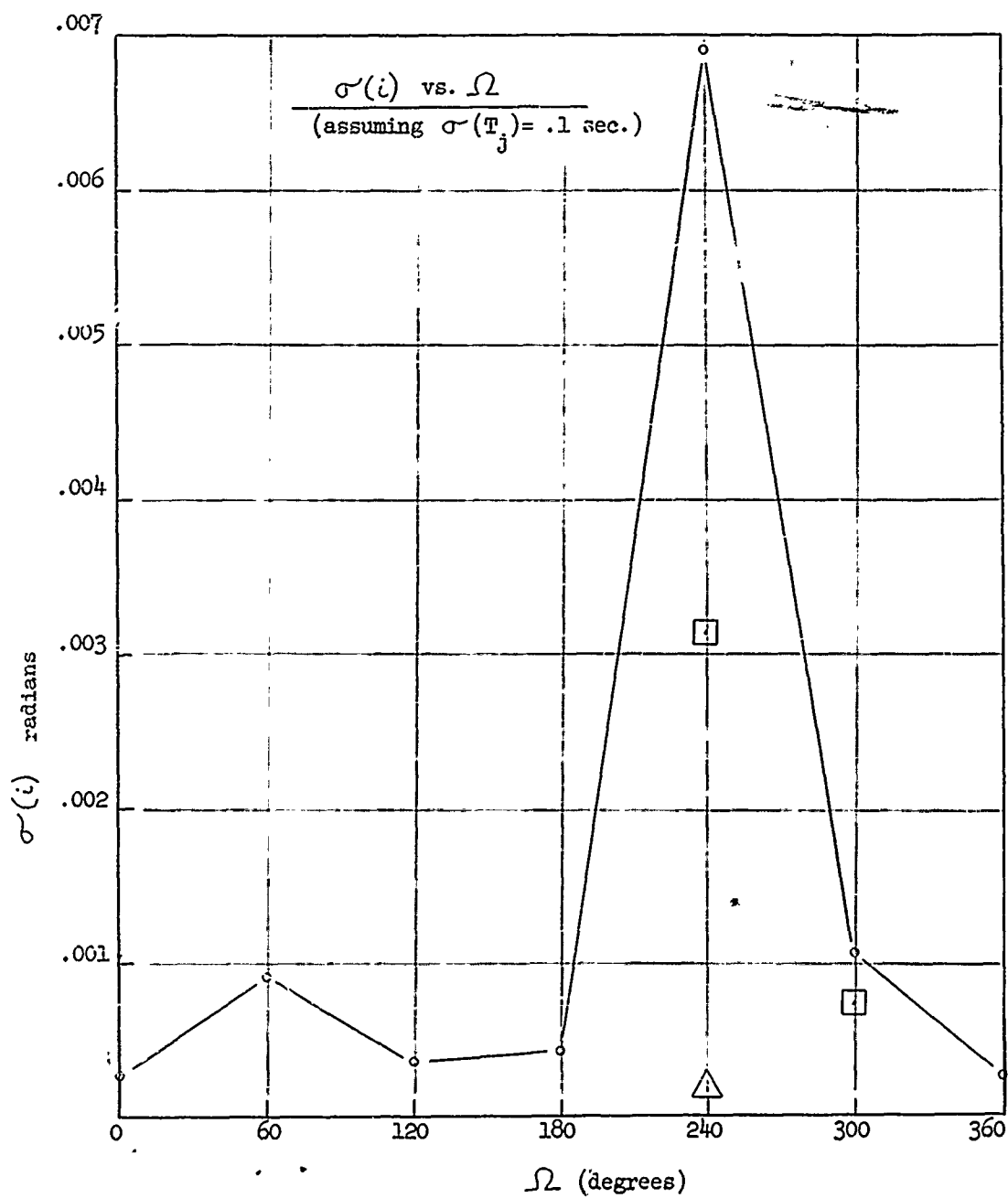


Figure 32

Error in Inclination

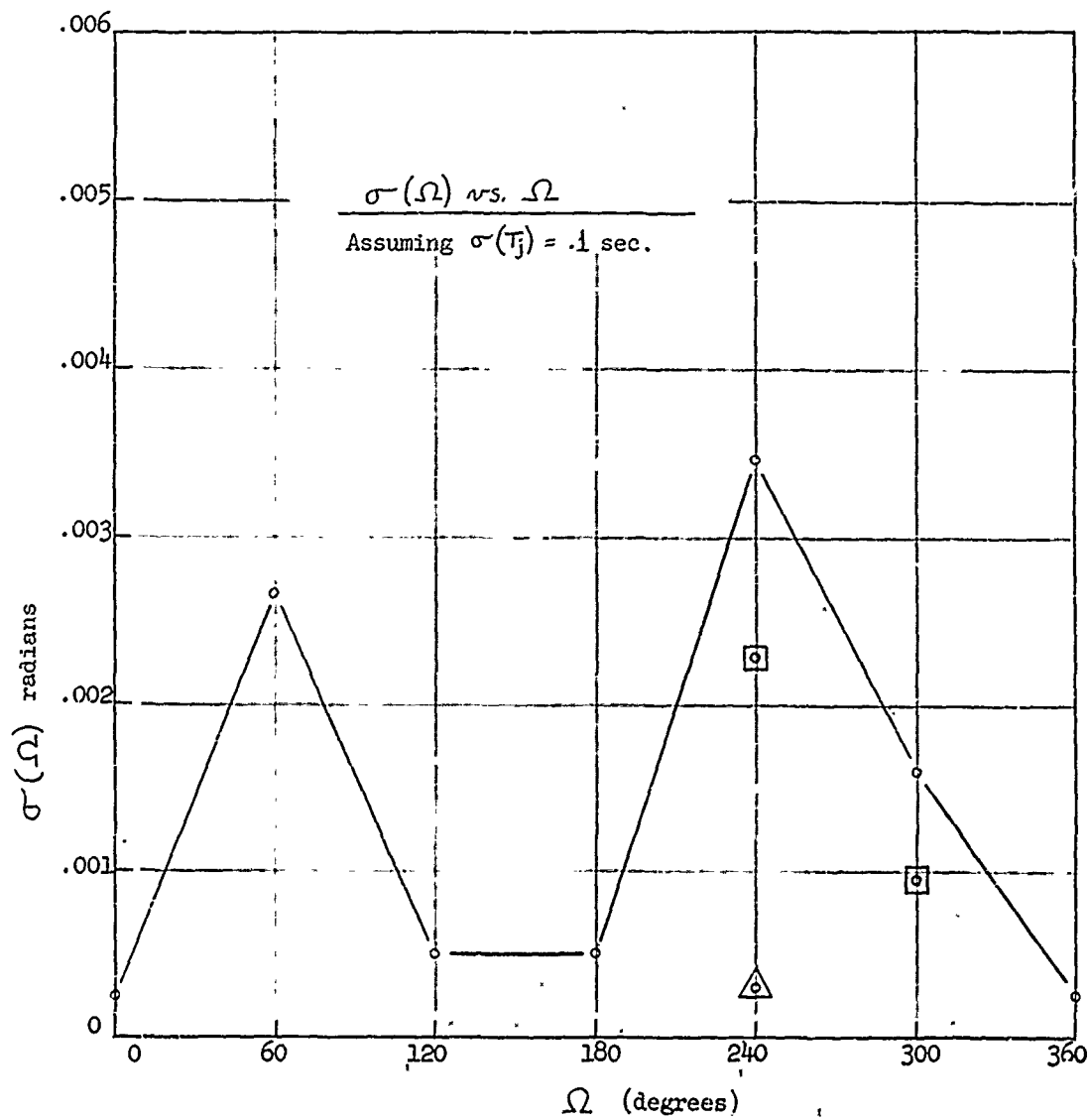
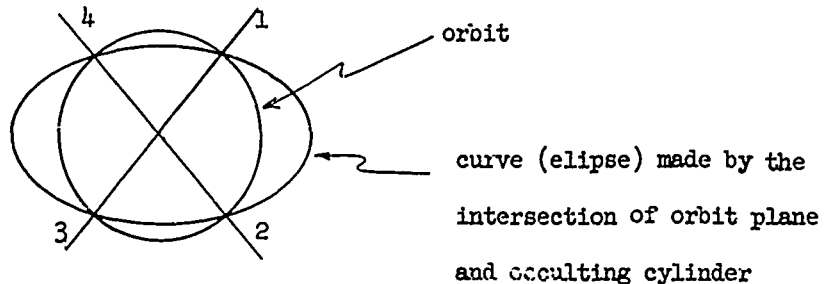


Figure 33  
Error in Angle to the Line of Nodes

all of the inputs come from this pair, the general conclusion can be drawn that stars which lie in the plane of the orbit lead to large errors in the determination of that plane. This conclusion is supported by the other classes of orbits considered, though not discussed here.

Another conclusion can be obtained by considering the relationship between the eccentricity of the orbit and the diametricity of the stars. If we select a circular orbit, i.e. one with  $e = 0$ , then, since the occulting surface cuts the orbit plane in an ellipse, we have the relation shown in the figure below:



It can easily be seen that a measurement of the times at 1 and 2 leads uniquely to a determination of the times at position 3 and 4. Thus the equation derived for these are dependent upon those for position 1 and 2 and hence do not yield additional data, but merely repetitive data. This is a consequence of the diametricity of the star pair coupled with the circular shape of the orbit. To apply this to our case, we see

that the orbital eccentricity  $e = .01$  is quite small yielding a nearly circular orbit while the stars are within a few minutes of arc of being diametrically opposite. Thus from the above discussion, an explanation of the large errors encountered in the graphs is attained. Note that this does not only apply for the two peaks at  $\Omega = 60^\circ$  and  $240^\circ$ . This is a general effect dependent only on the circularity of the orbit and diametricity of the star pairs.

In the light of these observations, three other points were calculated and plotted on the graphs. In all of these it was assumed that  $a$ ,  $e$ , and  $\omega$  are given from other sources in order to do the calculations by hand. In other words, only  $\sigma(i)$ ,  $\sigma(\Omega)$ , and  $\sigma(T_0)$  were found, assuming the remaining to be zero. Also the interaction between the low eccentricity of the orbit and the near diametricity of the star pairs was taken into account in the selection of input data.

The point at  $\Omega = 240^\circ$  denoted by  $\square$  used inputs:

Star	Ingress	Egress
1	X	X
2		
3	X	
4		

It is seen that the errors are indeed smaller, but still do not become as low as desired. However, this is the very value of  $\Omega$  for which star pair 1 and 2 lie in the orbit plane. Thus what should be investigated is an  $\Omega$  value not  $60^\circ$  or  $240^\circ$ .



The point at  $\Omega = 300^\circ$  denoted by  $\square$  satisfies this somewhat. The same inputs were used and the errors also are reduced to some extent; however, while pair 1 and 2 are not in the orbit plane, pair 3 and 4 are fairly close and hence may contribute to the error.

The point at  $\Omega = 240^\circ$  labeled  $\Delta$  used inputs:

Star	Ingress	Egress
1		
2		
3	X	X
4		

This star does not lie in this plane of the orbit, nor do we use dependent information from diametrically opposite stars. Only two pieces of data are therefore available at this value of  $\Omega$ . Therefore, it was decided to calculate only  $\Omega$  and  $i$  using  $T_0$  from some other source. It is seen that in this instance,  $\sigma(\Omega)$  and  $\sigma(i)$  are considerably reduced though still not as far as we would like in view of the possibility of  $\sigma(t)$  being greater than .1 second. However, it must be noted that star #3, while not in the orbit plane, is not displaced considerably from it. The angular distance is about  $33^\circ$ .

In summary, the conclusions which can be drawn from the analysis are as follows:

- 1) It seems most important that information derived from occultations of stars lying in the orbit plane be not used to calculate this plane.
- 2) If the satellite orbit is nearly circular, information from diametrically opposed star pairs, even though they be out of the orbital plane is redundant and cannot therefore be used to generate a set of simultaneous equations which are uniquely solvable.

In spite of these restrictions, if we have at least one star pair out of the plane of the orbit, and we make use of solar occultations in the necessary cases, we can determine with the required accuracy all of the orbital parameters. For instance, if one star pair line lies in the orbit plane and one stellar egress occurs in a sun-lit atmosphere (thereby introducing sufficient noise to render this time measurement unusable), the semi-major axis,  $a$ , can be determined by a period measurement using the in-plane stars while the remaining 5 parameters can be calculated from the 3 remaining out-of-plane stellar occultations plus two solar occultations. If the orbit is circular, we have more occultations than unknown parameters and can therefore select the combination that produces the most accurate results.

## V. INSTRUMENT DESIGN

### A. General Description

In the previous quarterly report, emphasis was placed on the analysis of an instrument which was capable of measuring aberration angles, and from these measurements, the position of the satellite over the earth was computed. At the same time, consideration was given to the phenomena of refraction and stellar occultation. It was noted that by measuring the time at which refraction built up to a prescribed level and by ascribing this time as the time of occultation, a very accurate determination of the orbital period can be made. By noting occultations of several stars in sequence, the orbital elements can be determined by the solution of five simultaneous equations with five unknowns.

Since the measurement of the refraction phenomena and the subsequent occultation time holds promise of more accurate position determination than the aberration measurement, GMI proposes to build a satellite guidance instrument based on the refraction measuring capability. The proposed instrument will be capable of measuring aberration as well as refraction; however, since the refraction rate is much greater than the aberration rate, the instrument will have a higher response rate but will require less accuracy. An occultation time measuring instrument will require to measure the time at which the angle between two stars changes to some arbitrary value. As the line of sight to a particular star dips down into the atmosphere of the earth, this sight line will be refracted to a magnitude of 10 seconds of arc in a matter of only 10 seconds of time. The arbitrarily selected value will fall within this range of refraction.

The star tracker arrangement which is proposed for the occultation technique is similar to that previously proposed for the aberration technique in the following respects:

- 1) The complete system is composed of 4 star trackers.
- 2) Two pairs of diametrically opposed stars are used.
- 3) The star pairs are approximately orthogonal to one another.
- 4) The measurement of the relative positions of the stars is independent of the direction of pointing of the telescopes.
- 5) Photomultipliers are used for radiation detection.
- 6) Two Cassigrainian telescopes are mounted back-to-back.
- 7) A knife edge prism to be used for image splitting.

The star tracker arrangement which is proposed for the occultation technique differs from that previously proposed for the aberration technique in the following respects:

- 1) No rotation of the aberrascopes is used.
- 2) No optical elements external to the telescopes are used (such as collinearizing wedges or Herschel wedges).
- 3) The diametricity requirement is relaxed.
- 4) Brighter stars can be found because of the relaxation of the diametricity requirement.
- 5) The ultimate accuracy requirement in the measurement of relative star positions is relaxed by one order of magnitude.
- 6) The response rate of the error detector is increased by approximately one order of magnitude.
- 7) A smaller, lighter weight optical system can be used.
- 8) The electronics can be simplified.

It is recognized that under certain restricted geometries, the occultation technique does not supply adequate information. An

investigation of other sources of information has indicated that these problems can be avoided. Thus the occultation technique provides almost as general a solution for the determination of the orbital elements as the aberration technique.

The important concept concerning the occultation measuring instrument is the fact that instrument stability is required over a very short period of time, a matter of 15 seconds at best. This means that the absolute alignment of the star trackers relative to one another is less important and that the effects of thermal transients are small. When refraction measurements are not being made the instrument is used for attitude control which can be maintained to an accuracy of at least 5 seconds of arc. The absolute alignment errors of the optical system (between the opposed telescopes) are not significant and rotation of the system to cancel out these errors will not be necessary. This change from the aberration measuring instrument is very advantageous in that the problem of designing a large bearing of high accuracy to operate in the hard vacuum environment is eliminated. Also, the requirement for slip rings to provide power and take out electrical signals is removed. With these changes, it is easy to see that a substantial simplification has been effected in the instrument design.

Now since aberration is not being measured, the requirement for the Herschel Wedges is no longer present. An angle measurement is still necessary, but a higher response rate will be necessary. The Herschel Wedges, being massive devices, could not conceivably be considered for this use. Extremely high drive forces would be necessary to accelerate the wedges and the resultant dynamic error would be large. Without the Herschel Wedges, the burden of making angle

measurements falls upon measuring the displacement of the center of the knife edge detector. This alternate was mentioned in our Quarterly Report<sup>23</sup> and represents a clean design, provided that adequate accuracy can be preserved. The use of an interferometer is one possible method by which this measurement can be made.

Since the entire instrument will not be rotated, the requirement for diametricity can be relaxed. Without the rotational feature, the knife edge detector is not required to be driven thru an angle proportional to the deviation from diametricity with each revolution. The collinearizing wedge can also be disposed and stars can be selected which deviate from diametricity by larger angles, for example, 2 degrees. This in turn will permit the selection of brighter stars and the aperture of the optical system will be reduced to 4 inches. It will also be shortened from about 32 inches to 24 inches in over-all length.

A single axis detector (a knife edge prism) will be used for the error detector of the instrument. Since the entire system is non-rotating, it will now be necessary to rotate the knife edge detector. This can be done quite readily by building the knife edges on the ends of the shaft of a small motor. This motor will be hermetically sealed with its own atmosphere and windows will be provided on each end of the package to admit the incoming stellar radiation. The rotor of the motor will be mounted on air bearings so as to remove the possibility of oil settling on the optical surfaces. This rotating error detector will be the heart of the refraction measuring instrument.

The stellar radiation which impinges on the rotating error detector will be reflected outward in a conical pattern. This energy must be collected and refocused on a photomultiplier tube. The use of a section of an ellipsoid of revolution will accomplish the necessary collection of energy and chopping can be performed by making alternate portions of the ellipsoid black or mirrored surfaces. Thus the image is rotating and the chopper is stationary; a reversal of the usual procedure but nonetheless an adequate solution.

The signals from the photomultipliers will be combined in suitable logic circuitry and appropriate error signals will be produced. These error signals will be used to drive four servo motors which will articulate the ends of the rotating error detector package in directions normal to the optical axis. The servo motors (two on each end, one for up-down motion and one for sidewise motion) will position the rotating error detector so as to reach a null position where the incoming image is centered on the knife edge. The magnitude of the linear motions required at the ends of the rotating knife edge package is plus or minus 0.050 inches. This figure is obtained by assuming an effective focal length (EFL) for the optical system of 100 inches; then allowances for the following motions are made:

Annual aberration	20 seconds
Satellite aberration	10 seconds
Attitude errors	10 seconds
Refraction	<u>10 seconds</u>
Total	50 seconds

To be conservative and also to allow for acquisition, the maximum travel will be assumed to be more than twice the value totaled above

Allowing for both positive and negative values, a total range of 400 seconds of arc can be achieved which in turn is equivalent to a linear motion of 0.20 inches or plus or minus 0.10 inches.

The servo drive mechanisms which will articulate the rotating error detector package will be hermetically sealed units. Each unit will contain a servo motor, tachometer, gearhead, and mechanism for converting the rotary output into a linear output. With the linear motion requirement only 0.20 inches, the output motion can be transmitted thru a bellows or a diaphragm thus permitting the rotary components to be sealed from the outer environment. Using the size 8 servo components, the entire sealed unit need not be larger than one inch in diameter and four inches in length.

The output from the non-rotating aberrascopes will come from two encoders which will measure the translation of the center of the rotating error detector package. These encoders could conceivably be interferometers as already mentioned where displacements of between 5 and 10 millionths of an inch can be sensed. This can be done by using the blue or violet lines of helium light, noting of course, that interference produces dark bands whenever the distance between the reflecting surfaces is one-half wave length or a multiple thereof. The techniques of interferometry are known arts and we feel that this approach can be implemented in the non-rotating aberrascopes in a straight forward manner to produce the desired outputs.

From the interferometer outputs, some digital computing type logic networks will be necessary to finally determine the required parameters which will produce the occultation time as required.



## B. Optical System

### 1. Structural Analysis

In previous reports the mechanical structural requirements of the aberrascopes and possible sources of aberrascopes structural disturbance were considered.<sup>24</sup> The present discussion is an analysis of an assumed structure for the rotating portion of the aberrascopes. The structural requirements for a rotating aberrascopes are much more stringent than the requirements for a non-rotating instrument. Thus, if the requirements of a rotating instrument can be met, no problems will exist with the design of a new non-rotating instrument.

The mechanical structural analysis has two objectives: First, to determine feasibility of designing a structure of practical weight which has sufficient rigidity to meet the accuracy requirement; and second, to establish reasonable estimates of structural design parameters to serve as starting points for more detailed analysis during actual instrument design.

In previous discussions the sources of aberrascopes structural disturbance were classified according to their origin in the aberrascopes, the satellite, or the orbital environment and according to the manner in which the disturbing forces would be generated. In connection with the structural analysis these disturbing forces may be grouped in a more general way into the following classification:

- 1) Static forces
- 2) Vibration
- 3) Thermal effects

Static forces may be either actual static loads or forces which vary slowly relative to the lowest resonant frequency of the structure. Examples of such slowly varying forces are acceleration forces due to unbalance of the rotating aberrascope about its axis of rotation, bearing eccentricity and wobble, and nonorthogonality of bearing surface and aberrascope geometric axis. Acceleration forces from these sources will be periodic with the rotation of the aberrascope structure. Since the speed of rotation will be very low compared to the lowest resonant frequency of the structure, the structural deflection under these slowly varying loads will be essentially the same as under static loads of an equal magnitude.

Dynamic loading of the structure may result from vibrations. Examples of possible vibration sources are bearing and gear mechanical noise, drive motor vibrations, and vibrations due to moving parts or rotating elements in the satellite. If the frequency of the disturbing vibration is near a resonant frequency of the structure, a large dynamic force amplification will occur. In a lightly damped structure, such as the aberrascope, amplification factors in the range of 25 to 50 may be obtained at resonance.

Deflections can occur because of thermal effects on the aberrascope structure. The heat sources may be in the aberrascope, in the satellite or in the orbit environment.

The aberrascope structure may be considered to be divided into an inner structure and an outer structure. The inner structure is the rotating part of the aberrascope which supports the primary mirror, secondary mirror, and the knife edge bar. The outer aberrascope structure provides attachment to the satellite and interconnection between crossed aberrascopes.

The structural analysis up to the present time has been concerned with the inner or rotating aberrascope structure.

For analysis, the rotating aberrascope structure is assumed to consist of a central cylindrical section and two conical sections. The main bearing is located midway between the ends of the cylindrical section. The primary mirrors are supported at the ends of the cylindrical section. The conical sections, which are fastened at their large ends to the ends of the cylindrical section, support the secondary mirrors. This structural arrangement is shown schematically in Figure 34.

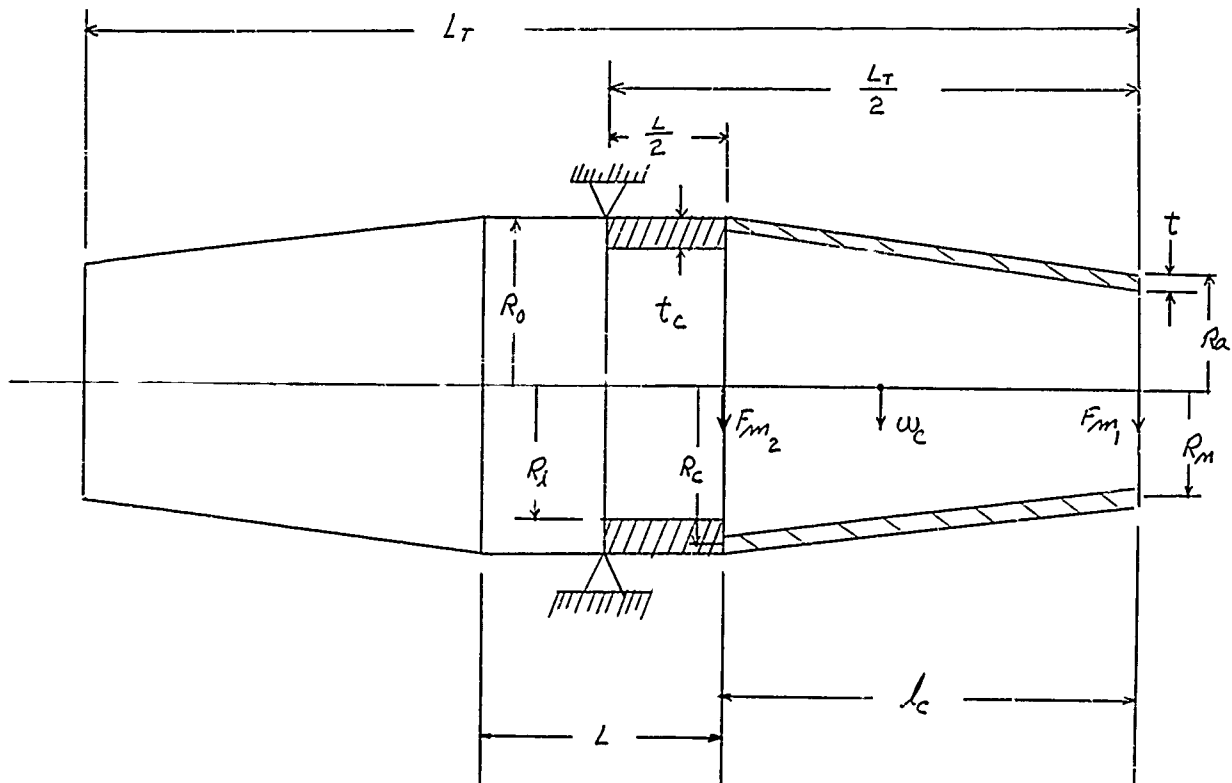


Figure 34

Aberrascope Structural Arrangement

In the structural analysis it is assumed that both the cylindrical section and the conical sections will be made of invar.

a. Structural Deflections Under Static Forces

Maintenance of the alignment of the secondary mirrors with respect to the primary mirrors is the most critical of the structural requirements. The aberrascope structure may be regarded as a beam supported at the center. The action of static forces will cause this structure to undergo deflections with respect to its support. The magnitudes of the deflection and slope at the small end of the conical structure relative to the deflection and slope at the end of the cylindrical section determine the misalignment of the secondary mirror with respect to the primary mirror due to static forces on the aberrascope structure. Since the aberrascope structure is symmetrical about its bearing, it is necessary to consider only one side of the structure in carrying out the analysis of deflections and slopes

Figure 34 shows the structural dimensions and forces acting on the structure which are involved in the analysis of slopes and deflections.

$L_T$  = total length of the rotating aberrascope structure.

$L$  = length of the cylindrical section.

$L_c$  = length of the conical section.

$R_o$  = outside radius of cylindrical section and large end of conical section.

$R_i$  = inside radius of cylindrical section.

$R_c$  = mean radius of large end of conical section.

$R_{c_s}$  = outside radius of small end of conical section.

$R_m$  = mean radius of small end of conical section.

$t_c$  = thickness of cylindrical section.

$t$  = thickness of conical section.

$F_{m1}$  = force due to weight of secondary mirror.

$F_{m2}$  = force due to weight of primary mirror.

$W_c$  = force due to weight of cone.

The thickness of the conical section,  $t$ , and the thickness of the cylindrical section,  $t_c$ , are the parameters which are varied in the analysis.

The analysis of deflections and slopes is based on the assumption that the aberrascopes are in a force field of one g. This assumption is made merely for convenience in carrying out the analysis. Since the deflections and slopes, in the range considered, are linear functions of the loads, the results obtained for a one g loading can be used to determine the deflections and slopes for the actual force levels which will be encountered by the aberrascopes once these force levels are known.

In evaluating the results of the analysis in terms of the structural accuracy requirements, it will be assumed that the static loads on the aberrascopes structure will be those corresponding to a force field of  $10^{-2}$  g. Obtaining deflections and slopes for a  $10^{-2}$  g field from the analytical results for a 1 g field involves simply multiplying the analytical results by  $10^{-2}$ . The assumption of a  $10^{-2}$  g level for the static disturbing forces on the aberrascopes during actual operation is believed to be very conservative.

Figure 35 shows a cantilever beam equivalent of one side of the aberrator structure of Figure 34.

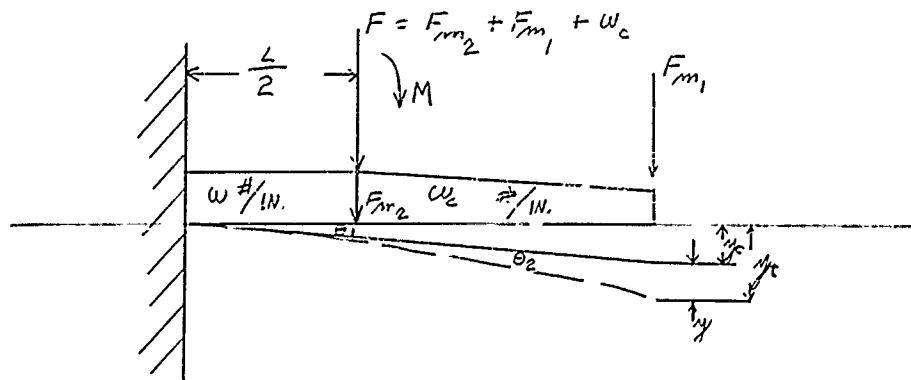


Figure 35

Cantilever Beam Equivalent

Consider first only the cylindrical section, Figure 34, of length  $L/2$ . The deflection and slope of this section at distance  $L/2$  from the fixed end, Figure 36, is produced by the combination of a force, a moment, and the cylinder weight. The force,  $F$ , is a summation of the weight of two mirrors ( $F_{m1}$  and  $F_{m2}$ ) and the weight of the conical section. The moment effect in turn is a sum of the moments due to the mirror,  $F_{m1}$ , and the weight of the cone. Evaluation of each of these effects yields the following equations.

$$\text{Slope:} \quad \theta_F = \frac{FL^2}{8EI} \quad (1)$$

$$\text{Deflection:} \quad y_F = \frac{FL^3}{24EI} \quad (2)$$

$$\text{Slope:} \quad \theta_m = \frac{ML}{2EI} \quad (3)$$

$$\text{Deflection:} \quad y_m = \frac{FL^3}{24EI} \quad (4)$$

$$\text{Slope:} \quad \theta_w = \frac{WL^2}{24EI} \quad (5)$$

$$\text{Deflection} \quad y_w = \frac{WL^3}{64EI} \quad (6)$$

Applying the principle of superposition one can now say that the slope and deflection for the cylindrical section are

$$\theta_{\text{cylinder}} = \theta_F + \theta_m + \theta_w \quad (7)$$

and

$$y_{\text{cylinder}} = y_F + y_m + y_w \quad (8)$$

Consider now the conical section of length  $l_c$ , Figure 34. The conical shell may be regarded as a cantilever beam fixed at the intersection of the cylinder and cone. The slope and deflection for the loaded conical shell cantilever beam, Figure 42 are calculated by the double integration method which considers the position of the beams neutral elastic curve. Effects due to the concentrated force and the beam weight are calculated separately and then combined using the principle of superposition.

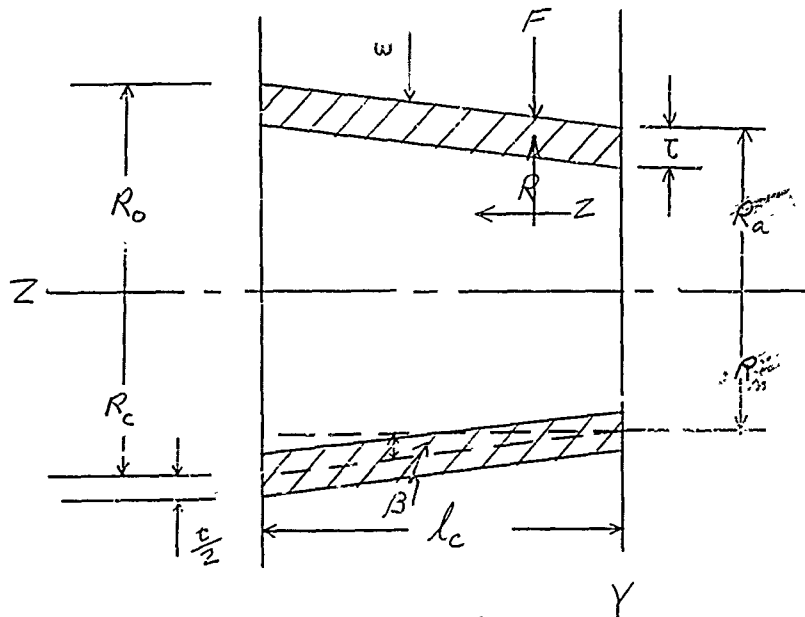


Figure 36  
Conical Shell

From Figure 36 the following relationships hold:

$$R = [R_n + Z \tan \beta] \quad (9)$$

$$R_n = R_a - \frac{t}{2} \quad (10)$$

$$R_c = R_o - \frac{t}{2} \quad (11)$$

$$\tan \beta = \frac{R_c - R_n}{l_c} \quad (12)$$

The differential equation of the elastic curve is

$$\frac{d^2 y}{dx^2} = \frac{M}{EI} \quad (13)$$

Where:  $M$  = Bending moment  
 $E$  = Modulus of elasticity  
 $I$  = Moment of inertia



The moment of inertia for a thin walled conical section is derived from the configuration of Figure 37.

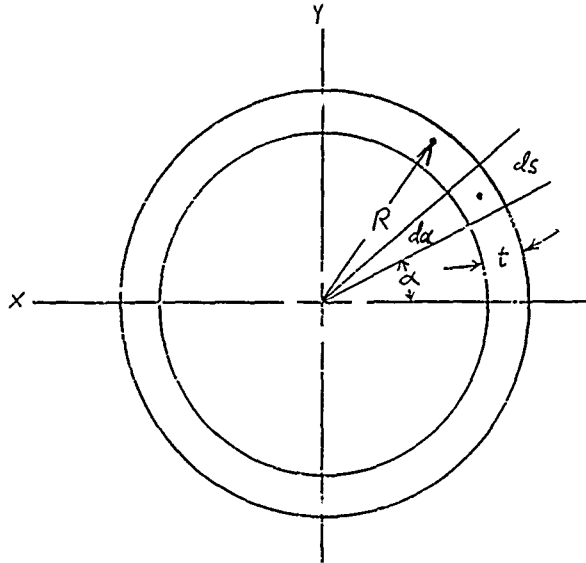


Figure 37  
Moment of Inertia Consideration

Using the classical definition for moment of inertia one has the equation

$$I = \sum dA y^2 = \int y^2 dA \quad (14)$$

Referring to Figure 37,

$$dA = ds t \quad (15)$$

$$ds = R d\alpha \quad (16)$$

$$y^2 = (R \sin \alpha)^2 \quad (17)$$

Substituting equations (15), (16), and (17) in equation (14) yields:

$$\frac{1}{4} I_x = \int_0^{\frac{\pi}{2}} (R \sin \alpha)^2 R d\alpha t \quad (18)$$

Solving equation (18) gives:

$$\frac{1}{4} I_x = t R^3 \left[ \frac{1}{2} \alpha - \frac{1}{4} \sin 2\alpha \right]_0^{\frac{\pi}{2}} = t R^3 \left( \frac{1}{4} \pi \right)$$

Therefore, the moment of inertia I for a conical section is:

$$I_x = \pi t R^3 \quad (19)$$

Referring to Figure 36 and considering the slope and deflection for the concentrated load yields the equation  $y'' = \frac{M}{EI}$  and therefore

$$y'' = \frac{-FZ}{\pi t E [R_n + Z \tan \beta]^3} \quad (20)$$

where

$-FZ = m = \text{bending moment}$

$$I = [R_n + Z \tan \beta]^3 \pi t$$

or

$$y' = \frac{-F}{\pi t E} \int \frac{Z \, dZ}{(R_n + Z \tan \beta)^3} \quad (21)$$

Integration of equation (21) gives the following:

$$y' = \frac{-F}{\pi t E} \left[ \frac{1}{\tan^2 \beta} \left\{ -\frac{1}{R_n + Z \tan \beta} + \frac{R_n}{2(R_n + Z \tan \beta)^2} \right\} + C \right]$$

Solving equation (22) for C, where the conditions apply that  $y = 0$  and  $(R_n + Z \tan \beta) = R_c$  when  $Z = l_c$ , one contains

$$0 = \frac{-F}{\pi t E} \left[ -\frac{1}{R_c \tan^2 \beta} + \frac{R_n}{2 R_c \tan^2 \beta} + C \right] \quad (23)$$

or

$$C = \frac{1}{R_c \tan^2 \beta} - \frac{R_n}{2 R_c^2 \tan^2 \beta}$$

Substituting the value of C in equation (22) yields

$$y' = \frac{-F}{\pi t E} \left[ \frac{1}{\tan^2 \beta} \left\{ -\frac{1}{R_n + Z \tan \beta} + \frac{R_n}{2 (R_n + Z \tan \beta)^2} \right\} + \frac{1}{R_c \tan^2 \beta} - \frac{R_n}{2 R_c^2 \tan^2 \beta} \right] \quad (24)$$

Solving equation (24) for the special case, where  $y' = \theta_{c_F}$  and  $(R_n + Z \tan \beta) = R_n$  when  $Z = 0$ , yields

$$\theta_{c_F} = -\frac{R l_c^2}{\pi t E (R_c - R_n)^2} \left[ \frac{R_n}{2 R_n^2} - \frac{1}{R_n} + \frac{1}{R_c} - \frac{R_n}{2 R_c^2} \right]$$

or after simplification, the slope, at end of beam due to a concentrated load at point  $Z = 0$  is

$$\theta_{c_F} = \frac{-F}{2 \pi E t R_n} \left( \frac{l_c}{R_c} \right)^2$$

Integrating equation (24) for beam deflection yields

$$y = \frac{-F}{E \pi t} \left[ \frac{R_n}{2 \tan^2 \beta} \left\{ -\frac{1}{\tan \beta (R_n + Z \tan \beta)} \right\} - \frac{1}{\tan^2 \beta} \left\{ \frac{l_n (R_n + Z \tan \beta)}{\tan \beta} \right\} \right. \\ \left. + \frac{Z}{R_c \tan^2 \beta} - \frac{R_n Z}{2 R_c^2 \tan^2 \beta} + C_1 \right] \quad (26)$$

Solving equation (26) for  $C_1$ , where the conditions specify that  $y = 0$  and  $(R_n + Z \tan \beta) = R_c$  when  $Z = l_c$ , one obtains

$$0 = \frac{-F}{E \pi t} \left[ -\frac{R_n}{2 \tan^3 \beta (R_c)} - \frac{l_n R_c}{\tan^3 \beta} + \frac{l_c}{R_c \tan^2 \beta} - \frac{R_n l_c}{2 R_c^2 \tan^2 \beta} + C \right] \quad (27)$$

or

$$C_1 = \frac{R_n}{2 R_c \tan^3 \beta} + \frac{l_n R_c}{\tan^3 \beta} - \frac{l_c}{R_c \tan^2 \beta} + \frac{R_n l_c}{2 R_c^2 \tan^2 \beta}$$

Substituting the value of  $C_1$  in Equation (26) yields

$$y = \frac{-F}{E \pi t} \left[ -\frac{R_n}{2 \tan^3 \beta (R_n + Z \tan \beta)} - \frac{l_n (R_n + Z \tan \beta)}{\tan^3 \beta} + \frac{Z}{R_c \tan^2 \beta} \right. \\ \left. - \frac{R_n Z}{2 R_c^2 \tan^2 \beta} + \frac{R_n}{2 R_c \tan^3 \beta} + \frac{l_n R_c}{\tan^3 \beta} - \frac{l_c}{R_c \tan^2 \beta} + \frac{R_n l_c}{2 R_c^2 \tan^2 \beta} \right]$$

Solving the deflection equation (28) for the special case, where  $y' = y_{CF}$  and  $(R_n + Z \tan \beta)$  when  $Z = 0$ , yields

$$y_{c_F} = - \frac{-F}{E \pi t} \left[ - \frac{R_n}{2 \tan^3 \beta (R_n)} - \frac{l_n R_n}{\tan^3 \beta} + \frac{P_n}{2 R_c \tan^3 \beta} + \frac{l_n R_c}{\tan^3 \beta} - \frac{l_c}{R_c \tan^2 \beta} + \frac{R_n l_c}{2 R_c^2 \tan^2 \beta} \right]$$

or after simplification, the deflection at end of beam, due to a concentrated load at point  $Z = 0$ , is •

$$y_{c_F} = \frac{-F l_c^3}{2 \pi t E (R_c - R_n)^3} \left[ \frac{R_n - R_c}{R_c} + \frac{2 l_n R_c}{R_n} + \left( \frac{R_c - R_n}{R_c} \right) \left( \frac{R_n}{R_c} - 2 \right) \right] \quad (29)$$

Now considering the slope and deflection due to the beam weight, Figure 34, one again has the equation

$$\frac{d^2 y}{d x^2} = \frac{M}{EI}$$

where  $E$  and  $I$  are as in equation (20) and  $M$  is a function of weight and distance.

The moment equation is

$$M = \rho \int Z A d Z \quad (30)$$

Taking any distance  $Z$  one finds that the cross-sectional area,  $A$ , is given by the expression

$$A = \pi \left( R + \frac{t}{2} \right)^2 - \pi \left( R - \frac{t}{2} \right)^2 \quad (31)$$

or

$$A = 2 \pi R t$$

Evaluating R, in equation (31), as a function of Z gives

$$A = 2\pi(R_n + Z \tan \beta) t \quad (32)$$

Substituting equation (32) in equation (30) and integrating gives the moment as

$$M = 2\pi t \rho \left[ \frac{(R_n + Z \tan \beta)^3}{3 \tan^2 \beta} - \frac{R_n (R_n + Z \tan \beta)^2}{2 \tan^2 \beta} + C_0 \right] \quad (33)$$

Solving equation (33) for  $C_0$  where  $M = 0$  when  $Z = 0$  gives

$$C_0 = \frac{R_n^3}{2 \tan^2 \beta} - \frac{R_n^3}{3 \tan^2 \beta} \quad (34)$$

Substituting for  $C_0$  in equation (33) gives the moment equation as

$$M = 2\pi t \rho \left[ \frac{(R_n - Z \tan \beta)^3}{3 \tan^2 \beta} - \frac{R_n (R_n + Z \tan \beta)^2}{2 \tan^2 \beta} + \frac{R_n^3}{2 \tan^2 \beta} - \frac{R_n^3}{3 \tan^2 \beta} \right] \quad (35)$$

Substituting equations (19) and (35) in equation (13) yields the equation

$$y'' = \frac{2\pi t \rho \left[ 2(R_n + Z \tan \beta)^3 - 3 R_n (R_n + Z \tan \beta)^2 + R_n^3 \right]}{6 \tan^2 \beta \pi t \left[ R_n + Z \tan \beta \right]^3 E} \quad (36)$$

Integrating expression (36) yields the slope equation

$$y' = \frac{\rho}{3 E \tan^2 \beta} \left[ 2 \int dZ - 3 R_n \int \frac{dZ}{(R_n + Z \tan \beta)} + R_n^3 \int \frac{dZ}{(R_n + Z \tan \beta)^3} + C_2 \right] \quad (37)$$

$$y' = \frac{\rho}{3 E \tan^2 \beta} \left[ 2 Z - 3 R_n \left\{ \ln \frac{(R_n + Z \tan \beta)}{\tan \beta} \right\} + R_n^3 \left\{ -\frac{1}{2 \tan \beta (R_n + Z \tan \beta)^2} \right\} + C_2 \right]$$

Solving the slope equation (37) for  $C_2$ , where the conditions apply that  $y' = 0$  and  $(R_n + Z \tan \beta) = R_c$  when  $x = l_c$ , one obtains

$$C_2 = \frac{3 R_n \log R_c}{\tan \beta} + \frac{R_n^3}{2 R_c^2 \tan \beta} - 2 l_c \quad (38)$$

Replacing  $C_2$  with the solved value gives the equation

$$y' = \frac{\rho}{3 E \tan^2 \beta} \left[ 2 Z - \frac{3 R_n \log (R_n + Z \tan \beta)}{\tan \beta} - \frac{R_n^3}{2 \tan \beta (R_n + Z \tan \beta)} - \frac{3 R_n \log R_c}{\tan \beta} + \frac{R_n^3 l_c}{2 R_c^2 \tan \beta} - 2 l_c \right] \quad (39)$$

Solving equation (39) for the special case where  $y = \theta_c$  and  $(R_n + Z \tan \beta) = R_n$  when  $Z = 0$  yields the slope equation at the end of the beam due to its own weight.

$$\theta_{cw} = \frac{\rho l_c^3}{3 E (R_c - R_n)^3} \left[ 3 R_n \log \left( \frac{R_c}{R_n} \right) + \frac{3}{2} R_n + \frac{R_n^3}{2 R_c^2} - 2 R_c \right] \quad (40)$$

Integrating equation (39) for beam deflection yields

$$y = \frac{\rho}{3 E \tan^2 \beta} \left[ Z^2 - \frac{3 R_n^2}{\tan \beta} \left\{ \log R_n + Z \tan \beta \right\} - \tan \beta \left[ \frac{1}{\tan^2 \beta} \left\{ (R_n + Z \tan \beta) - R_n \log (R_n + Z \tan \beta) \right\} \right] \right] - \frac{R_n^3}{2 \tan \beta} \left[ - \frac{1}{\tan \beta (R_n + Z \tan \beta)} \right] + \frac{3 R_n Z \log R_c}{\tan \beta} + \frac{R_n^3}{2 R_c^2 \tan \beta} - 2 l_c Z + C_3 \quad (41)$$

Solving the deflection equation (41) for  $C_3$ , where the conditions apply that  $y = 0$  and  $(R_n + Z \tan \beta) = R_c$  when  $Z = c$ , one obtains

$$C_3 = -l_c^2 + \frac{3 R_n}{\tan \beta} \left\{ l_c \log R_c - \tan \beta \left[ \frac{1}{\tan^2 \beta} \left\{ R_c - R_n \log R_c \right\} \right] \right\} - \frac{R_n^3}{2 R_c \tan^2 \beta} - \frac{3 R_n l_c \log R_c}{\tan \beta} - \frac{R_n^3 l_c}{2 R_c^2 \tan \beta} + 2 l_c^2 \quad (42)$$

Substituting this value of  $C_3$  in equation (41) yields the general deflection

$$y = \frac{\rho}{3 E \tan^2 \beta} \left[ \left[ Z^2 - \frac{3 R_n}{\tan \beta} \left\{ Z \log (R_n + Z \tan \beta) - \tan \beta \left[ \frac{1}{\tan^2 \beta} \left\{ (R_n + Z \tan \beta) - R_n \log (R_n + Z \tan \beta) \right\} \right] \right\} \right] + \frac{R_n^3}{2 \tan^2 \beta (R_n + Z \tan \beta)} + \frac{3 R_n Z \log R_c}{\tan \beta} + \frac{R_n^3 Z}{2 R_c^2 \tan \beta} - 2 l_c Z - l_c^2 + \frac{3 R_n}{\tan \beta} \left\{ l_c \log R_c - \tan \beta \left[ \frac{1}{\tan^2 \beta} (R_c - R_n \log R_c) \right] \right\} - \frac{R_n^3}{2 R_c \tan^2 \beta} - \frac{3 R_n l_c \log R_c}{\tan \beta} - \frac{R_n^3 l_c}{2 R_c^2 \tan \beta} + 2 l_c^2 \right] \quad (43)$$

Solving the general deflection equation (43) for the special case, where  $y = y_c$  and  $(R_n + Z \tan \beta) = R_n$  when  $Z = 0$ , yields the deflection equation for the deflection, at end of beam, due to the beam weight.



$$y_{cw} = \frac{\rho l_c^4 R_n^2}{3 E (R_c - R_n)^4} \left[ \frac{7}{2} + 3 \log \left( \frac{R_c}{R_n} \right) - \frac{3 R_c R_n}{R_n R_c} + \frac{R_n^2}{2 R_c^2} + \frac{(R_c - R_n)^2}{R_n^2} \right] \quad (44)$$

The deflection and slope at the small end of the conical section due to a concentrated force,  $F_{ul}$ , may be obtained from equations (25) and (29) of the above development.

$$\theta_{\text{Force cone}} = \frac{-F}{2 \pi E t R_n} \left( \frac{l_c}{R_c} \right)^2 \quad (25)$$

$$y_{\text{Force cone}} = \frac{-F l_c^3}{2 \pi t E (R_c - R_n)^3} \left[ \frac{R_n - R_c}{R_c} + 2 \log \left( \frac{R_c}{R_n} \right) + \left( \frac{R_c - R_n}{R_c} \right) \left( \frac{R_n}{R_c} - 2 \right) \right] \quad (29)$$

The deflection and slope at the small end of the conical section due to the weight of the conical section is given by equations (40) and (44).

$$\theta_{\text{Cone Weight}} = \frac{\rho l_c^3}{3 E (R_c - R_n)^3} \left[ 3 R_n \log \frac{R_c}{R_n} + \frac{R_n^3}{2 R_c^2} + \frac{3}{2} R_n - 2 R_c \right] \quad (40)$$

$$y_{\text{Cone Weight}} = \frac{\rho l_c^4 R_n^2}{3 (R_c - R_n)^4 E} \left[ \frac{7}{2} + 3 \log \left( \frac{R_c}{R_n} \right) - 3 \frac{R_c}{R_n} - \frac{R_n}{R_c} + \frac{R_n^2}{2 R_c^2} + \frac{(R_c - R_n)^2}{R_n^2} \right] \quad (44)$$

Equations (25), (29), (40), and (44) have been restated on this page in order to summarize the results of the previous analysis.

The principle of superposition is now applied to give the slope and deflection, for the conical section, as

$$\theta_{\text{Cone}} = \theta_F \text{ Cone} + \theta_W \text{ Cone} \quad (45)$$

$$y_{\text{Cone}} = y_F \text{ Cone} + y_W \text{ Cone} \quad (46)$$

Total deflection of the free end on the aberrascop section,  $\frac{l_T}{2}$ , is now obtained by translating the cylinder deflection to the free end and adding cylinder and cone components directly.

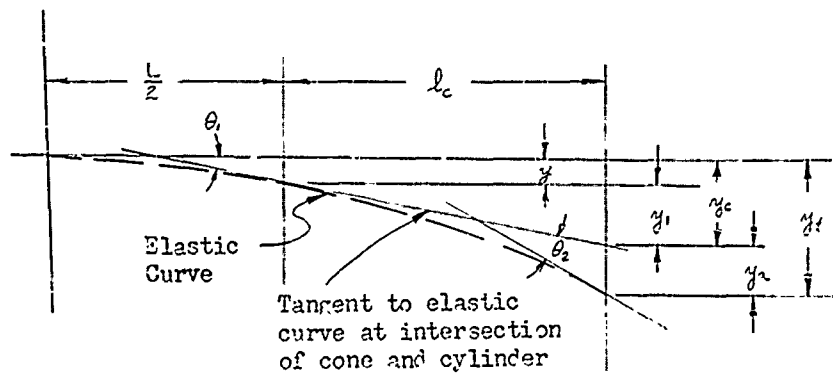


Figure 38

Beam Problem Parameters

Translated cylinder deflection,  $y_c$ , (Figure 38) is given by the equation

$$y_c = y + l_c \theta_1$$

where:  $l_c \theta_1 = y_1$

(47)

The total deflection of the aberrascopes section,  $\frac{L_T}{2}$ , can now be stated as

$$y_t = y_a + y_c \quad (48)$$

where:  $y_a$  = cone deflection

$y_c$  = cylinder deflection

and the slope of the configuration can be stated as

$$\theta_t = \theta_1 + \theta_2$$

where:  $\theta_1$  = slope due to cylinder

$\theta_2$  = slope due to cone

Utilization of the above equations will provide information as to the most desirable cylinder and cone wall thickness consistent with allowable secondary mirror deviation.

b. Evaluation of Deflections and Slopes

Calculations of deflections and slopes for the aberrascopes structure were made using the following numerical values.

$L = 5$ inches	$t_c = .1, .2, .3, .4, .5$ inches
$L_c = 13$ inches	$t = .05, .10, .15, .20, .25$ inches
$R_o = 4$ inches	$F_{m1} = .03$ #
$R_1 = (4 - t_c)$ inches	$F_{m2} = 1.51$ #
$R_a = 2.5$ inches	$\rho = .294$ #/in. <sup>3</sup>
$R_n = (2.5 - t)$ inches	$E = 20 \times 10^6$ #/in. <sup>2</sup>

The data obtained, assuming a one g loading, is tabulated in Table VIII.

Figure 39 shows the total deflection at the small end of the aberrascope for a  $10^{-2}$  g loading. Since the deflection at the end of the cylindrical section is negligible compared to the total deflection, the curves of Figure 39 also show the deflection of the secondary mirror relative to the primary mirror for various values of wall thickness for the cylindrical and conical sections under the assumed loading. Figure 40 shows the total slope at the small end of the aberrascope structure for a  $10^{-2}$  g loading. The slope at the secondary mirror relative to the position of the primary mirror is shown in Figure 41.

c. Weight Calculations

In addition to meeting the accuracy requirements of the instrument, the aberrascope structure must be kept within reasonable weight limits. Calculated weights of the aberrascope structure for various combinations of cone and cylinder wall thickness are tabulated in Table VIII and are plotted in Figure 41. The calculated values include the weight of one cylindrical section and two conical sections. Weights of the bearings or components mounted on the structure are not included.

d. Conclusions from Static Load Analysis and Weight Calculations

The curves of Figures 39, 40, and 41 show that both deflection and slope increase with increasing cone wall thickness. Deflection and slope decrease with increasing wall thickness of the cylindrical section. Therefore, the best structural arrangement for minimizing misalignment between the primary and secondary mirrors is one having thin walled conical section and a thick walled cylindrical section. However,

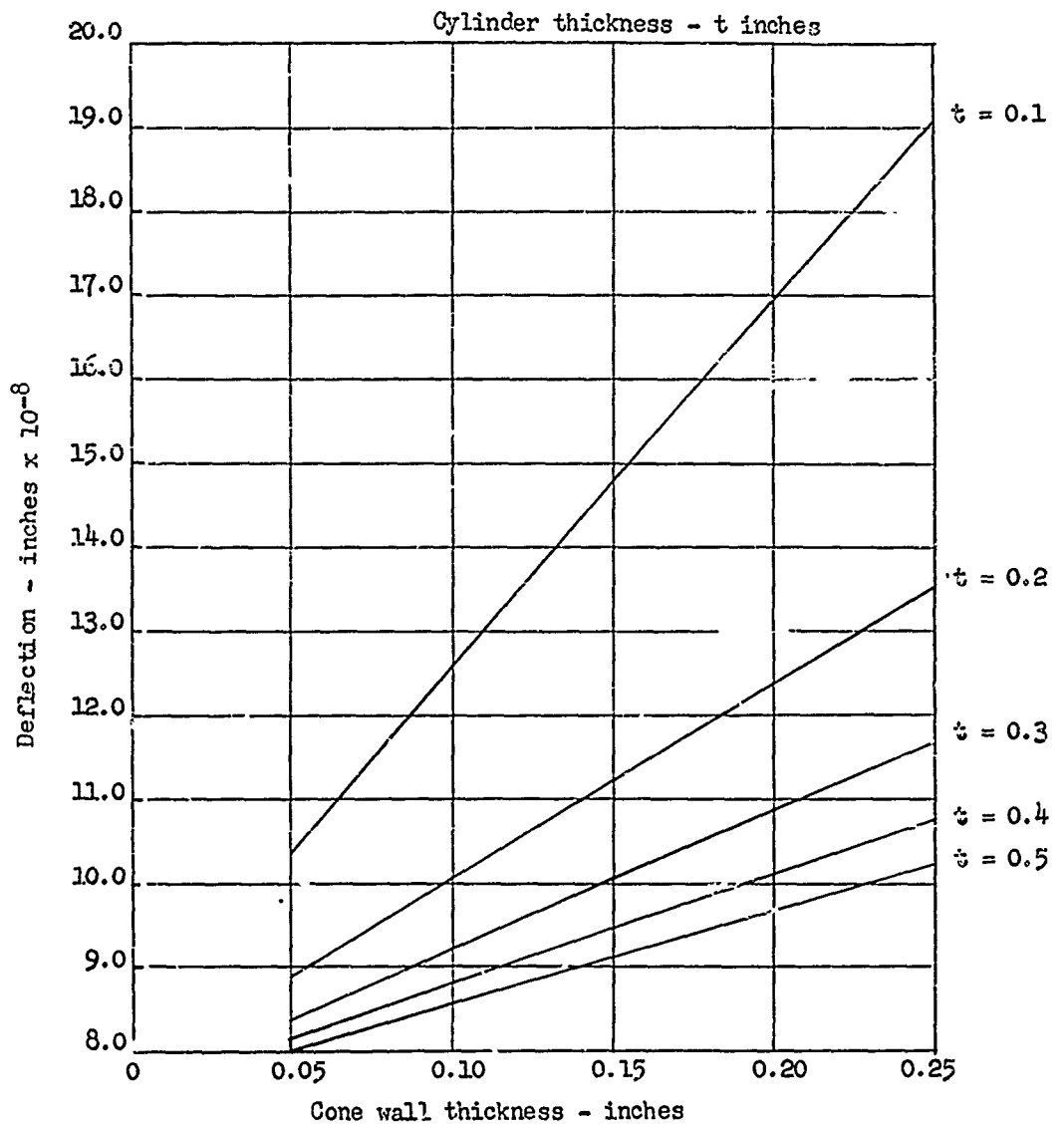


Figure 39

DEFLECTION AT END POSITION OF THE APERRASCOPE  
UNDER  $10^{-2}$  g LOADING

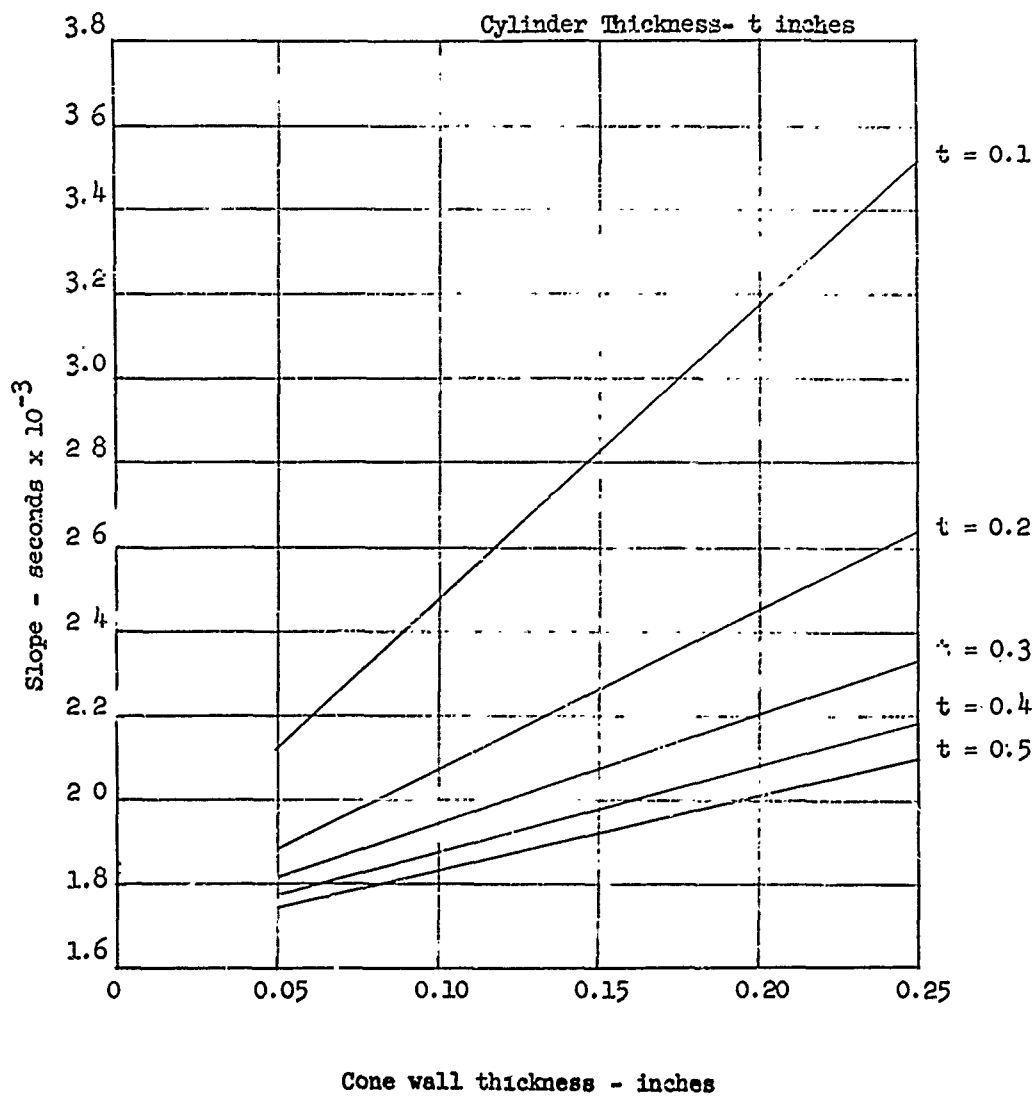


Figure 40

SLOPE AT END POSITION OF THE ABERRASCOPE  
UNDER  $10^{-2} g$  LOADING

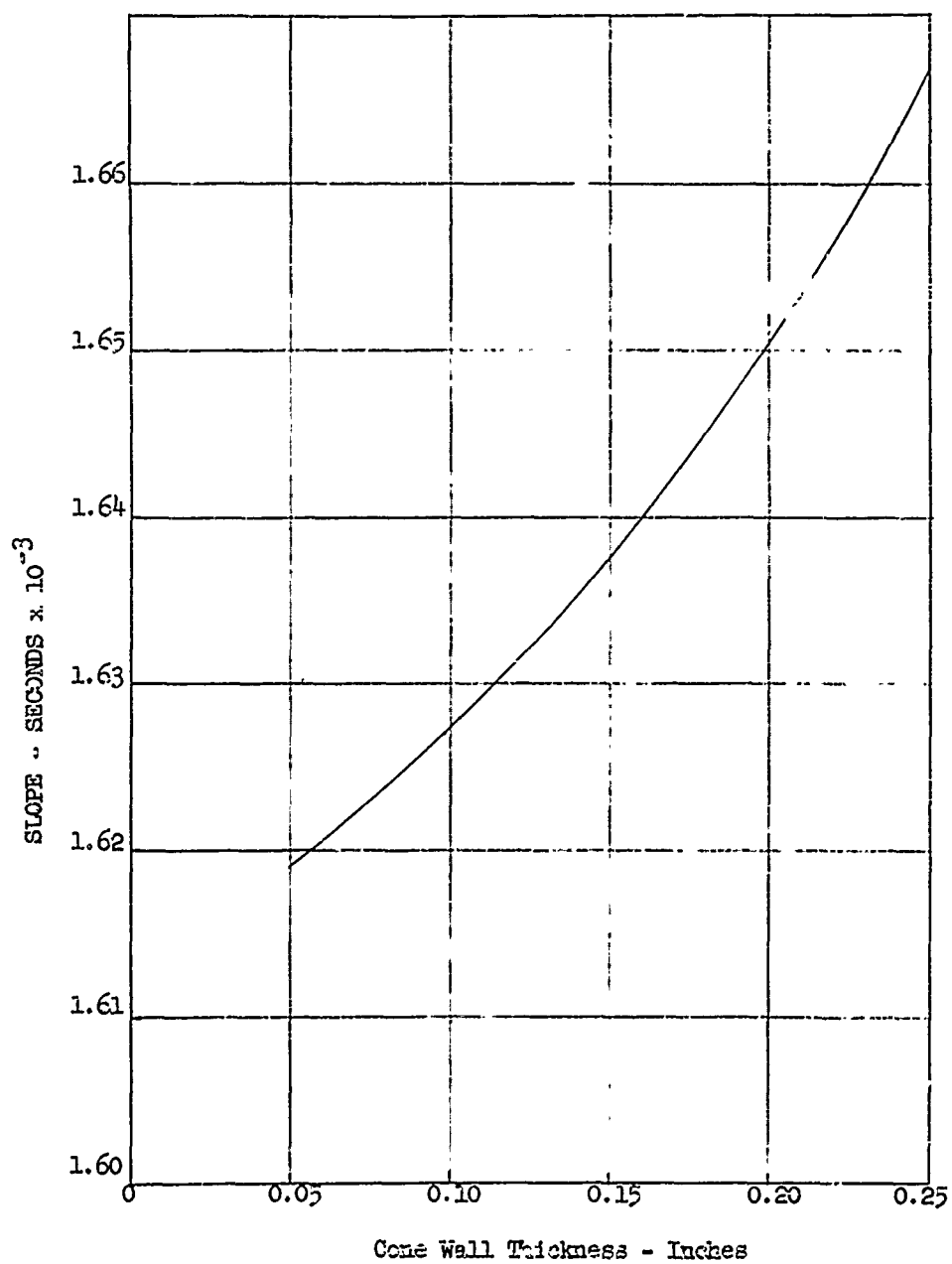


Figure 41

SLOPE AT SECONDARY MIRROR RELATIVE TO  
PRIMARY MIRROR

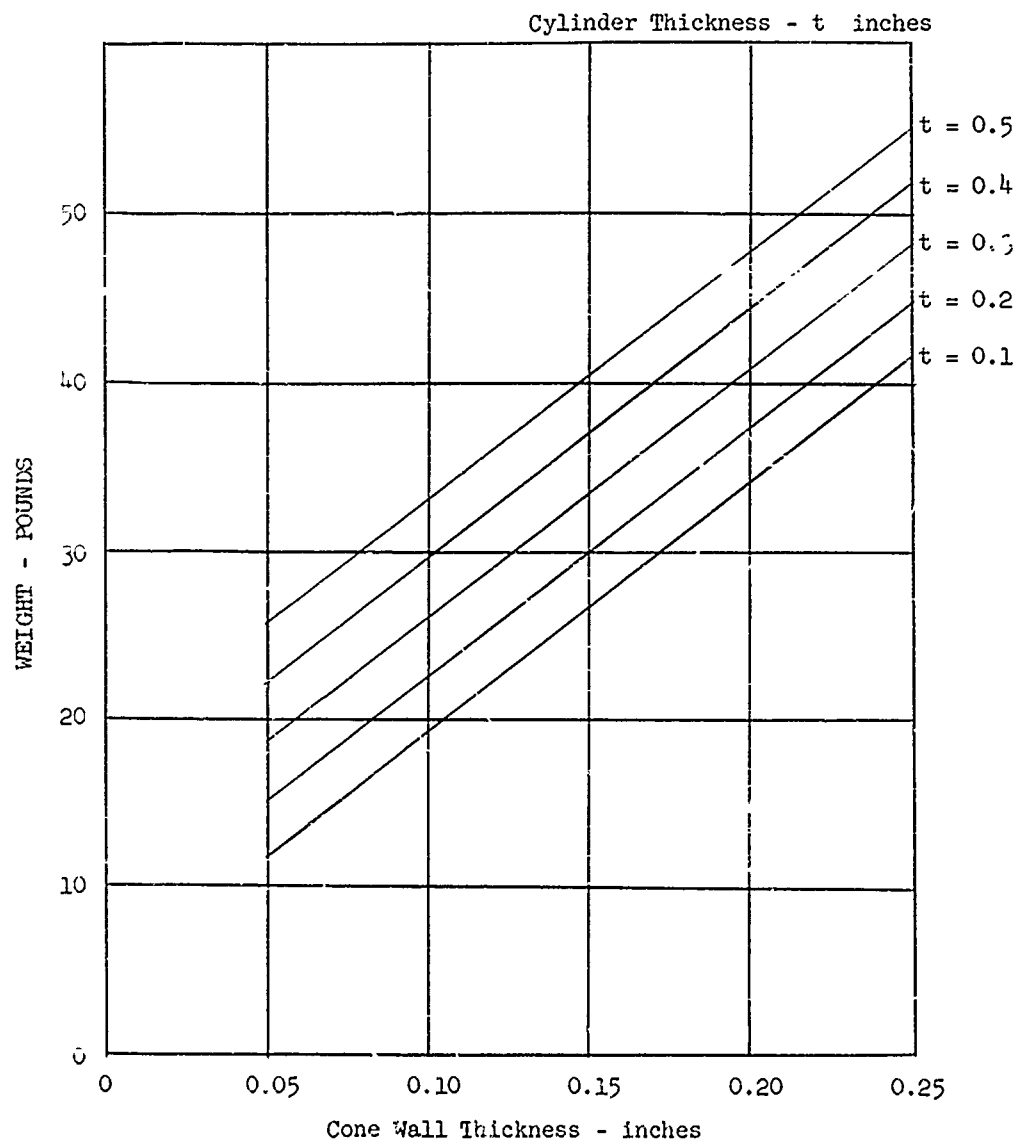


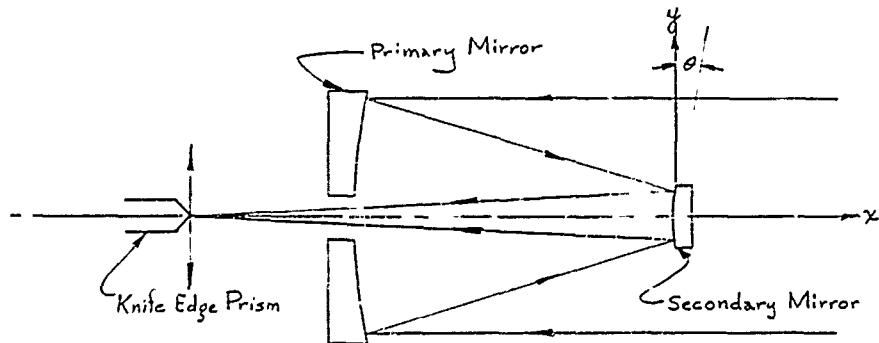
Figure 42

STRUCTURE WEIGHT OF ABERRASCOPE  
CONFIGURATION



the overall weight of the structure increases with increasing wall thickness of the cylindrical section, so that a compromise must be made between structural and weight requirements. Also, the cylindrical section must be sufficiently rigid to provide support for the aberrascope main bearing.

From the above consideration wall thicknesses of .05 inches for the conical section and .2 inches for the cylindrical section appear to be reasonable choices. The weight of such a structure would be approximately 15 pounds as shown in Figure 42. Comparison of the deflection and slope magnitude for a loading of  $10^{-2}$  g on this structure with the accuracy requirements may be made from a consideration of the sketch below.



x coordinate lies along optical axis.

y is normal to x.

$\theta$  measures rotation with respect to a plane perpendicular to x.

The quantities  $\delta x$ ,  $\delta y$ , and  $\delta \theta$  indicate small displacements relative to x, y,  $\theta$  coordinate system.

Displacements  $\delta y$  and  $\delta \theta$  correspond to deflection and slope respectively. The allowable errors in alignment during one rotation of the aberrascopes due to disturbing forces are:

$$\delta y \leq 2 \times 10^{-5} \text{ inches}$$

$$\delta \theta \leq .01 \text{ seconds of arc}$$

The calculated values of deflection and slope for the structure and loading assumed above are shown in Figures 39 and 41. Using a cone wall thickness of 0.05 inches and a cylinder wall thickness of 0.20 inches, the following values are obtained:

$$\delta y = 8.9 \times 10^{-8} \text{ inches}$$

$$\delta \theta = .0016 \text{ seconds of arc}$$

The deflection is less than the allowable error by a factor of 200 and the slope is less than the allowable angular misalignment by a factor of 6.

e. Structural Response to Dynamic Loads

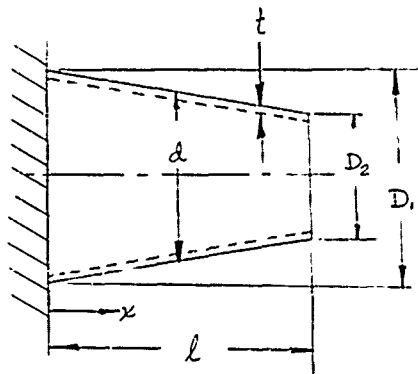
While the above analysis of slope and deflections under static loading showed that conical structural sections with very thin walls would meet the accuracy requirements with larger factors of safety, it is also necessary to investigate the behavior of the structure under vibrational disturbances. In order to avoid instrument errors due to vibration it is desirable to have the lowest resonant frequency of the structure significantly higher than the frequency of any disturbing vibration.

Since the cylindrical section of the structure will be much more rigid than the conical sections, the vibration analysis is concentrated on the conical sections. The ways in which the conical sections may vibrate may be classified as:

1. Cantilever beam vibrations.
2. Thin shell vibrations.
3. Torsional vibrations.

Each of these forms of vibration will be considered in turn below.

(1) Cantilever Beam Vibration



$$A = \frac{\pi}{4} [d^2 - (d - 2t)^2]$$

$$I = \frac{\pi}{64} [d^4 - (d - 2t)^4]$$

$A$  = Cross sectional area of shell

$I$  = Moment of in inertia of shell

The first mode of vibration as a cantilever beam is calculated by the Rayleigh method. Elementary beam theory is used in the calculations. This introduces some error in the results due to neglecting transverse shear and rotary inertia. However, the frequencies obtained should be sufficiently accurate for the purpose under consideration.

The deflection curve under vibration is assumed to be the same shape as the deflection curve for a uniform cross-section cantilever beam under a uniform static load. The actual shape of the vibration deflection curve will be somewhat different than the assumed curve. This, however, will introduce only a small error into the calculated frequency.

Taking

$$X = a (6\lambda^2 X^2 - 4\lambda X^3 + X'') \quad (3)$$

where

$X$  = mode shape

$a$  = a constant

the boundary conditions of the problem are:

$$\begin{aligned} \left(\frac{dX}{dx}\right) &= 0 & (EI \frac{d^2 X}{dx^2}) &= 0 \\ X &= 0 & X &= \lambda \\ (X) &= 0 & \frac{d}{dx} (EI \frac{d^2 X}{dx^2}) &= 0 \\ x &= 0 & x &= \lambda \end{aligned} \quad (4)$$

The resonant frequency is obtained from the equation:

$$\omega^2 = \frac{Eg}{\rho} \frac{\int_0^\lambda I \left(\frac{d^2 X}{dx^2}\right) dx}{\int_0^\lambda A X^2 dx} \quad (5)$$

$\omega$  = resonant frequency

$E$  = Modulus of Elasticity

$g$  = acceleration of gravity

$\rho$  = density per unit volume

$l$  = length of shell

$x$  = distance from fix end of shell

$$d = \left[ D_1 - \frac{D_1 - D_2}{l} x \right] \quad (6)$$

$d$  = outside diameter of shell at any cross section

$D_1$  = outside diameter of large end of shell

$D_2$  = outside diameter of small end of shell

Letting

$$\frac{D_1 - D_2}{l} = c \quad (7)$$

Substituting equation (7) in equation (6)

$$d = \left[ D_1 - cx \right] \quad (8)$$

Substituting equation (8) in equation (2) and expanding the terms gives

$$I = \frac{\pi}{8} t \left[ A_1 x + A_2 x^2 + A_3 x^3 + A_4 \right] \quad (9)$$

where

$t$  = shell thickness

$$A_1 = (6tD_1 c - 3D_1^2 c - 4t^2 c)$$

$$A_2 = (3D_1 c^2 - 3tc^2)$$

$$A_3 = c^3$$

$$A_4 = (D_1^3 - 3tD_1^2 + 4t^2 D_1 - 2t^3)$$

Substituting equation (8) in equation (1):

$$A = \pi t \left[ (D_1 - t) - cx \right] = \pi t \left[ (D_1 - t) - \left( \frac{D_1 - D_2}{l} \right) x \right] \quad (10)$$

$$\int_0^l \frac{1}{I} \left( \frac{d^2 X}{dx^2} \right)^2 dx = \frac{3 a^2 \pi t l^5}{140} \left[ 28 A_1 l + 8 A_2 l^2 + 3 A_3 l^3 + 168 A_4 l^4 \right] \quad (11)$$

$$\int_0^l A X^2 dx = \frac{a^2 \pi t l^9}{315} \left[ 144 D_1 + 584 D_2 - 728 t \right] \quad (12)$$

Setting equation (11) equal to equation (12) and solving for  $\omega^2$  gives:

$$\omega^2 = 6.75 \frac{Eg}{\rho} \left[ \frac{\frac{28 A_1}{l^3} + \frac{8 A_2}{l^2} + \frac{3 A_3}{l} + \frac{168 A_4}{l^4}}{144 D_1 + 584 D_2 - 728 t} \right] \quad (13)$$

Equation (13) may be solved for  $\omega$ .

#### (u) Numerical Calculations

$$D_1 = 8$$

$$D_2 = 5$$

$$l = 13$$

$$c = \frac{8-5}{13} = .231$$

$$E = 20 \times 10^6$$

$$\rho = .294$$

$$t = .05, .1, .2$$

$$f_n = \frac{\omega}{2\pi}$$

(b) Results of Calculations

$$t = .05 \qquad f_n = 1665 \text{ cps}$$

$$t = .1 \qquad f_n = 1648 \text{ cps}$$

$$t = .2 \qquad f_n = 1616 \text{ cps}$$

The resonant frequencies for the conical shells for cantilever beam vibrations are very high. Variation of the thickness over the range considered makes little difference in the resonant frequency (about 3%). This is probably less than the error in frequency due to the various simplifying assumptions made in the analysis.

(2) Thin Shell Vibrations

The thin shell vibration of a cone may be composed of circumferential modes, axial modes, or a combination of these modes. If a section perpendicular to the axis of the shell is considered, the vibration may consist of the periodic movement of a number of stationary waves distributed around the circumference. This form of vibration is illustrated in Figure 43. The number of circumferential waves is indicated by "S".

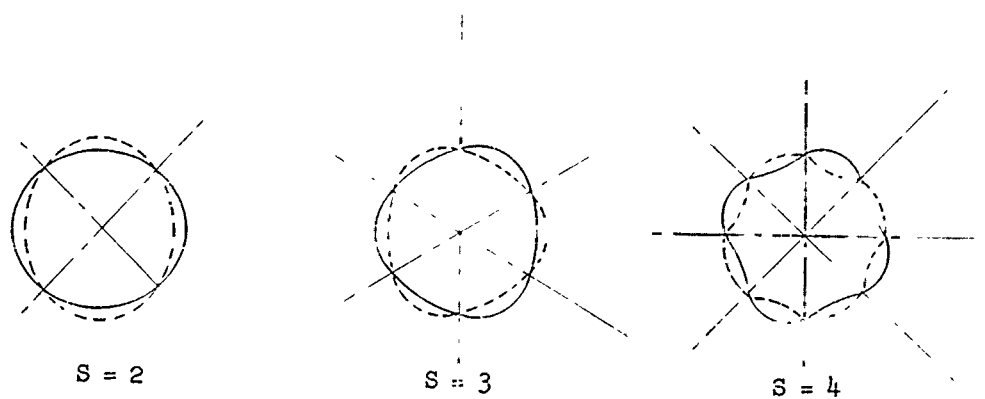


Figure 43. Circumferential Waves

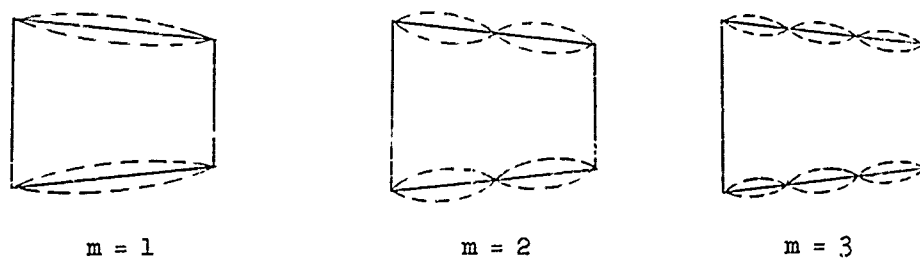


Figure 45. Axial Waves

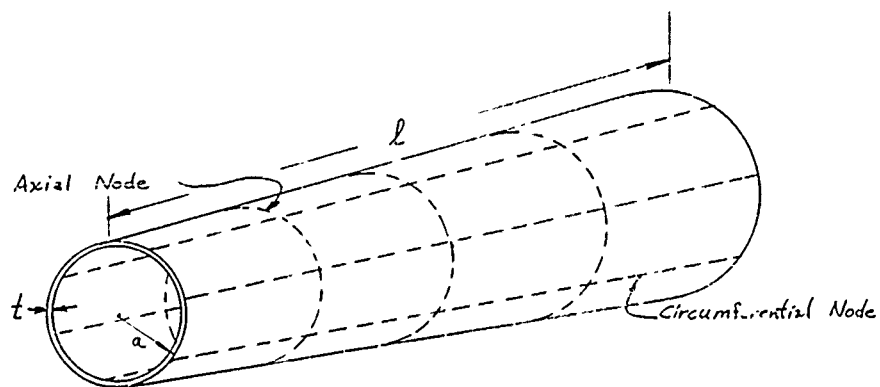


Figure 46. Location of Nodes



Figure 45 shows the first three axial vibration modes of a conical shell with one free and one built in end. Figure 46 shows the location of nodes for one case of combined circumferential and axial vibration ( $n = 3, m = 4$ ).

The calculation of resonant frequencies of thin walled conical shells is a complex and time consuming process. Since the information of principal interest is the lowest resonant frequency of the shell, the analysis is limited to the case of circumferential vibration only, ( $m = 0$ ). The frequencies of the axial modes or the combined axial and circumferential mode will all be higher than the lowest frequency of purely circumferential vibration.

A Rayleigh-Ritz procedure is used to determine resonant frequencies of circumferential modes of vibration of a conical shell which is built in at its large ends and is free at its small end.

The Rayleigh-Ritz procedure equates maximum potential energy to maximum kinetic energy. A displacement is, first, assumed for the mode shape of the vibration. The assumed mode shape must satisfy the displacement boundary conditions and contain arbitrary constants. The maximum potential and kinetic energies of the system are obtained from the assumed mode shapes. The resonant frequencies are calculated by applying the Rayleigh-Ritz procedure to the resulting statement of Hamilton's principle.

The analytical development follows that given in the paper "Vibrations of Conical Shells" by H. Saunders and E. J. Wisniewski,<sup>21</sup> except that modifications are introduced due to the different boundary conditions of the present problem.

The middle surface strains of the shell are expressed in terms of middle surface displacements  $u_1$ ,  $u_2$ , and  $w$  as shown in Figure 47. Each displacement is assumed to be a sinusoidal function of time.

$$w(Z, \theta, t) = w(Z, \theta) \sin \omega t$$

$$u_1(Z, \theta, t) = u_1(Z, \theta) \sin \omega t$$

$$u_2(Z, \theta, t) = u_2(Z, \theta) \sin \omega t$$

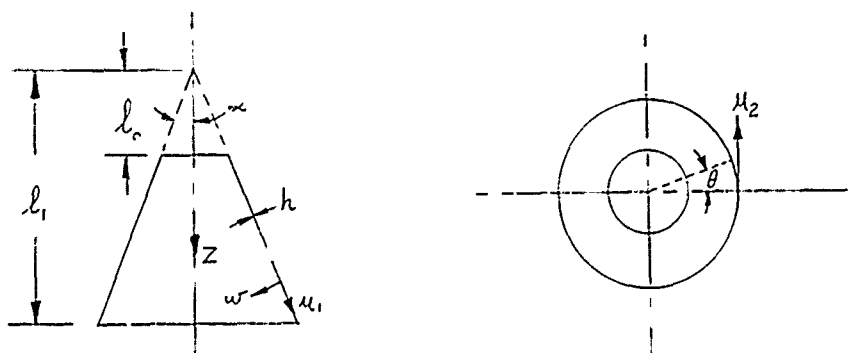


Figure 47. Middle Surface Displacements

$Z$  = cylindrical coordinate measured along axis of cone from apex

$u_1$  = meridional displacement at position  $Z$ ,  $\theta$ , and time  $t$

$u_2$  = Tangential displacement at position  $Z$ ,  $\theta$ , and time  $t$

$w$  = inward displacement normal to the tangent plane to the shell surface at position  $Z$ ,  $\theta$ , and time  $t$

$l_0$  =  $Z$  coordinate to smaller edge of conical shell

$l_1$  =  $Z$  coordinate to larger edge of conical shell

$\alpha$  = one-half the included angle of the cone

$h$  = shell thickness

Linearized expressions given by Love<sup>22</sup> are used for the middle surface strains,  $\epsilon_1$ ,  $\epsilon_2$ ,  $\epsilon_{12}$  and the changes of curvature,  $K_1$ ,  $K_2$ , and  $K_{12}$ .

$$\epsilon_1 = \frac{\partial u_1}{\partial Z} \cos \alpha$$

$$\epsilon_2 = \frac{\partial u_2 \cos \alpha}{\partial \theta Z \sin \alpha} + \frac{u_1}{Z} \cos \alpha - \frac{w}{Z} \frac{\cos^2 \alpha}{\sin \alpha}$$

$$\epsilon_{12} = Z \cos \alpha \frac{\partial}{\partial Z} \left( \frac{u^2}{Z} \right) + \frac{1}{Z} \frac{\cos \alpha}{\sin \alpha} \frac{\partial u_1}{\partial \theta}$$

$$K_1 = \frac{\partial^2 w}{\partial Z^2} \cos^2 \alpha$$

$$K_2 = \frac{\partial u_2}{\partial \theta} \frac{\cos^3 \alpha}{Z^2 \sin^2 \alpha} + \frac{\cos^2 \alpha}{Z^2 \sin^2 \alpha} \frac{\partial^2 w}{\partial \theta^2} + \frac{\cos^2 \alpha}{Z} \frac{\partial w}{\partial Z}$$

$$K_{12} = \frac{\partial u_2}{\partial Z} \frac{\cos^3 \alpha}{Z \sin \alpha} - \frac{\cos^3 \alpha}{Z^2 \sin \alpha} u_2 + \frac{\cos^2 \alpha}{Z \sin \alpha} \frac{\partial^2 w}{\partial Z \partial \theta} - \frac{\cos^2 \alpha}{Z^2 \sin \alpha} \frac{\partial w}{\partial \theta}$$

$\epsilon_1$  = meridional strain of the middle surface of the shell

$\epsilon_2$  = circumferential strain of the middle surface

$\epsilon_{12}$  = shear strain of middle surface

$K_1$  = change of curvature of middle surface in meridional direction due to deformation of the middle surface

$K_2$  = change of curvature of middle surface in circumferential direction

$K_{12}$  = twist of middle surface

The maximum kinetic and potential energies are:

$$T = \frac{1}{2} \int_A \rho h (\dot{u}_1^2 + \dot{u}_2^2 + \dot{w}^2) dA \quad (3)$$

$$V = \frac{1}{2} \frac{Eh}{(1-\nu^2)} \int_A \left\{ \frac{h^2}{12} \left[ (K_1 + K_2)^2 - 2(1-\nu)(K_1 K_2 - K_{12}^2) \right] + (\xi_1 + \xi_2)^2 - 2(1-\nu) \left( \xi_1 \xi_2 - \frac{1}{4} \xi_{12}^2 \right) \right\} dA \quad (4)$$

Substituting Equations (1) into Equations (3) and (4) together with proper limits gives:

$$T = \frac{1}{2} \rho h \omega^2 \int_0^1 \int_0^{2\pi} \int_0^1 (\omega^2 + u_1^2 + u_2^2) \frac{Z \sin \alpha}{\cos^2 \alpha} dZ d\theta \quad (5)$$

$$V = \frac{1}{2} \frac{Eh}{(1-\nu^2)} \int_0^1 \int_0^{2\pi} \int_0^1 \left\{ \frac{h^2}{12} \left[ (K_1 + K_2)^2 - 2(1-\nu)(K_1 K_2 - K_{12}^2) \right] + (\xi_1 + \xi_2)^2 - 2(1-\nu) \left( \xi_1 \xi_2 - \frac{1}{4} \xi_{12}^2 \right) \right\} \frac{Z \sin \alpha}{\cos^2 \alpha} dZ d\theta \quad (6)$$

$T$  = maximum kinetic energy of the vibrating shell

$V$  = maximum potential energy of the vibrating shell

$E$  = Modulus of elasticity

$\nu$  = Poisson's ratio

$\rho$  = density of shell material

$\omega$  = frequency

The displacement boundary conditions for a conical shell built in on the edge at the large end and free at small end are:

$$\omega = 0 \text{ at } Z = \lambda_1 \quad (7)$$

$$\frac{\partial \omega}{\partial Z} = 0 \text{ at } Z = \lambda_1$$

The mode shape assumed for  $\omega$  is:

$$\omega = (\lambda_1' - Z)^2 [A + B Z] \sin S \theta \quad (8)$$

$S$  = number of complete waves around circumference

$A, B$  = independent constants

The other two displacements  $u_1$  and  $u_2$  are selected so that  $\epsilon_1$  and  $\epsilon_2$  are zero.

$$\text{Then:} \quad u_1 = 0$$

$$u_2 = \frac{\cos \alpha}{S} (\lambda_1' - Z)^2 [A + B Z] \cos S \theta \quad (9)$$

$$\epsilon_{12} = -\frac{Z \cos^2 \alpha}{S} \left[ A \left( 1 - \frac{\lambda_1'^2}{Z^2} \right) + 2 B \lambda_1' \left( \frac{Z}{\lambda_1'} - 1 \right) \right] \cos S \theta$$

$$K_1 = \cos^2 \alpha \left[ 2A + B \lambda_1' \left( 6 \frac{Z}{\lambda_1'} - 4 \right) \right] \sin S \theta$$

$$K_2 = \cos^2 \alpha \left\{ A \left[ \beta \left( 1 - \frac{2 \lambda_1'}{Z} + \frac{\lambda_1'^2}{Z^2} \right) + 2 \left( 1 - \frac{\lambda_1'}{Z} \right) + B \lambda_1' \left[ \beta \left( \frac{Z}{\lambda_1'} - 2 + \frac{\lambda_1'}{Z} \right) + \left( \frac{3Z}{\lambda_1'} - 4 + \frac{\lambda_1'}{Z} \right) \right] \right] \right\} \sin S \theta$$

$$K_{12} = \frac{\beta \cos^2 \alpha \sin^2 \alpha}{S \sin \alpha} \left[ A \left( \frac{\lambda_1'^2}{Z^2} - 1 \right) + 2 B \lambda_1' \left( 1 - \frac{Z}{\lambda_1'} \right) \right] \cos S \theta$$

Substituting  $u_1$ ,  $u_2$ , and  $\omega$  from equations (9) and (8) into equation (5) and carrying out the integration gives the maximum kinetic energy.

$$\begin{aligned}
T = \frac{\pi}{2} \rho h \omega^2 l_1^6 \left( \frac{\tan \alpha}{\cos \alpha} \right) \left( 1 + \frac{\cos^2 \alpha}{s^2} \right) & \left\{ A^2 \left[ \frac{1}{6} \left( 1 - \frac{l_0^6}{l_1^6} \right) \right. \right. \\
& - \frac{4}{5} \left( 1 - \frac{l_0^5}{l_1^5} \right) + \frac{3}{2} \left( 1 - \frac{l_0^4}{l_1^4} \right) - \frac{4}{3} \left( 1 - \frac{l_0^3}{l_1^3} \right) + \frac{1}{2} \left( 1 - \frac{l_0^2}{l_1^2} \right) \\
& + 2 AB l_1 \left[ \frac{1}{7} \left( 1 - \frac{l_0^7}{l_1^7} \right) - \frac{2}{3} \left( 1 - \frac{l_0^6}{l_1^6} \right) + \frac{6}{5} \left( 1 - \frac{l_0^5}{l_1^5} \right) \right. \\
& - \left. \left( 1 - \frac{l_0^4}{l_1^4} \right) + \frac{1}{3} \left( 1 - \frac{l_0^3}{l_1^3} \right) \right] + B^2 l_1^2 \left[ \frac{1}{8} \left( 1 - \frac{l_0^8}{l_1^8} \right) \right. \\
& \left. \left. - \frac{4}{7} \left( 1 - \frac{l_0^7}{l_1^7} \right) + \left( 1 - \frac{l_0^6}{l_1^6} \right) - \frac{4}{5} \left( 1 - \frac{l_0^5}{l_1^5} \right) + \frac{1}{4} \left( 1 - \frac{l_0^4}{l_1^4} \right) \right] \right\} \quad (10)
\end{aligned}$$

The corresponding expression for the potential energy is obtained by substituting  $K_1$ ,  $K_2$ ,  $K_{12}$ , and  $\mathcal{E}_{12}$  from equations (9) in equation (6) and integrating.

For convenience the potential energy is divided into two parts

$$V = V_b + V_e \quad (11)$$

$V_b$  = the portion of the potential energy due to  $K_1$ ,  $K_2$ , and  $K_{12}$ .

$V_e$  = the portion of the potential energy due to  $\mathcal{E}_{12}$ .

$$V_b = \frac{E h^3 \tan \alpha}{24 (1 - \nu^2)} \pi \cos^3 \alpha l_1^2 \left\{ A^2 \left[ \frac{1}{2} \left( 1 - \frac{l_0^2}{l_1^2} \right) + \beta \left[ \frac{1}{2} \left( 1 - \frac{l_0^2}{l_1^2} \right) \right. \right. \right. \right.
\quad (12)$$

$$\begin{aligned}
& + 6 \log \frac{\lambda_1}{\lambda_0} - 4 \left(1 - \frac{\lambda_0}{\lambda_1}\right) + 4 \left(1 - \frac{\lambda_1}{\lambda_0}\right) - \frac{\lambda_1}{2} \left(1 - \frac{\lambda_1^2}{\lambda_0^2}\right) \Big] \\
& + 4\beta \left[ \frac{1}{2} \left(1 - \frac{\lambda_0^2}{\lambda_1^2}\right) - 3 \left(1 - \frac{\lambda_0}{\lambda_1}\right) + 3\lambda_1 \frac{\lambda_1}{\lambda_0} + \left(1 - \frac{\lambda_1}{\lambda_0}\right) \right. \\
& + 2 \left(1 - \frac{\lambda_0^2}{\lambda_1^2}\right) - 8 \left(1 - \frac{\lambda_0}{\lambda_1}\right) + 4 \log \frac{\lambda_1}{\lambda_0} + 2\gamma \left\{ \beta \left[ 1 - \frac{\lambda_0^2}{\lambda_1^2} \right] \right. \\
& \left. \left. - 4 \left(1 - \frac{\lambda_0}{\lambda_1}\right) + 2 \log \frac{\lambda_1}{\lambda_0} + 2 \left(1 - \frac{\lambda_0^2}{\lambda_1^2}\right) - 4 \left(1 - \frac{\lambda_0}{\lambda_1}\right) \right\} \right. \\
& + 2 (1 - \gamma) \sin^2 \alpha \frac{\beta^2}{s^2} \left[ \frac{1}{2} \left(1 - \frac{\lambda_0^2}{\lambda_1^2}\right) - 2 \log \frac{\lambda_1}{\lambda_0} \right. \\
& \left. \left. - \frac{1}{2} \left(1 - \frac{\lambda_1^2}{\lambda_0^2}\right) \right] \right] + A B \lambda_1 \left\langle 8 \left(1 - \frac{\lambda_0^3}{\lambda_1^3}\right) - 8 \left(1 - \frac{\lambda_0^2}{\lambda_1^2}\right) \right. \\
& + \beta^2 \left[ \frac{2}{3} \left(1 - \frac{\lambda_0^3}{\lambda_1^3}\right) - 4 \left(1 - \frac{\lambda_0^2}{\lambda_1^2}\right) + 12 \left(1 - \frac{\lambda_0}{\lambda_1}\right) - 8 \log \frac{\lambda_1}{\lambda_0} \right. \\
& \left. - 2 \left(1 - \frac{\lambda_1}{\lambda_0}\right) + \beta \left[ \frac{10}{3} \left(1 - \frac{\lambda_0^3}{\lambda_1^3}\right) - 16 \left(1 - \frac{\lambda_0^2}{\lambda_1^2}\right) + 36 \left(1 - \frac{\lambda_0}{\lambda_1}\right) \right. \right. \\
& \left. \left. - 16 \log \frac{\lambda_1}{\lambda_0} - 2 \left(1 - \frac{\lambda_1}{\lambda_0}\right) \right] + 4 \left(1 - \frac{\lambda_0^3}{\lambda_1^3}\right) - 14 \left(1 - \frac{\lambda_0^2}{\lambda_1^2}\right) \right. \\
& \left. + 20 \left(1 - \frac{\lambda_0}{\lambda_1}\right) - 4 \log \left(\frac{\lambda_1}{\lambda_0}\right) + 2\gamma \left\{ \beta \left[ \frac{8}{3} \left(1 - \frac{\lambda_0^3}{\lambda_1^3}\right) \right. \right. \right.
\end{aligned}$$

$$\begin{aligned}
& - 10 \left( 1 - \frac{\lambda_0^2}{\lambda_1^2} \right) + 16 \left( 1 - \frac{\lambda_0}{\lambda_1} \right) - 4 \log \frac{\lambda_1}{\lambda_0} \Big] + 6 \left( 1 - \frac{\lambda_0^3}{\lambda_1^3} \right) \\
& - 14 \left( 1 - \frac{\lambda_0^2}{\lambda_1^2} \right) + 10 \left( 1 - \frac{\lambda_0}{\lambda_1} \right) \Big\} + 2 (1 - \nu) \sin^2 \alpha \frac{\beta^2}{s_2} \left[ \frac{4}{3} \left( 1 - \right. \right. \\
& \left. \left. - \frac{\lambda_0^3}{\lambda_1^3} \right) - 2 \left( 1 - \frac{\lambda_0^2}{\lambda_1^2} \right) - 4 \left( 1 - \frac{\lambda_0}{\lambda_1} \right) + 4 \log \frac{\lambda_1}{\lambda_0} \right] \Bigg\rangle \\
& + \beta^2 \lambda_1^2 \left\langle 9 \left( 1 - \frac{\lambda_0^4}{\lambda_1^4} \right) - 16 \left( 1 - \frac{\lambda_0^3}{\lambda_1^3} \right) - 8 \left( 1 - \frac{\lambda_0^2}{\lambda_1^2} \right) \right. \\
& + \beta^2 \left[ \frac{1}{4} \left( 1 - \frac{\lambda_0^4}{\lambda_1^4} \right) - \frac{4}{3} \left( 1 - \frac{\lambda_0^3}{\lambda_1^3} \right) + 3 \left( 1 - \frac{\lambda_0^2}{\lambda_1^2} \right) - 4 \left( 1 - \frac{\lambda_0}{\lambda_1} \right) \right. \\
& + \log \frac{\lambda_1}{\lambda_0} + 2 \beta \left[ \frac{3}{4} \left( 1 - \frac{\lambda_0^4}{\lambda_1^4} \right) - \frac{10}{3} \left( 1 - \frac{\lambda_0^3}{\lambda_1^3} \right) + 6 \left( 1 - \frac{\lambda_0^2}{\lambda_1^2} \right) \right. \\
& \left. \left. - 6 \left( 1 - \frac{\lambda_0}{\lambda_1} \right) + \log \frac{\lambda_1}{\lambda_0} \right] + \frac{9}{4} \left( 1 - \frac{\lambda_0^4}{\lambda_1^4} \right) - 8 \left( 1 - \frac{\lambda_0^3}{\lambda_1^3} \right) \right. \\
& + 11 \left( 1 - \frac{\lambda_0^2}{\lambda_1^2} \right) - 8 \left( 1 - \frac{\lambda_0}{\lambda_1} \right) + \log \frac{\lambda_1}{\lambda_0} + 2 \nu \left\{ \beta \left[ \frac{3}{2} \left( 1 - \frac{\lambda_0^4}{\lambda_1^4} \right) \right. \right. \\
& \left. \left. - \frac{16}{3} \left( 1 - \frac{\lambda_0^3}{\lambda_1^3} \right) + 7 \left( 1 - \frac{\lambda_0^2}{\lambda_1^2} \right) - 4 \left( 1 - \frac{\lambda_0}{\lambda_1} \right) \right] + \frac{9}{2} \left( 1 - \frac{\lambda_0^4}{\lambda_1^4} \right) \right.
\end{aligned}$$



$$\begin{aligned}
& - 12 \left( 1 - \frac{l_o^3}{l_1^3} \right) + 11 \left( 1 - \frac{l_o^2}{l_1^2} \right) - 4 \left( 1 - \frac{l_o}{l_1} \right) \Big\} \\
& + 2 (1 - \nu) \sin^2 \alpha \frac{\beta^2}{s^2} \left[ 2 \left( 1 - \frac{l_o^2}{l_1^2} \right) - \frac{8}{3} \left( 1 - \frac{l_o^3}{l_1^3} \right) \right] \\
& + \left( 1 - \frac{l_o^4}{l_1^4} \right) \Big] \gg \gg \gg \\
v_e = & \frac{E h \pi \tan \alpha \cos^3 \alpha}{4 (1 + \nu) s^2} \frac{l_1^4}{l_1^4} \left\{ A^2 \left[ \frac{1}{4} \left( 1 - \frac{l_o^4}{l_1^4} \right) - \left( 1 - \frac{l_o^2}{l_1^2} \right) \right. \right. \quad (13) \\
& + \log \frac{l_1}{l_o} \Big] + 4 A B l_1 \left[ \frac{1}{5} \left( 1 - \frac{l_o^5}{l_1^5} \right) - \frac{1}{4} \left( 1 - \frac{l_o^4}{l_1^4} \right) \right. \\
& - \frac{1}{3} \left( 1 - \frac{l_o^3}{l_1^3} \right) + \frac{1}{2} \left( 1 - \frac{l_o^2}{l_1^2} \right) \Big] + 4 \beta^2 l_1^2 \left[ \frac{1}{6} \left( 1 - \frac{l_o^6}{l_1^6} \right) \right. \\
& \left. \left. - \frac{2}{5} \left( 1 - \frac{l_o^5}{l_1^5} \right) + \frac{1}{4} \left( 1 - \frac{l_o^4}{l_1^4} \right) \right] \right\}
\end{aligned}$$

Since the assumed functions  $u_1$ ,  $u_2$ , and  $w$  are linear sums in the independent constants  $A$  and  $B$ , the expressions for the maximum kinetic and potential energies become quadratic forms in  $A$  and  $B$ . The Rayleigh-Ritz procedure applied to Hamilton's principle gives

$$\frac{\partial}{\partial A} (T - V) = 0$$

(14)

$$\frac{\partial}{\partial B} (T - V) = 0$$

Introducing the expressions for T and V from equations (10), (12), and (13) into equations (14) and carrying out the differentiation gives:

$$\begin{aligned} \frac{\partial(T - V)}{\partial A} = & \frac{\pi}{2} \rho h \omega^2 \lambda_1^2 \left( \frac{\tan \alpha}{\cos \alpha} \right) \left( 1 + \frac{\cos^2 \alpha}{s^2} \right) \left\{ 2A \frac{1}{6} \left( 1 - \frac{\lambda_0^6}{\lambda_1^6} \right) \right. \\ & - \frac{4}{5} \left( 1 - \frac{\lambda_0^5}{\lambda_1^5} \right) + \frac{3}{2} \left( 1 - \frac{\lambda_0^4}{\lambda_1^4} \right) + \frac{4}{3} \left( 1 - \frac{\lambda_0^3}{\lambda_1^3} \right) \\ & + \frac{1}{2} \left( 1 - \frac{\lambda_0^2}{\lambda_1^2} \right) \left. \right\} + 2B \lambda_1 \frac{1}{7} \left( 1 - \frac{\lambda_0^7}{\lambda_1^7} \right) - \frac{2}{3} \left( 1 - \frac{\lambda_0^6}{\lambda_1^6} \right) \\ & + \frac{6}{5} \left( 1 + \frac{\lambda_0^5}{\lambda_1^5} \right) - \left( 1 - \frac{\lambda_0^4}{\lambda_1^4} \right) + \frac{1}{3} \left( 1 - \frac{\lambda_0^3}{\lambda_1^3} \right) \left. \right\} \\ & - \frac{E h^3 \tan \alpha}{24 (1 - \nu^2)} \pi \cos^3 \alpha \lambda_1^2 \left\{ 2A \left\langle 2 \left( 1 - \frac{\lambda_0^2}{\lambda_1^2} \right) \right. \right. \\ & + \beta^2 \left[ \frac{1}{2} \left( 1 - \frac{\lambda_0^2}{\lambda_1^2} \right) + 6 \log \frac{\lambda_1}{\lambda_0} - 4 \left( 1 - \frac{\lambda_0}{\lambda_1} \right) + 4 \left( 1 - \frac{\lambda_1}{\lambda_0} \right) \right. \right. \\ & - \frac{1}{2} \left( 1 - \frac{\lambda_1^2}{\lambda_0^2} \right) \left. \right] + 4\beta \left[ \frac{1}{2} \left( 1 - \frac{\lambda_0^2}{\lambda_1^2} \right) - 3 \left( 1 - \frac{\lambda_0}{\lambda_1} \right) + 3 \log \frac{\lambda_1}{\lambda_0} \right. \\ & + \left. \left. \left( 1 - \frac{\lambda_1}{\lambda_0} \right) \right] + 2 \left( 1 - \frac{\lambda_0^2}{\lambda_1^2} \right) - 8 \left( 1 - \frac{\lambda_0}{\lambda_1} \right) + 4 \log \frac{\lambda_1}{\lambda_0} \right. \end{aligned}$$

$$\begin{aligned}
& + 2 \gamma \left\{ \beta \left[ \left( 1 - \frac{l_o^2}{l_1^2} \right) - 4 \left( 1 - \frac{l_o}{l_1} \right) + 2 \log \frac{l_o}{l_1} \right] + \left( 1 - \frac{l_o^2}{l_1^2} \right) \right. \\
& - 4 \left( 1 - \frac{l_o}{l_1} \right) \left. \right\} + 2 (1 - \gamma) \sin^2 \alpha \frac{\beta^2}{s^2} \left[ \frac{1}{2} \left( 1 - \frac{l_o^2}{l_1^2} \right) 2 \log \frac{l_1}{l_o} \right. \\
& - \frac{1}{2} \left( 1 - \frac{l_1^2}{l_o^2} \right) \left. \right] \left. \right\} + B l_1 \left\langle 8 \left( 1 - \frac{l_o^3}{l_1^3} \right) - 10 \left( 1 - \frac{l_o^2}{l_1^2} \right) \right. \\
& + \beta^2 \left[ \frac{2}{3} \left( 1 - \frac{l_o^2}{l_1^3} \right) - 4 \left( 1 - \frac{l_o}{l_1} \right) + 12 \left( 1 - \frac{l_o}{l_1} \right) - 8 \log \frac{l_1}{l_o} \right. \\
& - 2 \left( 1 - \frac{l_1}{l_o} \right) \left. \right] + \beta \left[ \frac{10}{3} \left( 1 - \frac{l_o^3}{l_1^3} \right) - 16 \left( 1 - \frac{l_o^2}{l_1^2} \right) + 36 \left( 1 - \frac{l_o}{l_1} \right) \right. \\
& - 16 \log \frac{l_1}{l_o} - 2 \left( 1 - \frac{l_1}{l_o} \right) \left. \right] + 4 \left( 1 - \frac{l_o^3}{l_1^3} \right) - 14 \left( 1 - \frac{l_o^2}{l_1^2} \right) \\
& 20 \left( 1 - \frac{l_o}{l_1} \right) - 4 \log \frac{l_1}{l_o} - 2 \gamma \left\{ \beta \frac{8}{3} \left( 1 - \frac{l_o^3}{l_1^3} \right) - 10 \left( 1 - \frac{l_o^2}{l_1^2} \right) \right. \\
& + 16 \left( 1 - \frac{l_o}{l_1} \right) - 4 \log \frac{l_1}{l_o} \left. \right] + 6 \left( 1 - \frac{l_o^3}{l_1^3} \right) - 14 \left( 1 - \frac{l_o^2}{l_1^2} \right) \\
& + 10 \left( 1 - \frac{l_o}{l_1} \right) \left. \right\} + 2 (1 - \gamma) \sin^2 \alpha \frac{\beta^2}{s^2} \left[ \frac{4}{3} \left( 1 - \frac{l_o^3}{l_1^3} \right) \right.
\end{aligned}$$

$$- 2 \left( 1 - \frac{\lambda_0^2}{\lambda_1^2} \right) - 4 \left( 1 - \frac{\lambda_0}{\lambda_1} \right) + 4 \log \frac{\lambda_1}{\lambda_0} \Big] \gg \gg \gg$$

$$- \frac{E h \pi \tan \alpha \cos^3 \lambda_1^4}{4 (1 + \nu) s^2} \left\{ 2 A \left[ \frac{1}{4} \left( 1 - \frac{\lambda_0^4}{\lambda_1^4} \right) - \left( 1 - \frac{\lambda_0^2}{\lambda_1^2} \right) \right. \right.$$

$$+ \log \frac{\lambda_1}{\lambda_0} \Big] + 4 B \lambda_1 \left[ \frac{1}{5} \left( 1 - \frac{\lambda_0^5}{\lambda_1^5} \right) - \frac{1}{4} \left( 1 - \frac{\lambda_0^4}{\lambda_1^4} \right) \right.$$

$$\left. - \frac{1}{3} \left( 1 - \frac{\lambda_0^3}{\lambda_1^3} \right) + \frac{1}{2} \left( 1 - \frac{\lambda_0^2}{\lambda_1^2} \right) \right] \Big\} = 0 \quad (15)$$

$$\frac{\partial (T - V)}{\partial B} = \frac{\pi}{2} \rho h \omega^2 \lambda_1^6 \left( \frac{\tan \alpha}{\cos \alpha} \right) \left( 1 + \frac{\cos^2 \alpha}{s^2} \right) \left\{ 2 A \lambda_1 \right.$$

$$\left[ \frac{1}{7} \left( 1 - \frac{\lambda_0^7}{\lambda_1^7} \right) - \frac{2}{3} \left( 1 - \frac{\lambda_0^6}{\lambda_1^6} \right) + \frac{6}{5} \left( 1 - \frac{\lambda_0^5}{\lambda_1^5} \right) - \left( 1 - \frac{\lambda_0^4}{\lambda_1^4} \right) \right.$$

$$+ \frac{1}{3} \left( 1 - \frac{\lambda_0^3}{\lambda_1^3} \right) \Big] + 2 B \lambda_1^2 \left[ \frac{1}{8} \left( 1 - \frac{\lambda_0^8}{\lambda_1^8} \right) - \frac{4}{7} \left( 1 - \frac{\lambda_0^7}{\lambda_1^7} \right) \right.$$

$$+ \left( 1 - \frac{\lambda_0^6}{\lambda_1^6} \right) - \frac{4}{5} \left( 1 - \frac{\lambda_0^5}{\lambda_1^5} \right) + \frac{1}{4} \left( 1 - \frac{\lambda_0^4}{\lambda_1^4} \right) \Big] \Big\}$$

$$- \frac{E h^3 \tan \alpha}{24 (1 - \nu^2)} \pi \cos^3 \alpha \lambda_1^2 \left\langle \left\langle A \lambda_1 \left\langle 8 \left( 1 - \frac{\lambda_0^3}{\lambda_1^3} \right) \right. \right. \right.$$

$$\begin{aligned}
& - 8 \left( 1 - \frac{\lambda_0^2}{\lambda_1^2} \right) + \beta^2 \left[ \frac{2}{3} \left( 1 - \frac{\lambda_0^3}{\lambda_1^3} \right) - 4 \left( 1 - \frac{\lambda_0^2}{\lambda_1^2} \right) \right. \\
& + 12 \left( 1 - \frac{\lambda_0}{\lambda_1} \right) - 8 \log \frac{\lambda_1}{\lambda_0} - 2 \left( 1 - \frac{\lambda_1}{\lambda_0} \right) \left. \right] + \beta \left[ \frac{10}{3} \left( 1 - \frac{\lambda_0^3}{\lambda_1^3} \right) \right. \\
& - 16 \left( 1 - \frac{\lambda_0^2}{\lambda_1^2} \right) + 36 \left( 1 - \frac{\lambda_0}{\lambda_1} \right) - 16 \log \frac{\lambda_1}{\lambda_0} - 2 \left( 1 - \frac{\lambda_1}{\lambda_0} \right) \left. \right] \\
& + 4 \left( 1 - \frac{\lambda_0^3}{\lambda_1^3} \right) - 4 \left( 1 - \frac{\lambda_0^2}{\lambda_1^2} \right) + 20 \left( 1 - \frac{\lambda_0}{\lambda_1} \right) - 4 \log \frac{\lambda_1}{\lambda_0} \\
& + 2\gamma \left\{ \beta \left[ \frac{8}{3} \left( 1 - \frac{\lambda_0^3}{\lambda_1^3} \right) - 10 \left( 1 - \frac{\lambda_0^2}{\lambda_1^2} \right) + 16 \left( 1 - \frac{\lambda_0}{\lambda_1} \right) \right. \right. \\
& \left. \left. - 4 \log \frac{\lambda_1}{\lambda_0} \right] + 6 \left( 1 - \frac{\lambda_0^3}{\lambda_1^3} \right) - 14 \left( 1 - \frac{\lambda_0^2}{\lambda_1^2} \right) + 10 \left( 1 - \frac{\lambda_0}{\lambda_1} \right) \right. \\
& \left. + 2 (1 - \gamma) \sin^2 \alpha \frac{\beta^2}{s^2} \left[ \frac{4}{3} \left( 1 - \frac{\lambda_0^3}{\lambda_1^3} \right) - 2 \left( 1 - \frac{\lambda_0^2}{\lambda_1^2} \right) \right. \right. \\
& \left. \left. - 4 \left( 1 - \frac{\lambda_0}{\lambda_1} \right) + 4 \log \frac{\lambda_1}{\lambda_0} \right] \right\} + 2\theta \lambda_1^2 \left\langle 9 \left( 1 - \frac{\lambda_0^4}{\lambda_1^4} \right) \right. \\
& \left. - 16 \left( 1 - \frac{\lambda_0^3}{\lambda_1^3} \right) + 8 \left( 1 - \frac{\lambda_0^2}{\lambda_1^2} \right) + \beta^2 \left[ \frac{1}{4} \left( 1 - \frac{\lambda_0^4}{\lambda_1^4} \right) \right. \right.
\end{aligned}$$

$$\begin{aligned}
& -\frac{4}{3} \left( 1 - \frac{\lambda_0^3}{\lambda_1^3} \right) + 3 \left( 1 - \frac{\lambda_0^2}{\lambda_1^2} \right) - 4 \left( 1 - \frac{\lambda_0}{\lambda_1} \right) + \log \frac{\lambda_1}{\lambda_0} \Big] \\
& + 2\beta \left[ \frac{3}{4} \left( 1 - \frac{\lambda_0^4}{\lambda_1^4} \right) - \frac{10}{3} \left( 1 - \frac{\lambda_0^3}{\lambda_1^3} \right) + 6 \left( 1 - \frac{\lambda_0^2}{\lambda_1^2} \right) \right. \\
& \left. - 6 \left( 1 - \frac{\lambda_0}{\lambda_1} \right) + \log \frac{\lambda_1}{\lambda_0} \right] + \frac{9}{4} \left( 1 - \frac{\lambda_0^4}{\lambda_1^4} \right) - 8 \left( 1 - \frac{\lambda_0^3}{\lambda_1^3} \right) \\
& + 11 \left( 1 - \frac{\lambda_0^2}{\lambda_1^2} \right) - 8 \left( 1 - \frac{\lambda_0}{\lambda_1} \right) + \log \frac{\lambda_1}{\lambda_0} + 2\gamma \left\{ \beta \left[ \frac{3}{2} \left( 1 - \frac{\lambda_0^4}{\lambda_1^4} \right) \right. \right. \\
& \left. \left. - \frac{16}{3} \left( 1 - \frac{\lambda_0^3}{\lambda_1^3} \right) + 7 \left( 1 - \frac{\lambda_0^2}{\lambda_1^2} \right) - 4 \left( 1 - \frac{\lambda_0}{\lambda_1} \right) \right] + \frac{9}{2} \left( 1 - \frac{\lambda_0^4}{\lambda_1^4} \right) \right. \\
& \left. \left. - 12 \left( 1 - \frac{\lambda_0^3}{\lambda_1^3} \right) + 11 \left( 1 - \frac{\lambda_0^2}{\lambda_1^2} \right) - 4 \left( 1 - \frac{\lambda_0}{\lambda_1} \right) \right\} \right. \\
& + 2(1-\gamma) \sin^2 \alpha \frac{\beta^2}{s^2} \left[ 2 \left( 1 - \frac{\lambda_0^2}{\lambda_1^2} \right) - \frac{8}{3} \left( 1 - \frac{\lambda_0^3}{\lambda_1^3} \right) \right. \\
& \left. + \left( 1 - \frac{\lambda_0^4}{\lambda_1^4} \right) \right] \gg \gg \gg - \frac{E h \pi \tan \alpha \cos^3 \alpha}{4(1+\gamma) s^2} \lambda_1^4 \left( 4 A \lambda_1 \left[ \frac{1}{5} \left( 1 - \frac{\lambda_0^5}{\lambda_1^5} \right) \right. \right.
\end{aligned}$$

$$\begin{aligned}
& -\frac{1}{4} \left(1 - \frac{\lambda_0^4}{\lambda_1^4}\right) - \frac{1}{3} \left(1 - \frac{\lambda_0^3}{\lambda_1^3}\right) + \frac{1}{2} \left(1 - \frac{\lambda_0^2}{\lambda_1^2}\right) \\
& + 8B \lambda_1^2 \left[ \frac{1}{6} \left(1 - \frac{\lambda_0^6}{\lambda_1^6}\right) - \frac{2}{5} \left(1 - \frac{\lambda_0^5}{\lambda_1^5}\right) + \frac{1}{4} \left(1 - \frac{\lambda_0^4}{\lambda_1^4}\right) \right] \Bigg\} = 0
\end{aligned}
\tag{16}$$

The two linear homogeneous algebraic equations (15) and (16) may be solved simultaneously for the square of the resonant frequency,  $\omega^2$ .

$$\begin{aligned}
\lambda_0 &= 21.666 \\
\lambda_1 &= 34.666 \\
\alpha &= \tan^{-1} (.115) \\
\rho &= 7.61 \times 10^{-4} \\
E &= 20 \times 10^6 \\
\nu &= .29
\end{aligned}$$

Substituting the above numerical values into equations (15) and (16) gives:

$$\begin{aligned}
\frac{d(T - V)}{dA} &= [A] \left[ 4.93633 \times 10^2 (h \omega^2) \left( \frac{.986 - s^2}{.013} \right) \right. \\
&\quad \left. - (h^3) \left\langle 8.93044 \times 10^8 - 9.97709 \times 10^6 \left( \frac{.986 - s^2}{.013} \right) \right. \right. \\
&\quad \left. \left. + 3.62061 \times 10^6 \left( \frac{.986 - s^2}{.013} \right) + 2.06560 \times 10^6 \left( \frac{.986 - s^2}{s^2} \right)^2 \right. \right]
\end{aligned}$$

$$\begin{aligned}
& - 2.87160 \times 10^{11} \left( \frac{h}{s^2} \right) \Big] + \Big[ B \Big] \Big[ 11.57618 \times 10^3 (h \omega^2) \left( \frac{.986 - s^2}{.013} \right) \\
& - (h^3) \left\langle 1.53066 \times 10^{10} - 3.49983 \times 10^8 \left( \frac{.986 - s^2}{.013} \right) \right. \\
& + 8.60880 \times 10^7 \left( \frac{.986 - s^2}{.013} \right) + 4.18490 \times 10^7 \left( \frac{.986 - s^2}{.013} \right)^2 \Big\rangle \\
& - 5.98823 \times 10^{12} \left( \frac{h}{s^2} \right) \Big] = 0 \tag{17}
\end{aligned}$$

$$\begin{aligned}
\frac{\partial (T - V)}{\partial B} &= \Big[ A \Big] \Big[ 11.57618 \times 10^3 (h \omega^2) \left( \frac{.986 - s^2}{.013} \right) \\
& - (h^3) \left\langle 1.53067 \times 10^{10} - 3.49983 \times 10^8 \left( \frac{.986 - s^2}{.013} \right) \right. \\
& - 8.60880 \times 10^7 \left( \frac{.986 - s^2}{.013} \right)^2 + 4.18490 \times 10^7 \left( \frac{.986 - s^2}{.013} \right)^2 \Big\rangle \\
& - 5.98823 \times 10^{12} \left( \frac{h}{s^2} \right) \Big] + \Big[ B \Big] \Big[ 2.96673 \times 10^5 (h \omega^2) \left( \frac{.986 - s^2}{.013} \right) \\
& - (h^3) \left\langle 3.80788 \times 10^{11} - 1.14657 \times 10^{10} \left( \frac{.986 - s^2}{.013} \right) \right. \\
& + 1.9993 \times 10^9 \left( \frac{.986 - s^2}{.013} \right)^2 + 8.64814 \frac{1}{s^2} \left( \frac{.986 - s^2}{.013} \right)^2 \Big\rangle \\
& - 1.28199 \times 10^{14} \left( \frac{h}{s^2} \right) \Big] = 0 \tag{18}
\end{aligned}$$



Substituting values of  $S$  and  $h$  into equations (17) and (18) and setting the determinant of the equation equal to zero will yield the equations which may be solved for the resonant frequencies,  $\omega$ . Thus, in order to obtain a preliminary estimate of the resonant frequencies of a conical shell, an analysis based on the vibration of a thin walled cylindrical shell was made

The resonant frequencies of a conical shell having a small semi-vertical angle and a small length-to-radius ratio differ only slightly from the resonant frequencies of a cylindrical shell whose diameter is equal to the mean diameter of the conical shell. A freely supported cylinder is considered where the ends are forced to remain circular. The slope in the axial direction is not constrained to be zero as it is in the case of a fixed end.

The end condition at the large end of the aberrascop conical shell structure will be somewhere between a fixed end and freely supported end condition, since the fastening between the aberrascop cylindrical structure and the conical structure will not be completely rigid. The end condition at the small end of the conical structure will depend upon whether or not a stiffening flange or ring is used at the end of the shell. If a stiffening ring is used, the end condition will be between that of a fixed end and a freely supported end. If a stiffening flange or ring is not used, the small end of the conical structure will be a free end. Thus, the end conditions taken for the mean diameter cylindrical shell will not correspond exactly to the end conditions of the conical shell in either case.

In the case of a stiffening flange or ring at the small end of the conical shell, the assumed end conditions are conservative. If the small end of the conical shell is not stiffened, the actual vibration frequencies will probably be lower than those calculated for a mean diameter cylinder. However, the frequencies obtained from consideration of a mean diameter cylindrical shell with freely supported ends should give satisfactory approximations to actual conical shell frequencies to serve as a guide for the selection of conical shell design parameters for more exact analysis.

The equations used in the calculation of resonant frequencies of the mean diameter cylindrical shell are:

$$f = \frac{1}{2\pi A} \sqrt{\frac{Eg}{\rho(1-\nu^2)}} \sqrt{\Delta} \quad (1)$$

$f$  = frequency - cycles per second

$a$  = mean radius of cylinder

$\rho$  = density of cylinder material

$E$  = modulus of elasticity

$\nu$  = Poisson's ratio

$\Delta$  = frequency factor obtained from Figures 4, 5, 6, and 7 of reference paper.

$$\lambda = \frac{\text{mean circumference}}{\text{axial wavelength}} = \frac{m\pi a}{l} \quad (2)$$

$m$  = number of axial half-waves

$l$  = length of cylinder

$\alpha' = \frac{\text{thickness}}{\text{mean radius}} = \frac{t}{a}$

$t$  = thickness of cylinder wall

The calculation of resonant frequencies was effected for a cylinder fabricated of Invar. The significant parameters of the material and dimensions of the cylinder are listed below.

$$E = 20 \times 10^6$$

$$\rho = .294$$

$$a = 3.25$$

$$g = 386.4$$

$$t = .05, .10, .15, .20, .25$$

$$l = 13$$

Table IX

t	.05	.1	.15	.20	.25
$\alpha$	.015	.031	.046	.062	.077

Table X

m	1	2	3	4	5
$\lambda$	.785	1.57	2.36	3.14	3.93

Calculations were carried out for  $n = 2, 3, 4, 5$  and  $m = 0.1$ . Larger values of  $n$  and  $m$  would give frequencies which are too high to require consideration.

The results of the calculations are shown in Table XI and Figures 48 and 49. Only those frequencies at integral values of  $n$  in Figures 48 and 49 have any significance. The dotted curves merely interconnect points corresponding to the same shell thickness. From Table XI, the lowest natural frequency is seen to be  $10^3$  cps, which is comparable to the motor

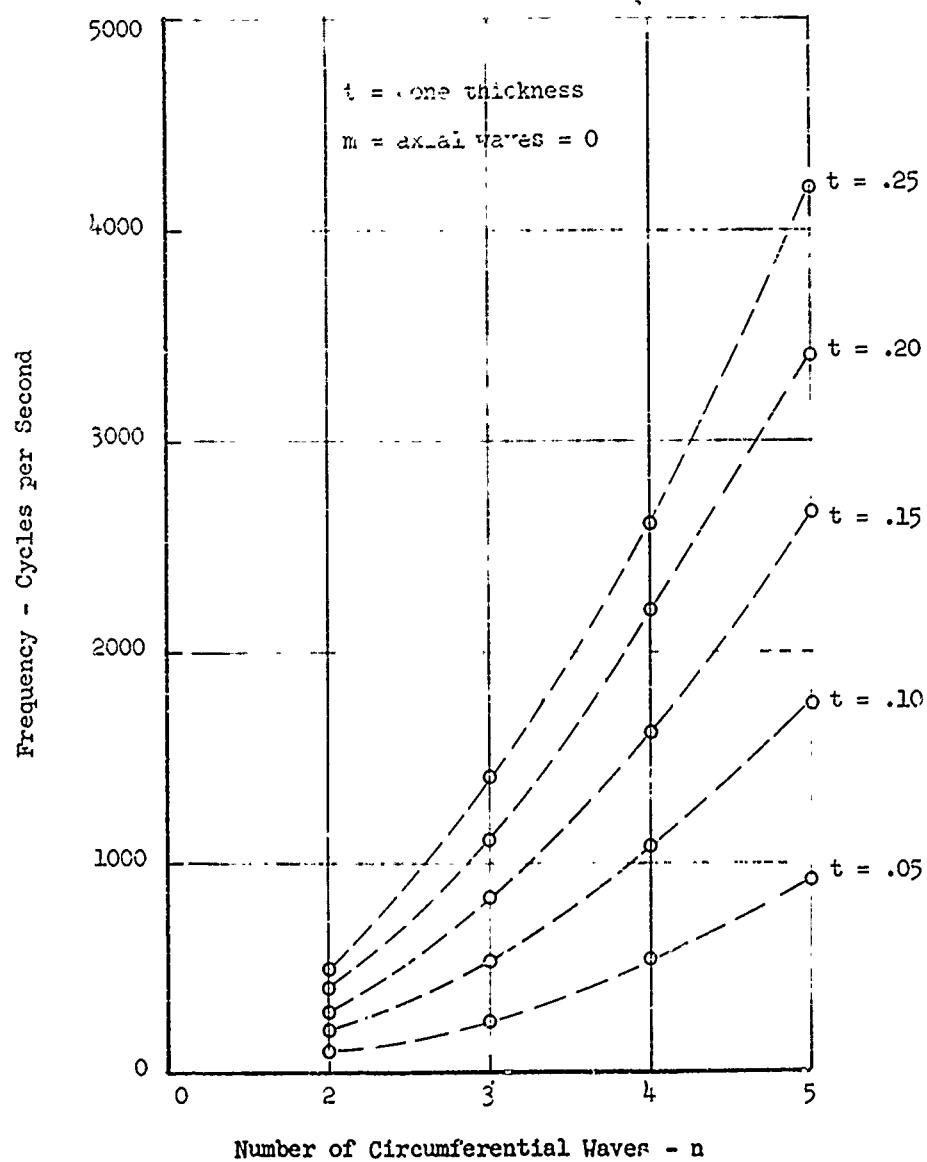


Figure 48

FREQUENCY OF VIBRATION WITH NO AXIAL WAVES

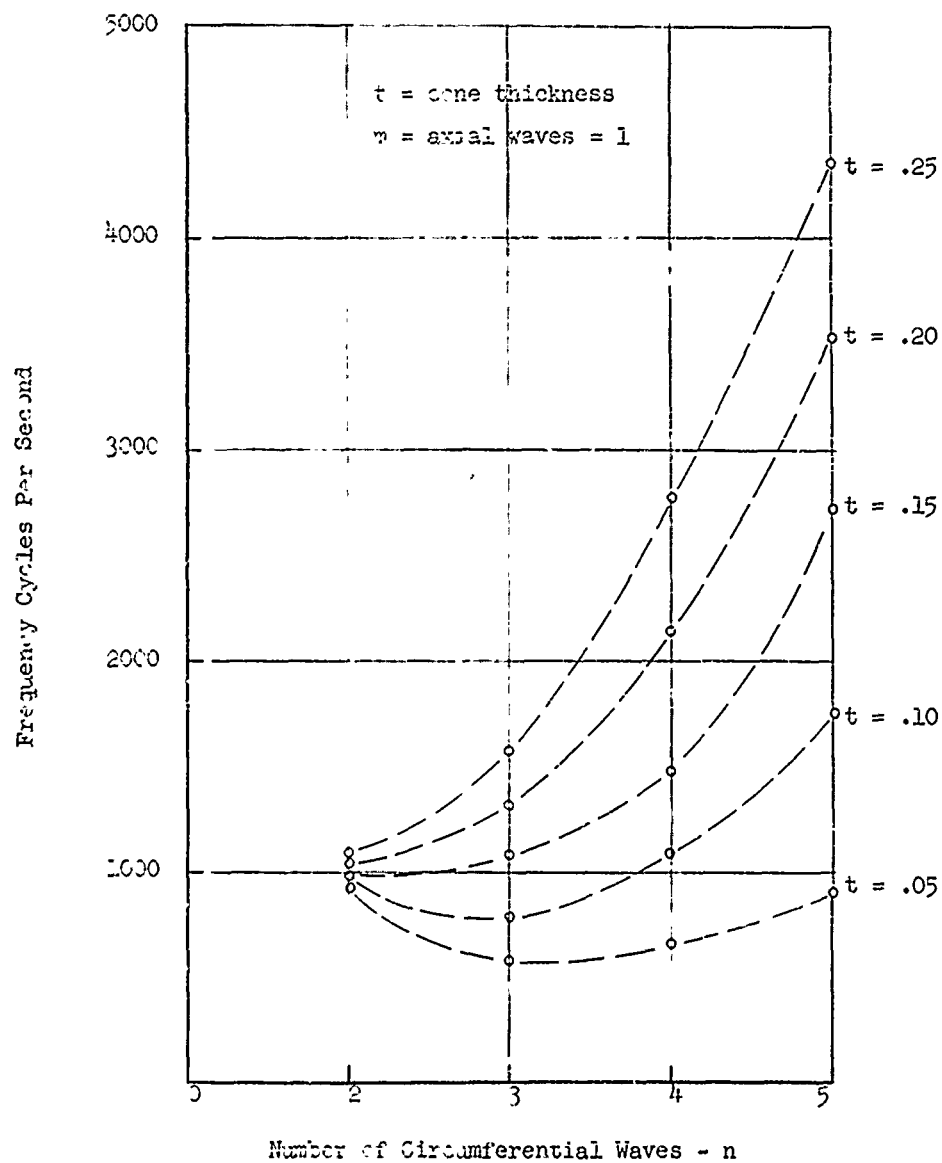


Figure 49  
Frequency of Vibration with One Axial Wave

Table XI

Frequency - cps										
$\frac{\alpha}{n/m}$	.015		.031		.046		.061		.077	
	0	1	0	1	0	1	0	1	0	1
2	108	930	207	955	291	971	408	1038	498	1087
3	249	581	540	789	830	1079	1120	1311	1411	1577
4	540	644	1079	1080	1619	1494	2199	2130	2615	2781
5	912	913	1743	1743	2656	2739	3403	3528	4192	4358

speed of a rotating aberrascope. If the motor rotor is properly balanced, the vibrational energy which is induced into the structure can be kept to a minimum below a value which might be detrimental to the operation of the instrument. Frequencies of vibration other than the fundamental are much higher than any energy source and thus will not pose a problem.

### (3) Torsional Vibrations

Although the aberrascope structure may have torsional vibration modes about its axis of rotation, it is not likely that this type of vibration will cause any difficulty. The frequencies of the torsional modes of vibration will be high and it is unlikely that there will be disturbing forces in the aberrascope or satellite of the type required to excite these modes of vibration. No detailed analysis was made of the torsional vibration behavior of the aberrascope structure. However, in order to obtain an estimate of the order of magnitude of the lowest torsional resonant frequency, a calculation based on the equation for the resonant frequency of a cylindrical tube fixed at one end and built in at

the other was made. A value of 1,985 cps was obtained. This indicates that the lowest resonant frequency of torsional vibration is high enough so that it will not be excited in the satellite environment.

f. Thermal Effects

Some discussion of structural deflections due to thermal effects was presented in the quarterly report of September 15, 1960. No further work has been done on this problem.

g. Gyroscopic Torque

During satellite maneuvers, gyroscopic torques can be generated by a rotating aberrascope structure. These torques could cause deflections of the aberrascope structure or difficulty in satellite attitude control. The magnitude of the gyroscopic torque is given by the equation:

$$T = I_A \omega_A \omega_S$$

where:

$I$  = moment of inertia of rotating aberrascope about its axis of rotation

$\omega_a$  = aberrascope angular velocity

$\omega_s$  = component of satellite angular velocity about an axis perpendicular to the aberrascope axis of rotation

$$I_A = \frac{1}{2} m_{cyl.} \left[ R_o^2 + (R_c - t)^2 \right] + \left\{ \frac{3m_c (R_o^5 - R_a^5)}{10 (R_o^3 - R_a^3)} - \frac{3m_l [(R_o - t)^5 - (R_c - t)^5]}{10 [(R_o - t)^3 - (R_c - t)^3]} \right\}$$

Values of  $I_a$  corresponding to several different combinations of cylinder and cone wall thickness are shown in Figure 50. Using these values of  $I_a$  and  $\omega_a$  equal 90 revolutions per minute, gyroscopic torques

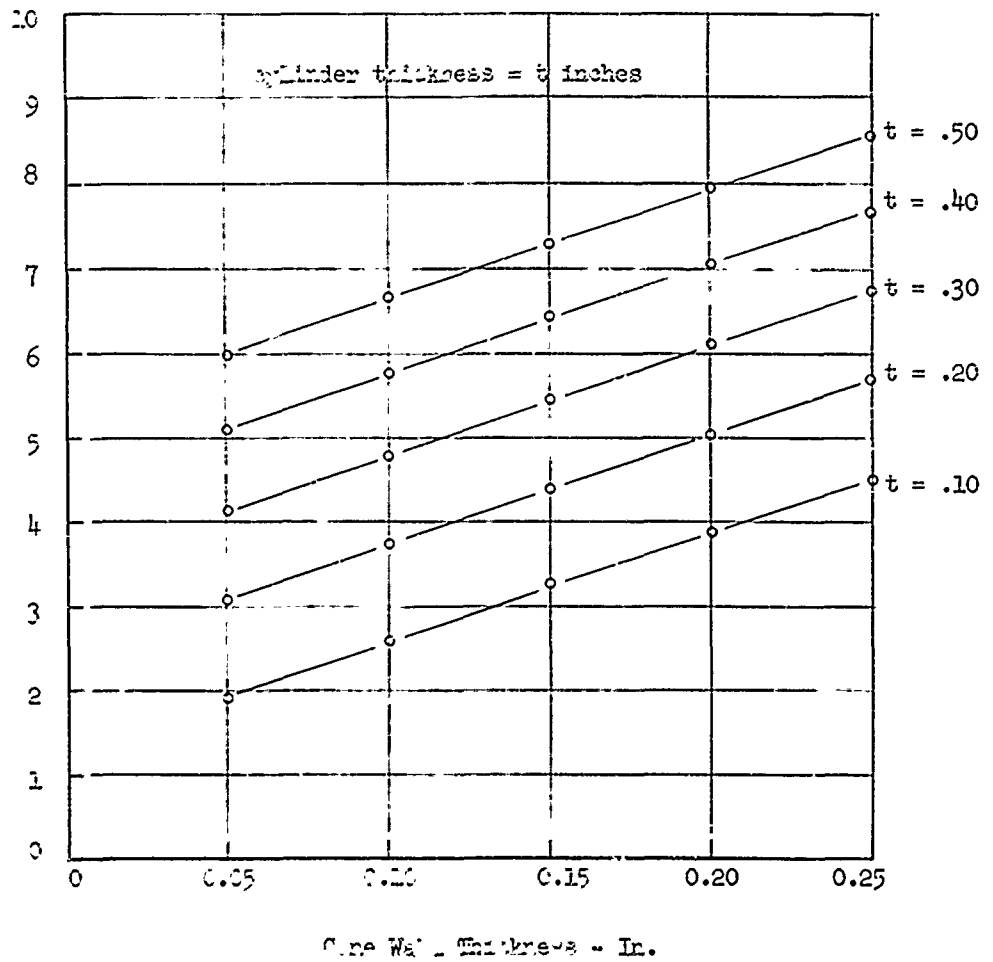


Figure 50 \*

MASS MOMENT OF INERTIA ABOUT AXIS  
OF ROTATION FOR ABERRASCOPE



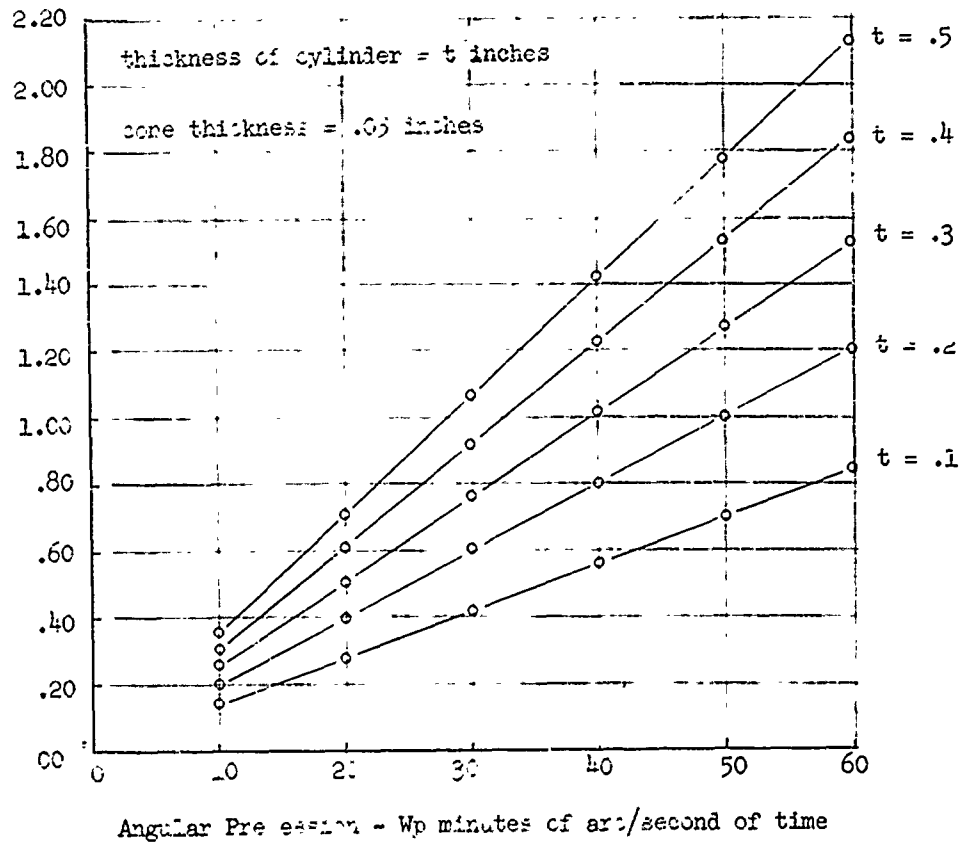


Figure 51  
 GYROSCOPIC REACTION TORQUES  
 ABERFASCOPE CONFIGURATION

for values of  $\omega_s$  from 10 to 60 minutes of arc per second where calculated. The torque magnitudes obtained are plotted in Figure 51. To minimize gyroscopic torque effects, structure wall thicknesses should be kept as thin as possible consistent with structural requirements.

#### h. Summary and Conclusions

For purposes of analysis, a structure consisting of a cylindrical section and two conical sections was assumed for the aberrascope. It is believed that this assumed structure is a good model of the most practical design for an actual aberrascope structure. Analysis of the response of the structure to static and dynamic loading for several different wall thicknesses of both the cylindrical and conical sections was made.

From consideration of static deflections, cantilever beam vibration, and torsion vibration, the wall thickness variations of the conical sections over the range of values considered were not significant. The analysis indicated that conical sections with a .050 inch wall thickness would meet the structural requirements relative to static loads with substantial factors of safety. A wall thickness of .2 inches for the cylindrical section should meet the static load structural requirements. From the point of view of minimizing weight and gyroscope torques the walls of both the cylindrical and conical sections should be made as thin as is compatible with other structural requirements. Practical limitations on wall thickness reduction are set by consideration of thin shell vibration support of concentrated loads and mounting attachments, and in the case of the cylindrical section, support of the main bearing. The thickness of .05 inches and .2 inches for the conical and cylindrical sections would

give a total structural weight of about 15 pounds. These wall thicknesses should also give sufficient structural strength to meet requirements of the main bearing support, and support of concentrated loads and mounting attachments. Although the thin shell vibration frequencies for the conical sections have not been evaluated, approximate calculations based on cylindrical tubes whose radius was equal to the mean radius of the conical sections gave a lowest resonant frequency of about 110 cps for a wall thickness of .05 inches. This frequency is probably higher than the frequency of any disturbing force to which the aberrascopes would be subjected in actual operation.

In general, the analysis indicates that an aberrascopes structure of reasonable weight will have sufficient rigidity to maintain required instrument alignment requirements when subjected to the mechanical disturbing forces which are likely to be encountered in operation. A more detailed investigation of thermal effects should be made, since these may present more serious problems than the mechanical disturbing forces, particularly for an aberrascopes whose structure does not rotate. The strength and rigidity of the structure analyzed will be substantially improved with only a slight increase in weight by use of stiffening ribs and flanges. In actual design, flanges are necessary for interconnecting the structural components. Thus, we are assured of a structure which will be completely adequate for the requirements of either a rotating or non-rotating aberrascopes.

## 2. Detail Design

On the basis of the structural analysis given above, a preliminary design of the optical system has been made and is shown in Figure 52. The mechanical structure is shown to consist of three castings, two of which will house mirrors and the third is the central housing. The primary cell will mount the primary mirror, the principle light baffle and will also provide a means of attaching the optical system to the balance of the aberrascopes. The primary mirror must of course be polished on its outside diameter to minimize the possibility of cracking during assembly. The primary mirror will be seated against a flange in the primary cell; however, the mirror will contact the flange only at three points. At these points, a film of aluminum between .003 - .005 inches thick will separate the mirror from the flange. On the back side of the mirror, the restraint will be at three points so that the force applied to the back of the mirror is directly opposite to the support points on the front. By this means, no bending torques will be applied to the mirror.

The secondary mirror will be mounted in its housing by the same principle as the primary mirror. A spacer is shown between the secondary mirror face and the housing flange. The purpose of this spacer is to allow for adjustment of position of the secondary with respect to the primary. The final stipulation on the position of the focal plane is that it be located appropriately with respect to the optical system mounting flange. In order to hold the dimension from the focal plane to the mounting flange to a tolerance of  $\pm 0.005$  inches, the position of the secondary mirror must be adjusted. This adjustment can be effected by changing the length of the spacer in front of the secondary and by adding (or subtracting) an appropriate spacer on the back side of the secondary mirror.

The design of the secondary cell is such that the collinearity requirements between the secondary mirror mounting flange and the cell mounting face can be met. By mounting the secondary cell to the central housing on a flat face, a minimum of distortion occurs when the fasteners are secured in place.

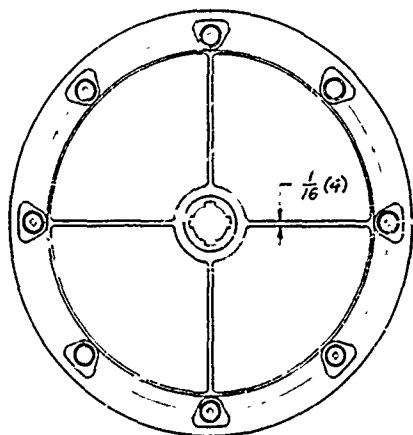
The central housing is simply a conical shell which constitutes the major portion of the optical system housing. The material which will be used for this housing as well as the mirror cell housings is Invar. For the first prototype model, GMI recommends the use of commercial Invar and Vycor brand glass #7909 (Corning Glass Works). These materials have closely matched coefficients of expansion, however the coefficients are larger than the coefficient of expansion of fused silica. In the quarterly report,<sup>26</sup> GMI recommended the use of fused silica for the mirrors and a low expansion alloy (IA-685 produced by the General Communications Company) for the structure. This low expansion alloy is presently being experimented to demonstrate its castability. Should casting prove feasible, the combination of IA-685 and fused silica will be used in future instruments. For the present, commercial Invar and Vycor glass will meet the instrument requirements, since the extreme environmental problems will not be encountered in the first prototype.

GMI is not attempting to perform any lens design on the optical system; however, the basic parameters have been worked out and this information will in turn be supplied to the people from whom GMI will purchase the optics. The mechanical components of the optical system will be fabricated "in house" and furnished to the optical supplier who must finally mount the over-all optical system specification.

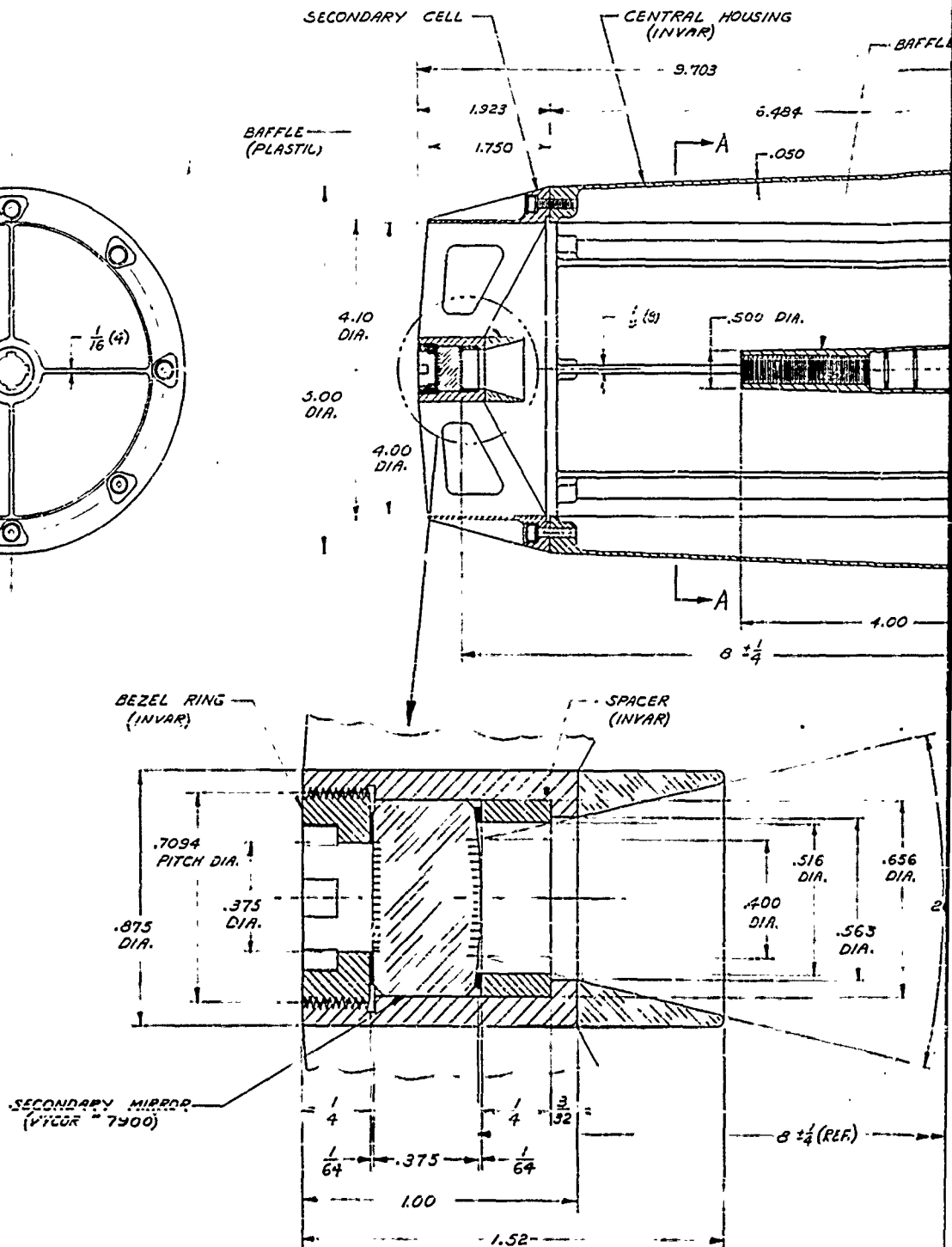
The type of optical system will be a variant from the true Casagrain in that a spherical secondary will be used. This is known as a Dahl-Kirkham

system. The effective focal length will be 100 inches  $\pm$  4 inches with an aperture of 4 inches. This is essentially an  $f/25$  optical system. The system tolerances which have been established are the following: tolerance on the distance from the focal plane to the mounting face of the optical system will be  $\pm$  0.005 inches; the diameter of the blur circle at the focal plane containing 60% of the energy will be 0.0025 inches; and the location of the focal point from the optical axis in the focal plane will be  $\pm$  0.010 inches. The requirement for a plane mirror surface on the back side of the secondary mirror is for the purpose of alignment in test of the complete aberrascopes: to align the optical axis of the aberrascopes with the collimators which will simulate stars.

The optical system design is such that it can be completely dissociated from the balance of the aberrascopes; i.e., no electrical connections are required in this unit. The two optical systems required for one aberrascopes will be identical. The problem of designing the aberrascopes to track a pair of stars which are not exactly diametrically opposed can be solved by designing a pair of wedge-shaped spacers. These spacers will be inserted between the optical system mounting flange and the central portion of the aberrascopes which houses the error detector and the electronics. With the use of these wedge-shaped spacers, the optical systems can be interchangeable and also, only the spacers need be changed if the star selection need be changed before the design is completed. The machining requirements with this type of design are thus relaxed and the tilt between optical systems can be introduced with spacers, not with complicated machining of the basic structure.



1



SCALE: 4=1

ALL FASTENERS TO BE #302 STAINLESS STEEL

Sheet Title PTH 304	NEEDS DETERMINING SPECIFIED DIMENSIONS ARE IN INCHES TOLERANCES FRACTIONS DECIMAL ANGLES RADI	ORIGINAL DATE OF DRAWING BY B DAIN CHK CRR 10-26-60 ENGR CMM/SLM APPD	NAME OPTICAL SYSTEM FOR ABERRASCOPE	General Mills, Inc MECHANICAL DIVISION 1401 CENTRAL AVENUE MINNEAPOLIS, MINNESOTA
DESCRIPTION	HEAT TREATMENT		Figure 32 SCALE FULL 1:1	DWG NO DWG SIZE D SK-16499-00



### C. Rotating Error Detector

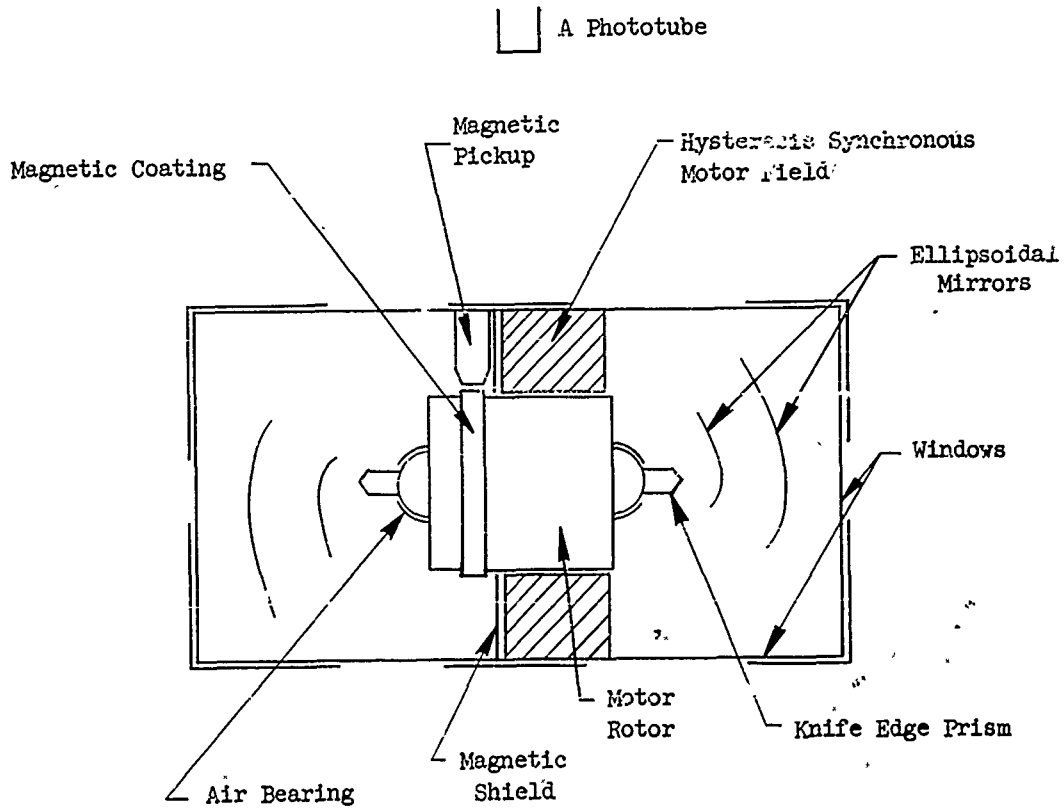
The rotating error detector measures the pointing errors of the two Cassagrainian optical systems. The electronics which is most immediately associated with the error detector yields the pointing error in polar coordinates, and additional electronics converts the polar error signal to cartesian coordinates. The cartesian coordinate error signals are used to position the respective optical systems, tending to reduce the pointing errors to zero.

#### 1. Principles of Operation

Light from the Cassagrainian optical systems falls upon the rotating knife edge prisms which are driven by a hysteresis motor. See Figure 53. The reflected beams from the two surfaces of each prism fall upon ellipsoidal mirrors, and are reflected from the surfaces of these mirrors into phototubes. The surfaces of the inner ellipsoidal mirrors (those closest to the prisms) are silvered in serrated bands, so that the light beams are optically switched alternately into one phototube and then the other as the prisms are rotated. The electrical signals developed by the phototubes are then combined with electronic logic to produce the error signals.

#### 2. Optical System

The inner ellipsoidal mirrors are silvered in serrated bands as shown in Figure 54. Light reflected onto these mirrors by the rotating knife edge prism will pass through the mirrors at the clear areas and will be reflected at the silvered areas. The two inner mirrors are identical in



□ B Phototube

Figure 53

SIMPLIFIED DIAGRAM OF ERROR DETECTOR

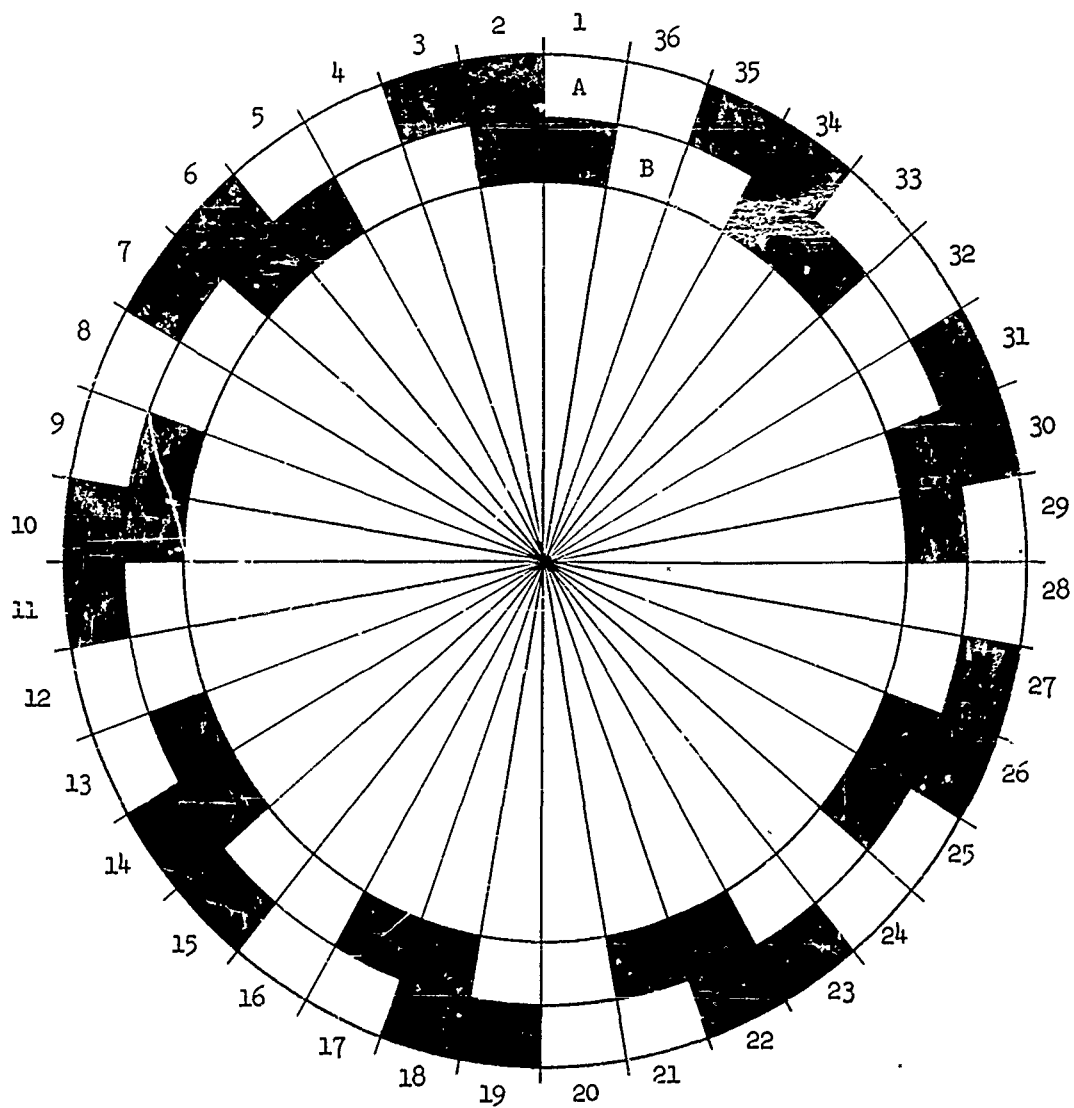


Figure 54

SILVERED MIRROR PATTERNS

shape and are silvered identically with the exception that the serrated band on one mirror is rotated 10 degrees in relation to the other. The relationship is shown in Figure 54. This figure erroneously shows the silvered bands of the two mirrors as being concentric in order to illustrate the phase relationship between them.

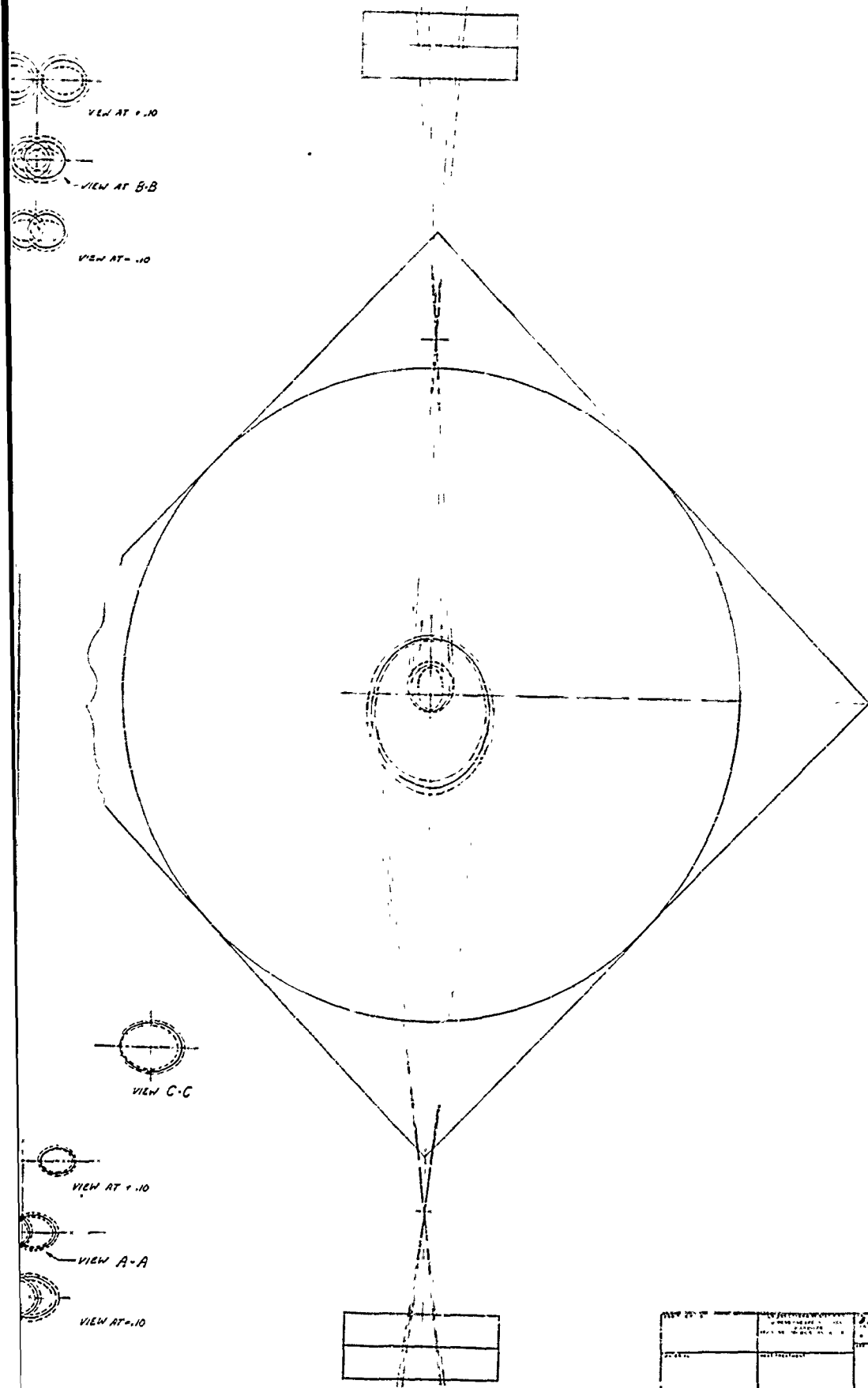
Light which is reflected from the silvered surfaces of the inner mirrors is reflected directly into one phototube. Light which passes through the clear areas of the inner mirrors falls upon the wholly silvered outer mirrors, and is reflected into the other phototube by another optical path.

As the prism rotates, four sequential optical situations exist. These are illustrated in Figure 55. The situation changes for each 10 degrees of rotation of the prism, so the sequence is repeated nine times for each revolution of the prism. The entire sequence for one revolution is given in Table XII.

### 3. Mechanical Configuration

The error detector is contained in a cylindrical housing with square end caps. Windows are provided at the center of each end cap of the housing to permit entry of light from the Cassagrainian optical systems into the detector housing. Windows along the sides of the detector housing pass light from the ellipsoidal mirrors to the phototubes. Each of the windows must be high quality plane-parallel with minimum wedge angle. The field of the hysteresis synchronous motor fits inside the cylindrical housing, and the rotor is suspended at each end with an air bearing. The reason for selecting air bearings is to avoid the possibility of oil fogging the optical surfaces, and to avoid mechanical noise. Figure 55c shows the optical lay out in greater detail.





2

VIEW AT F-F	VIEW AT G-G	VIEW AT H-H	VIEW AT I-I	VIEW AT J-J	VIEW AT K-K	VIEW AT L-L	VIEW AT M-M	VIEW AT N-N	VIEW AT O-O	VIEW AT P-P	VIEW AT Q-Q	VIEW AT R-R	VIEW AT S-S	VIEW AT T-T	VIEW AT U-U	VIEW AT V-V	VIEW AT W-W	VIEW AT X-X	VIEW AT Y-Y	VIEW AT Z-Z
OPTICAL DIAGRAM - ROTATING AIR DETECTOR Figure 55										General Notes: 1. SEE DRAWING FOR DIMENSIONS, TOLERANCES AND FINISHES. 2. SEE DRAWING FOR MATERIALS. 3. SEE DRAWING FOR TREATMENTS. 4. SEE DRAWING FOR ASSEMBLY. 5. SEE DRAWING FOR TESTING. 6. SEE DRAWING FOR INSPECTION. 7. SEE DRAWING FOR PACKAGING. 8. SEE DRAWING FOR STORAGE. 9. SEE DRAWING FOR HANDLING. 10. SEE DRAWING FOR MAINTENANCE. 11. SEE DRAWING FOR REPAIRS. 12. SEE DRAWING FOR REPLACEMENTS. 13. SEE DRAWING FOR MODIFICATIONS. 14. SEE DRAWING FOR UPGRADES. 15. SEE DRAWING FOR DECOMMISSIONING. 16. SEE DRAWING FOR DISPOSAL. 17. SEE DRAWING FOR SAFETY. 18. SEE DRAWING FOR ENVIRONMENTAL PROTECTION. 19. SEE DRAWING FOR RECORDS. 20. SEE DRAWING FOR TRAINING. 21. SEE DRAWING FOR SUPPORT. 22. SEE DRAWING FOR LOGISTICS. 23. SEE DRAWING FOR COMMUNICATIONS. 24. SEE DRAWING FOR INFORMATION. 25. SEE DRAWING FOR SECURITY. 26. SEE DRAWING FOR COMPLIANCE. 27. SEE DRAWING FOR QUALITY. 28. SEE DRAWING FOR COST. 29. SEE DRAWING FOR RISK. 30. SEE DRAWING FOR SUSTAINABILITY.										

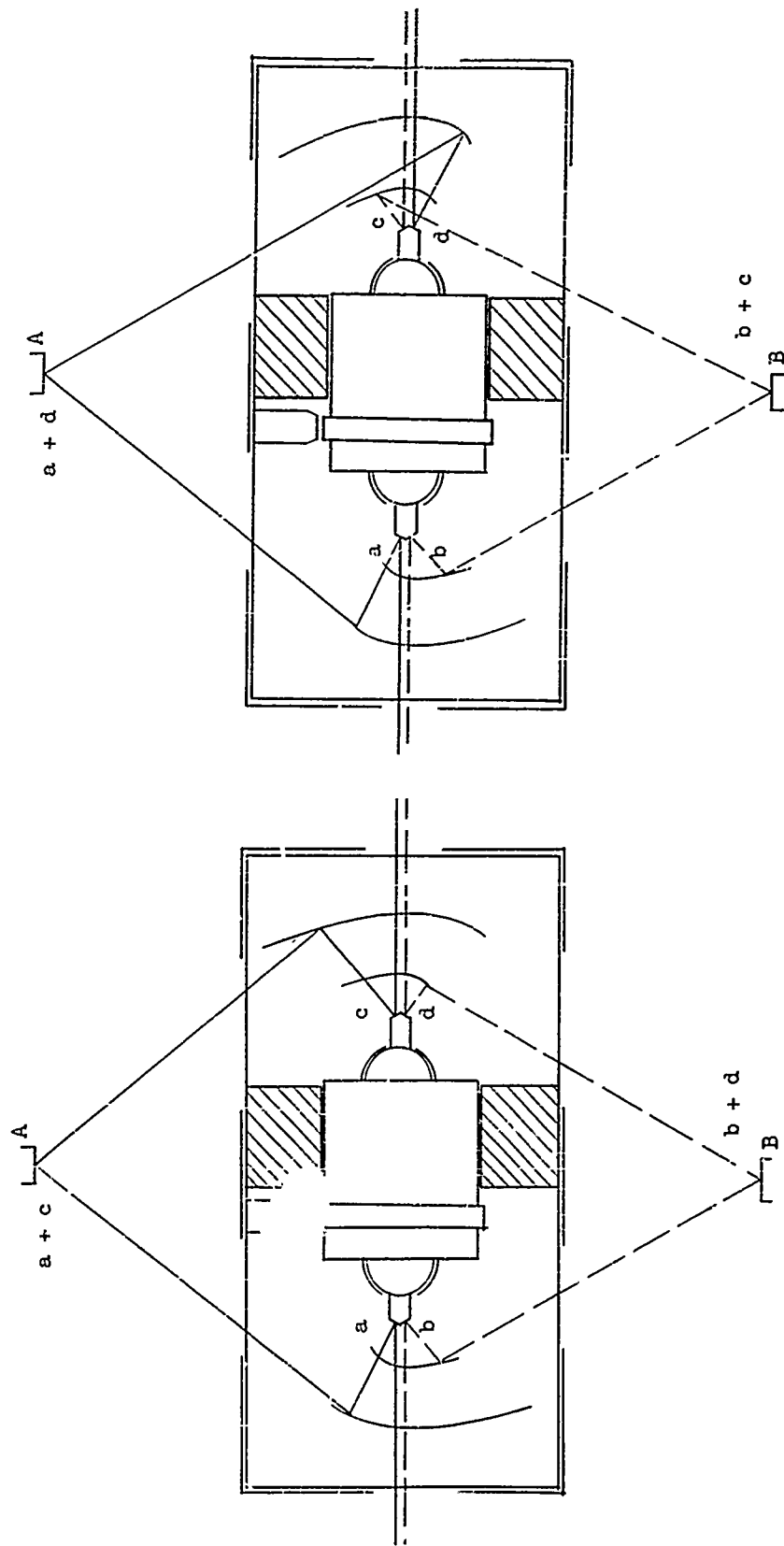


Figure 55a  
OPTICAL CONDITIONS IN ERROR DETECTOR

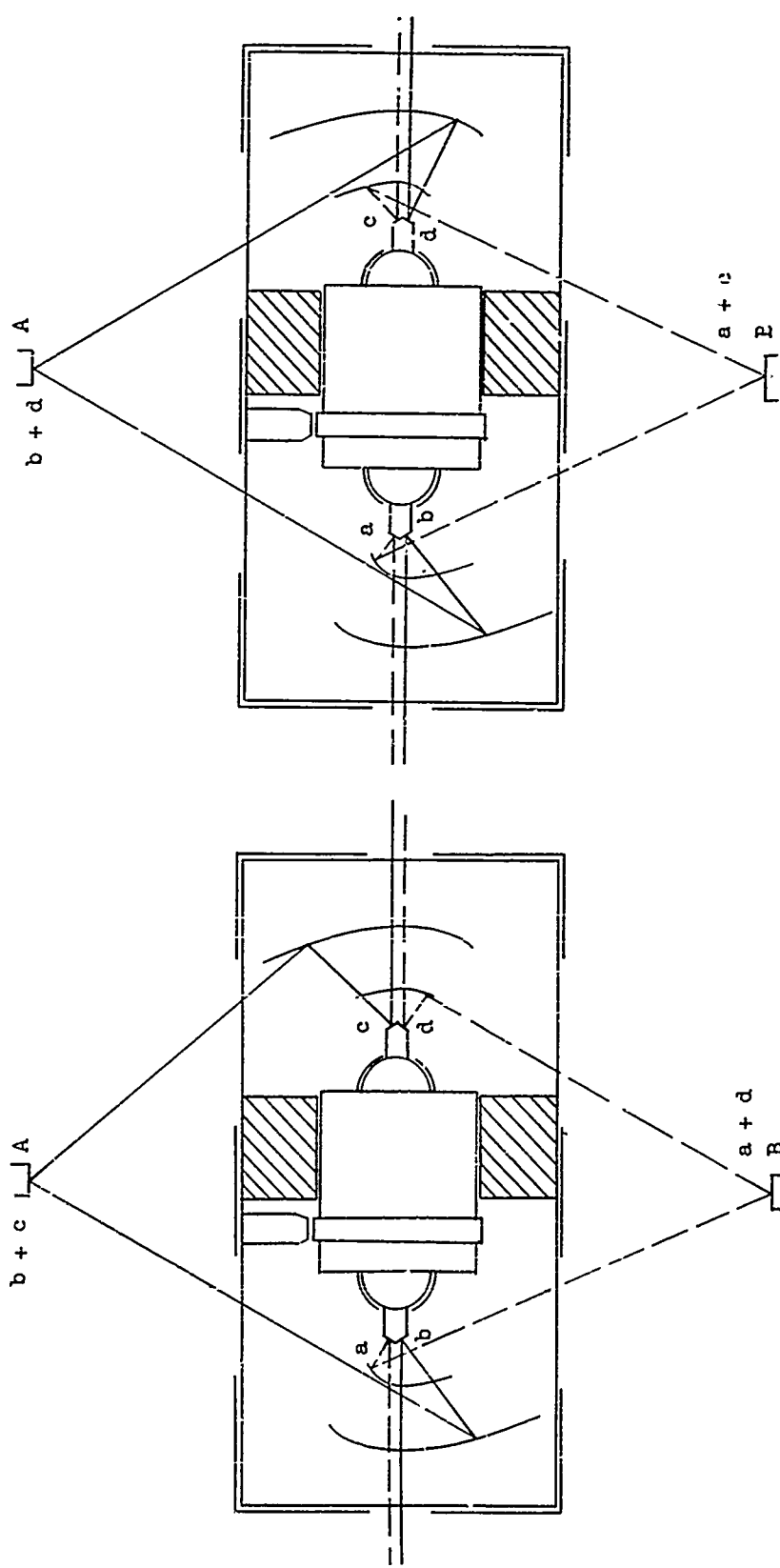


Figure 55b  
OPTICAL CONDITIONS IN ERROR DETECTOR



The air bearings will probably have the shape of a hemisphere to provide the rotor with both lateral and thrust support. The shafts which contain the knife edge prisms will protrude through the centers of the air bearings.

The electronic logic circuits which convert the phototube signals to coordinate error signals must be synchronized with the rotation of the prisms. To accomplish this, a coating or strip of magnetic material is attached to the circumference of the motor rotor, and a magnetic pickup is placed close to the surface. Synchronizing pulses and reset tones are recorded on the magnetic material, and this information is repeated in the magnetic pickup as the motor rotor rotates. Magnetic shielding is used to prevent the magnetic field of the motor from disturbing the synchronizing tape.

TABLE XII

Pointing Direction Side A	Phototube A Sees	Phototube B Sees
1	a + d	b + c
2	a + c	b + d
3	b + c	a + d
4	b + d	a + c
5	a + d	b + c
6	a + c	b + d
7	b + c	a + d
8	b + d	a + c
.	.	.
.	.	.
.	.	.
33	a + d	b + c
34	a + c	b + d
35	b + c	a + d
36	b + d	a + c

#### 4. Error Detector Logic

The required polar error signal at end "a b" is (a-b). Similarly, the required polar error signal at end "c d" is (c-d). These signals can be obtained by switching in the sequence shown in Table XIII and then smoothing to obtain the polar error signal as a function of time.

TABLE XIII

Rotor Position	Error at a,b	Error at c,d
1	A - B	B - A
2	A - B	A - B
3	B - A	A - B
4	B - A	B - A
5	A - B	B - A
6	A - B	A - B
7	B - A	A - B
8	B - A	B - A
33	A - B	B - A
34	A - B	A - B
35	B - A	A - B
36	B - A	B - A

It is significant that this switching sequence gives the correct error signals when both phototubes are working or if only one phototube is working. When both phototubes are working the gain of the error signal is  $\propto$ . If one

phototube becomes inoperative, the error signal is reduced to  $\propto 1/2$ . It will be necessary to include the capability of detecting one phototube operation and accordingly increase the electronic gain by a factor of 2 during periods of single tube operation.

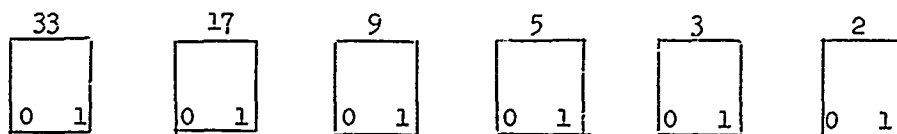
In addition to the desired error signal, there is an undesirable AC signal at nine times the frequency of the rotor speed, i.e. polar error signal. This undesirable signal can be raised to an odd harmonic of the rotor speed by changing the number of segments on the inner mirrors, but the width of the light beams compared to the segment width limits the number of segments which can be used.

#### a. Polar Coordinate Logic

A series of pulses and a burst of tone are recorded on the magnetic material attached to the motor rotor. The pulses are phased to the transition of mirror segments, and the burst of tone is located between pulses 36 and 1. The tone (20-40 KC) is an activation signal for resetting the detector logic, and the actual reset is accomplished by pulse 1. The error detector logic is reset with each revolution of the rotor to prevent loss of synchronization which could be caused by a stray or missed synchronizing pulse. Any error from either of these causes can exist only for one rotor revolution.

Pulses from the magnetic pickup are applied to a 6 stage counter. This counter has a capacity of 64 bits, but only 36 are used. The first two stages of the counter (4 bits) are used to operate the polar coordinate logic.

Binary to decimal equivalents of the counter are shown below:



Binary Code	Arabic Code
00	1
01	2
10	3
11	4
100	5

As shown in the schematic diagram of Figure 56 a diode matrix obtains the error signals for end "a, b". When the Flip Flop #2 is in the zero condition the error signal is obtained by taking the output of phototube A minus phototube B. When Flip Flop #2 is in the one condition the error signal is obtained by taking the output of phototube B minus phototube A. Stated in other terms, binary counts 00 and 01 yield A-B and binary counts 10 and 11 yield B-A. Circuits used to obtain the polar error signal for end "c, d" are slightly more complicated but still straight-forward. For end "c, d", binary counts 00 and 11 yield B-A and binary counts 01 and 10 yield A-B. End "c, d" requires 4 times the diode matrix circuits as end "a,b".

The filtered output of the error signal as a function of error detector position has the general form shown in Figure 57a. This wave form can be separated into its X and Y components shown in Figure 57 b and c.

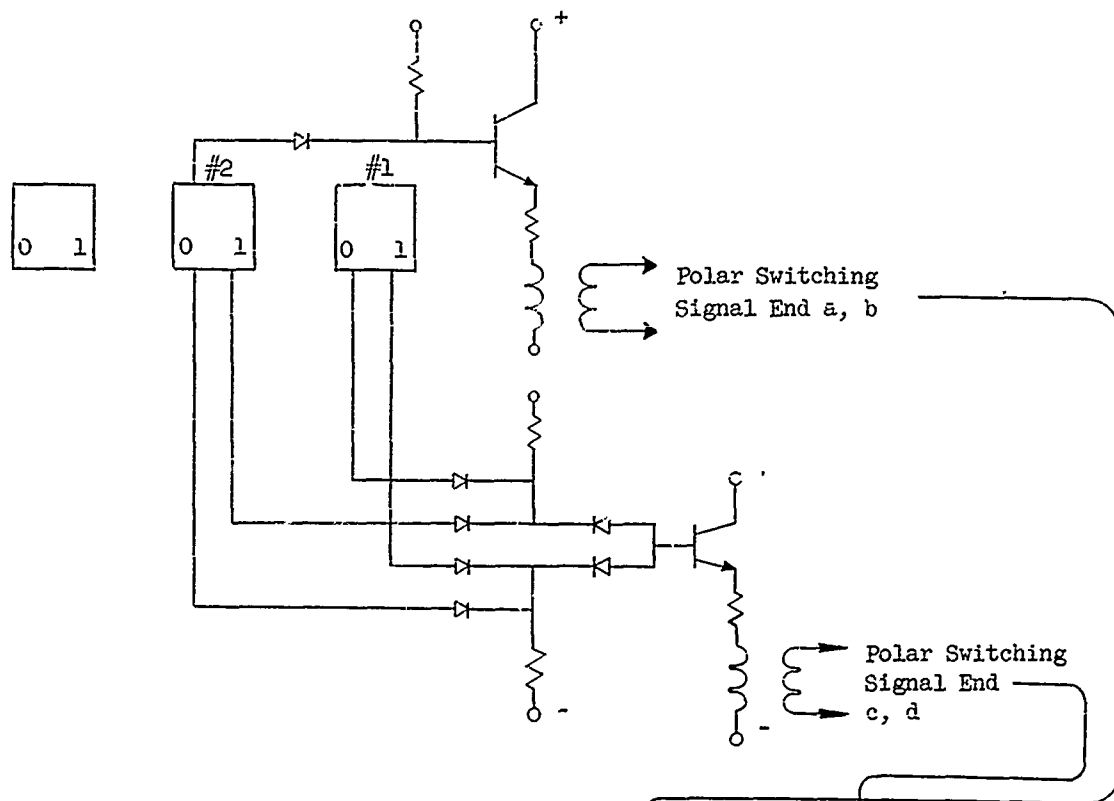
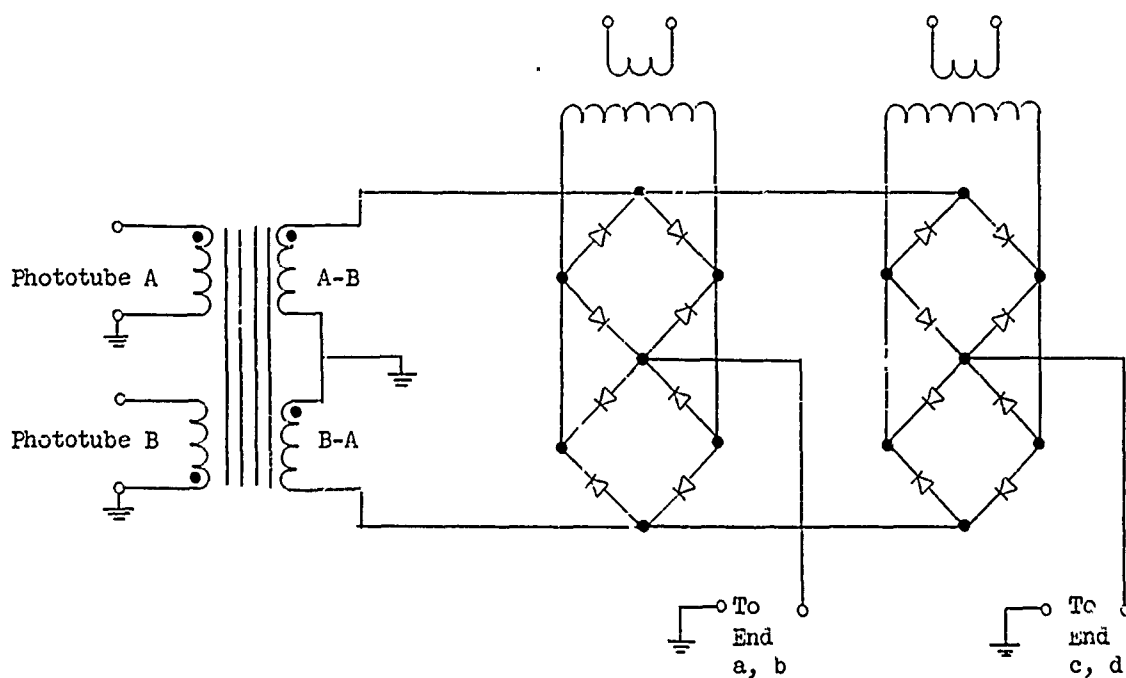
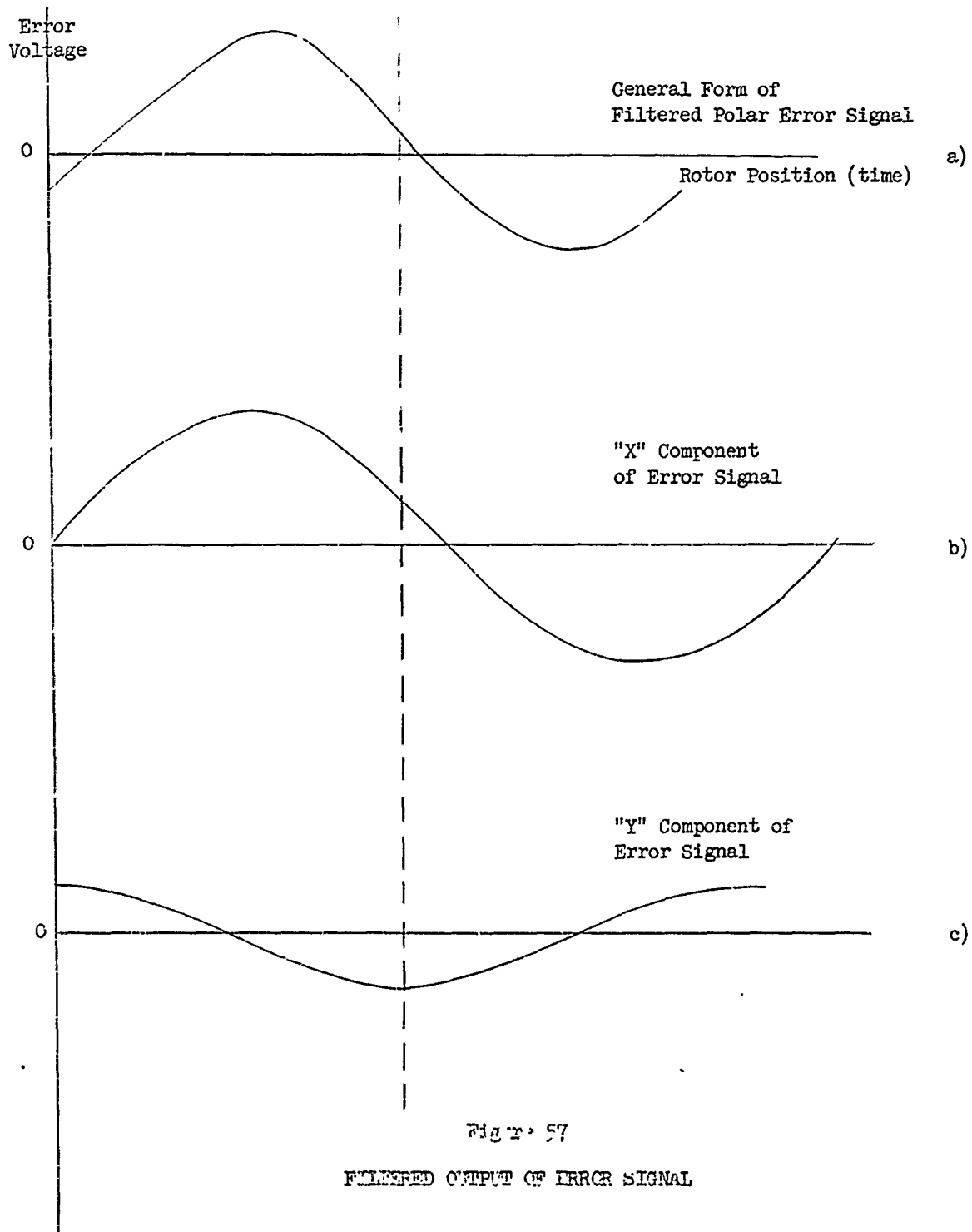


Figure 56  
CIRCUIT FOR  
OBTAINING POLAR ERRORS

Logic for end  
a, b yields (A-B) for  
00, 01 and (B-A) for  
10, 11

Logic for end  
c, d yields (A-B) for  
00, 11 and (B-A) for  
01, 10





#### b. Cartesian Coordinate Logic

The error signals b and c are in the form of a suppressed carrier. To transform these error signals into cartesian coordinates it is necessary to use a synchronous demodulator. The circuit is simple, requiring only two diode bridges and two transformers. The reference signals for the demodulator originate in the 36 bit counter.

Diode matrices are used to determine the following counts: 1, 10, 19, 28. Diagrams of these matrices are shown in Figure 58 through 61. For the "Y" component the diode bridges are switched at counts 1 and 19. For the "X" component the diode bridges are switched at 10 and 28. The same logic applies for the error signals at both ends.

The processes required to generate the polar and cartesian coordinate error signals resulted in significant harmonic generation at 2, 4, 9, and 27 times the rotor rotational frequency. These harmonics require filtering, and the requirements and effects of this filtering are discussed in the paragraph devoted to servo problems.

The binary counter will be reset after each revolution of the motor rotor. The tone burst will be separated from the synchronizing pulses with an audio filter, and will be rectified and filtered to provide a reset pulse.

#### c. Synchronous Demodulation

A suggested circuit for synchronus demodulation is shown in Figure 62 . The demodulator is a conventional double ring diode bridge which requires two transformers per modulator. A transformer with a center tapped secondary is used as the input for the polar error signal. In accordance with standard

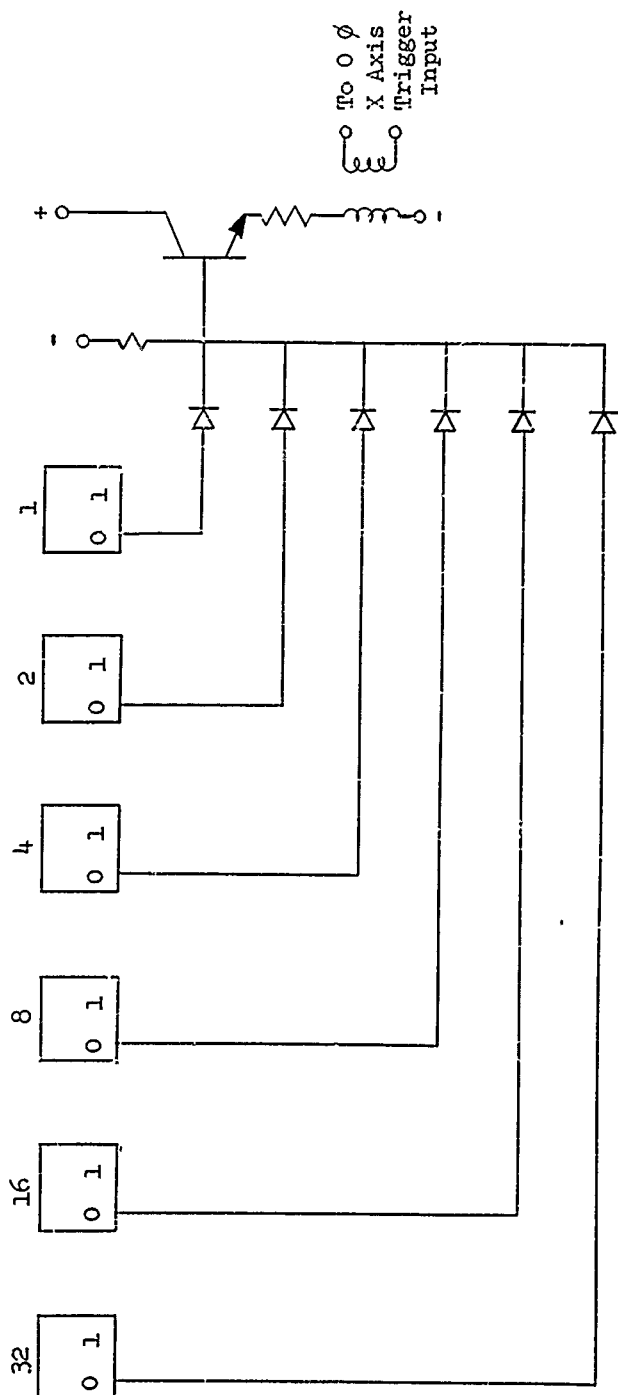


Figure 58  
DIODE MATRIX, SENSOR COUNT "1"



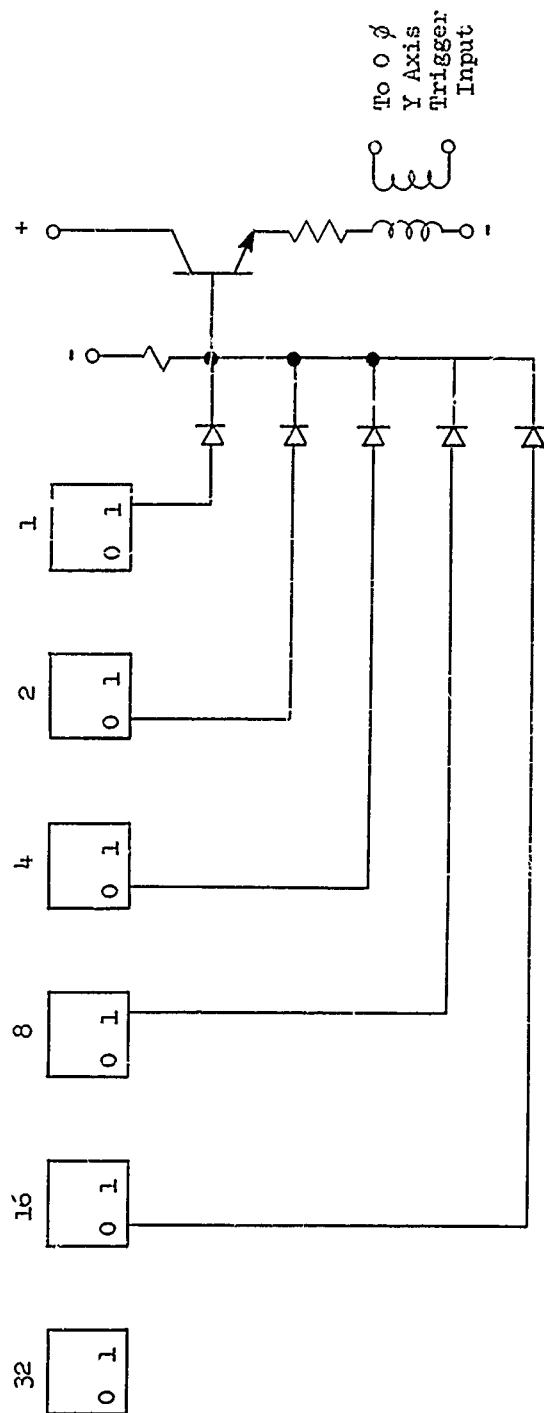


Figure 59  
DIODE MATRIX, SENSOR COUNT "10"

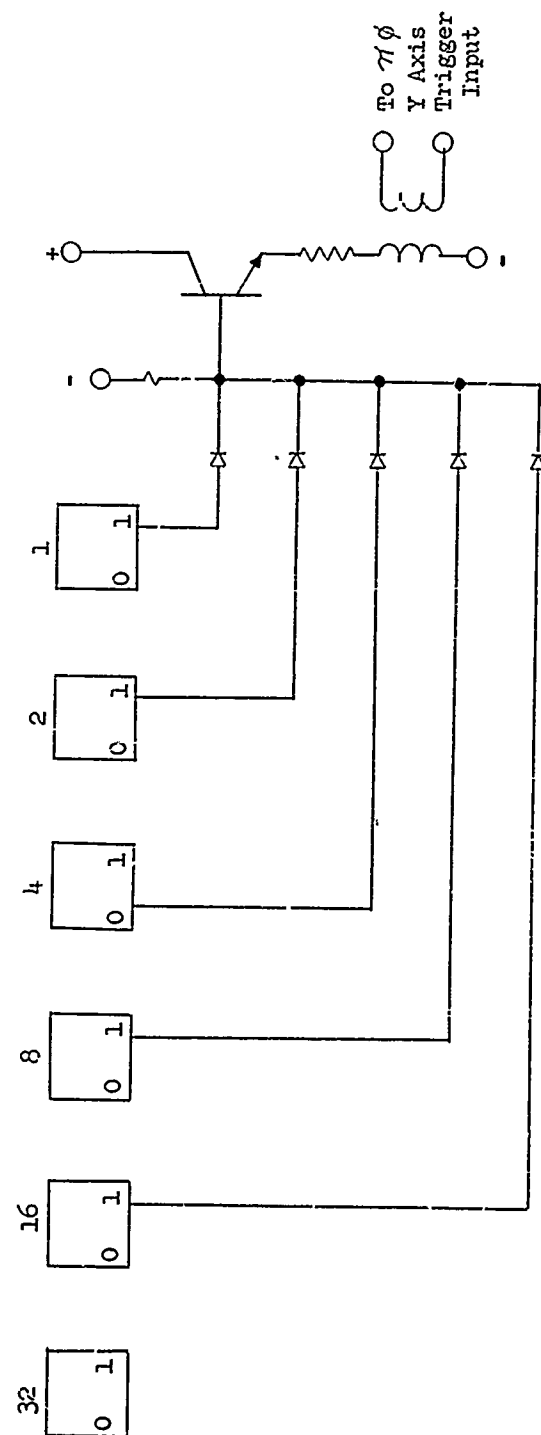


Figure 60  
DIODE MATRIX, SENSOR COUNT "28"

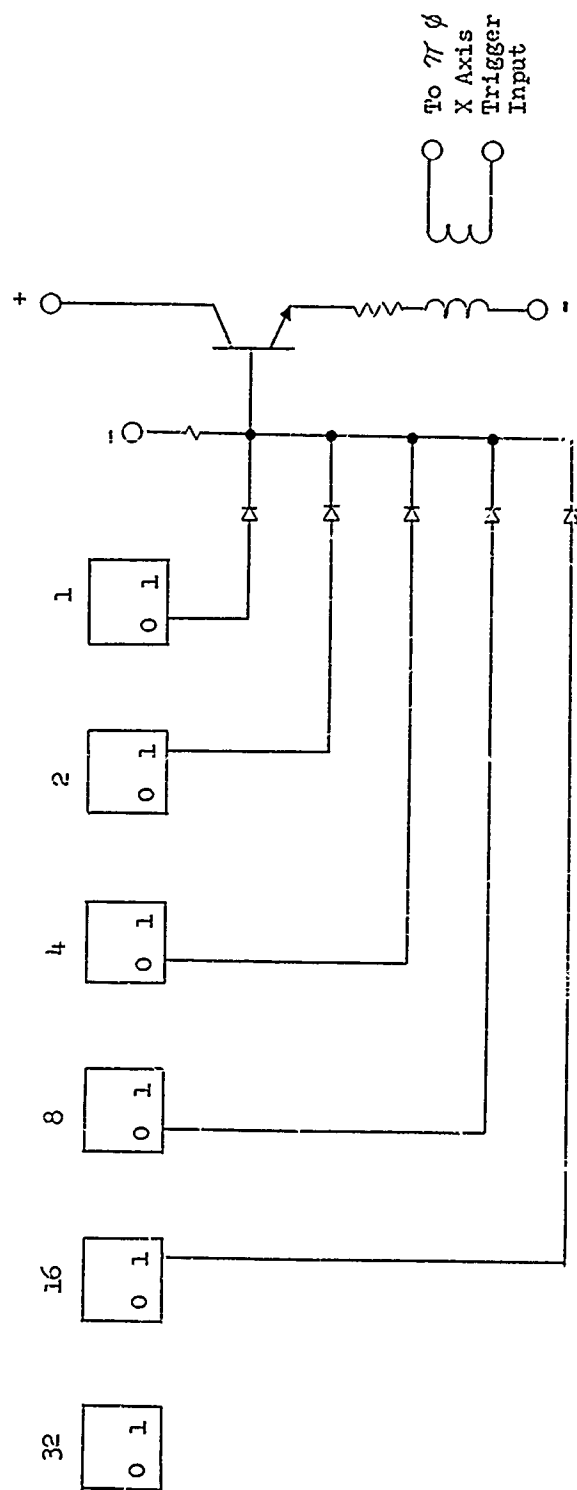


Figure 61  
DIODE MATRIX, SENSOR COUNT "19"

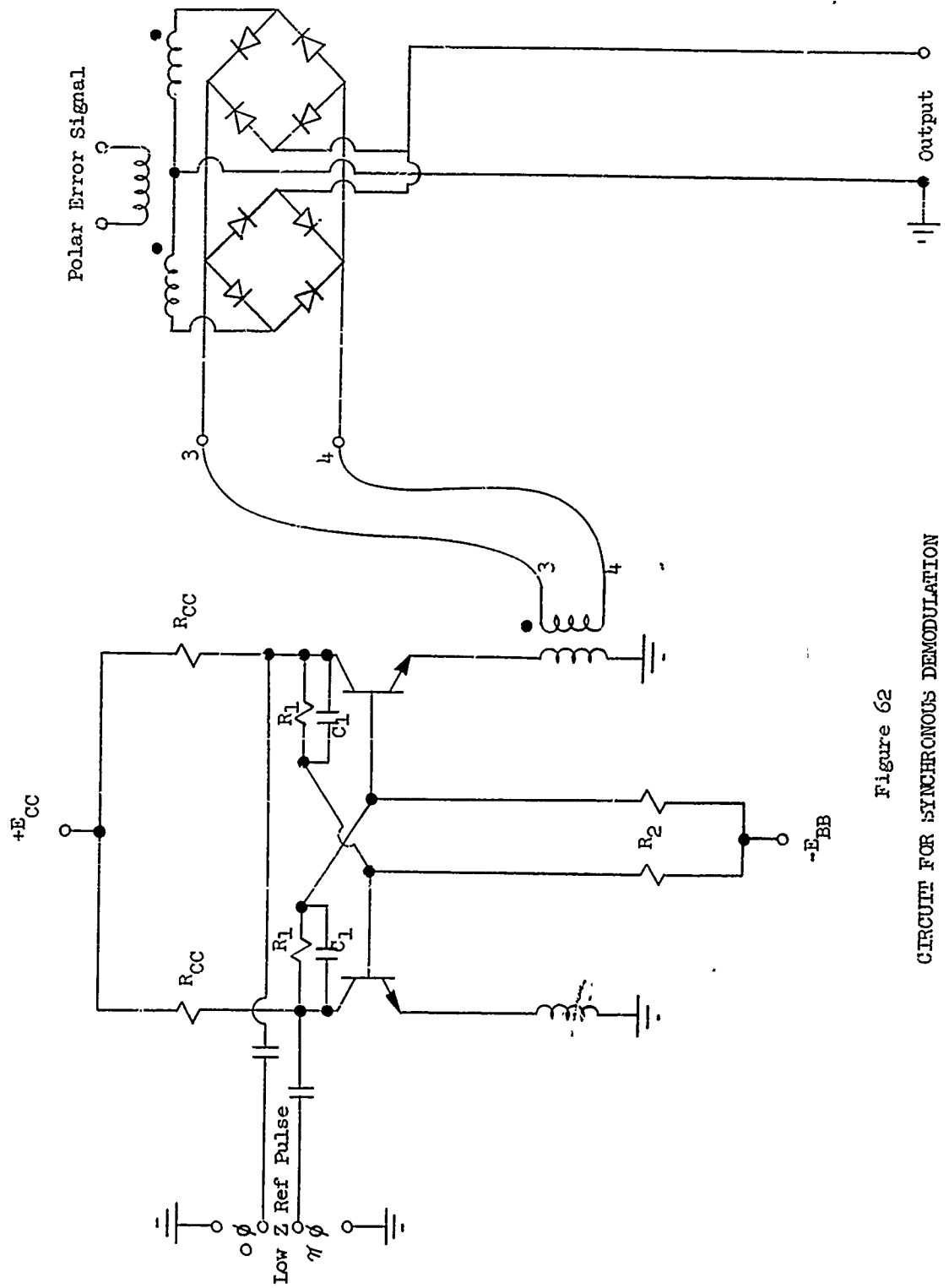


Figure 62  
CIRCUIT FOR SYNCHRONOUS DEMODULATION

practice the diodes should be operated far into their conducting region during the on condition, perhaps half of maximum current.

References for the demodulation bridge are taken from a flip flop. The signal from the flip flop is transformer coupled from one of the emitter legs. It will be noted that the flip flop has two reset inputs, labeled  $o\phi$  and  $\pi\phi$ , and no counting input. For the "X" axis the  $o\phi$  input is triggered by the 1 count and the  $\pi\phi$  input is triggered by the 19 count. For the "Y" axis the  $o\phi$  input is triggered by the 10 count and the  $\pi\phi$  input is triggered by the 28 count.

A total of 4 synchronous demodulators will be required for each error detector.

The circuit shown was selected because it illustrates the important functions while remaining free of electronic sophistication. It is recognized that the final circuit will have many refinements.

## D Articulation of Rotating Error Detector

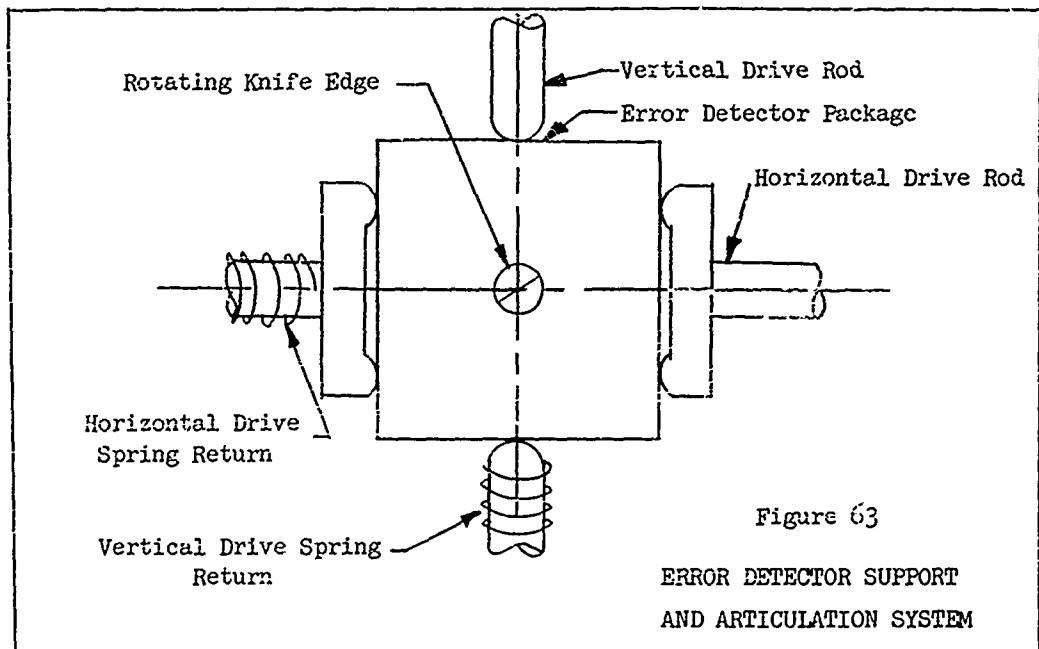
### 1. Detector Mounting

The rotating error detector must be mounted at the center of the aberrascopes such that the axis of the rotating knife edge is parallel with the optical axis of the instrument. Of the six possible degrees of freedom, this rotating error detector must be capable of having four, two in translation and two in rotation. Restraint must be provided for the other two possible degrees of freedom: rotation about the optical axis and translation along the optical axis. The straightforward manner in which this can be accomplished is by mounting each end of the rotating error detector in a pair of linear slides as in machine tools where the vertical slide is carried on the horizontal slides. This, of course, is a complicated method of accomplishing the end result and involves many sliding surfaces. In a hard vacuum environment, it is necessary to keep the number of moving parts to a minimum; thus the approach of one slide upon another will be ruled out.

Consideration was given to the use of linkages to perform the required task, but the difficulty here is the cross coupling between the horizontal and vertical motions. To separate the two, one mechanism would be required to carry the second mechanism, again involving a large number of parts. The most desirable mechanism is one which could provide independent motion.

Since the final motion required is simply a translation (the rotation of the error detector package in a given plane can be effected by difference in translation of the two ends), consideration was given to using simply four push-rods to articulate the ends of the error detector. Restraint from rotation about the optical axis could be provided by shaping the ends

of the push-rod like a "crow's foot". An end view of the error detector with the push-rod drives is shown in Figure 63.



The ends of the rotating error detector will be shaped as a square and thus the horizontal push-rods shaped as shown in Figure 63 will prevent rotation of the entire package.

The requirement that no rotation of the entire package take place should not be confused with the requirement that the knife edge rotate inside of the package.

Figure 64 illustrates the side view of the detector mounting. Restraint along the optical axis is provided by making the end of one of the push-rods a spherical end. This spherical end is seated in a precision "V" groove normal to the optical axis. Only one such axial restraint can be provided; it is obvious that two such restraints would yield a redundant support. Thus, if the vertical drive articulates the error detector package, it will simply slide across the faces of the horizontal drive-rods.

Lubrication of these surfaces can be accomplished by the use of molybdenum disulfide. This lubricant is suitable for surfaces where sliding contact is taking place.

## 2. Detector Drive

As mentioned above, the error detector package will be articulated by four push-rods; two in the vertical plane and two in the horizontal plane. The package will be retained in place with four additional push-rods which will spring load the detector package against the driving push-rods.

Figure 64 illustrates a drive mechanism which uses servo motors. Size 8 components are envisioned. Each motor (four are necessary) will have a gearhead and a tachometer, the tachometer will be used for rate feedback into the servo loop. The motor will drive one stage of external gearing which in turn will rotate a cam. A cam follower roller will be attached to the push-rod; thus the rotation of the cam will be transmitted into linear motion of the push-rod. The rise of the follower roller will be linear with respect to the rotation of the cam. The cam center will be offset from the push-rod axis in order to provide an advantageous pressure angle to the follower roller. The cam becomes the critical element in the design; however, the accuracy requirement on the cam is not positional accuracy but that the incremental changes in the slope of the cam be no greater than 20% of the average slope. This is true because the servo motor will finally drive the error detector package to the point where the stellar image impinges on the center of the knife edge.

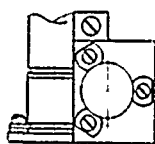
In Figure 64 a synchro is shown geared to the cam and servo motor. The purpose of this transducer is to indicate the satellite attitude error;



the attitude error in the plane which includes the synchro is the difference between the synchro signals from the two ends of the error detector package.

Previously in this report, it was mentioned that the maximum displacement which the error detector would experience (normal to the optical axis) was plus or minus 0.10 inches, both in the horizontal and vertical directions. This represents a capability of tracking stellar images thru a range of 400 seconds of arc. Assuming tentatively that the cam will rotate  $320^\circ$  in order to provide the plus or minus 0.10 inch travel, if the synchro is geared directly to the cam, the scale factor at the synchro will be 450 seconds of arc of attitude error per synchro revolution. Considering synchro accuracy alone, the capability then exists of measuring attitude errors to an accuracy of 0.1 seconds of arc.

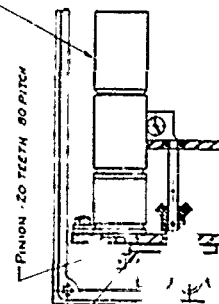
The motor-tach-gearhead unit and associated gearing, cam and synchro can be mounted as an integral sub-assembly. Two such sub-assemblies would nest into one area of the main aberrascope housing; an area which can be designed to be completely sealed from the ambient environment. The push-rods will of necessity be required to emerge from the sealed area; however, these rods can be sealed with metal bellows since the range of linear motion is so small. Thus, there will be two sealed areas in the main aberrascope structure; these areas will be located at right angles to each other (with respect to the optical axis).



SECTION E-E

GEAR - 100 TEETH 80 PITCH

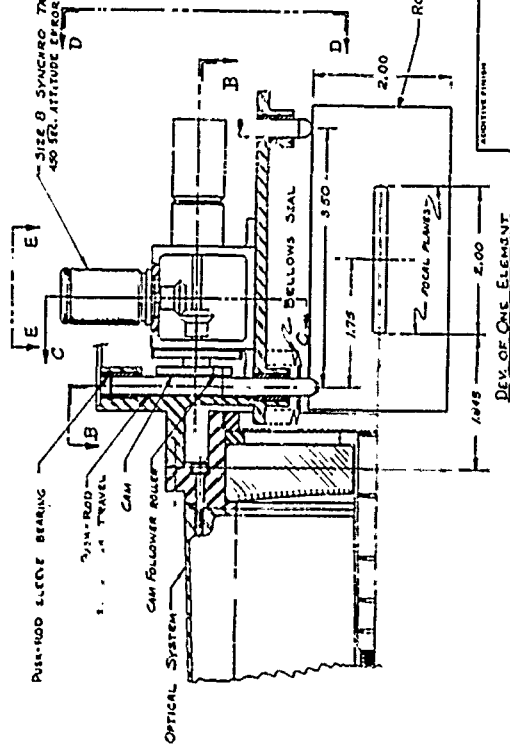
SIZE B GEARED SERVO MOTOR GENERATOR



SECTION B-B

VIEW DD

SIZE B SYNCHRO TRANSMITTER  
400 SER. ATTITUDE ERROR/REV



SECTION CC

ROTATING ERROR DETECTOR

DEV. OF ONE ELEMENT

FINISHING FINISH MATERIAL	UNLESS OTHERWISE SPECIFIED DIMENSIONS ARE IN INCHES FRACTIONS SHALL BE IN 16ths, 32nds, 64ths, AND 128ths	OF ORIGINATING ORGANIZATION DATE BY CHECKED APPROVED	NAME DRIVE MECHANISM FOR ROTATING ERROR DETECTOR ABERLASCOPE Figure 64	General Mills, Inc. MECHANICAL DIVISION 1115 CENTRAL AVENUE S.E. MINNEAPOLIS, MINNESOTA DRAWING SIZE SK-18499-003 C
SCALE FULL	FIG. 64	SCALE FULL	FIG. 64	SK-18499-003

#### E. Photomultiplier Configuration

In the previous quarterly report,<sup>27</sup> consideration was given to the arrangement of the photomultiplier tubes to provide a maximum of reliability. Two different types of mounting systems were considered. One was the conventional type of system which we called Type I where each stellar image was uniquely associated with only one photomultiplier tube. The incoming energy upon striking a knife edge prism would be directed to the photomultiplier tube after passing thru a chopper from either of two paths from the two faces of the knife edge. The two telescopic systems would be completely independent of each other as far as the detection system is concerned. If the probability of failure of one photomultiplier tube is designated as  $p_f$ , then the probability of failure of the entire aberrascope system (which involves two aberrascopes) expressed as  $\pi_f$  is the following:

$$\pi_f = [p_f (2 - p_f)]^2 + 2 p_f (2 - p_f) (1 - p_f)^2$$

In an alternate system which we called the Type II system, the stellar images from both stars were combined in a unique chopping system such that each of the two photomultipliers received energy from both stars. While the Type I system blocked out the stellar energy 50% of the time, this (Type II) system utilizes all the incoming energy 100% of the time. Again, if  $p_f$  is the probability of failure of one photomultiplier tube, the probability of failure of the aberrascope system  $\pi_f$  is given as follows:

$$\pi_f = p_f^4 + 2 p_f^2 (1 - p_f^2)$$

The probability of failure functions for the two types of systems are shown in Figure 59. The advantage of the Type II system is shown quite forcibly in Figure 60. If the probability of failure of the individual

photomultiplier tubes is not greater than 0.1, then it can be seen that the Type II system has an advantage of a factor of 17 over the Type I system. It is probably doubtful whether a photomultiplier tube would be considered for use if its probability of failure was greater than 0.1

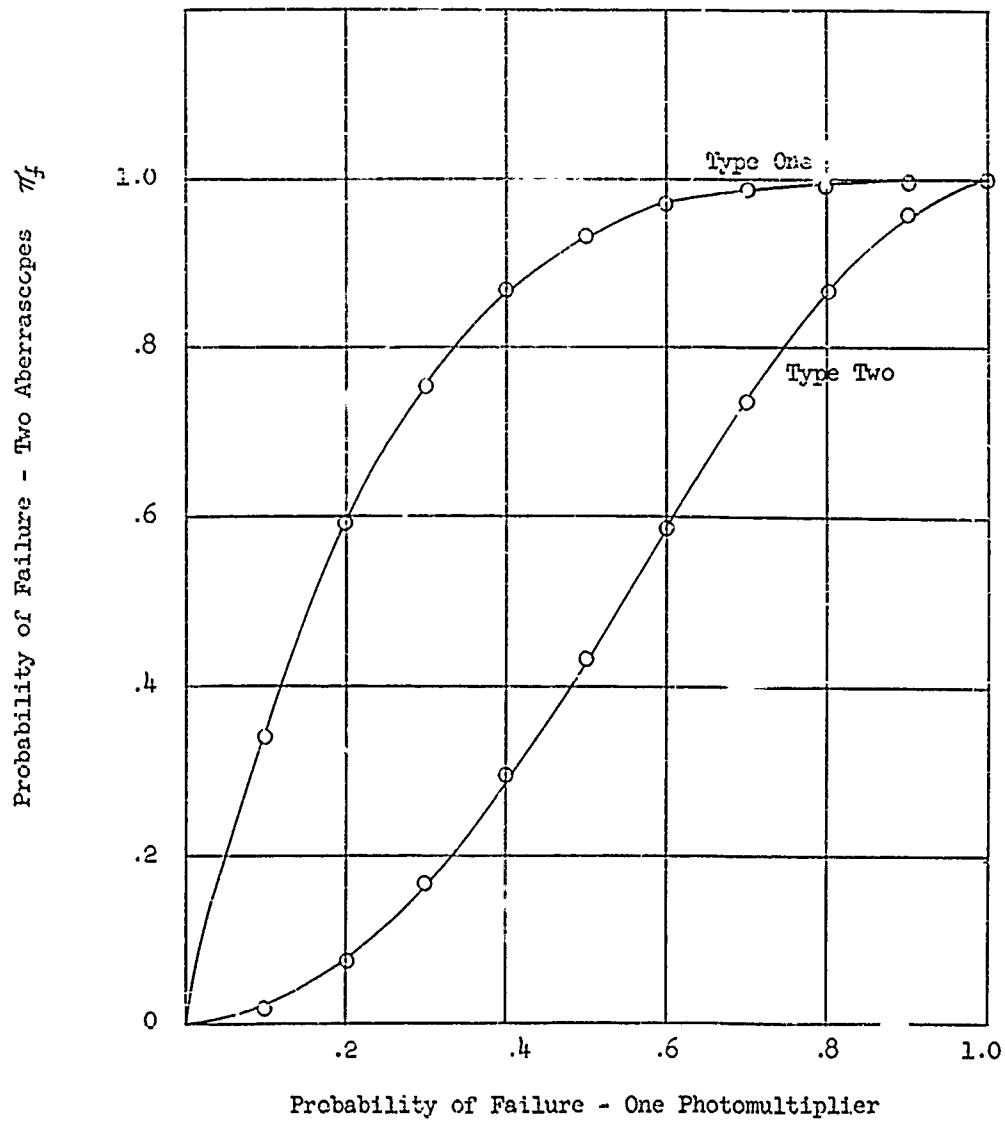


Figure 65

RELIABILITY COMPARISON OF  
PHOTOMULTIPLIER ARRANGEMENTS

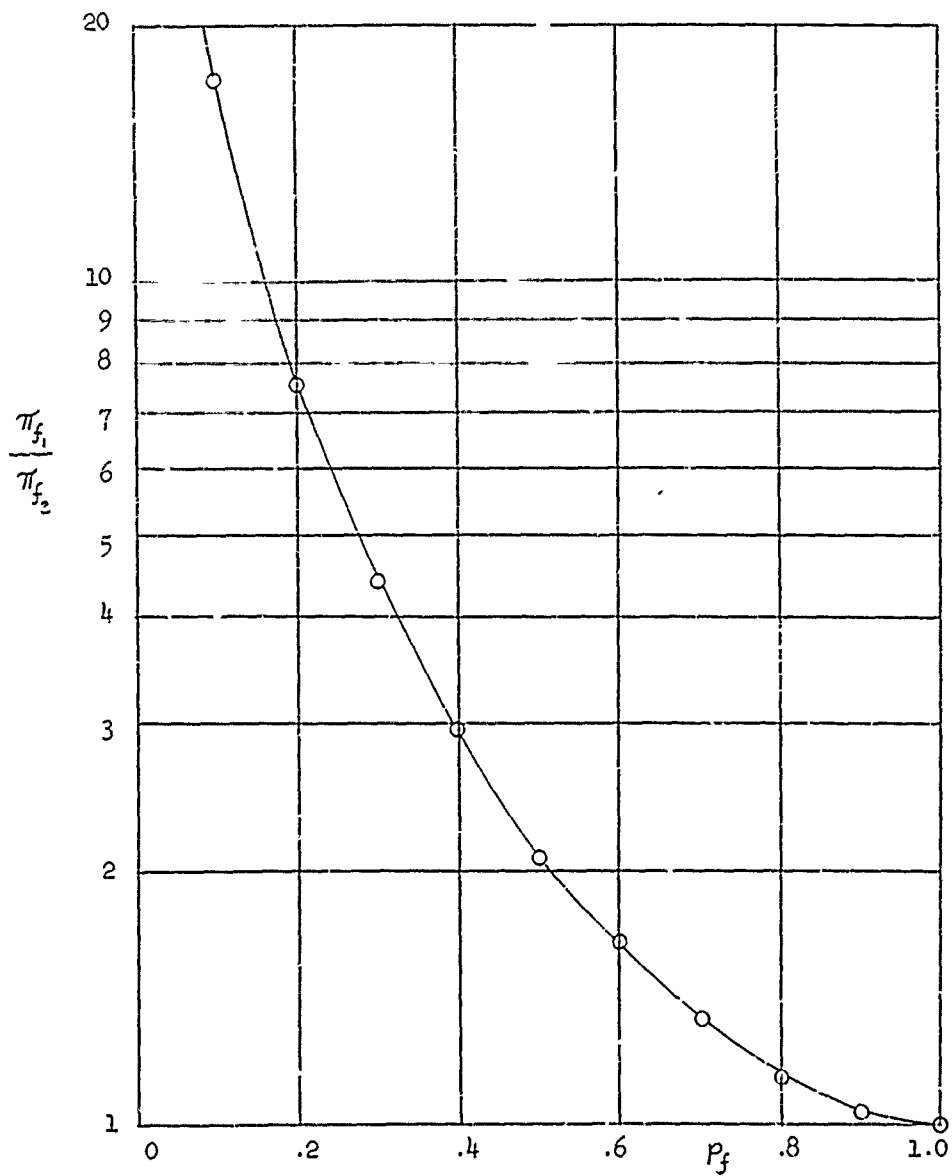


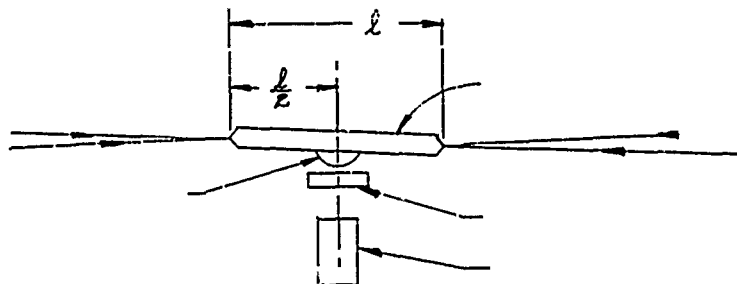
Figure 66

RATIO OF PROBABILITIES OF FAILURE

#### F. Position Measuring Device

It has been mentioned already that the final output of the aberrascopes will be the data obtained from measuring the displacement of the center of the error detector package. This measurement will be accomplished by means of a pair of interferometers: one in each of the two significant planes (horizontal and vertical). The interferometer will simply produce Newtonian fringes in a pattern of concentric circles. We are assuming here that the central element on the error detector has a spherical surface so that the attitude changes of the satellite which will cause the error detector package to pivot about its center will not cause changes in the number of fringes.

With the use of helium light, the distance between fringes which is one-half wave length will be  $11.6 \times 10^{-6}$  inches. Then the change from a dark area to a light area will be one-half of this distance or  $5.8 \times 10^{-6}$  inches. By using a photo sensor to detect either a dark or light area, an electrical on-off type signal will be produced for every displacement larger than  $5.8 \times 10^{-6}$ . In terms of angle in the aberrascopes, this minimal displacement represents 0.012 seconds of arc. Since this measurement is made at the center of the knife edge, the actual error sensitivity will be twice as large, or 0.024 seconds of arc. This illustrated in the sketch below.



Thus, the error sensitivity capability is more than adequate to meet the requirements of the refraction measuring aberrascopes.

It can be recognized that a single photo sensor will not be able to distinguish between the increase or decrease of the distance between the fixed and moving elements of the interferometer. This problem can be circumvented by using two sensors: the spacing between positions will be such that while one is sensing a dark area the other is sensing a light area. The fact that the second sensor is observing either a light or dark area while the first sensor is changing from light to dark will establish the direction of the motion.



## VI. CONFIGURATION OF STAR TRACKERS

Since we are required to know precisely which star is being occulted at a given time in order to derive useful information, it is necessary that we employ star trackers for collecting the basic data. By measuring both the time of ingress and the time of egress of each star it is possible to derive two transit\* time measurements from each star tracker during each rotation of the satellite. Thus a minimum system requires that we use at least 3 star trackers.

However, for certain orbits, 2 of the 3 stars can be occulted by the earth and since one star is inadequate to maintain the inertial orientation of the star trackers, a problem of reacquiring the stars is presented. If we add a fourth star tracker and arrange them as shown in Figure 67 at least two stars will be in the field of view at all times. Thus we will be able to maintain continuous altitude control and, depending on the orbit, we will have either 4 or 8 star transit time measurements per satellite rotation.

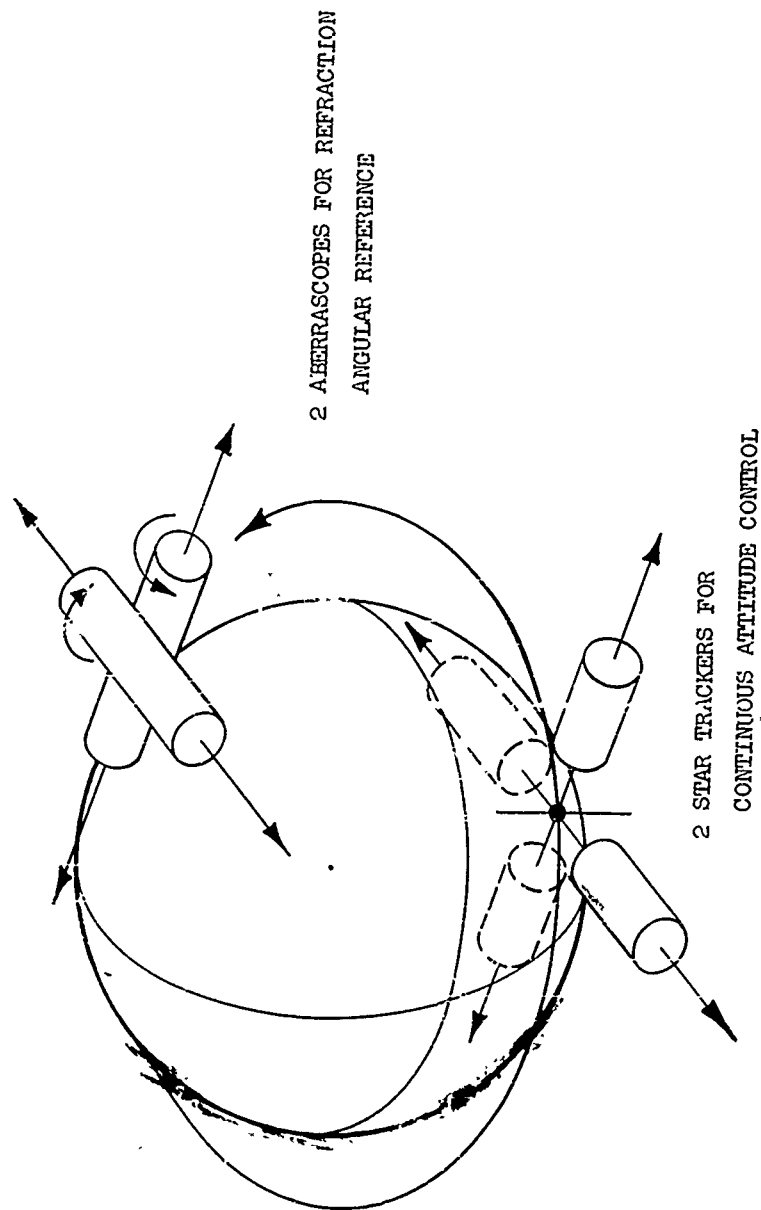
With the arrangement shown in Figure 67 the stars are picked in diametrically opposite pairs which are approximately orthogonal to one another. The star selection is made in this manner because of the possibility of mounting the two telescopes back-to-back and canceling their alignment errors by rotating them about their common optical axis; also in this way the refraction of the starlight which is passing through the earth's atmosphere can be more accurately measured if it is compared with its diametrically opposite companion.

---

\*The word "transit" in this case is taken to mean "the passage of a smaller body across the disk of a larger". Thus an ingress and an egress of a given star represents two transits across a planetary limb.

Figure 67

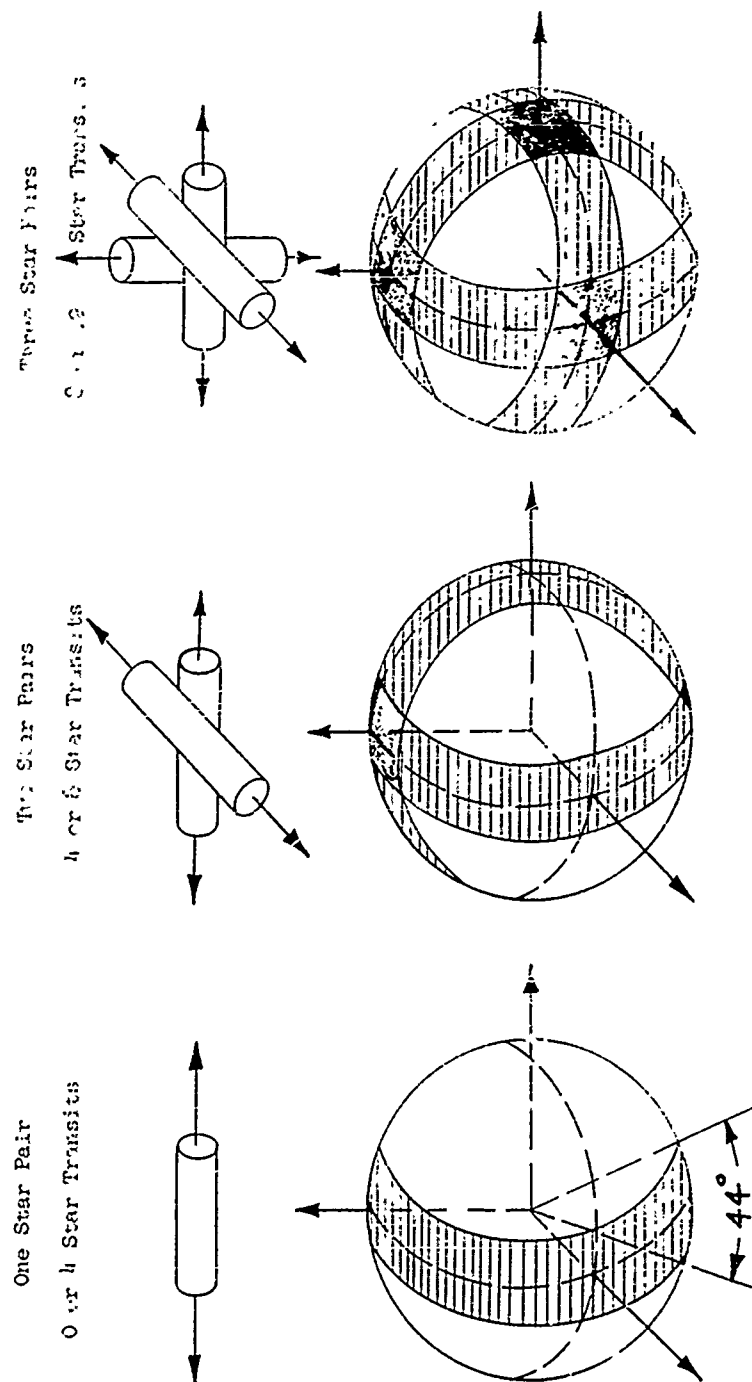
STAR TRACKERS FOR SATELLITE ATTITUDE  
CONTROL AND TRANSIT TIME MEASUREMENT



Assume that the orbit is such that one pair of stars is never occulted by the earth. In this case there will be only 4 star transit time measurements per rotation and we do not have enough information to completely define the elements of the orbit. Since we can determine the semi-major axis from one complete rotation, the remaining information enables us to calculate all the other orbital elements except the orbital inclination. Since the inclination of the orbit relative to the equatorial plane is constant, a previous determination of this parameter could be used. Another method of deriving the orbital elements in the special case where only one pair of stars is occulted is to measure the transit time of ingress or egress of the sun. This would involve the addition of some extremely simple instrumentation to the basic system and along with the star transit times would provide a basis for calculating all orbital parameters directly.

In order to better understand the problem of star selection for various orbital planes, consider Figure 68. In this figure we have shown the transit boundaries for one, two and three aberrascopes. In drawing these transit boundaries a 300 n. mile circular orbit was assumed. In this case both members of each diametrically opposite pair can be tracked over a central arc of about  $44^\circ$  as shown. For the case in which one star pair is used, orbits which lie within  $22^\circ$  of the X-Y plane will involve no occultations. All other orbits will involve at least 4 star transits. For the case in which two star pairs are used, the least number of occultations is seen to be 4. This occurs for orbital inclination lying within  $22^\circ$  of either the X-Z or Y-Z planes. For all other orbital inclinations 8 star

Figure 68  
 OCCULTATION BOUNDARIES FOR VARIOUS NUMBERS  
 OF DIAMETRICALLY OPPOSED 300 N.M.I.  
 CIRCULAR ORBIT ALTITUDE STAR PAIRS



transits will be observed. In the last case with 3 orthogonal star pairs, either 8 or 12 star transits will be observed. The shaded areas of Figure 68 denote positions where no stars will be occulted.

The transit boundaries shown in Figure 68 are dependent on the positions of the stars only and earth's pole or the plane of the orbit may be in any position relative to these patterns. For most orbits, it is only necessary to track 4 stars and for this case either 4 or 8 star transit time measurements will be obtained per rotation. If the plane of the orbit should happen to intersect with the plane defined by the two pairs of diametrically opposite pairs, the error in the computation of the orbital plane,  $\Omega$  and  $i$  will be very large as shown in Section IV-c.

The two major problems in tracking two diametrically opposite star pairs are that (1) in certain cases orbits can be obtained in which only 4 star transit time measurements are available, and (2) large errors will exist in the calculation of the plane of the orbit if it coincides with the plane of the stars.

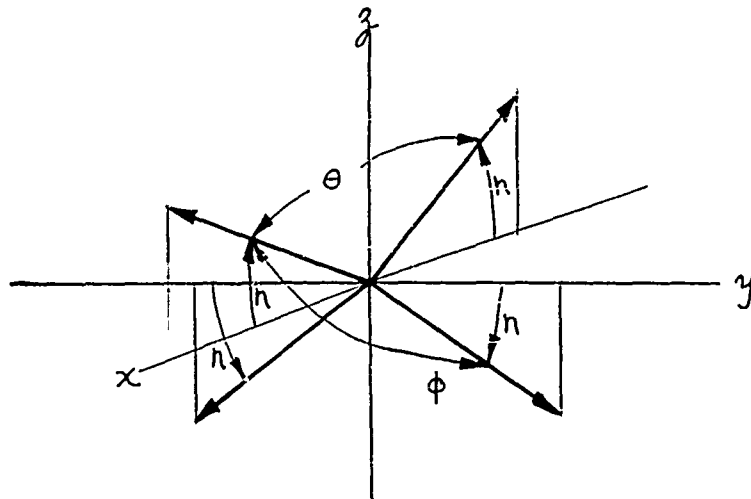


Figure 69

Star Tracker Geometry

In order to circumvent these two problems one might consider a geometrical arrangement of 4 star trackers in which the angles between all of the stars are the same.

With the planar configuration shown in Figure 69 as a starting condition, assume  $\theta = 180^\circ$ ,  $\phi = 90^\circ$ . We now wish to increase  $\eta$  until  $\phi = \theta$ . Therefore, from the geometry we may write

$$\theta = 180 - 2\eta$$

$$\cos\left(\frac{\phi}{2}\right) = \frac{\cos\eta}{\sqrt{2}}$$

Therefore

$$2 \cos^{-1}\left(\frac{\cos\eta}{\sqrt{2}}\right) = 180 - 2\eta$$

$$\tan\eta = \frac{1}{\sqrt{2}}$$

$$\eta = 35^\circ 17'$$

Thus we now have an arrangement of star trackers in which the angles between all of the stars are the same and equal to  $180^\circ - 2(35^\circ 17') = 109^\circ 26'$ . This is shown in Figure 70. We now no longer have all 4 stars lying in the same plane, but we have 6 different planes. Because of this there is no degeneracy in the calculation of any of the orbital elements. In addition, if the altitude of the orbit is not greater than 800 n. miles, 6 star transits will be obtained for all orbital inclinations.

It is not possible to specify a preferred geometrical arrangement of the 4 star trackers which is the best one for a completely self-contained navigation. In general, one must consider:

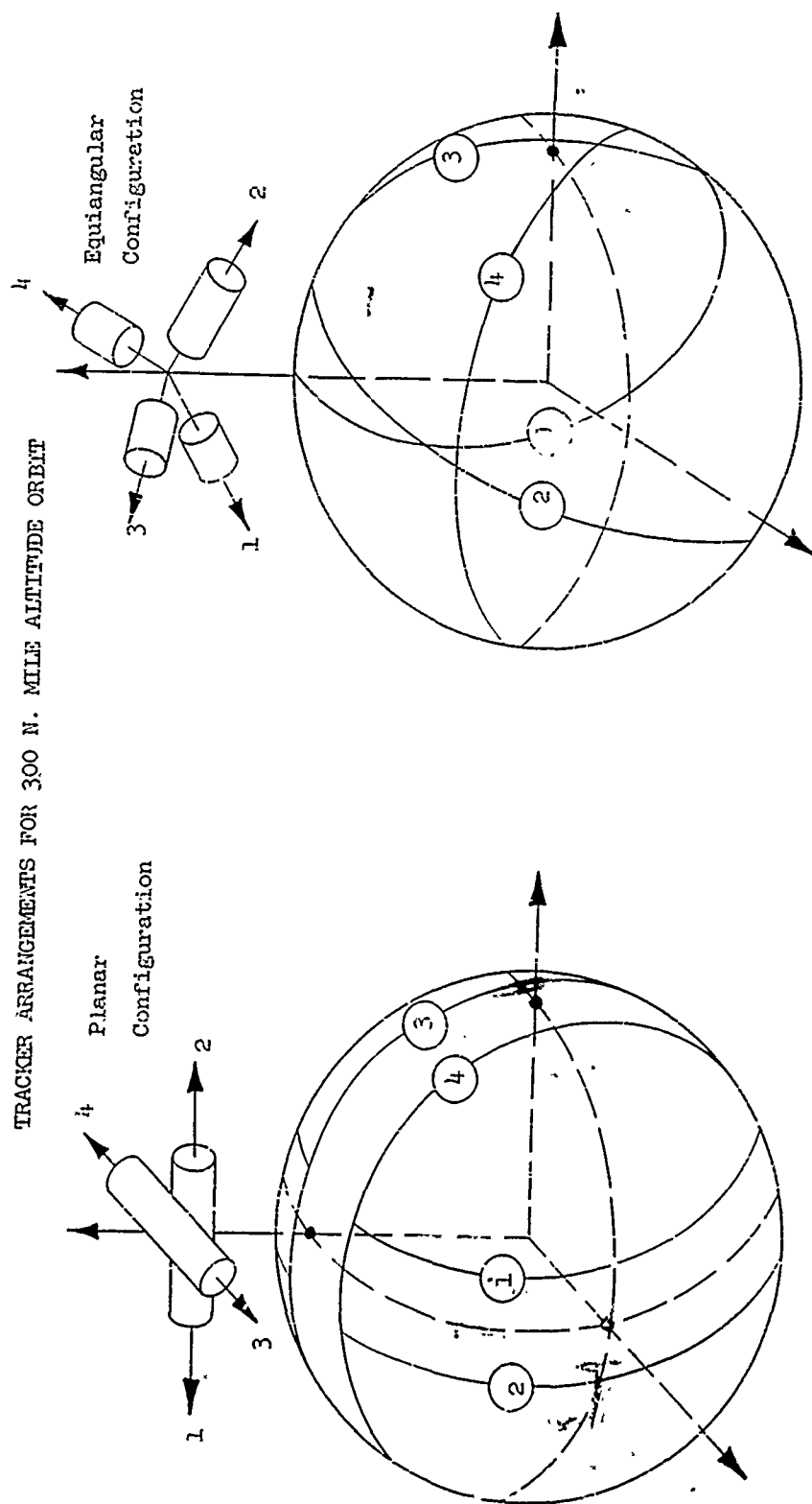
- 1) the semi-major axis,
- 2) the eccentricity,
- 3) the orbital inclination,
- 4) the argument of the perigee,
- 5) the longitude of the nodes, and
- 6) the shape of the planet as it effects the rate of change of 4) and 5).

A configuration of star trackers should be selected which provides:

- 1) a minimum of five stellar transits per rotation,
- 2) the minimum/maximum values of the error parametric sensitivity coefficients, and
- 3) the simplest or most precise instruments for the measurement of star transit times.

Figure 70

# OCCULTATION BOUNDARIES FOR TWO STAR





## REFERENCES

1. U. S. Air Force. Cambridge Research Center. Geophysics Research Directorate. Handbook of geophysics. Rev. ed. New York, Macmillan, 1960.
2. Kuiper, Gerard P., ed. The solar system, vol. 2. The earth is a planet. Chicago, University of Chicago Press, 1954. p. 442.
3. Nort, H. ... Bull. Astron. Inst. Netherlands 11: 181 (1950).
4. Pressly, E. C. Air mass between an observer and outer space. Phys. Rev. 89: 654-55 (1953).
5. Moon, Parry. Proposed standard solar radiation curve for engineering use. J. Franklin Inst. 230: 538-616 (1940).
6. Newell, Homer E. High altitude rocket research. New York, Academic Press, 1953.
7. U.S. Army. Ballistic Missile Agency. Report no. DA-TR-60-59. ABMA climatological ringbook, part 2. Ambient density as a function of altitude for ten selected stations (1959).
8. Goody, R. M. The physics of the stratosphere. Cambridge, England, University Press, 1954.
9. Whipple, F. L. Density, pressure and temperature data above 30 kilometers. In The solar system, vol. 2. The earth as a planet, ed. by Gerard P. Kuiper. Chicago, University of Chicago Press, 1954. pp. 491-513.
10. Kellogg, W. W. IGY rockets and satellites: a report on the Moscow meetings, August 1958. Planet. Space Science 1: 71-84 (1959).
11. LaGow, K. E., R. Horowitz and J. Ainsworth. Arctic atmospheric structure to 250 km. Planet. Space Science 2: 33-38 (1959).
12. Jones, L. M. et al. Upper-air density and temperature: some variations and an abrupt warming in the mesosphere. J. Geophys. Res. 64: 2331-40 (1959).
13. U. S. Army. Signal Engineering Laboratories. Technical Memo M-1933. Signal Corps - Air Weather Service high altitude radiosonde flights, July 1955, part 3, by M. J. Lowenthal (1957).
14. U. S. Air Force. Cambridge Research Center. Geophysical Research Paper no. 29. Seasonal trends of temperature, density and pressure in the stratosphere obtained with the searchlight-probing technique, by L. Elterman (1954).

15. Whipple, F. L., L. Jacchia and Z. Kopal. Seasonal variations in the density of the upper atmosphere. In The atmospheres of the earth and planets, ed. by Gerard P. Kuiper. Rev. ed. Chicago, University of Chicago Press, 1952. pp. 149-58.
16. Harvard Observatory and Massachusetts Institute of Technology, Center of Analysis. Technical Report no. 4. Atmospheric density profile and gradients from early parts of photographic meteor trails, by L. G. Jacchia (1949).
17. General Electric Co. Advanced Electronics Center. A procedure for calculation of atmospheric transmission of infrared, by Thomas Altshuler (1957).
18. Ibid
19. General Mills, Inc. Mechanical Division. Report no. 2111. Stellar aberrascopes study, by R. Lillestrand et al. Contract AF33(616)-7400. Quarterly Report (Sept. 15, 1960). p. 2-8.
20. Martin Co. Report no. 10470-6. Dynamic and analysis and design performance requirements for satellite vehicle guidance systems (Jan. 31, 1959). p. II-7.
21. Saunders, H., E. J. Wisniewski and P. R. Paslay. Vibrations of conical shells. J. Acoust. Soc. Amer. 32: 765-72 (1960).
22. Love, A. E. H. A treatise on the mathematical theory of elasticity. 4th ed. New York, Dover Publications, 1944.
23. General Mills, Inc., op. cit., p. 4-30.
24. Ibid, p. 4-73.
25. Arnold, R. N. and G. B. Warburton. The flexural vibrations of thin cylinders. Inst. Mech. Engrs. (London) Proc. A167: 62-74 (1953).
26. General Mills, Inc., op. cit., p. 4-101.
27. Ibid, p. 3-34.

# DISTRIBUTION LIST

The Martin Company, Baltimore, Maryland  
Attention: Mr. J. Jensen  
Mail No. G-325

Goodyear Aircraft Corporation  
210 Massillon Road  
Akron 15, Ohio  
Attention: Mr. W. Steiner  
Dept. 475G

Radiation, Inc.  
P.O. Box 6904  
Orlando, Florida  
Attention: Mr. P. Button

Massachusetts Institute of Technology  
Instrumentation Laboratory  
68 Albany Street  
Cambridge, Massachusetts  
Attention: Mr. N. Sears

Institute of Technology  
Wright-Patterson Air Force Base  
Attention: Library

Commander  
ARDC Office, USAF  
Naval Research Laboratory  
Washington, D.C.

Air Technical Intelligence Center  
Wright-Patterson AFB, Ohio  
Attention: AFCIN-4E1B

Commander  
Headquarters ARDC  
Andrews AFB  
Washington 25, D.C.  
Attention: RDRWGG. Capt. Speaker

Commander  
Air Force Ballistic Missile Division  
Air Force Unit Post Office  
Los Angeles 45, California  
Attention: WDTG, Lt. Col. F. M. Box  
Attention: WDWWS, Lt. Col. J. Brigham

Commander  
WADD Los Angeles Office  
Los Angeles 45, California  
Attention: WWDML, Capt. Stephenson

Commander  
Air Force Missile Development Center  
Holloman AFB, New Mexico  
Attention: 4DW2

Commander  
Air Force Command and Control Development Division  
Laurence G. Hanscom Field  
Bedford, Massachusetts  
Attention: Library

Aeronautical Research Laboratory  
AF Research Division  
Attention: RRIO, Mr. Callan  
Wright-Patterson AFB, Ohio

Commander  
Rome Air Development Center  
Griffiss AFB, New York  
Attention: RCENN

The Rand Corporation  
1700 Main Street  
Santa Monica, California

NASA  
1520 H. Street, N.W.  
Washington 25, D.C.  
Attention: J. Crocker, Code DA

NASA  
Lewis Research Center  
2100 Brookport Road  
Cleveland, Ohio  
Attention: H. Heppler

Jet Propulsion Laboratory  
4800 Oak Grove Drive  
Pasadena, California  
Attention: H. A. Curtis

Commander  
ASTIA (10 copies)  
Arlington Hall Station  
Arlington 12, Virginia

Commander  
Wright-Air Development Division  
Attention: WWRNGC-2, Captain May  
Attention: WWRNGC-2, Mr. Zingg (2 copies)  
Attention: WWRNGC-2, Mr. Coombs  
Attention: WWRNGC-3, Mr. Moothart  
Attention: WWRMCM, Mr. Woodcock  
Attention: WWRPSG, Mr. Xenakis  
Attention: WWDSI, Library  
Attention: WWAT  
Attention: WWAD, Library

Astrionics Laboratory of ITT Laboratories  
Fort Wayne, Indiana  
Attention: Robert Reis